ABSTRACT

Title of dissertation: NEUTRON DETECTION BY SCINTILLATION OF NOBLE-GAS EXCIMERS

Jacob Collin McComb,
Doctor of Philosophy, 2012

Dissertation directed by: Professor Mohamad al-Sheikhly
Nuclear Engineering Program

Neutron detection is a technique essential to homeland security, nuclear reactor instrumentation, neutron diffraction science, oil-well logging, particle physics and radiation safety. The current shortage of helium-3, the neutron absorber used in most gas-filled proportional counters, has created a strong incentive to develop alternate methods of neutron detection. Excimer-based neutron detection (END) provides an alternative with many attractive properties. Like proportional counters, END relies on the conversion of a neutron into energetic charged particles, through an exothermic capture reaction with a neutron absorbing nucleus (^{10}B, ^{6}Li, ^{3}He). As charged particles from these reactions lose energy in a surrounding gas, they cause electron excitation and ionization. Whereas most gas-filled detectors collect ionized charge to form a signal, END depends on the formation of diatomic noble-gas excimers (Ar_2^*, Kr_2^*, Xe_2^*). Upon decaying, excimers emit far-ultraviolet (FUV) photons, which may

be collected by a photomultiplier tube or other photon detector. This phenomenon provides a means of neutron detection with a number of advantages over traditional methods.

This thesis investigates excimer scintillation yield from the heavy noble gases following the boron-neutron capture reaction in ^{10}B thin-film targets. Additionally, the thesis examines noble-gas excimer lifetimes with relationship to gas type and gas pressure. Experimental data were collected both at the National Institute of Standards and Technology (NIST) Center for Neutron Research, and on a newly developed neutron beamline at the Maryland University Training Reactor. The components of the experiment were calibrated at NIST and the University of Maryland, using FUV synchrotron radiation, neutron imaging, and foil activation techniques, among others. Computer modeling was employed to simulate charged-particle transport and excimer photon emission within the experimental apparatus.

The observed excimer scintillation yields from the $^{10}\mathrm{B}(n,\alpha)^{7}\mathrm{Li}$ reaction are comparable to the yields of many liquid and solid neutron scintillators. Additionally, the observed slow triplet-state decay of neutron-capture-induced excimers may be used in a practical detector to discriminate neutron interactions from gamma-ray interactions. The results of these measurements and simulations will contribute to the development and optimization of a deployable neutron detector based on noble-gas excimer scintillation.

NEUTRON DETECTION BY SCINTILLATION OF NOBLE-GAS EXCIMERS

by

Jacob Collin McComb

Dissertation submitted to the Faculty of the Graduate School of the
University of Maryland, College Park in partial fulfillment
of the requirements for the degree of
Doctor of Philosophy
2012

Advisory Committee:
Professor Mohamad al-Sheikhly, Chair/Advisor
Professor Michael A. Coplan, Dean's Representative
Professor Charles W. Clark
Professor Mohammad Modarres
Professor Gary Pertmer

To my grandfathers,

Robert Lewis Chapman and Dr. Robert Bradbury McComb.

Acknowledgments

The hard work, expertise, and patience of many contributed to this research. Their support has been fundamental to my success. I must first thank my advisor, Professor Mohamad al-Sheikhly, for his mentorship during the past four years. His devotion to his students, myself included, is an inspiration. Secondly, I must thank Professor Michael Coplan for his unparalleled enthusiasm, and attention to detail. It has been a privilege to work with him throughout the course of this project. I am also obliged to the remainder of my thesis committee, Dr. Charles Clark, Professor Mohammad Modarres, and Professor Gary Pertmer, for taking time to review this document, and the work it entails.

Thank you to the FUND group, of which I am honored to be a part. To Dr. Alan Thompson for his empathy, wit, and endless supply of ingenious solutions. To Dr. Robert Vest for many lessons on FUV detection, vacuum systems, and the tricks of building an apparatus. To Dr. Patrick Hughes for conferring to me a mountain of knowledge on the experiments leading up to my own. Thank you again to Dr. Clark, Professor Coplan, and Professor Al-Sheikhly for bringing me into the group and supporting this project.

Thank you to my groupmates past and present, Layla Shahamat, Slavica Grdanovksa, Chanel Tissot, Cameron Goodwin, Ian Gifford, Dr. Ali Mohamed, Amy Beasten, and Daniel Vega. To Vince Adams for teaching me how to sweat pipes, melt wax, and operate a nuclear reactor. To Dr. Timothy Koeth for breathing life back into the MUTR, and for his assistance with the PMT electronics. To the Radiation Safety Office and the Reactor Safety Committee for enduring my experimental proposals.

Thank you to everyone in the Neutron Interactions Group at the NCNR for their assistance, encouragement, and good humor. To Dr. Daniel Hussey, Dr. David Jacobsen, Dr. David Gilliam, Dr. Craig Heimbach, Dr. Jeffrey Nico, Dr. Pieter Mumm, and Dr. Muhammad Arif.

Thank you to the entire SURF staff for being incredibly welcoming and helpful. To Dr. Uwe Arp, Alex Farrell, Dr. Edward Hagley, Dr. Thomas Lucatorto, Dr. Mitchell Furst, Dr. Ping Shaw, and Dr. Steve Grantham.

Thank you to Dr. Gerard Henein at the CNST for teaching me the first thing about boron EBPVD. Additionally, thank you to Dr. John Abrahams and Dr. Thomas Loughran at the UMD FabLab for all of their help in the clean room.

Thank you to Dr. June Tveekrem at NASA Goddard Space Flight Center for her assistance with the photon collection efficiency modeling. Thank you to Dr. Lis Nanver at Delft University of Technology for her insight on boron film fabrication, and for providing us with epitaxial substrates.

Thank you to Dr. Karen Gaskell for her assistance with XPS, Rich Suchoski for his assistance with XRD, and Charlie Chen for his assistance with SEM. Thank you to Howie Grossenbacher and Edd Cole at the Aerospace and IPST Machine Shops for turning my hasty drawings and vague requests into perfectly functioning components.

Thank you to everyone who kept the administrative aspects of my graduate life rolling. To Dr. Kathleen Hart, JoAnne Kagle, Mike McNicholas, Ginette Villeneuve, Olivia Noble, Kay Morris, and Martha Neviaser.

Thank you to those who encouraged and nurtured my pursuit of higher education, including my undergraduate advisor, Professor Jeffrey Dunham, my mentors at ORNL, Dr. Marc Garland and Dr. Saed Mirzadeh, and all of my professors at UMD.

Lastly, and most importantly, thank you to my friends and family. You have always been my biggest source of encouragement and inspiration.

Contents

List of Tables

List of Figures

List of Abbreviations

$^{10}B(n,\alpha)^{7}Li$	Boron-neutron capture reaction
BL-4	Beamline 4
boPET	biaxially-oriented Polyethylene Terephthalate
BRDF	Bidirectional-Reflectance Distribution Function
BT2	NCNR Neutron Imaging Facility
C/T	Counter/Timer
CCD	Charge-Coupled Device
CNST	Center for Nanoscale Science and Technology
CVD	Chemical Vapor Deposition
DHS	Department of Homeland Security
DoD	Department of Defense
DOE	Department of Energy
EBPVD	Electron-Beam Physical Vapor Deposition
END	Excimer-based Neutron Detection
FUV	Far Ultraviolet
GUI	Graphical User Interface
LAND	Lyman-Alpha-based Neutron Detection
LET	Linear Energy Transfer
MCA	Multichannel Analyzer
MCNP	Monte Carlo N-Particle transport code
MRI	Magnetic Resonance Imaging
MRSEC	Materials Research Science and Engineering Center
MUTR	Maryland University Training Reactor
NBSR	National Bureau of Standards Reactor
NCNR	NIST Center for Neutron Research
NG-6	Neutron Guide 6
NGBD	Noble-Gas-Based Detector
NIF	Neutron Imaging Facility
NISP	Nanoscale Imaging Spectroscopy Laboratory
NIST	National Institute of Standards and Technology
NNSA	National Nuclear Security Administration
PCD	Pulse-Charge Distribution
PHD	Pulse-Height Distribution
PMT	Photomultiplier Tube
PSF	Point Spread Function
PSL	Photostimulated Luminescence
PVD	Physical Vapor Deposition
RF	Radio Frequency
RGA	Residual Gas Analyzer
RMS	Root Mean Square
RPM	Radiation Portal Monitor
RTV	Room Temperature Vulcanizer

SEM	Scanning Electron Microscope
SF	Spontaneous Fission
SNM	Special Nuclear Material
SRIM	Stopping and Range of Ions in Matter
SURF	Synchrotron Ultraviolet Radiation Facility
TAC	Time-to-Amplitude Converter
TRIGA	Training, Research, Isotopes, General Atomics
TRIM	Transport of Ions in Matter
UMD	University of Maryland
XPS	X-Ray Photoelectron Spectroscopy
XRD	X-Ray Diffraction

Chapter 1

Introduction

The goal of this research is to provide a fundamental understanding of noble-gas excimer scintillation as a means of neutron detection. This introductory chapter reviews various applications of neutron detection and the demand for alternative detection methods, including a discussion of the helium-3 shortage and the disadvantages of current detectors. Additionally, a brief introduction to excimer-based neutron detection accompanies an overview of the research project. Further details on current neutron detection methods, and other background relevant to the research, are presented in the following chapter.

1.1 Applications of Neutron Detection

Neutron detection is an essential tool in a wide range of scientific and industrial applications. It provides both a means of analyzing nuclear reactions and interrogating material properties. Starting with Fermi's Chicago Pile, in 1942, neutron detectors have been used in every fission reactor core to monitor reactor power levels by measuring neutron flux. These detectors, individually or in arrays, must often cover a flux range of 10 orders of magnitude, and provide spatial flux profiles, as well

as signals for safety trip channels [1, 2, 3, 4]. Today, nuclear fusion research relies on neutron yield and energy distribution measurements to diagnose fusion plasma behavior. These measurements, obtained with neutron detectors, enable estimates of fusion plasma ion velocity, ion density, and reaction rates [5, 6, 7, 8, 9].

A variety of disciplines use neutron scattering techniques to investigate material structure, composition, and dynamics, including biological membrane behavior, magnetism, atomic motion, and material stresses. These methods require large detectors, with small spatial resolutions, to identify where neutrons impinge on a detector's surface. By creating images or patterns, indicative of how neutrons are scattered, absorbed, or transmitted, a great deal may be inferred about the nature of a sample [10, 11, 12, 13, 14]. Neutrino research, dark matter detection, and nuclear physics also rely on neutron detection as a scientific tool [15, 16, 17]. For example, neutrons may interact in large cosmic-ray detection experiments and generate troublesome backgrounds. Neutron detectors are frequently used to identify and veto these signals [18].

Neutron detection plays a role in a number of industrial applications. Oil- and gas-well prospectors use neutron detectors for pulsed-neutron well logging. By attaching neutron generators and multiple neutron detectors to wireline logging packages, it is possible to determine the porosity of the strata surrounding a borehole. In non-shale formations, neutron porosity is indicative of hydrogen content due to hydrogen's efficacy as a neutron moderator. This enables such methods to identify the location of gas and oil reserves [19, 20, 21].

Most recently, neutron detection has become a critical instrument of the Department of Homeland Security (DHS). Special nuclear material (SNM), which includes the fissile isotopes uranium-233, uranium-235 and plutonium-239, and other isotopes associated with such material (^{238}U, ^{240}Pu), undergo spontaneous fission (SF) with non-zero probabilities, providing distinct and detectable neutron signatures (see Table 1.1). This material could potentially be used in a nuclear weapon or dirty bomb, so the DHS has an interest in tracking its exchange and movement. In the U.S., more than 1,400 radiation detecting portal monitors (RPMs), stationed at ports and border crossings, contain neutron detectors to screen cargo and vehicles for SNM. Abroad, 2,000 U.S.-deployed RPMs are used for the same purpose. The DHS, the Department of Energy (DOE) and the Department of Defense (DoD) plan to deploy an additional 3,500 RPMs within the next 6 years [22]. However, due to the helium-3 shortage, these efforts, along with the neutron detection requirements of all other scientific and industrial endeavors, will rely on alternative neutron detection methods to meet their needs [23, 24, 25, 26, 27].

Nuclide	Half-life (years)	Branching ratio	ν	Neutron emission rate ($g^{-1}s^{-1}$)
^{235}U	7.04×10^{8}	7.0×10^{-11}	1.86	1.0×10^{-5}
^{238}U	4.47×10^{9}	5.4×10^{-7}	2.07	0.0136
^{239}Pu	2.41×10^{4}	4.4×10^{-12}	2.16	0.0220
^{240}Pu	6569	5.0×10^{-8}	2.21	920
^{252}Cf	2.638	3.09×10^{-2}	3.73	2.3×10^{12}

Table 1.1: Neutron emission rates of various actinides found in SNM [28]. ν = the average number of neutrons per spontaneous fission.

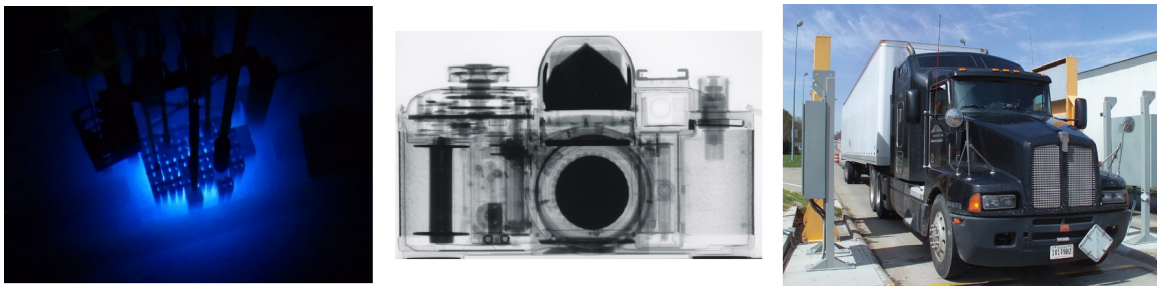

Figure 1.1: Left: Cherenkov radiation illuminating the MUTR reactor core, where power is monitored with various neutron detectors. Center: Neutron radiograph of a camera taken with a spatially sensitive neutron detector [29]. Right: A radiation portal monitor scanning cargo for SNM [30].

1.2 Demand for Alternative Methods

For the past 30 years, helium-3 (^{3}He) proportional counters have been considered the gold standard in thermal neutron detection [22]. However, today, ^{3}He is in short supply and readily available alternatives do not offer the stability, sensitivity, and discrimination capability of ^{3}He detectors [31].

While ^{3}He is a stable isotope, its abundance is very low, at 1.34 ppm of all naturally occurring helium [32]. Enriched ^{3}He is obtained predominantly through the radioactive decay of tritium,

$$^3\mathrm{H} \rightarrow {}^3\mathrm{He} + \beta \qquad \mathrm{T}_{\frac{1}{2}} = 12.3\mathrm{years} \tag{1.1}$$

and is made available as a byproduct of tritium stockpiles, maintained by the National Nuclear Security Administration (NNSA) for nuclear weapons refurbishment. Due to decommissioning efforts, the US halted tritium production in 1988. The supply of ^{3}He has, therefore, significantly diminished and continues to decline [22].

In 2010, the demand for ^{3}He was greater than 76,000 L, with annual domestic production at 8000 L, and total domestic supply at 48,000 L [33]. The detector-related ^{3}He requirements of the DOE, the DHS, and the DoD over the next 5 years is estimated at 100 kliter [34]. A separate estimate by GE Reuter Stokes projects the total demand, including safeguards, non-governmental, and scientific needs at 65 kliter per year, while total supply is less than 20 kliter per year [31]. Along with neutron detection, ^{3}He has other uses including MRI lung imaging, cryogenics, and fusion fuel, further diminishing its availability for use in detectors.

In the absence of ^{3}He, currently available neutron detection alternatives include boron-lined proportional counters, boron-trifluoride proportional counters, fission chambers, lithium-6 scintillators, and semiconductor detectors, among others. Many of these detector types are discussed in the following chapter. The disadvantages of these detectors, such as high cost, toxicity, poor discrimination, poor detection efficiency, and poor durability, have prevented them from replacing ^{3}He [35]. Boron-trifluoride (BF_3) proportional counters, for example, have been in use as long as ^{3}He. Yet, BF_3 is a toxic and corrosive gas, and, therefore, undesirable as a practical detection medium.

In light of the ^{3}He shortage, and the shortcomings of other neutron detectors, this thesis investigates the phenomenon of noble-gas excimer scintillation, which provides the basis for an alternative means of neutron detection.

1.3 Excimer-Based Neutron Detection

Excimer-based neutron detection (END) relies on the same conversion mechanism as most traditional, thermal-neutron detectors. First, a neutron is absorbed by a nucleus with a large neutron absorption cross section, in the form of a solid thin film or a gas. This results in an exothermic reaction and the emission of energetic charged-particle reaction products. Due to their mass and charge, these particles are subject to high rates of linear energy transfer (LET), and, therefore, readily deposit their energy within a compact detector volume. Examples of these reactions include,

$$^{3}\mathrm{He} + n \rightarrow {}^{3}\mathrm{H} + p + 0.764 \text{ MeV} \qquad (\sigma_0 = 5330 \text{ b}) \qquad (1.2)$$

$$^{6}\mathrm{Li} + n \rightarrow {}^{3}\mathrm{H} + \alpha + 4.78 \text{ MeV} \qquad (\sigma_0 = 940 \text{ b}) \qquad (1.3)$$

$$^{10}\mathrm{B} + n \rightarrow \begin{cases} {}^{7}\mathrm{Li} + \alpha + 2.792 \text{ MeV} \\ {}^{7}\mathrm{Li}^{*} + \alpha + 2.310 \text{ MeV} \end{cases} \qquad (\sigma_0 = 3840 \text{ b}) \qquad (1.4)$$

Unlike proportional-tube detectors, END does not depend on the collection of free charge to form an electrical pulse – a result of gas ionization by charged-particles accelerating across an electric potential. Rather, as a scintillation technique, END implements an optical signal as the characteristic neutron signature. By surrounding or mixing the absorbing target medium with a noble gas, the charged-particle reaction products induce the formation of noble-gas excimers as they dissipate kinetic energy.

Noble-gas excimers are loosely-bound, diatomic molecules that exist only in an excited electronic state. In the ground state, noble-gas atoms are repulsive. Therefore, excimers are short-lived and quickly decay by emitting far-ultraviolet (FUV) photons, with wavelengths between 120-180 nm. The emission spectra of argon, krypton, and xenon excimers appear in Figure 1.2.

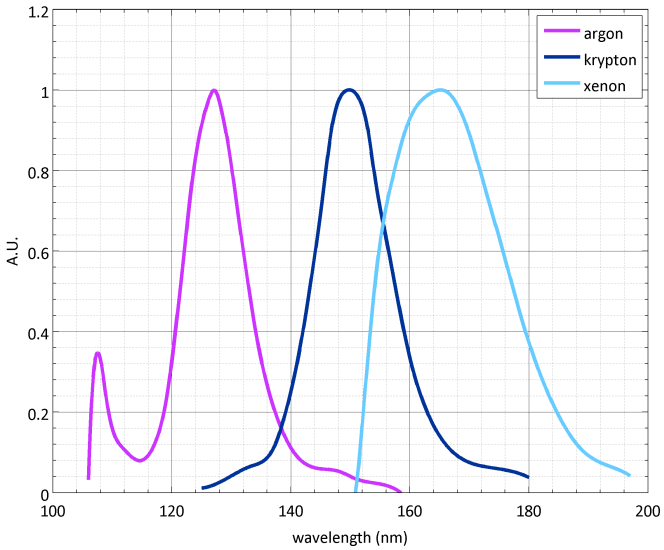

Figure 1.2: Emission spectra of Ar, Kr, and Xe excimers, produced by thyratron modulator excitation. Redrawn from [36]. Peak intensities have been normalized to 1.

This mechanism of FUV photon emission, known as excimer scintillation, provides a unique means of detecting neutrons. A single neutron absorption may liberate MeV of energy due to the exothermic nature of reactions like those shown in Eq. 1.2 - 1.4. Since excimer formation requires 20 - 70 eV [37, 38], depending on experimental conditions, a complete conversion of energy from neutron capture could theoretically produce 10^5 excimer photons. In this way, exothermic neutron absorption under a noble gas background generates a burst of scintillation light, which constitutes a

neutron detection signature. Preliminary experiments have previously demonstrated that this transfer of energy is perhaps greater than 30% efficient [39].

Effectively, END is a combination of processes from two conventional neutron detection methods – (1) gaseous excitation and ionization followed by (2) scintillation and light capture. Nonetheless, a neutron detector based on excimer scintillation has many potential advantages over traditional detectors: highly efficient signal, fast response time, wide dynamic range, flexible geometry, physically robust, low voltage, low pressure, and helium-3 free.

1.4 Research Objectives

This research project investigates noble-gas excimer scintillation following the boron-neutron capture reaction in boron-10 thin films. Specifically, experiments were performed to determine (1) the excimer scintillation yield per neutron absorption for various noble-gas types (Ar, Kr, Xe), gas pressures (50 - 800 torr), and film thicknesses (0.3 - 1.2 μm), and (2) the slow component of the excimer lifetime for various gas types and gas pressures. In addition, computer modeling of charged-particle transport was implemented to simulate energy transfer and photon emission under the same set of experimental conditions. Based on these experimental results and computer simulations, a number of conclusions are drawn regarding the fundamental nature of excimer scintillation from the $^{10}B(n,\alpha)^{7}Li$ reaction and the potential to employ this phenomenon in a deployable neutron detector.

Preliminary research for this project took place at the National Institute of Standards and Technology (NIST) Center for Neutron Research (NCNR) in Gaithersburg, MD. However, due to the construction of a new guide hall at the NCNR, starting in April 2011, research was transferred to the Maryland University Training Reactor (MUTR), in College Park. Many other facilities, including the Synchrotron Ultraviolet Radiation Facility (SURF), the Center for Nanoscale Science and Technology (CNST), and the Neutron Imaging Facility (NIF) at NIST, as well as the Maryland NanoCenter, and the Maryland Materials Research Science and Engineering Center (MRSEC), were also essential for the study.

This thesis is broken into chapters, corresponding to the various elements of the project. Background on neutron detection, the boron-neutron capture reaction, charged-particle transport, and noble-gas excimers is presented in Chapter 2. The preliminary experiments at the NCNR are discussed in Chapter 3. The excimer scintillation experiments at the MUTR are discussed in Chapter 4. Fabrication and characterization of the boron-10 thin-film targets are discussed in Chapter 5. The photomultiplier tube calibration is discussed in Chapter 6. The development and characterization of a thermal-neutron beam at the MUTR are discussed in Chapter 7. Computer modeling of charged-particle transport and excimer photon collection is discussed in Chapter 8. The results of the experiments and their analysis are discussed in Chapter 9. Appendices on α-particle scintillation measurements, and the construction of an FUV reflectometer are also provided.

Chapter 2

Background

The excimer scintillation experiments were based on knowledge from a number of topics which have been previously studied in depth. This chapter provides a brief background on some of these topics including a discussion of current neutron detection techniques, the boron-neutron capture reaction, charged-particle transport and noble-gas excimers.

2.1 The Neutron

The neutron is one of two constituents of all atomic nuclei, known as nucleons. Ernest Rutherford first conceived the neutron in 1920, as a form of nuclear glue, to account for the stability of the atomic nucleus, despite the electromagnetic repulsion of positively-charged protons. James Chadwick then demonstrated the existence of the neutron in 1932, after observing the ejection of energetic protons from paraffin, when bombarding nearby beryllium with alpha particles [40]. Noting similar observations in previous experiments performed by Bothe, Curie, and Joliot, Chadwick posited that the phenomenon was the result of massive, neutral particles, radiating from the (Be+α) interaction [41]. Following this discovery, Fermi's Chicago Pile,

and the Manhattan Project asserted the the neutron's profound impact and abrupt rise to the scientific forefront.

Today, the understanding of the neutron has greatly evolved since Chadwick's discovery. The neutron is no longer considered an elementary particle; rather, it is known to be a hadron composed of three quarks ($|uud\rangle$) and binding, strong force gauge bosons, called gluons [42]. Although the neutron has a neutral charge, it has a non-zero magnetic dipole moment as a result of this internal structure [43]. Additionally, while bound neutrons in stable nuclei are stable, free neutrons decay with a mean lifetime of 881.5 ± 1.5 s [44]. Some properties of the neutron are still under investigation, such as the possibility of a non-zero neutron electric dipole moment [45], and others, like the neutron lifetime, are being refined to higher precision.

2.2 Neutron Interactions

Fundamentally, radiation detection relies on (1) the interaction of radiation within a detection medium, (2) the formation of free charge following an interaction, and (3) the collection of charge to produce an electrical signal [1]. While ionizing radiation may be observed through the direct creation and collection of free charge, the neutron is uncharged and non-ionizing, and therefore more elusive. Neutron detectors, thus, rely on the conversion of neutrons into secondary radiations, often in the form of heavy charged particles. These conversions occur most frequently as one of two types of neutron interaction: elastic scattering (n, n), or exothermic ab-

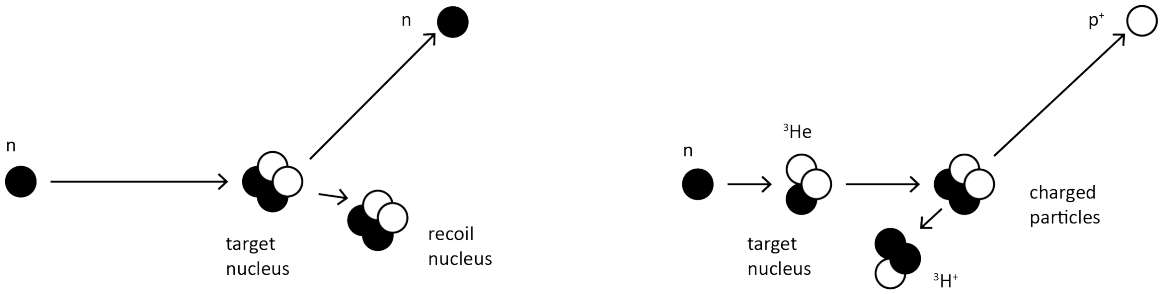

Figure 2.1: Two types of neutron interactions used for neutron detection. Elastic scattering (left) is most effective in detection of energetic neutrons, while exothermic absorption (right) is better suited to convert thermal neutrons.

sorption (n, α), (n, p), $(n, \text{fission})$. A diagram of these two interaction types appears in Figure 2.1. Other interactions, like radiative capture (n, γ) are used in passive neutron detection, such as foil activation, yet are not practical in active detectors, due to the difficulties of discriminating neutron signals from background. Inelastic scattering (n, n') may also contribute to interactions within detectors, but cross sections for this interaction type are typically at least an order of magnitude below elastic scattering cross sections [46].

A neutron-interaction cross section is a measure of the neutron's probability of interaction with a specific nucleus. Different nuclei have vastly different interaction cross-sections, according to their nuclear potential, as shown in Figure 2.2. Nuclei with large cross-sections are ideal for use as neutron detection media. Additionally, interaction cross sections depend on incident neutron energy. Cross sections for neutrons at thermal equilibrium with ambient temperatures ($E = 0.025$ eV) are often more than 3 orders of magnitude higher than those for fast neutrons ($E = 1$ MeV).

Neutron kinetic energy (E) is related to neutron velocity (v) by the relationship,

$$E = \frac{1}{2}mv^2 \tag{2.1}$$

where m is the mass of the neutron (939.565 MeV/c^2). A large number of nuclei are classified as $^1/_v$ absorbers because their neutron-absorption cross sections are inversely proportional to incident neutron velocity at thermal and, sometimes, epithermal energies [2]. Due to this relationship, fission neutrons, with an average energy of 1 MeV, are more difficult to detect than thermal neutrons. In many applications, the physical and practical challenges of fast-neutron detection have spurred more interest in the development of detectors based on thermal-neutron capture [23]. Neutron moderators, such as polyethylene, are often incorporated into neutron detector packages to slow high energy neutrons, and increase their probability of interaction, particularly when sources of interest include fissile material.

Interaction cross sections may be used to determine the neutron interaction rate within a target or detector. For a monodirectional neutron beam, this relationship takes the form of the Beer-Lambert law of exponential attenuation,

$$I = I_0\, e^{-N\sigma x} \tag{2.2}$$

where I is the intensity of the transmitted beam, I_0 is the intensity of the incident beam, N is the atom density of the target, σ is the microscopic cross section of the

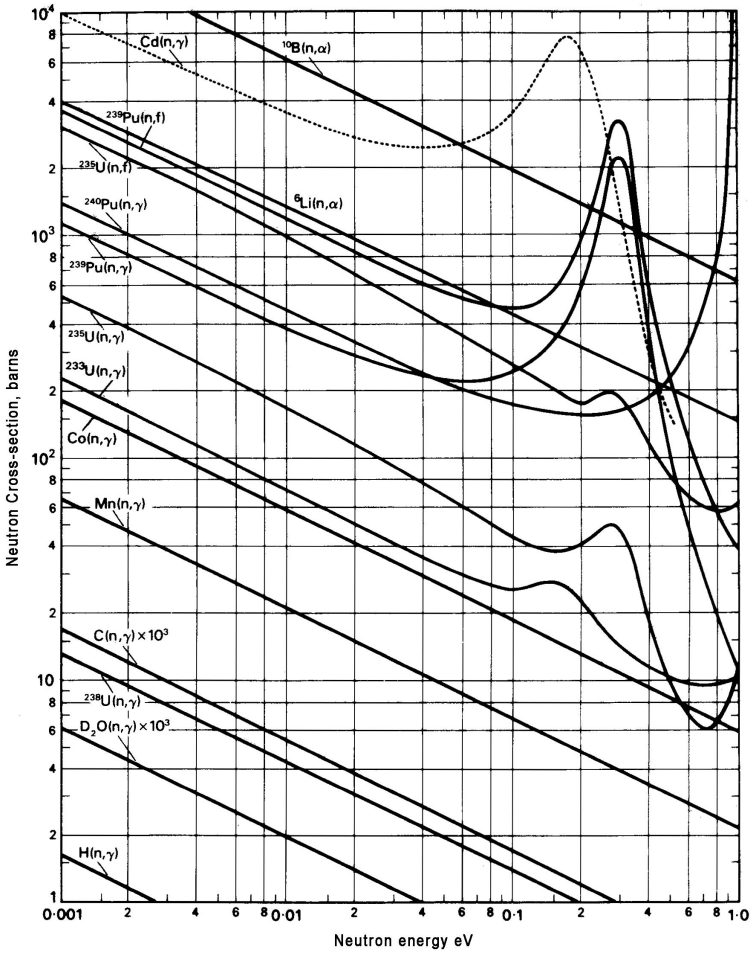

Figure 2.2: Energy-dependent neutron interaction cross sections of various nuclei over cold and thermal energy regions [47].

target, and x is the thickness of the target. The interaction rate is then determined by the equation,

$$F = I_0(1 - e^{-N\sigma x}) \tag{2.3}$$

Following an interaction, a neutron indirectly creates ionizing radiation through a transfer of energy – either from a fast neutron to a recoiling nucleus, or from nuclear binding energy to charged-particle reaction products. This secondary radiation may be detected in a proportional tube, scintillator, semiconductor, or other traditional detector configuration. In the case of exothermic absorption, written as $\mathrm{X}(n, b)\mathrm{Y}$, the reaction Q-value, which mostly appears as the total kinetic energy of the reaction products, may be calculated using the equation,

$$Q = (m_X + m_n - m_Y - m_b)c^2 \tag{2.4}$$

where m_n and m_X are the masses of the neutron and the neutron-absorbing nucleus, m_b and m_Y are the masses of the reaction products, and c is the speed of light (931.5 MeV/u). In the case of elastic scattering, the energy imparted to the recoiling nucleus is given by,

$$E_A = \frac{E + E' - 2\sqrt{EE'}\cos(\theta)}{A} \tag{2.5}$$

where E is the energy of the incident neutron, E' is the energy of the scattered neutron, θ is the scattering angle of the scattered neutron, and A is the atomic mass number of the scattering nucleus.

Ideally, the amount of energy deposited within a detector by each neutron interaction should be large in comparison to other types of radiation, and, therefore, distinguishable from background events. Thus, nuclei with large neutron-reaction Q-values, or large maximum recoil energies, make the best neutron detection media. In recoil-type detectors, for example, the maximum energy transferred to a nucleus in an elastic scattering collision is inversely proportional to that nucleus' mass. From Eq. 2.5, this is given by the equation,

$$E'_{min} = \left(\frac{A-1}{A+1}\right)^2 E \tag{2.6}$$

where E is the energy of the incident neutron, E' is the energy of the scattered neutron, and A is the atomic mass number of the scattering nucleus. Accordingly, low atomic mass materials make optimal detection media for fast neutron detectors.

Both the probability of interaction, and the average energy deposition per interaction, must be taken into account when designing an effective neutron detector. Other characteristics, such as background sensitivity, cost, and durability, must also be considered. Some of the most common detector configurations and their properties are discussed in the following section.

2.3 Neutron Detection

Neutron detectors come in several varieties. The most popular are based on gas-filled proportional tubes, scintillators, and semiconductors. Detectors are often compared on the basis of application specific requirements, which may include: intrinsic detection efficiency, collection efficiency, non-neutron event discrimination, energy resolution, spatial resolution, signal response times, and physical integrity.

Three definitions will be useful in this discussion of detectors, and the subsequent interpretation of the results from the excimer scintillation experiment. Intrinsic detector efficiency (or quantum efficiency) is defined as the probability of detecting a given quanta of radiation incident on a detector, and is represented by the equation,

$$\epsilon_{\text{int}} = \frac{\text{number of pulses recorded}}{\text{number of radiation quanta incident on detector}} \tag{2.7}$$

Collection efficiency (or absolute efficiency) considers both the intrinsic efficiency of a detector and its geometrical configuration with respect to a radiation source, and is given by the equation,

$$\epsilon_{\text{abs}} = \frac{\text{number of pulses recorded}}{\text{number of radiation quanta emitted by source}} \tag{2.8}$$

Gamma ray discrimination (or rejection efficiency) is a detector's ability to positively identify a neutron among various types of radiation interactions, and is represented by the equation,

$$\epsilon_{\text{reject}} = \frac{\text{number of false neutron counts}}{\text{number of gamma rays incident on detector}} \tag{2.9}$$

2.3.1 Gas-filled neutron detectors

Gas-filled neutron detectors include ^{3}He and BF_3 proportional counters, helium (^{4}He) and methane (CH_4) recoil detectors, ^{10}B-lined proportional counters and fission chambers. In this detector configuration, a neutron interacts with a gas or a solid coating, contained within an aluminum or stainless steel cathode enclosure. The neutron transfers kinetic energy to a recoil nucleus (fast neutron), or initiates a reaction with energetic charged-particle reaction products (thermal neutron). This energy transfer initiates the ionization of a gas detection medium. Typically, about 30 eV of energy is required to form an ion pair [1].

An electric field applied across the gas volume accelerates ionized electrons towards a central anode wire. The voltage difference between the anode wire and the cathode enclosure determines the gas multiplication characteristics of the detector and, consequently, the magnitude of the electrical output signal. Figure 2.3 shows the various gas multiplication regions with respect to the applied voltage of a gas-filled detector. In the proportional region, primary electrons in gas-filled detectors gain

enough energy to create 10^3 to 10^5 secondary and tertiary electrons (Townsend avalanche). When this charge is collected on the anode wire at the center of the tube, an electrical pulse is generated. Typically, proportional tube neutron detectors are operated in the 1-3 kV range [48]. A diagram of this detector configuration appears in Figure 2.3.

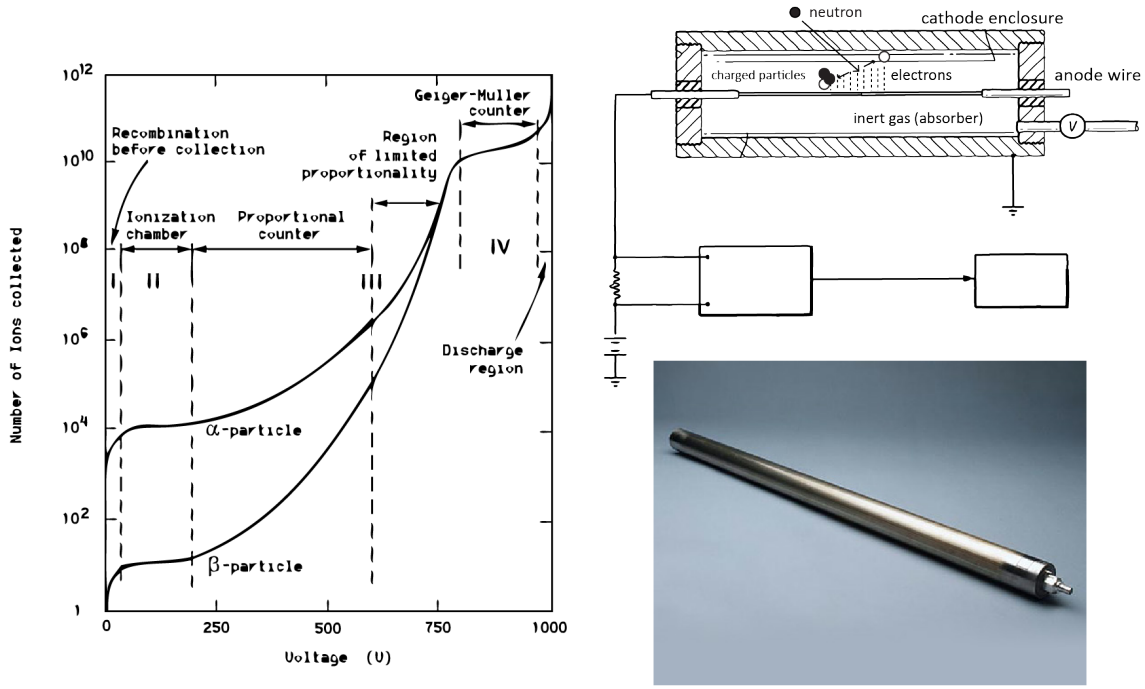

Figure 2.3: Left: Multiplication curves for gas ionization detectors showing the various regions of gas multiplication [49]. The abscissa values depend on gas type and detector characteristics. Upper right: Diagram of a gas filled proportional counter. Lower right: Photograph of a helium-3 proportional tube [4].

The mean free path of electrons in a proportional counter is 1-2 μm. While secondary electrons are collected within 10^{-8} s, the drift velocity of the positive ions is three orders of magnitude lower. Response and recovery times of gaseous detectors are limited to a few microseconds due to this slow collection of positive charge [48]. Pressures of gas-filled detectors range between 1 and 20 atm. However, pressures in the higher end of this range can lead to charge recombination in some gases and,

therefore, impose limitations. Heavy gases, such as Ar or CO_2, may be added to gas-filled detectors to reduce reaction-product ranges, enhance charge collection, and decrease charge collection time. Polyatomic gases may be added as quench gas to shorten the avalanche process, improve pulse height resolution, and prevent gamma-ray pile up. Non-neutron background events, such as Compton scattering of gamma rays, can plague these detectors with false positives. However, gamma rays have much lower LET than charged particles, especially in gaseous media, and give rise to lower amplitude output signals. To some extent, backgrounds may be dealt with through pulse-height discrimination.

Typical portal-monitor ^{3}He proportional counters have intrinsic efficiencies of 70-80%, and gamma-ray rejection efficiencies of 10^{-5} [23]. Boron-trifluoride tubes are limited to pressures of 1 atm due to high-voltage biasing, and achieve intrinsic efficiencies of $\sim$20% that of ^{3}He tubes [50]. Conversion-layer detectors, or lined detectors, have intrinsic efficiencies of 1-5% relative to ^{3}He-tube efficiencies, but may be bundled to increase the collection efficiency of a single detector package [51]. In ^{10}B and fissile-deposit lined detectors, the short ranges of charged-particle reaction products limit absorber layer thicknesses to $\sim$2 μm. These wall-layer detectors use standard detector gases, such as P-10, which are chosen for ideal charge collection properties. Lithium is not widely used as a thermal neutron absorber in gas-filled detectors due to its chemical reactivity. Fast-neutron, gas-filled recoil detectors, using natural helium or methane, have intrinsic efficiencies of $\sim$1% for neutrons between 20 keV and 20 MeV, and often have faster response times (10-100 ns) than

thermal neutron tubes [48]. Modern approaches to proportional neutron counters include boron-lined straw tube detectors, and multi-wire proportional chambers with anode wire grids [52, 53].

2.3.2 Scintillation-based neutron detectors

Scintillation neutron detectors consist of a scintillation medium coupled to a photomultiplier tube, CCD, photodiode, or other photon detector. In this configuration, a fast neutron elastically scatters in a scintillation medium, transferring some of its kinetic energy to a recoil nucleus. Alternatively, a thermal neutron may be absorbed by a nucleus with a large absorption cross section, embedded within or coupled to the scintillation medium. An exothermic reaction then emits charged particles, which scatter and transfer energy to a recoil nucleus or a phosphor dopant. The transfer of energy, by either fast or thermal neutrons, excites a phosphor and generates light. This light may then be collected by a photon detector. Scintillators are designed in the form of thin fibers, crystalline or amorphous solids, liquids, or, in the case of excimer-based detection, gaseous media. Common neutron detection scintillators include liquid and solid organics (proton-recoil plastics, ^{10}B, Gd, or ^{6}Li loaded plastics), and solid inorganics (Li crystals, ZnS(Ag) compounds, lithiated glass, and glass fibers). Fast-neutron scintillators have also been developed using ^{3}He [54, 55, 56]. A diagram of a typical scintillation detector appears in Figure 2.4.

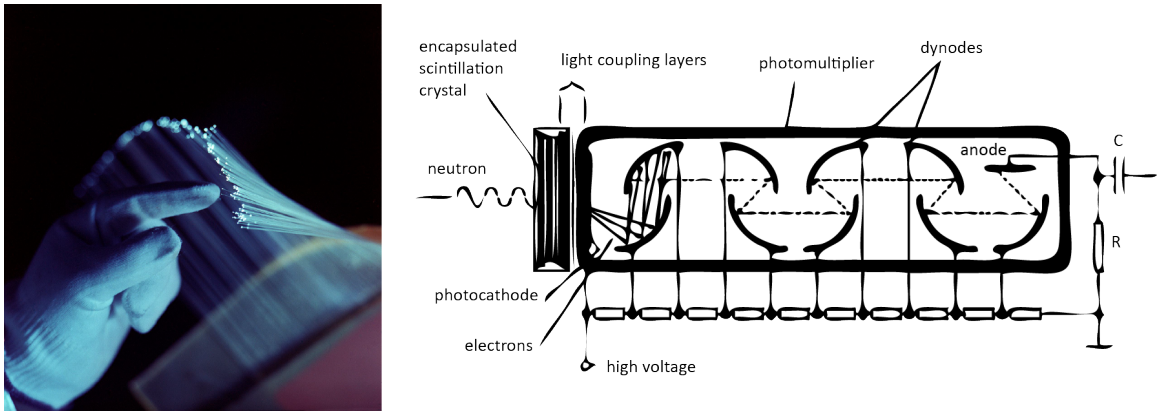

Figure 2.4: Left: Lithium-doped scintillating fibers used in a large-area neutron detector [23]. Right: Diagram of a scintillation-based neutron detector using a solid scintillation crystal and a photomultiplier tube. Redrawn from [57].

Characteristics of ideal scintillators include (1) transparency to their own radiation, (2) high conversion efficiency between recoil energy and fluorescent radiation, (3) short scintillation decay times, (4) linear conversion, and (5) glass-like indices of refraction [1]. Ranges of recoil nuclei and charged particles are significantly shorter in dense scintillators than in proportional tubes. As a result, fast response times, on the order of a few nanoseconds, make scintillators more attractive in specific applications [48]. One fundamental disadvantage of solid scintillation-based detectors are high sensitivities to gamma-ray backgrounds. In many cases, detection probabilities for neutrons and gamma rays are nearly comparable. However, some scintillators exhibit delayed fluorescence (phosphorescence) from triplet-state excitations. These delayed emissions enable pulse-shape discrimination for distinguishing neutron radiation in mixed fields [58]. High-LET particles produce higher triplet densities and are, therefore, distinguishable from low-LET radiation, as shown by the distinct decay pulses in Figure 2.5 [59]. This same phenomenon may prove useful for gamma ray discrimination in future excimer-based neutron detectors.

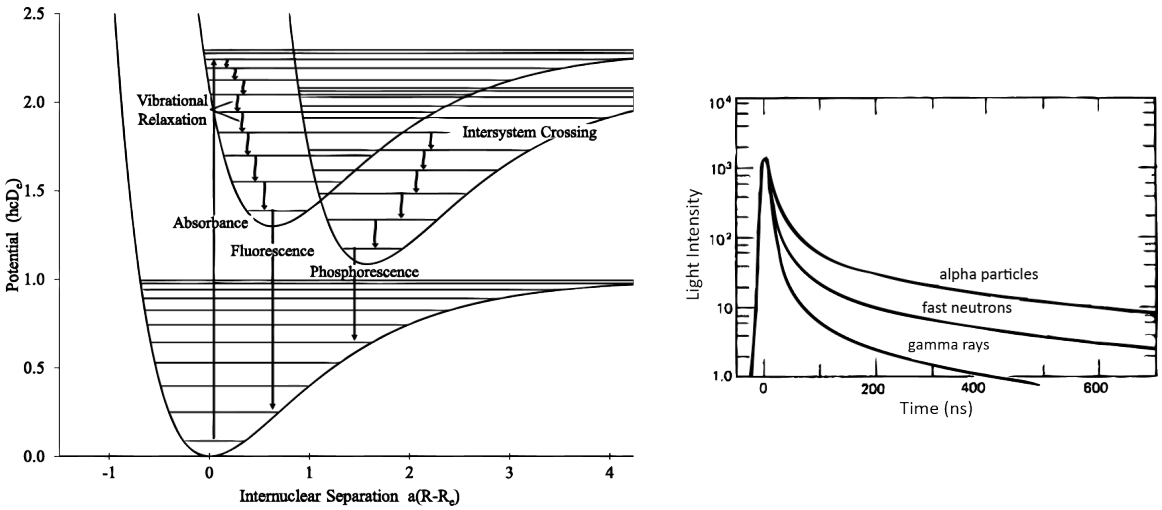

Figure 2.5: Left: Potential curve diagram of fluorescence and phosphorescence from singlet and triplet states [60]. Right: Plot of scintillation light intensity over time for particles with different LETs, demonstrating variable pulse shapes used to distinguish radiation types [61].

Scintillation-based neutron detectors have been developed predominantly for use in neutron radiography, rather than SNM detection [23]. Lithium-bearing solid plastics, for example, have been fabricated with intrinsic efficiencies near 100%, for thicknesses of 10 mm [62]. Inorganic scintillators are also widely used. Modern ZnS:Ag/^{6}LiF detectors have intrinsic thermal-neutron detection efficiencies of $\sim$40%. Similar detectors using ZnS:Ag/$^{10}B_2O_3$ have been fabricated with intrinsic efficiencies of near 60% [63]. These scintillators are usually kept quite thin (1-2 mm) due to their relative opaqueness. Even more modern scintillators (ie. Cs_2LiYCl_6:Ce) have shown promise of neutron-gamma signal separation through pulse-height discrimination [23]. Some characteristics of common scintillators, including typical light yields, appear in Table 2.1.

Table 2.1: Characteristics of various thermal-neutron scintillators, including light yields per neutron (Y_n) and gamma-ray (Y_γ) interaction, emission wavelengths ($\lambda_{h\nu}$), and scintillation decay times (τ) [64].

Host	Dopant	Density (g/cm^3)	Y_n	Y_γ	$\lambda_{h\nu}$ (nm)	τ (ns)
^{6}Li-glass	Ce	2.5	6000	4000	395	75
^{6}LiI	Eu	4.1	50,000	12,000	470	1400
^{6}LiF/ZnS	Ag	2.6	160,000	75,000	450	1000
$LiBaF_3$	Ce,K	5.3	3500	5000	190-330	1/34/2100
$LiBaF_3$	Ce,Rb	5.3	3600	4500	190-330	1/34/2400
$^6Li_6Gd(^{11}BO_3)_3$	Ce	3.5	40,000	25,000	385	200/800
$Cs_2{}^6LiYCl_6$	Ce	3.3	70,000	22,000	380	1000
$Cs_2{}^6LiYBr_6$	Ce	4.1	88,000	23,000	389	89/2500

2.3.3 Semiconductor neutron detectors

Semiconductor neutron detectors consist of a semiconductor layered with a thermal-neutron converter, or a fast-neutron recoil material. These detectors exploit the narrow band gap in specific materials to generate electron-hole pairs. After a neutron is absorbed or scattered in a material coupled to the semiconductor, charged particles or recoil nuclei excite electrons from the valance band into the conduction band, leaving behind positively-charged holes. The motion of these electron-hole pairs in an applied electric field constitutes the fundamental detection signature, with no need for further amplification. Neutron detectors of this type include planar, semiplanar (pyramidal), and pillared thin-film geometries, as well as multisurface detectors. Common materials in these detectors include ^{6}LiF and ^{10}B, on Si or GaAs semiconducting substrates, and bulk detectors of CdTe, HgI, B_4C and BN [62, 65]. A diagram of a semiconductor neutron detector appears in Figure 2.6.

Semiconductor detectors are sought after for their ruggedness and fast response times. Typical electron-hole lifetimes in pure Si are on the order of 100 ns [68].

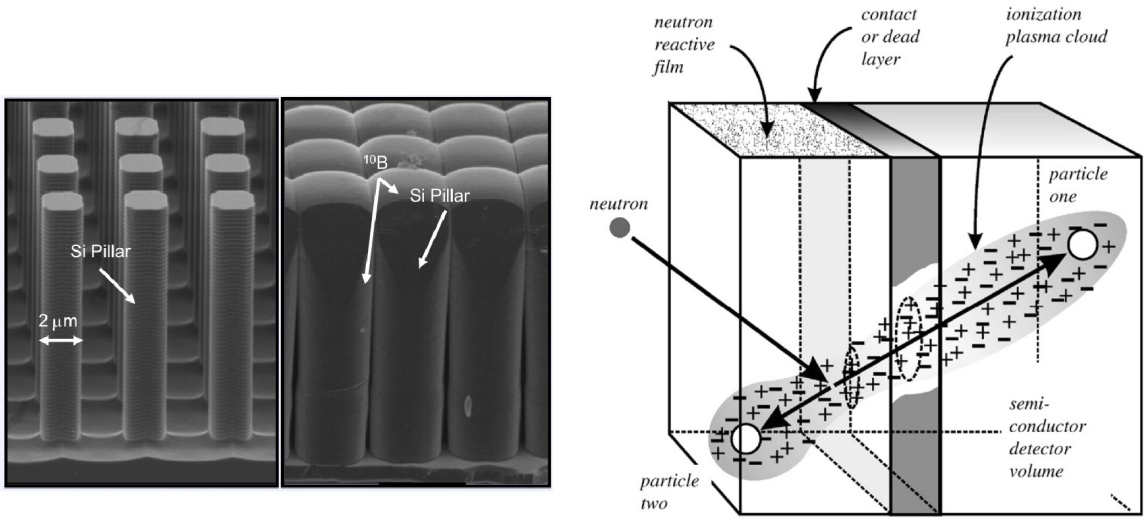

Figure 2.6: Left: SEM image of ^{10}B deposited on a Si pillar structure for a semiconductor neutron detector [66]. Right: Diagram of a semiconductor neutron dector [67].

In contrast to proportional tubes and some scintillation detectors, semiconductor neutron detectors do not require high voltage. Each neutron interaction has the potential to generate 1.5×10^6 electron-hole pairs [69]. However, much of the Q-value or recoil energy from a neutron interaction may be lost in a converter layer or contact layer, before the charged-particle reaction products reach the active semiconductor. Both the thickness of the conversion-layer films, and the orientation of the detector with respect to the neutron source, affect the average energy deposition within the active volume. Additionally, gamma-ray scattering in silicon is non-negligible, and has the potential to create significant background noise in mixed fields. Gamma-ray rejection efficiencies of semiconductor neutron detectors range between 10^{-2} and 10^{-6} [23].

Standard 2D layer designs in semiconductor neutron detectors typically have intrinsic efficiencies of 2-5%. Compound devices using multiple thin-film conversion

layers, or even multiple converter types, have achieved thermal efficiencies greater than 25% [67]. More recently, attempts to increase semiconductor detector efficiency have turned to advanced semiconductor processing techniques to fabricate more exotic structures. Pillar-type detectors, for example, have been fabricated with intrinsic efficiencies greater than 50% [70]. Single-crystal diamond has been used in combination with ^{6}Li to form a dual fast and thermal neutron detector with comparable efficiencies [71]. Despite their advantages, semiconductor neutron detectors are limited by size. The fabrication of semiconductor detectors with surface areas and collection efficiencies large enough for SNM-detection, still faces numerous practical challenges.

2.3.4 Other neutron detection methods

A variety of neutron detectors do not fall into the above categories. However, some of the technologies are immature, undeveloped, or unsuited for most applications. Microchannel plates rely on electron showers in narrow capillaries of borosilicate glass [72]. Water-based Cherenkov detectors contain large volumes of water and suspended gadolinium particles ($GdCl_3$), which, when activated, emit beta radiation to generate Cherenkov light [73]. Bubble chambers employ superheated or supertensioned fluids, which nucleate upon interaction with energetic radiation [74]. Calorimeters with minuscule heat capacities (10 nJ/K) can detect neutron reactions through small changes in temperature [75]. An array of passive detection techniques also exist, including foils, dosimeters, and imaging plates.

Excimer-based neutron detection is an alternative method which has not yet received significant attention. The remainder of this chapter addresses topics that directly relate to the investigation of this technique.

2.4 Boron-Neutron Capture

The excimer scintillation experiment at the University of Maryland used thin films of boron-10 to convert neutrons into charged particles. Boron is a metalloid, found in nature in oxide form, with an abundance in the earth's crust of 8.6 ppm by mass [76]. Boron-10 (^{10}B) is one of two stable isotopes of boron, with an isotopic abundance of 19.9%, and a large thermal-neutron absorption cross section ($\sigma_0 = 3842 \pm 8$ b) [32, 77]. A plot of the energy-dependent ^{10}B absorption cross section appears in Figure 2.7. The cross section is structureless below 100 keV, an example of a nearly ideal $1/v$ absorber.

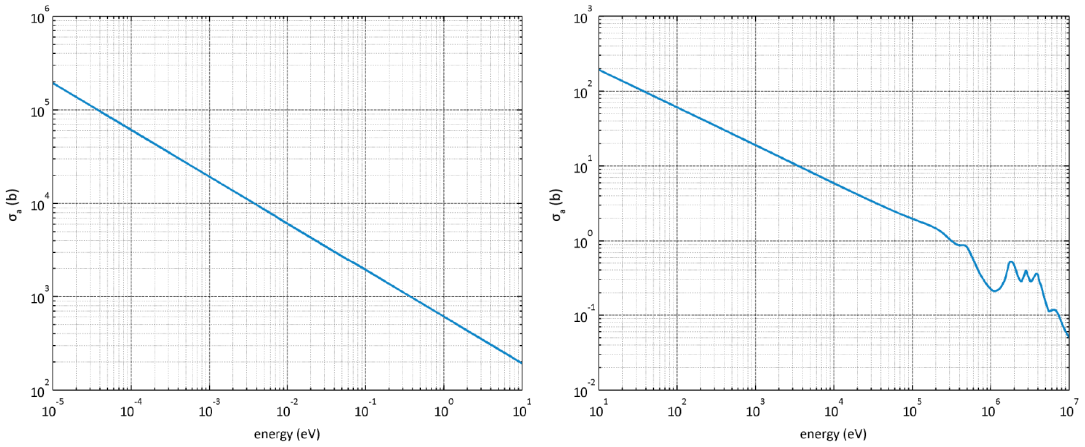

Figure 2.7: Boron-10 neutron absorption cross section between 0.01 meV and 20 MeV [77].

For 99.93% of thermal-neutron absorptions, ^{10}B undergoes an exothermic neutron-capture reaction, resulting in the emission of an alpha particle and a ^{7}Li ion, as shown in Figure 2.8. The products of the $^{10}\mathrm{B}(n,\alpha)^{7}\mathrm{Li}$ reaction are released with a total energy of either 2.792 or 2.310 MeV, depending on the final state of the ^{7}Li nucleus. In the first case, the ^{7}Li nucleus is emitted in the ground state. In the second case, it is emitted in an excited state, which decays with a 10^{-13} s half-life by emitting a 0.48 MeV gamma ray. The branching ratios for these two pathways are 6% and 94%, respectively. Following thermal-neutron absorption, the reaction products are emitted isotropically, in opposite directions, with equal momentum. This holds true for all neutrons of relatively low incident momentum. Thus, the total reaction Q-value is split among the products as 1.02 MeV (^{7}Li) and 1.78 MeV (α), for the ^{7}Li ground-state pathway, or 840 keV (^{7}Li) and 1.47 MeV (α), for the ^{7}Li excited-state pathway.

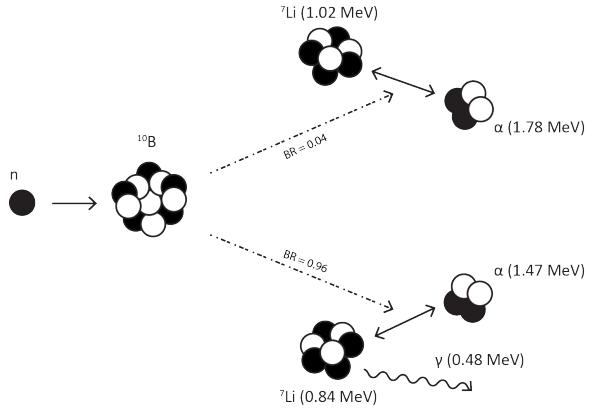

Figure 2.8: Boron-neutron capture reaction.

Due to its relative abundance, large absorption cross section, and large branching ratio to an exothermic reaction, ^{10}B is an ideal nucleus for conversion in a thermal-neutron detector. In many instances, it is a suitable replacement for ^{3}He. Following

the boron-neutron capture reaction, the kinetic energy of the reaction products may be used to generate detectable, secondary radiation. The transport of these charged particles is discussed in the following section.

2.5 Charged-Particle Transport

Heavy charged particles, such as atomic nuclei, are a form of directly ionizing radiation, which interact continuously when passing through matter. The interactions to which they are subject include the long-range Coulomb force, elastic scattering via collisions with atomic electrons, inelastic scattering, resulting in the excitation of atomic electrons, and nuclear recoil. Typically, energetic charged particles interact thousands or tens of thousands of times before accumulating electrons to become a neutral atom. This leads to an abundance of ionized and excited atoms along a charged particle's path, which may generate an electrical or optical signal within a radiation detector.

Several definitions are helpful to understand charged-particle transport, including stopping power, range, and straggling. Stopping power is defined as the total energy lost per unit path length, or the rate of energy loss at a given point along a particle's path [2]. Without accounting for energy loss due to nuclear interactions, linear stopping power may be represented by the relationship,

$$S = \left(\frac{dE}{dx}\right)_{\text{col}} + \left(\frac{dE}{dx}\right)_{\text{rad}} \tag{2.10}$$

where $\left(\frac{dE}{dx}\right)_{\text{col}}$ represents energy loss due to collisions involving ionization and electronic excitation, and $\left(\frac{dE}{dx}\right)_{\text{rad}}$ represents energy loss by radiation. For heavy charged particles, radiative energy loss only becomes significant at energies in the GeV range. This component may, therefore, be ignored when dealing with energies in the realm of thermal-neutron reactions.

The first term in Eq. 2.10 is often referred to as a particle's rate of linear energy transfer (LET). Heavy charged particles, such as those from the boron-neutron capture reaction, are considered high-LET radiation because they deposit their energy over very short distances. Classically, charged-particle energy loss for non-relativistic, high-energy ions can be described by the Bethe-Bloch stopping power relation,

$$S = -\frac{1}{N}\frac{\mathrm{d}E}{\mathrm{d}x} = \frac{1}{(4\pi\epsilon_0)^2}\frac{4\pi z^2 e^4}{m_0 v^2} NZ\left[\ln\left(\frac{2m_0 v^2}{J}\right)\right] \tag{2.11}$$

where z is the charge number of the particle, e is the charge of the electron, m_0 is the rest mass of an electron, v is the charged particle velocity, N is the atomic density of the material, Z is the atomic number of the material, ϵ_0 is the vacuum permittivity, and J is an experimentally determined quantity describing the average excitation potential of a representative atom in the material. For non-relativistic particles of mass m and energy E, particle velocity is given by the equation,

$$v = \sqrt{\frac{2E}{m}} \tag{2.12}$$

Range is defined as the point at which charged particle ionization falls to zero. Ranges for specific particle types, energies, and materials are often empirically tabulated, or calculated based on tabulated values, using scaling laws and the Bragg-Kleeman rule. If the range (R) of a particle is known, the stopping time of the particle may be calculated using the equation,

$$T = \frac{R}{\langle v \rangle} = \frac{R}{K}\sqrt{\frac{m}{2E}} \tag{2.13}$$

where $\langle v \rangle$ is the average particle velocity, and K is a factor used to account for non-uniform deceleration of the particle. Typically, because a particle's energy loss is greater towards the end of its range, K is approximated as a fraction somewhat greater than $1/2$ [1].

The maximum energy that can be transferred from a charged particle in a single collision with an electron, is about 1/500 of the particle energy per nucleon. Thus, the deflection of a charged particle by any one interaction is small, and its path will tend to be fairly straight until the end of its range. Specific energy loss and charged particle ranges are often represented by characteristic Bragg curves. The Bragg curves of charged-particle reaction products from the boron-neutron capture reaction, traveling through boron, appear in Figure 2.9. The maxima toward the end of the α-particle curves, represent the increase in the energy loss rate at the end of the particle's path. Additionally, the small tails at the very end of these curves are due to range straggling, the variation in ranges of charged particles of a given

type and energy. This effect is attributed to the stochastic nature of charged-particle interactions.

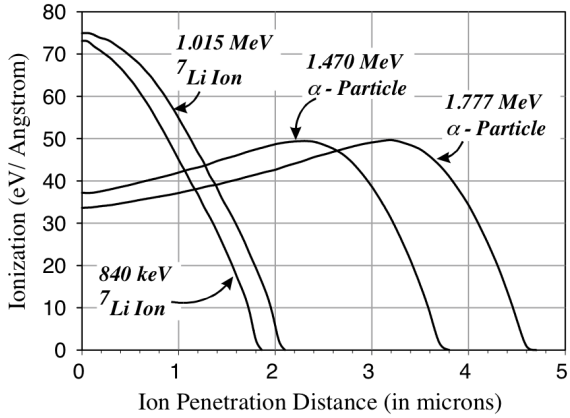

Figure 2.9: Ranges of charged particles in boron [67].

Knowledge of charged-particle ranges in various media is useful for predicting the behavior of thermal-neutron detectors. For example, Wang *et al.* describe analytical calculations of efficiencies of multi-layer boron thin-film semiconductor detectors using charged particle ranges [78]. It is also possible to simulate charged particle transport using Monte Carlo methods as statistical solutions for the Bethe-Bloch equation. In this research, the TRIM (Transport of Ions in Matter) code was used to simulate the transport of the charged particle products from the $^{10}\mathrm{B}(n,\alpha)^{7}\mathrm{Li}$ reaction, under conditions similar to those created in the scintillation experiments. The results of these simulations appear in Chapter 8.

Excimer-based neutron detection relies on the transfer of energy between charged-particle reaction products and the surrounding noble-gas atoms to generate noble-gas excimers. A neutron detection signal is provided by photon emissions from these excimers, as discussed in the following section.

2.6 Noble-Gas Excimers

Excimers were first identified in 1927 by Lord Rayleigh, who documented broad continuum emissions from mercury vapor in the ultraviolet region of the electromagnetic spectrum [79]. Later, in the 1930s, Hopfield and Mulliken recorded emissions from the first rare-gas excimers using high-pressure helium, and calculated potential curves for excited excimer states. Excimer lasers, widely used today in medical surgeries and photolithography, were conceived in 1960, and, in 1970, stimulated emission of noble gas excimers was first observed by Basov while irradiating liquid xenon with high-energy electrons [80, 81].

Ground state interactions of two closed-shell atoms are typically repulsive. The interaction of an excited closed-shell atom with the ground state of another closed-shell atom may, however, form a bound state. A noble-gas excimer is a dimer molecule of two noble-gas atoms that exists only in an excited electronic state (ie. Ar_2^*, Kr_2^*, Xe_2^*). When these excimers decay, they dissociate and emit far-ultraviolet radiation, characterized by broad continua, as shown by the spectra in Figure 2.10. The term excimer may also refer to excited dimers of other monatomic gases (ie. Hg_2^*), excited aromatic molecules, as well as mixed dimers, called exciplexes (KrXe*, ArF*, $HgNH_3$*). In this thesis, excimer will refer exclusively to excited homonuclear dimers of the rare gases. This specific type of excimer, when produced by the slowing down of charged particles, forms the basis of an optical neutron detection signal. Some of the relevant noble-gas properties appear in Table 2.2.

Table 2.2: Properties of noble gases, including atomic number (Z), atomic weight (A), density (ρ) and mean free path (l) at STP, peak excimer emission wavelength (λ_{peak}), and peak excimer photon energy ($E_{h\nu}$) [76, 54].

Gas	Z	A (u)	ρ (kg/m^3)	l (nm)	λ_{peak} (nm)	$E_{h\nu}$ (eV)
Argon	18	39.95	1.761	72.29	128	9.57
Krypton	36	83.80	3.696	55.66	150	8.42
Xenon	54	131.3	5.897	40.55	175	7.02

2.6.1 Excimer scintillation

As energetic charged particles travel through noble gases, they deposit their energy by excitation and ionization of the surrounding noble-gas atoms. These processes include,

$$R + A \rightarrow e + A^+ + R' \tag{2.14}$$
$$R + A \rightarrow A^* + R' \tag{2.15}$$
$$e + A^+ \rightarrow A^* \tag{2.16}$$

where R is a charged particle, A is a noble-gas atom, e is an electron, A^+ is an ionized noble-gas atom, R' is a charged particle of reduced energy, and A^* is a noble-gas atom in an excited electronic state [54]. Excited noble-gas atoms may decay through the radiative emission of a far-ultraviolet photon,

$$A^* \rightarrow A + h\nu_a \tag{2.17}$$

However, at increased pressures (10^3–10^4 Pa), the probability of another atom re-absorbing this atomic photon ($h\nu_a$) greatly increases. These photons are said to become "trapped" within the gas volume [54]. Independently, the likelihood of

three-body collisions also increases at higher pressures. This leads to the excimer forming process,

$$A^* + 2A \rightarrow A_2^* + A \tag{2.18}$$

where A_2^* is a noble-gas excimer. This reaction occurs on a time scale of 10^{-11} to 10^{-12} s [54]. The excimers may then decay by emitting a photon,

$$A_2^* \rightarrow 2A + h\nu_m \tag{2.19}$$

Variations in the amount of energy carried away by the third body, and the repulsive nature of the molecular ground state, enable emissions to occur over a broad molecular continuum. Examples of these continua appear in Figure 2.10. The two principal maxima in these spectra are the result of excimer vibrational levels. The short wavelength maxima are attributed to transitions from high vibrational levels, and the longer wavelength maxima are attributed to the same transitions following vibrational relaxation of the molecular states [82]. Because molecular excimer emissions do not coincide with atomic absorption resonances of the same gas, noble gases are highly transparent to their own excimer radiation. This transparency makes excimer photons ($h\nu_m$) ideal constituents of a radiation detection signal.

The atomic ground states of the noble gases beyond helium have the electron shell configuration s^2p^6 ($^1S_0$). The first excited configuration, s^2p^5s, describes both singlet ($^1P_1$) and triplet ($^3P_{0,1,2}$) spin states. The combination of an excited noble-gas atom with a ground-state noble-gas atom may form the molecular states $^1\Sigma_u^+$ or $^3\Sigma_u^+$.

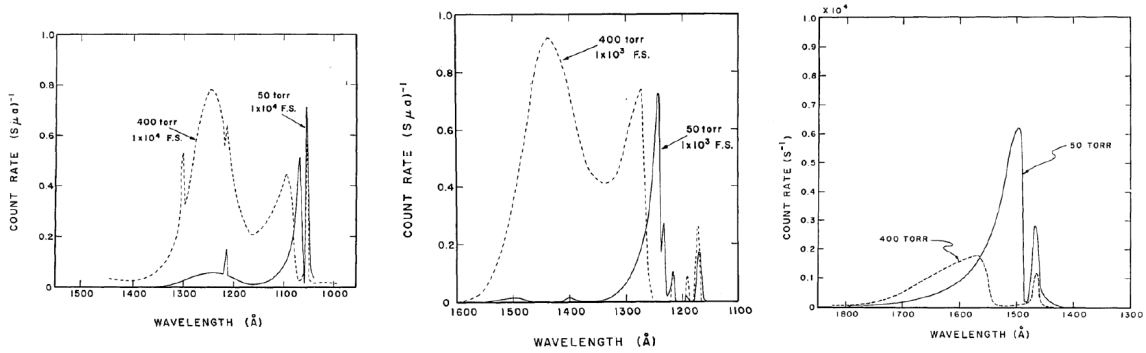

Figure 2.10: Excimer emission spectra from bombarding Ar (left), Kr (center) and Xe (right) with 4 MeV protons at 50 and 400 torr [83].

Transitions from the high vibrational levels of the $^1\Sigma_u^+$ and the $^3\Sigma_u^+$ states to the repulsive ground state, give rise to photon emission in the primary continuum of the excimer emission spectra [84]. Following excitation, noble-gas excimer systems typically evolve according to the flow patterns shown in Figure 2.11. However, the true complexity of these transitions is perhaps better illuminated by the argon molecular potential curves in the same figure. Relaxation occurs by transitions through a tightly nested set of electronic states. Following relaxation, the only available downward channel is by emission of FUV radiation. The numerous crossings of the excimer levels create a highly-efficient energy funnel toward this radiative pathway [81].

Spontaneous radiative decay times for simple excimers fall between 0.005–5 μs [79]. Comparatively, dissociation times for very weakly bound molecular states may be as short as 10^{-13} s, on the timescale of molecular rotation [85]. Excimers are known to exhibit both fast and slow decay times, due to the different probabilities of transition between the singlet and triplet excited states and the dissociative ground state.

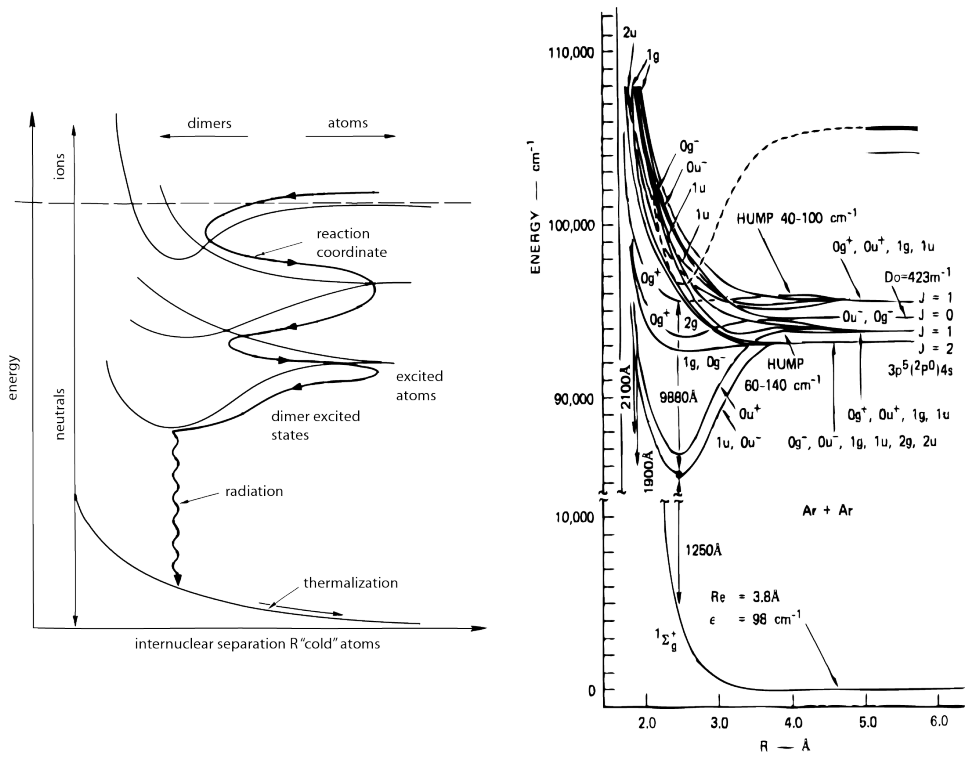

Figure 2.11: Right: Energy flow pattern for the decay of rare gas excimers [81]. Left: Potential curves for the Ar_2^* excimer [79].

Therefore, excimer scintillation exhibits a structured decay with two time constants, as shown by the oscilloscope traces in Figure 2.12. The classically-forbidden triplet-state transition may have a characteristic decay time two orders of magnitude longer than the singlet-state decay. Collisions play an important role in the decay process, making decay times strongly dependent on gas pressure [82]. At higher pressures, singlet-triplet transitions, aided by electronic and atomic collisions, occur with increased probability [79]. Therefore, both the formation and the decay of excimers are more rapid at high gas pressures.

Numerous sources report fast and slow decay times for gas-phase noble-gas excimer scintillation. For example, Mutterer *et al.* describe a series of experiments in which

noble gases were bombarded by relativistic heavy ions [86]. Their results show scintillation rise times in argon and xenon gas of $\leq$10 ns, fast decay constants of 140 ns (Ar) and 50 ns (Xe) at 57 torr, and slow decay constants of 900 ns (Ar) and 250 ns (Xe) at 300 torr. Koehler *et al.* report rise times and decay times for argon and xenon at pressures between 0.1 and 100 atm, as plotted in Figure 2.12. Morikawa *et al.* have compiled an extensive list of gas-phase excimer time constant measurements, which appears in Figure 2.13.

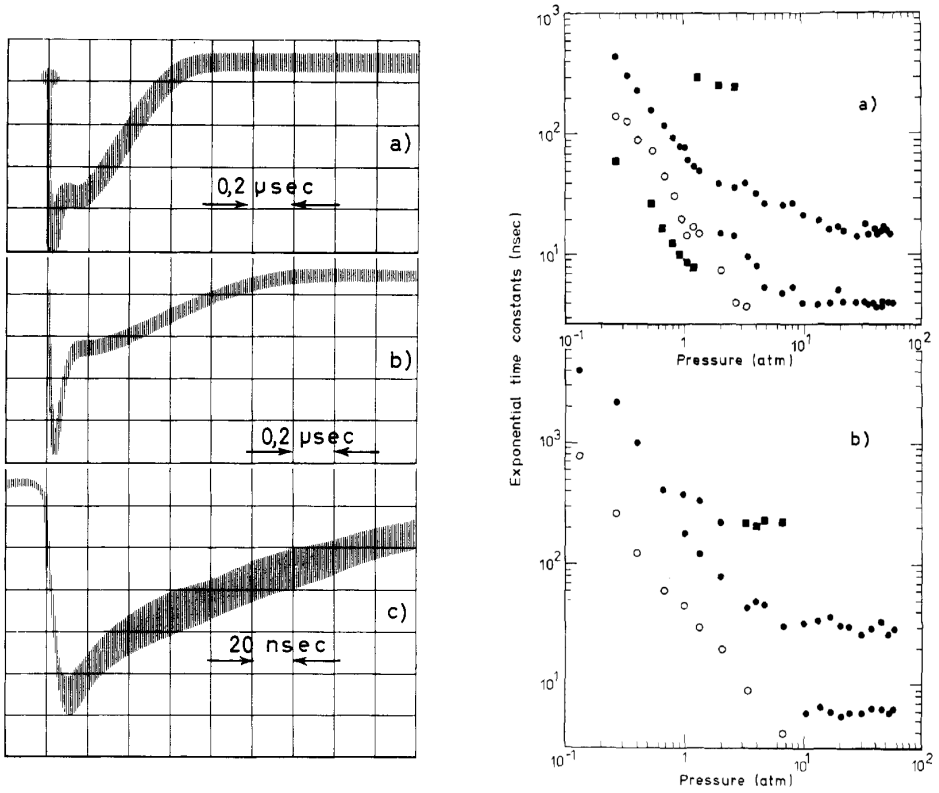

Figure 2.12: Left: Fast multiplier signals from scintillations of xenon at (a) 300 torr and (b) 150 torr, and in argon at (c) 57 torr [84]. Right: Time constants for (a) xenon, and (b) argon as a function of pressure, showing formation time constants (○), as well as fast and slow decay time constants (●) [87].

Knowledge of excimer scintillation yield is essential for understanding the efficiency of excimer radiation pathways, and for estimating the output amplitudes and energy

		Argon		Krypton		Xenon	
	Ref.	$^3\Sigma_u^+$	$^1\Sigma_u^+$	$^3\Sigma_u^+$	$^1\Sigma_u^+$	$^3\Sigma_u^+$	$^1\Sigma_u^+$
Wallace *et al.*	36					130	
Bouciqué *et al.*	37	3700		1700		500	
Thonnard *et al.*	38	2800					
Lorents *et al.*	39	4000[a]					
Keto *et al.*	40	3200	4.2			96	5.5
Oka *et al.*	41	3220		353			
Leichner *et al.*	42			300			
Leichner *et al.*	43					99	
Keto *et al.*	44	2880	4.2			100	6.2
Suemoto *et al.*	45	3000					
Kink *et al.*	46					110	
Gleason *et al.*	47	2840					
Quigley *et al.*	48			280			
Ermler *et al.*	49					172[a]	5.60[a]
Millet *et al.*	50					102	
Wenck *et al.*	51			149	5.2	101	5.5
Salamero *et al.*	52			250			
Thornton *et al.*	53					112	6.9
Carvalho *et al.*	54	4000 2900	4.8 4.5				
Haaks	55			265	5.2	101	
Bonifield *et al.*	56			264	3.4		
Bonifield *et al.*	57					99	4.6
Carvalho	58	3100	4.2				
Luches *et al.*	59			270			
Kasama *et al.*	60	3000					
Millet *et al.*	61	2860					
Salamero	62					100	
Janssens *et al.*	63			256			
Moutard *et al.*	8	3150					
Moutard *et al.*	9					103	4.5
Audouard *et al.*	10			265	3.4		
Firestone *et al.*	64			395			
Present results			3.3 ± 0.1	270 ± 5	3.4 ± 0.1	100 ± 5	4.5 ± 0.1

[a] Theoretical value.

Figure 2.13: Literature values for excimer radiative decay times in a dilute gas [88]. Times are listed in nanoseconds.

resolution of noble-gas-based detectors [38]. Yield characteristics of a scintillator are often represented by the value $W_{h\nu}$, given by,

$$W_{h\nu} = \frac{E}{Y} \tag{2.20}$$

where $W_{h\nu}$ is the average energy expended per scintillation photon, E is the energy deposited in the scintillator, Y is the number of photons generated in the scintillator. While numerous sources report $W_{h\nu}$ values for liquid noble-gases [89, 90], and others report secondary scintillation yields in gas-scintillation proportional counters [91, 92], few sources provide $W_{h\nu}$ values for gas-phase, noble-gas scintillators. Chan-

drasekharan *et al.* report $W_{h\nu}$ values of 67.9, 61.2, and 55.9 eV, for Ar, Kr, and Xe, respectively, at unspecified gas pressures [37]. Saito *et al.* report values for $W_{h\nu}$ from experiments with an alpha source, at pressures between 1 and 10 atm, as shown in Table 2.3 and plotted in Figure 2.14.

The lack of sufficient data on noble-gas scintillation yields and the overall disagreement among the reported values, demonstrate the necessity for careful measurements of this parameter before developing a deployable detector based on gas-phase excimer scintillation. A combination of features – (1) large light output, (2) fast decay, (3) transparency, (4) unique decay structure, (5) immunity to radiation damage – make noble gases particularly promising for use in radiation detectors [82]. A variety of existing noble-gas detectors are briefly discussed in the following section.

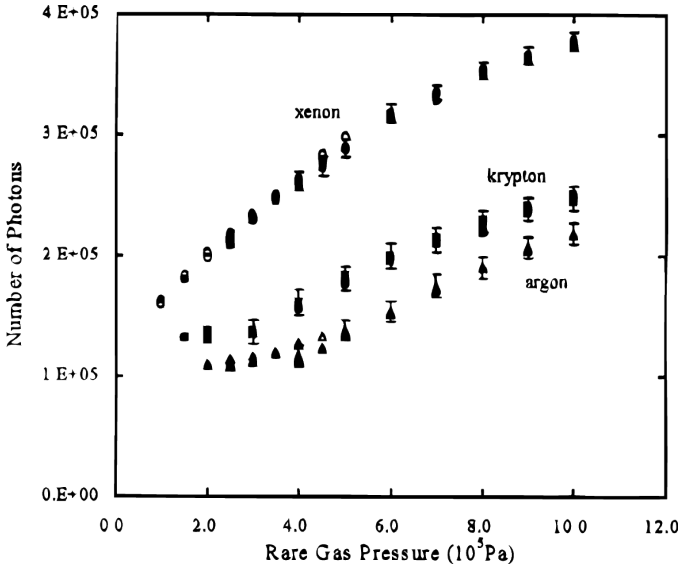

Figure 2.14: Absolute excimer photon yields in argon, krypton, and xenon at pressures between 1 and 10 atm, due to 5.49 MeV alpha particles [38].

	$W_{h\nu}$ (eV/photon)		
Pressure (Pa)	Argon	Krypon	Xenon
1.01×10^5		42.0 ± 3.0	34.3 ± 1.6
2.03×10^5	50.6 ± 2.6	41.3 ± 2.4	27.5 ± 1.3
4.05×10^5	46.3 ± 2.4	34.8 ± 1.8	21.0 ± 0.8
6.08×10^5	36.0 ± 1.9	27.9 ± 1.2	17.5 ± 0.6
7.09×10^5	32.1 ± 1.6	25.9 ± 1.0	16.5 ± 0.5
8.10×10^5	28.9 ± 1.3	24.3 ± 0.9	15.6 ± 0.5
1.01×10^6	25.3 ± 1.1	22.3 ± 0.8	14.6 ± 0.5

Table 2.3: $W_{h\nu}$ values of noble gases when subjected to 5.49 MeV α-particle radiation [38].

2.6.2 Noble-gas-based detectors

Noble-gas-based detectors (NGBD) were first developed in the 1940s, following observations of high electron mobility in liquid and solid argon. Today, NGBD are currently used in a number of applications, including x-ray astronomy, dark-matter detection, neutrino detection, particle physics calorimetry and medical imaging [54]. These detectors include gas-, liquid-, and solid-phase detection media, in the form of scintillation detectors, ionization chambers, gas-scintillation proportional counters, and two-phase electron emission detectors. NGBD rely on the direct interaction of radiation with a noble gas detection media to precipitate photon emission, electron emission, or both. A wealth of information on NGBD is available in [54, 84, 93, 94, 95]. Specifically, information on ^{3}He scintillators for fast neutron detection is provided in [54, 55, 56].

Chapter 3

Review of Preliminary Experiments

Prior to the excimer scintillation experiment at Maryland, which constitutes the majority of this research project, a number of experiments were carried out at NIST, to demonstrate the viability of noble-gas scintillation as a means of neutron detection. These experiments were conducted at the NIST Center for Neutron Research (NCNR), between Fall 2008 and Spring 2011. In April 2011, the NCNR was shutdown for expansion and reliability improvements, including the construction of a new guide hall, at which point all research was transferred to the MUTR.

3.1 The NIST Center for Neutron Research

The NIST Center for Neutron Research (NCNR), located on the NIST campus in Gaithersburg, MD, houses the National Bureau of Standards Reactor (NBSR), along with more than 26 instruments for scientific study using thermal and cold neutrons [96]. The NBSR consists of 30 highly-enriched fuel elements, which are cooled and moderated by heavy water surrounding the core. Operating at a thermal output of 20 MW, in 38-day cycles, the reactor has a peak in-core flux of 3.5×10^{14} $\mathrm{cm^{-2}s^{-1}}$ [97]. Nine beamlines surrounding the core supply thermal-neutrons to various instruments

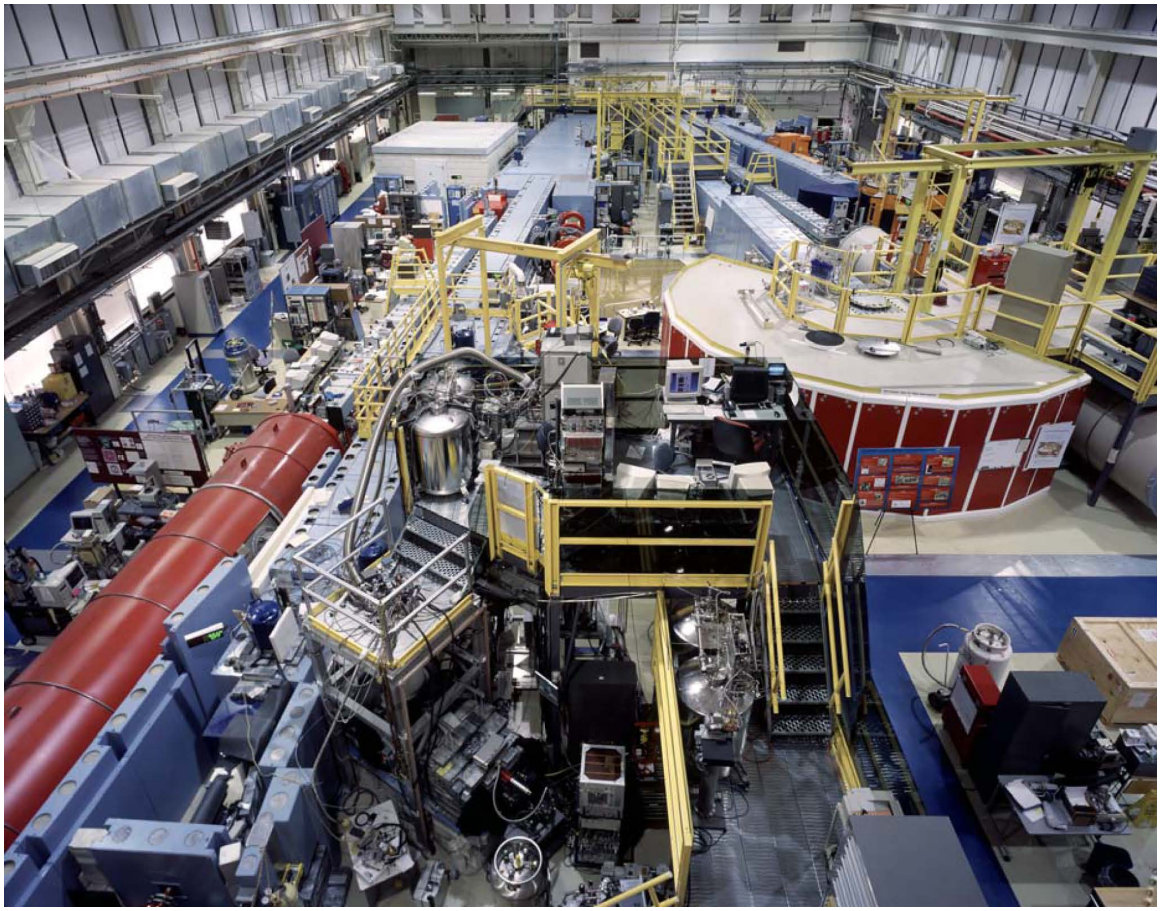

Figure 3.1: The NCNR guidehall [11].

within the reactor confinement building. Additionally, a 5-liter liquid-hydrogen cold source provides cold neutrons to 7 radial neutron guides and the instruments located in the NCNR guidehall. A photograph of the guidehall appears in Figure 3.1. A diagram of the reactor confinement and the guidehall appears in Figure 3.2.

All data for the preliminary excimer scintillation experiments were collected on beamline 6 (NG-6), at experimental stations NG-6A and NG-6M. Starting in the reactor core, neutrons stream from the cold source thimble into the various neutron guides. An 18-cm gap between the upper and lower fuel regions, and multiple bismuth filters upstream of the neutron instruments, prevent gamma-ray radiation

from streaming into the guides. The guides themselves are coated with nickel-58 to achieve nearly total reflection of low-momentum, low-angle-of-incidence neutrons. This enables neutrons to be transported to the far end of the guides, 20 - 60 m from the source, with minimal losses [98]. Beamline NG-6A consists of two monochromators: a pyrolytic graphite crystal and cooled slab of beryllium. These select 0.496-nm wavelength neutrons from a polychromatic neutron beam. Beamline NG-6M resides downstream of NG-6A, and contains an additional potassium-intercalated graphite monochromator, and additional filters for selecting 0.89 nm neutrons from the beam. At both locations, an aperture was used to collimate the monochromatic beam to a square profile, 4×4 mm. During the experiments, the nominal neutron flux at the sample locations was $(2.61 \pm 0.37) \times 10^5$ cm^{-2}s^{-1} [39].

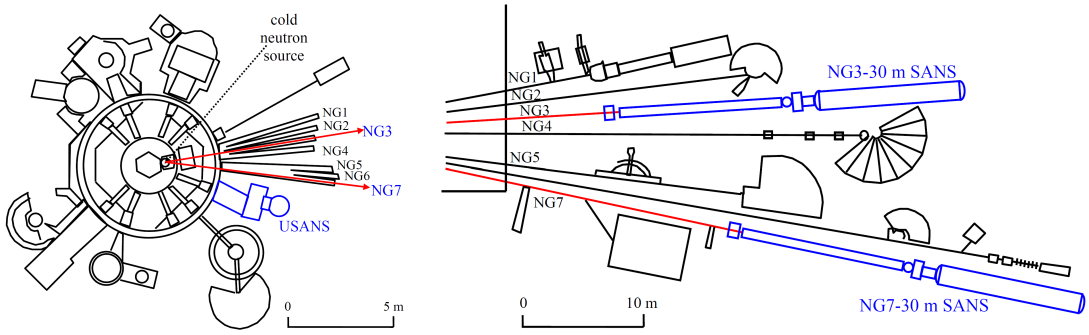

Figure 3.2: Plan view of the NBSR (left) and the the NCNR guide hall (right), including the thermal and cold neutron instruments [11].

3.2 Lyman-Alpha Experiment at the NCNR

The initial noble-gas scintillation measurements set out to observe Lyman-alpha radiation following the ^{3}He(n, tp) reaction, described by Eq. 1.2. With a Q-value

of 764 keV, this reaction was believed to produce Lyman-alpha photons (121.5 nm) through both charge transfer and excitation, in the processes,

$$H^+ + He \rightarrow H(2p^1) + He^+ \rightarrow H(1s^1) + He^+ + h\nu \quad (3.1)$$
$$H(1s^1) + He \rightarrow H(2p^1) + He \rightarrow H(1s^1) + He + h\nu \quad (3.2)$$

By joining a solar-blind photomultiplier tube to a scintillation cell filled with ^{3}He (25 - 800 torr), and irradiating the cell in a neutron beam, Lyman-alpha radiation was observed at rates of up to 46 photons/neutron absorption [99]. Filters were later placed between the cell and the photomultiplier tube to confirm that the observed radiations were Lyman-alpha photons. The results of these experiments, at various pressures of ^{3}He, are plotted in Figure 3.3. These measurements, their analysis, and modeling of the experimental processes are described in [99] and [100]. A description of an experimental apparatus similar to the apparatus used in these measurements, is provided in the following chapter.

3.3 Excimer-Based Experiments at the NCNR

Following the Lyman-alpha experiment, attempts were made to increase the observed photon signal by introducing noble gases into the scintillation cell assembly. These experiments involved mixtures of ^{3}He and heavier noble gases (Ar, Kr or Xe), as well as substitutions of ^{3}He with alternative neutron absorbing materials, mixed with the same noble gases. The excimer emission signal from various neutron reac-

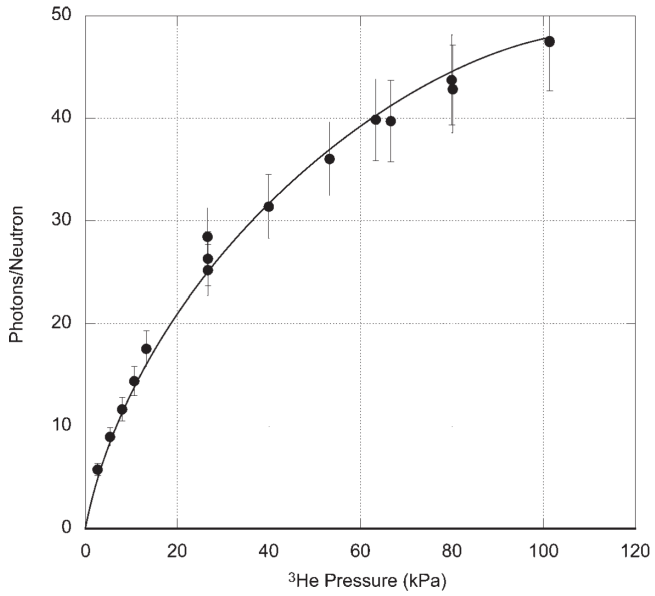

Figure 3.3: Lyman-alpha photons generated per neutron reacted with ^{3}He, as a function of ^{3}He pressure [99].

tions was measured to be a factor of a thousand more intense than light from the Lyman-alpha experiments.

A series of spectroscopic measurements were performed to confirm that the observed signal was a result of excimer radiation [39]. Using various spectral filters (sapphire, CaF_2, fused silica), the radiation was identified as broad-continuum, far-ultraviolet light, characteristic of noble-gas excimer emissions. By inserting these filters between the cell window and the PMT, the short-wavelength cutoff of the detector system was shifted from 115 nm to a longer wavelength: 122 nm for CaF_2, 142 nm for sapphire, and 160 nm for fused silica. The Ar_2* excimer emissions were detected only with the CaF_2 filter in place; the other two filters were opaque to the emitted radiation. Emissions from Kr_2* were detected through CaF_2 and weakly through sapphire, while emissions from Xe_2* were detected through all three filters.

The response of the photomultiplier tube to a range of monochromatic synchrotron light, while behind these filters, appears in Figure 3.4. The relative change in the observed scintillation signal from various noble gases, when placed behind these filters, appears in the same figure.

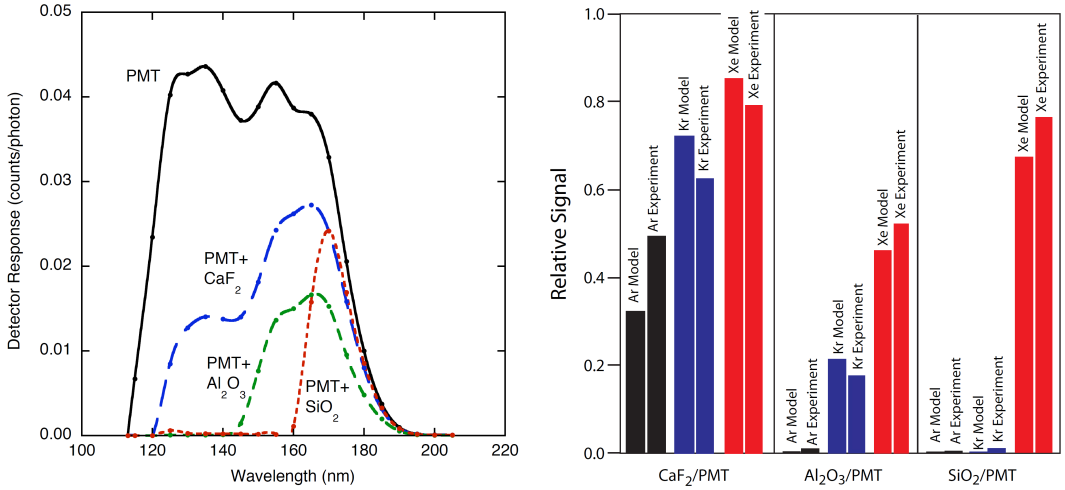

Figure 3.4: Left: Photomultiplier tube response to a range of monochromatic ultraviolet synchrotron radiation behind various filters [39]. Right: Relative excimer emission signals observed passing through various filters under identical experimental conditions [39].

3.3.1 Helium-3 and noble-gas mixtures

The first excimer-based neutron detection experiment consisted of a cell containing a mixture of ^{3}He and a single heavier noble gas (Ar, Kr, or Xe). This cell was joined to a calibrated filter-detector package, sensitive to various bands of far ultraviolet (FUV) radiation, between wavelengths of 120 and 200 nm. Helium-3 was introduced into the cell to a pressure of 200 torr, and noble gases were introduced at additional pressures between 25 - 1000 torr. When exposed to a cold neutron beam at the NCNR, the assembly produced tens of thousands of FUV photons per reacted neu-

tron. This output suggests a conversion efficiency of >30%, between the neutron reaction Q-value and the excimer scintillation emissions. The results are plotted in Figure 3.5. It is likely that this mechanism is also present in mixtures of ^{3}He and ^{4}He or Ne, but the peak emissions of these excimer species are outside the spectral range of the detector (80 and 77 nm respectively).

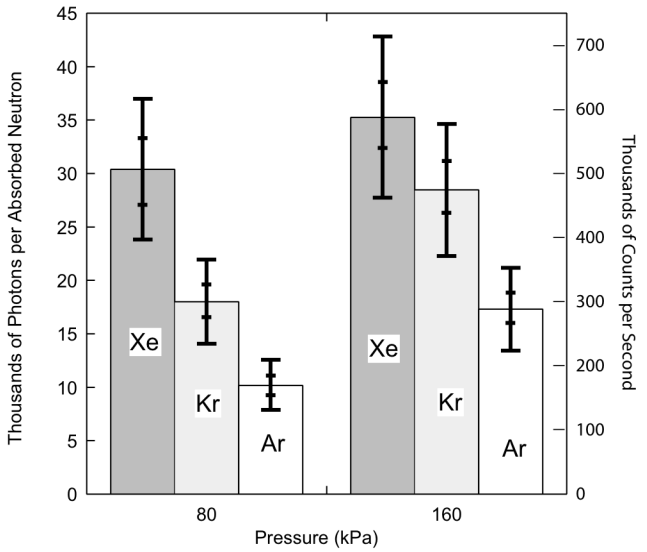

Figure 3.5: Left-hand scale: photons per neutron reacted with ^{3}He at 200 torr, with 600 and 1200 torr of Xe, Kr, and Ar. Wide error bars correspond to random and systematic uncertainties in the derived photon signal. Right-hand scale: counts from which the left-hand scale is derived. Narrow error bars correspond to statistical counting uncertainties in signal and background [39].

In consideration of the recent ^{3}He shortage, continued development of a neutron detector based on ^{3}He was deemed impractical. It was hypothesized that similar results could be attained from any exothermic neutron absorption reaction with a Q-value comparable to the ^{3}He(n, tp) reaction.

3.3.2 Preliminary thin-film experiment

The first measurements using thin-films were performed with an assembly similar to the ^{3}He experiments, including a few minor alterations to accommodate the film targets. Four different films were used in the experiments: three containing boron, and one containing lithium. The first boron sample was 200-nm thick, enriched ^{10}B, found in storage from a previous application. The other two boron samples were natural boron, fabricated by RF sputtering at the NIST CNST. These samples were 250-nm and 500-nm thick. The fourth sample, containing lithium-6 carbonate ($^{6}Li_2CO_3$), was fabricated at the University of Maryland Nanocenter, using thermal annealing to achieve thicknesses of 20 μm. All films were deposited on silicon.

By placing the films within the scintillation cell, and irradiating the cell in a cold-neutron beam, a large excimer scintillation signal was once again observed, on the order of many thousands of FUV photons per neutron absorption. Only xenon and argon gas were used, at pressures between 25 - 800 torr. However, the results of these experiments exhibited inconsistencies between the signals from the enriched and natural boron film samples. This discrepancy may potentially be attributed to the stability of the sputtered natural-boron films when exposed to air. Over the course of the experiments, visible changes were observed in the color and luster of the films, perhaps indicating oxidation. These results led to careful fabrication and storage procedures in the subsequent experiment at the MUTR.

The findings of the preliminary experiments at NIST provided a foundation for the excimer scintillation experiment at Maryland. The experiment at Maryland focused specifically on observing the scintillation from thermal-neutron irradiation of enriched ^{10}B thin films, in the presence of Ar, Kr, and Xe. This experiment and its results are the subject of the following chapters.

Chapter 4

Excimer Scintillation Experiment at Maryland

The excimer scintillation experiment at the Maryland University Training Reactor was designed to generate and observe far-ultraviolet noble-gas excimer emissions, as a result of the boron-neutron capture reaction. Measurements of these emissions were collected for different gas types, gas pressures, and boron target thicknesses. Careful calibrations and characterizations of the various components of the experiment complimented this scintillation data, to allow its interpretation as quantities which are relevant to the development of an excimer-based thermal-neutron detector. The end results of the analysis include:

1. Scintillation yield per neutron absorption
2. Scintillation yield per unit energy deposited
3. Excimer lifetime

Specifically, this experiment examined excimer emission following thermal-neutron absorption by boron-10 thin films, under pressures of argon, krypton, and xenon, between 50 - 800 torr. This chapter describes the experimental setup and procedures. The results of the experiments and the calibrations contributing to those results are discussed in the subsequent chapters.

4.1 The Maryland University Training Reactor

The Maryland University Training Reactor (MUTR) is a TRIGA reactor located on the University of Maryland campus in College Park, MD. Initially fueled with highly-enriched, plate-type MTR fuel, the reactor achieved criticality in October of 1960, becoming the first nuclear reactor in the state of Maryland [101]. In 1974, 93 TRIGA-type fuel elements (19% enrichment) were installed to replace the plate fuel, increasing the reactor power to 250 kW. Today, the reactor's primary functions are operator training and scientific research. Five experimental facilities allow access to the MUTR's radiation fields, including a through tube, two beam ports, a pneumatic rabbit system, and a thermal column. The layout of the MUTR core, and the respective positions of these facilities, appear in Figure 4.1.

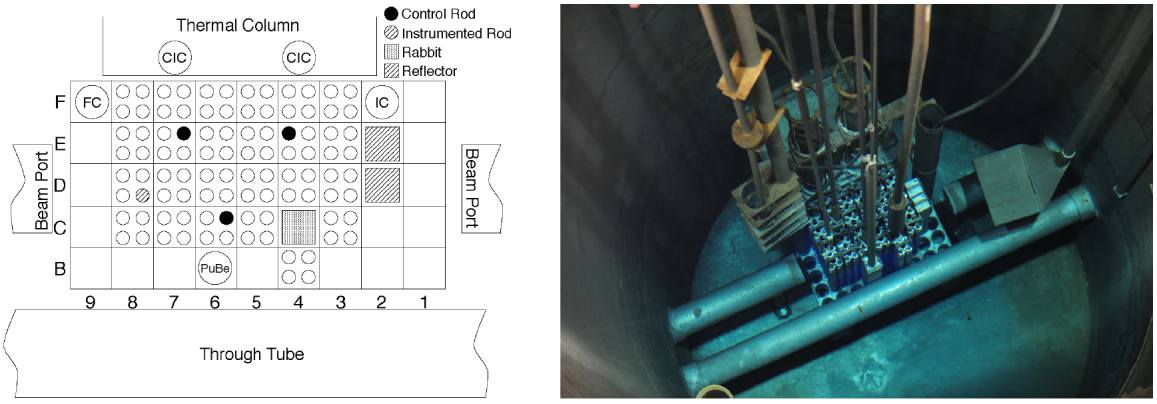

Figure 4.1: Left: Plan view diagram of the MUTR core [101]. Right: The MUTR core from the reactor bridge [102].

For this experiment, the MUTR thermal column was utilized as a source of neutrons. A collimator insert was designed for this facility, to allow only a narrow directional beam of neutrons to stream past the boundary of the concrete containment. The thermal column earns its name from the large quantity of graphite separating the

reactor core and the inner face of its access cavity. Fission neutrons diffusing through this graphite volume are moderated to thermal energies with a high probability, making this facility ideal for the development of a thermal-neutron detector. A diagram of the thermal-column access cavity appears in Figure 4.2. The fabrication of the neutron-beam collimator, and the characterization of the thermal-column neutron beam are discussed in Chapter 7.

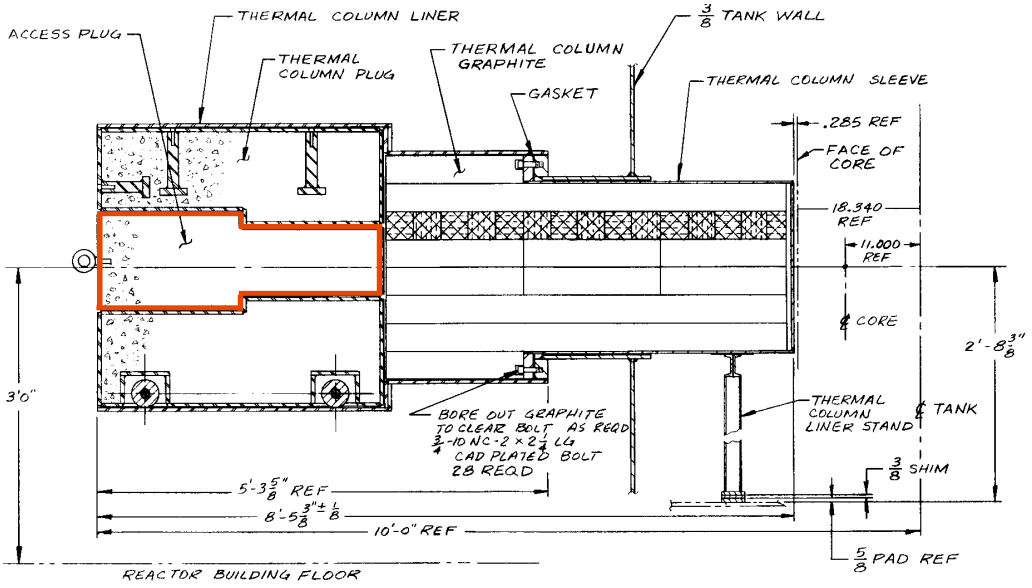

Figure 4.2: Elevation view of the MUTR thermal column. The access plug is highlighted in red. The core centerline is labeled on the right. The edge of the concrete reactor containment appears on the left [101].

4.2 Experimental Apparatus

The equipment used in this experiment included various boron-10 thin-film targets, a gas-scintillation cell, a photomultiplier tube, a gas-handling system, a fission-chamber beam monitor, counting electronics for both the photomultiplier tube and

the beam monitor, a neutron-beam collimator, a neutron-beam aperture, lead and borated polyethylene shielding, and a lithium-glass beam block.

4.2.1 Scintillation cell

The scintillation cell was designed to produce and detect excimer radiation when exposed to a neutron beam, by providing a high-purity noble-gas environment, surrounding a thin-film neutron-absorbing target. The cell consisted of a 70-mm stainless-steel cube, with metal-seal flange ports on all sides, attached to a photomultiplier tube (PMT). The PMT (Hamamatsu R6835) was a solar-blind head-on tube, tailored specifically for FUV detection (115-200 nm), with a 23-mm CsI photocathode, and an integrated MgF_2 window. The tube was contained in end-on housing (McPherson 658), and placed behind a second, discrete MgF_2 window (MPF A4530) and a differential volume, which was continuously evacuated for the duration of the experiments. Magnesium fluoride is transparent to photons of wavelengths >120 nm, and, therefore, provided a suitable transmissive barrier between the cell and the PMT. The discrete window on the scintillation cell was 2.5 mm thick. The calibration of the PMT/MgF_2 detector package is discussed in Chapter 6. A diagram of the scintillation cell appears in Figure 4.3.

Boron-10 thin-film targets, 0.3 - 1.2 μm thick, deposited on silicon substrates (6.45 cm^2), were placed at the center of the cube beneath the PMT. The films were angled at 45° with respect to the incident neutron beam to increase the pathlength

of the beam by a factor of $\sqrt{2}$. The films were held in place by a slotted aluminum cylinder (2.54 cm diameter). The cylinder, in turn, was held in place by a groove in the Conflat flange at the bottom of the cube. The inner surface of this cylinder was coated with black copper-oxide (Ebonol C) to reduce reflections of FUV photons within the cell. The fabrication and characterization of the boron-10 films are discussed in Chapter 5.

Silica windows (0.5 mm thick), attached to opposing sides of the cell, provided a throughway for the thermal-neutron beam with little attenuation. To minimize backgrounds from stray FUV light, these windows were covered with aluminum foil during PMT operation. All flanges on the scintillation cell were sealed with copper gaskets, with the exception of the seal between the PMT and the differential volume, for which a Viton gasket was used.

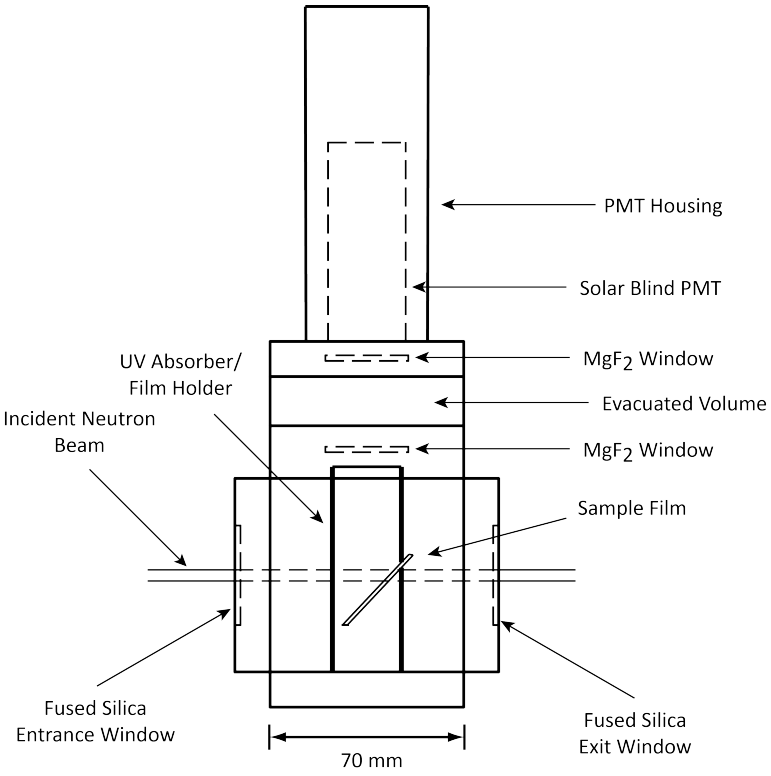

Figure 4.3: Diagram of the scintillation cell.

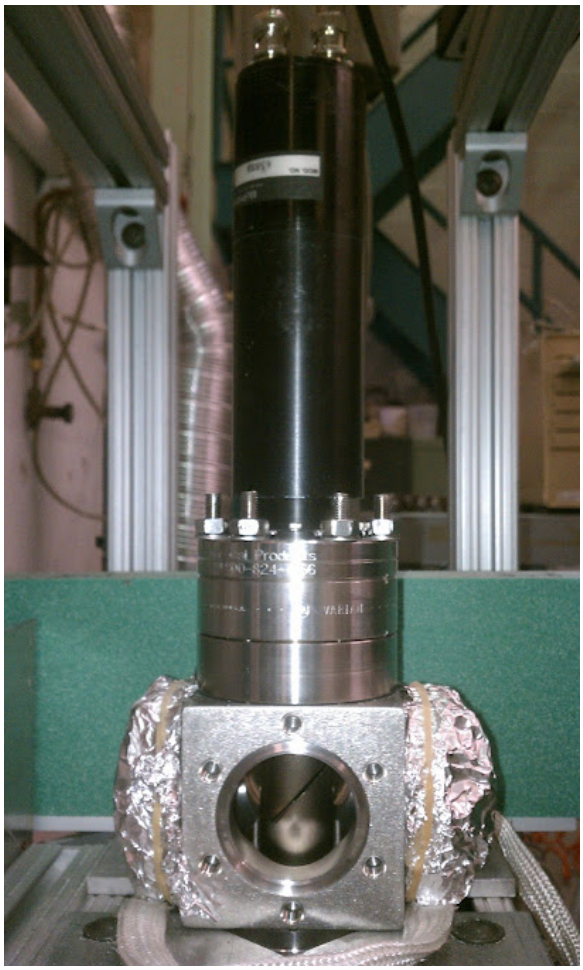

Figure 4.4: The scintillation cell with one flange port open, exposing the thin-film target and the slotted film holder.

4.2.2 Gas-handling system

A gas-handling system was designed to evacuate and fill the scintillation cell. This system consisted of various components connected by a stainless steel manifold: a turbomolecular pump, a diaphragm pump, gas lecture bottles, a digital pressure indicator, a vacuum gauge, a residual-gas analyzer, a gas purifier, a metering valve, a series of bellows-sealed valves, and VCR, Conflat, and Swagelock interconnections. Diagrams of the gas-handling system appear in Figures 4.6 and 4.7.

Prior to each data collection run, the turbomolecular pump (Pfeiffer TPH/TPU 180 HM) and the diaphragm pump (Vacuubrand MD4T) were used to evacuate the gas handling system and the scintillation cell to high vacuum (0.5 - 1.0 $\times$ 10^{-6} mbar). Vacuum pressure in the evacuated cell was measured with a cold-cathode vacuum gauge (Pfeiffer PKR251). Whenever the system was opened and resealed, such as to change thin-film targets, it was baked at 60°C overnight to remove water and other adsorbed contaminants from the chamber walls. A residual-gas analyzer (SRS RGA-100) was used to perform a helium leak check of the system upon initial assembly, and to monitor contaminants in the system prior to filling with noble gas. A typical RGA scan appears in Figure 4.5.

All noble gases were passed through a purifier (Microtorr MC1-902-F) designed to remove trace contaminants (H_2O, O_2, CO, CO_2, H_2, and hydrocarbons) to $<$ 1 ppb. The gases used in these experiments were of research grade purity. Noble-gas purities and contaminants, determined by manufacturers' analyses, appear in Table

4.1. A metering valve (SS-MGVR4-MH) was used to control the flow of noble gases into the scintillation cell. Additional valves isolated the cell, the gas manifold, and the differential volume. A digital pressure indicator (Omega DPI 705) with a silicon transducer was used to measure the pressures of the admitted gases to an accuracy of $< 0.1\%$ of a 30 psi full scale, or $\pm$ 1.55 torr.

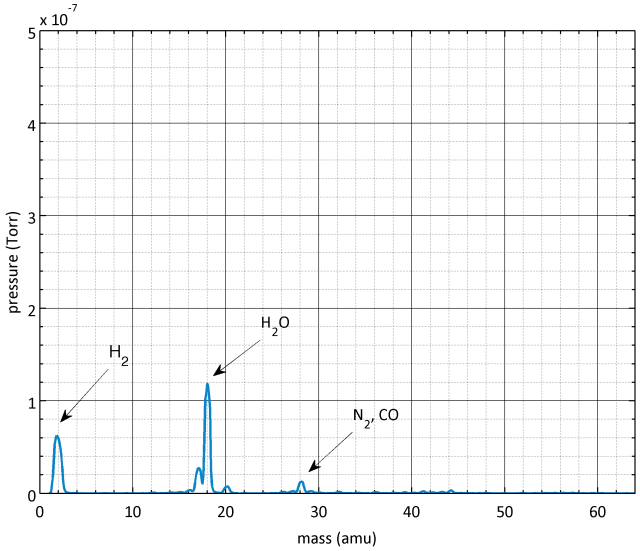

Figure 4.5: Typical scan of residual gases after gas-handling system evacuation and bake out.

Gas Type	Purity (%)	Contaminants ($< n$ ppm)
Ar	99.9995	CO_2 (0.1), CO (0.1), O_2 (0.05), THC (0.1), H_2O (0.05)
Kr	99.999	Ar (1), CF_4 (1), CO (1), CO_2 (1), H_2 (1), He (1) H_2O (4), Xe (10), N_2 (10), O_2 (2), THC (0.1)
Xe	99.999	Ar (1), CF_4 (0.5), CO_2 (1), H_2 (2), H_2O (0.004), Kr (5), N_2 (1), O_2 (0.10), THC (0.5)

Table 4.1: Noble-gas purities and contaminant concentrations as listed by the manufacturers. THC: total hydrocarbons.

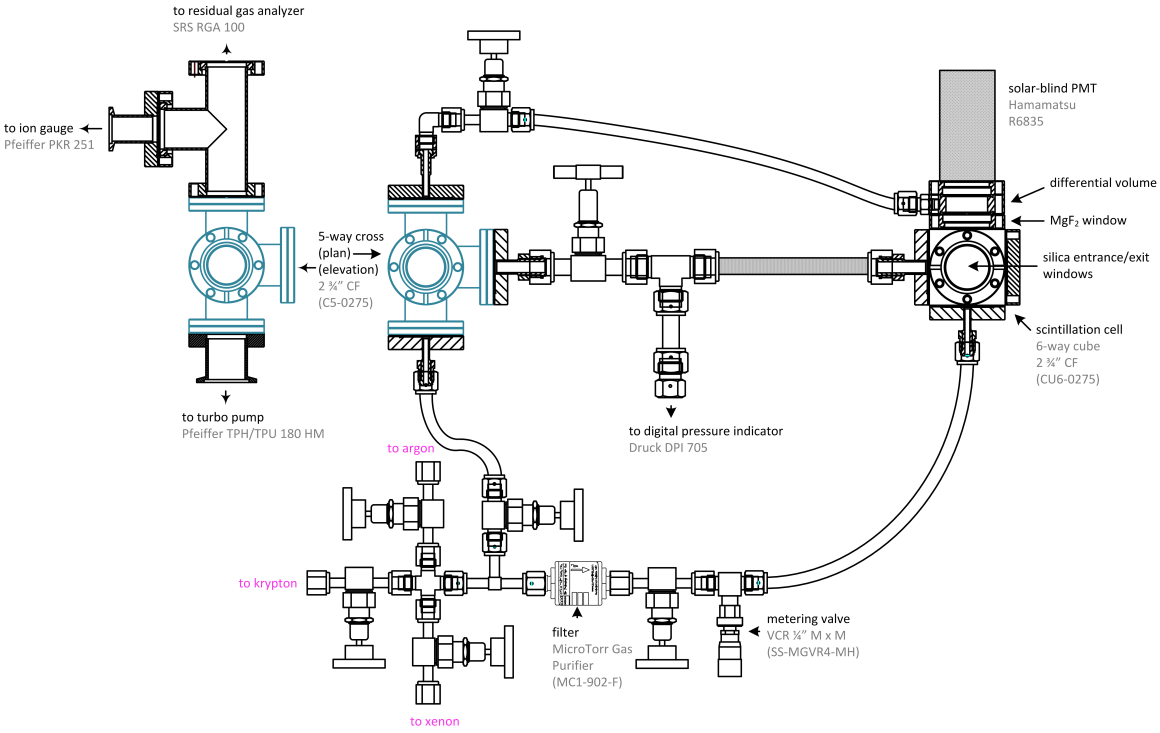

Figure 4.6: Gas-handling system layout. The 5-way cross (highlighted in blue) appears in two orientations.

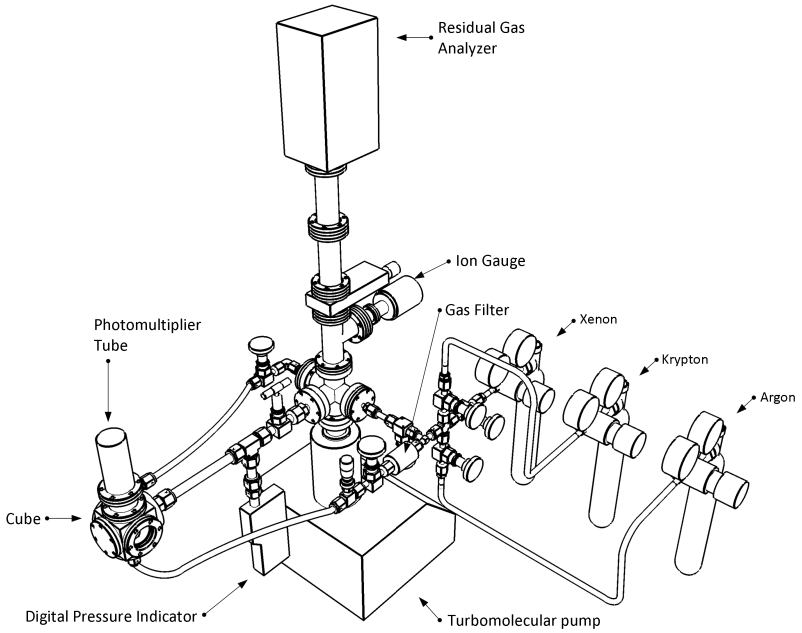

Figure 4.7: Gas-handling system model.

4.2.3 Neutron beamline

A new thermal-column insert was fabricated for use in this project. The insert was designed to allow only a narrow beam of neutrons (5.08-cm diameter) to stream beyond the reactor containment. The collimator consisted of a carbon-steel compartmented frame and a central steel tube. Portions of the box were filled with a mixture of steel shot, paraffin wax, and boron-carbide (B_4C) powder. Construction of this plug is described in Chapter 7. A diagram of the insert appears in Figure 4.8.

During the scintillation measurements, neutrons were allowed to stream into the scintillation cell through the collimator opening. Before reaching the beam tube, neutrons propagating from the core first diffused through the thermal column, composed of water (0.953 cm), aluminum (0.635 cm), graphite (150 cm), and lead (5.08 cm). While both the graphite and the lead bricks in the thermal column attenuate a significant portion of the gamma-ray radiation originating in the core, the gamma-ray dose rates measured in front of the scintillation cell were not insignificant (90 - 100 mR/hr). Gamma-ray dose rates in the vicinity of the PMT, just outside the beam, were measured at 5 - 10 mR/hr. Fitted lead bricks were placed around the photomultiplier tube to reduce direct gamma-ray interactions with the photocathode. Borated-polyethylene blocks were used as a neutron-beam stop behind the scintillation cell. Additional blocks were placed around the cell to reduce signal contributions from neutrons external to the beam. A remotely-operated beam

shutter, consisting of a lead brick and a thick boral plate, was mounted on tracks on the outer face of the collimator access plug. This shutter was used to block both neutrons and gamma-rays in the beam, when working with the experiment.

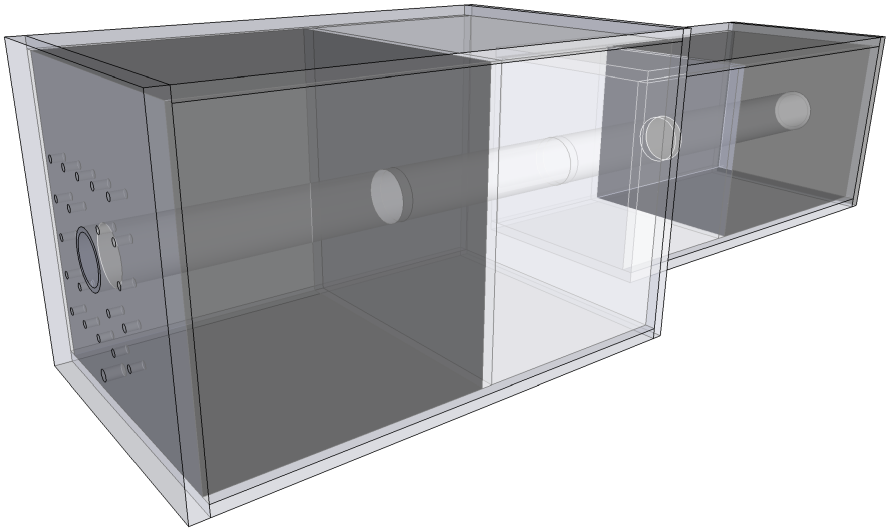

Figure 4.8: Collimator insert for the MUTR thermal column. Black shading defines segments filled with the shielding mixture.

Beyond the outlet of the collimator plug, the neutron beam was further reduced to a 4-mm diameter by a Boral aperture, 8 cm in front of the scintillation cell. The neutron fluence behind this aperture was monitored with a NIST-calibrated fission-chamber reference detector. Data obtained with this detector are discussed in Chapter 7. The areal density of the ^{235}U deposit (25S-5-4) in this detector was 458.073 μg/cm^2, with a relative uncertainty of 0.5%, as measured by Dr. David Gilliam. A beam block, consisting of a small slab of ^{6}Li glass, was placed on a slide between the fission-chamber beam monitor and the scintillation cell. This beam block presented little obstruction to gamma radiation within the beam, while absorbing nearly all thermal neutrons. In this way, the beam block was used to isolate

the gamma-ray contribution to the PMT signal. Diagrams of these components and their arrangement appear in Figures 4.9 and 4.10.

The gas-handling system, the scintillation cell, the fission-chamber beam monitor, the beam aperture, the beam block, and the shielding were supported by an extruded aluminum frame (80/20). This frame was designed to enable centering of the scintillation cell within the neutron beam, and was fixed to the reactor structure to prevent changes in the setup geometry. Photographs of the experimental setup in place at the MUTR appear in Figures 4.11 and 4.12.

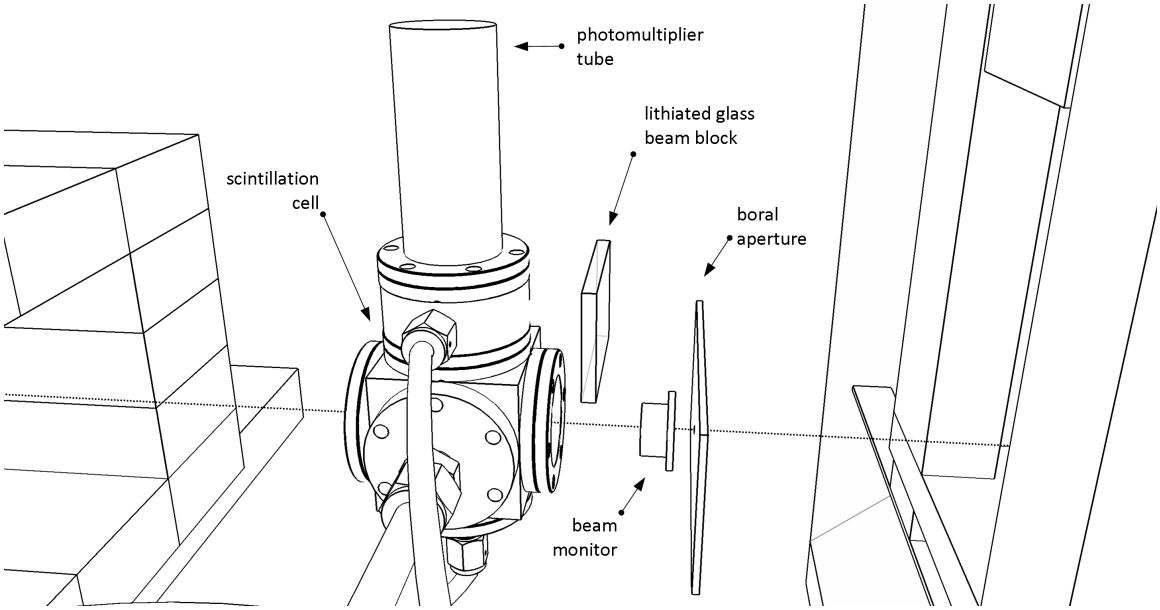

Figure 4.9: Scintillation experiment configuration (close view).

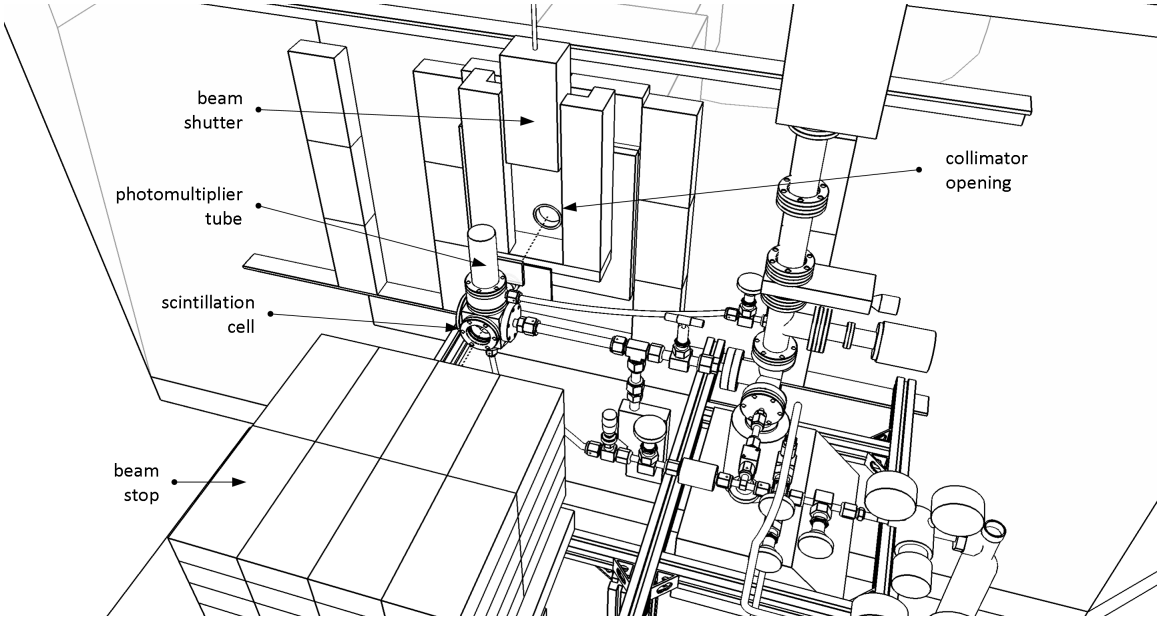

Figure 4.10: Scintillation experiment configuration (wide view).

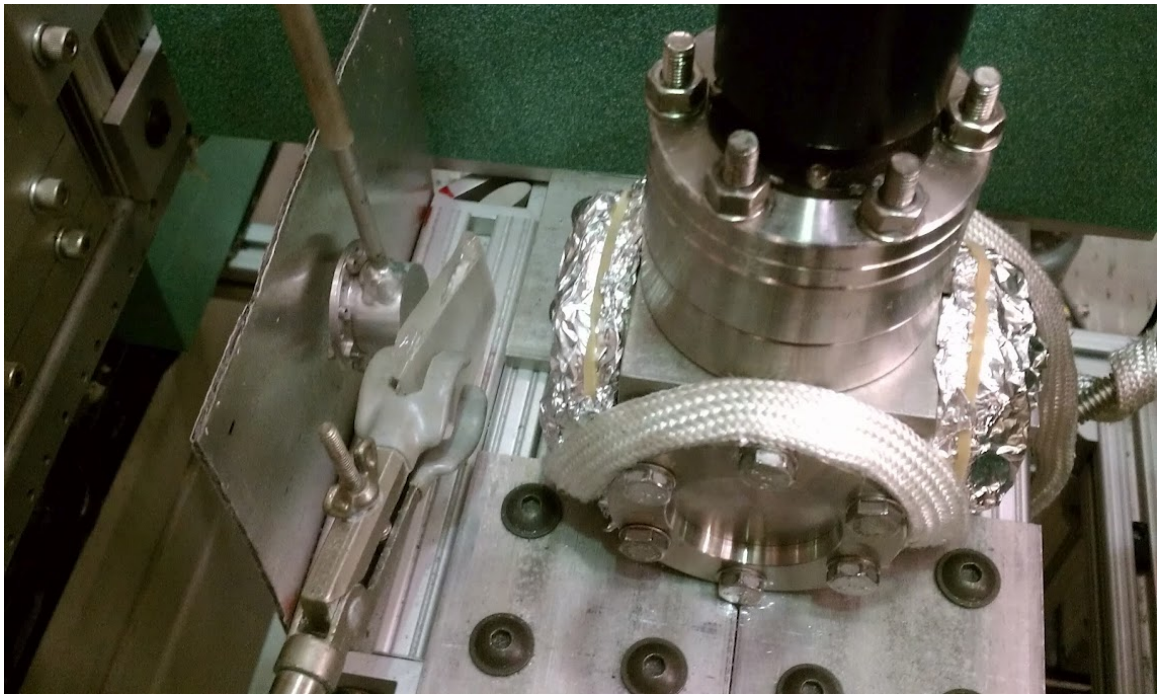

Figure 4.11: The scintillation cell in the beamline. Neutrons propogate through the cell from left to right.

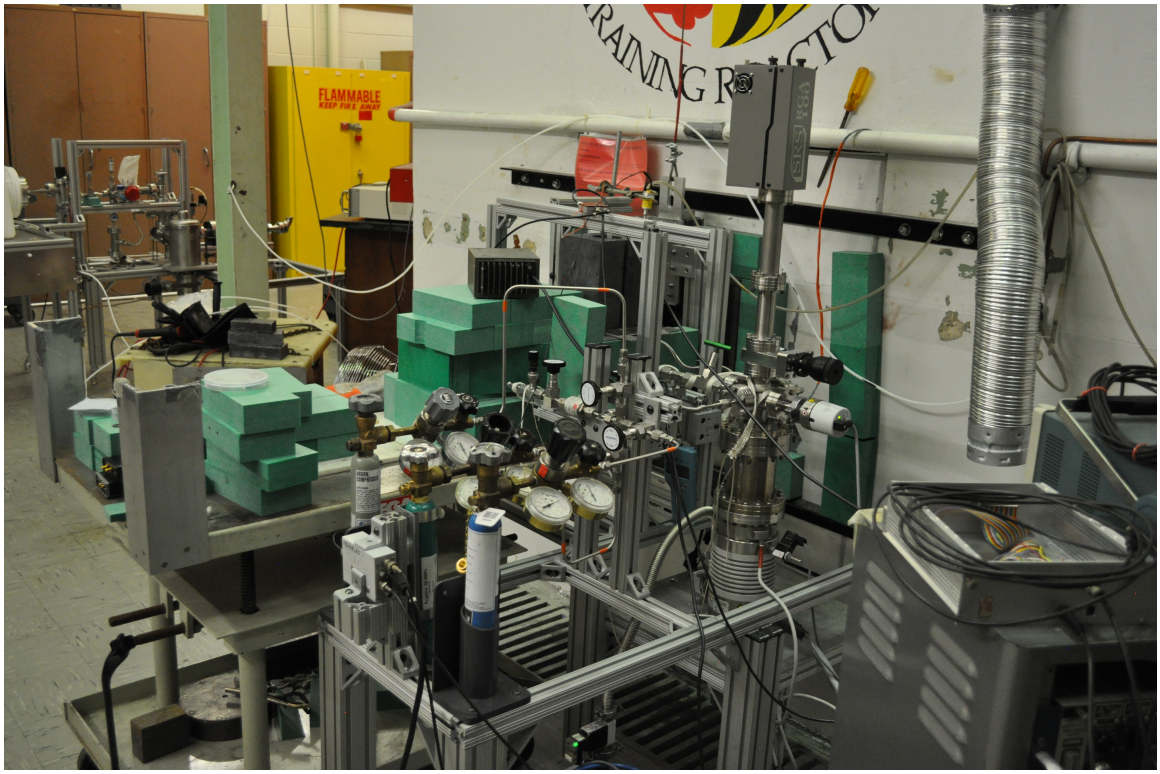

Figure 4.12: The scintillation experiment beside the MUTR containment.

4.2.4 Electronics configuration

Two sets of electronics were configured to analyze pulses from the scintillation-cell photomultiplier tube. The first set was used to count PMT pulses with a counter/timer (C/T), and to obtain pulse-charge distributions with a multichannel analyzer (MCA). These data were collected to calculate excimer scintillation photon yield. The second set was used to obtain distributions of the times between pulses from the PMT. These data were collected to determine the slow decay component of the excimer lifetime. A third set of electronics was used to gather pulse-height distributions from the fission-chamber beam monitor. These data were collected to extrapolate the neutron-beam fluence during the photon yield measurements. Schematics of these electronics appear in Figures 4.14, 4.16, and 4.17.

With sufficient energy, a photon impinging on a PMT photocathode may liberate an electron due to the photoelectric effect. This photoelectron is directed by a focusing electrode to a series of dynodes, held at successively increasing voltages. The dynodes amplify the signal through secondary emission, until charge is accumulated at the anode to form an electrical pulse. The total number of photon events may be determined by counting these pulses over a given period of time.

During all of the excimer scintillation measurements, the scintillation-cell photomultiplier was operated at -2300 V, corresponding to a gain of 3×10^5 [103]. Pulses from the PMT were further amplified by a fast preamplifer (Ortec VT120A), with a non-inverting gain of 200, and a rise time of ≤ 1 ns. The amplified pulses were divided

to two outputs by a power splitter (Minicircuits ZFSC-2-4+). Oscilloscope traces of characteristic output pulses from these components appear in Figure 4.13.

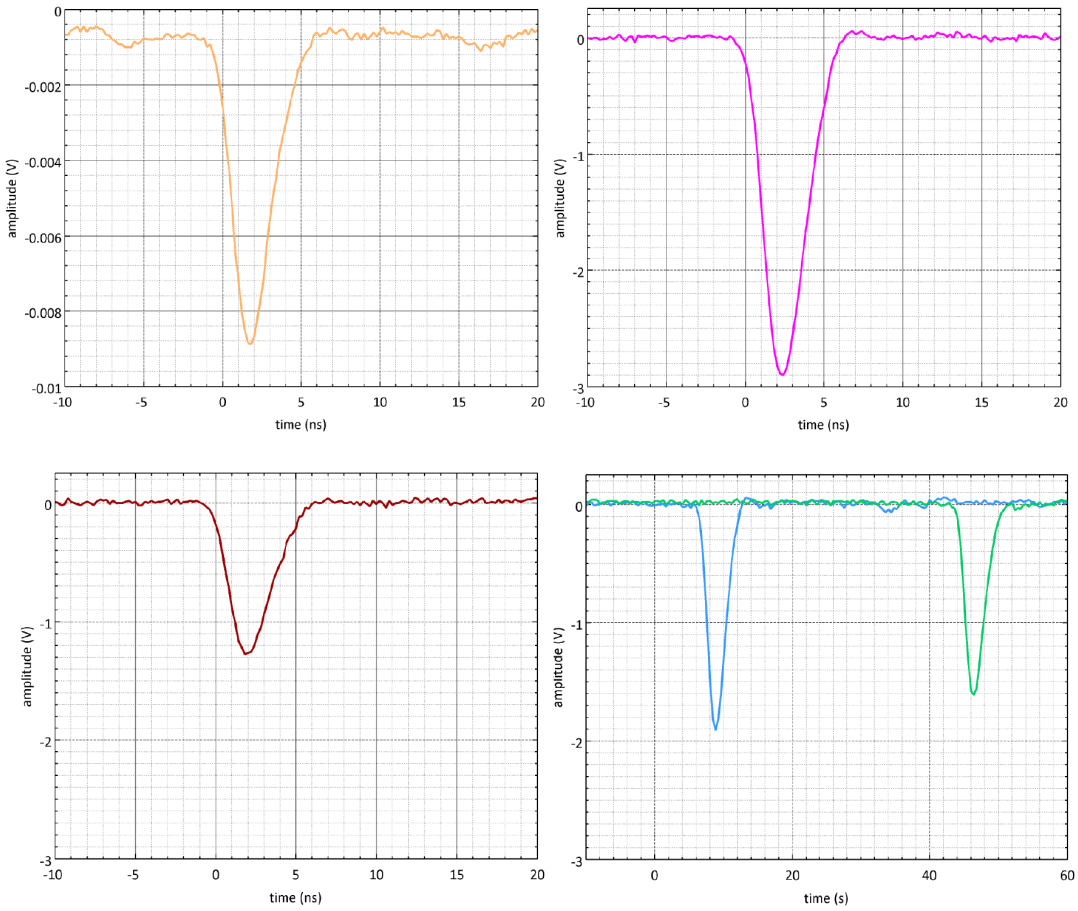

Figure 4.13: Oscilloscope traces of output pulses from the PMT (top left), the fast preamplifier (top right), a single output from the splitter (bottom left) and both outputs from the splitter, with one output run through the TAC-setup delay line (bottom right). 50 Ω scope termination.

In the photon-counting configuration, one splitter output was connected to the C/T (Ortec 994), and the other was connected to the MCA (LeCroy qVt 3001). The MCA was used to obtain pulse-charge distributions (PCDs). Observation of these PCDs was necessary to ensure that multi-photoelectron pulses were not contributing significantly to the number of pulses counted by the C/T. The MCA was operated

in the charge mode (q-mode), with an integration width of 20 ns, and a resolution of 0.25 pC/channel, over 1024 channels. Data from the MCA were transferred to a laptop via a Perl script and a custom microcontroller board (Wiring v1.0). The digitization time of the MCA (12 μs + 0.05 μs/channel) was long with respect to the typical decay time of each scintillation event. Therefore, not every pulse from the PMT was collected by the MCA. The resulting PCDs were assumed to be only representations of the true distributions. The C/T was used to count the absolute number of PMT pulses. The specifications of this module include a maximum count rate of 100 MHz, a pulse-pair resolution of <10 ns, and a fixed discriminator threshold of -250 mV for negative polarity inputs.

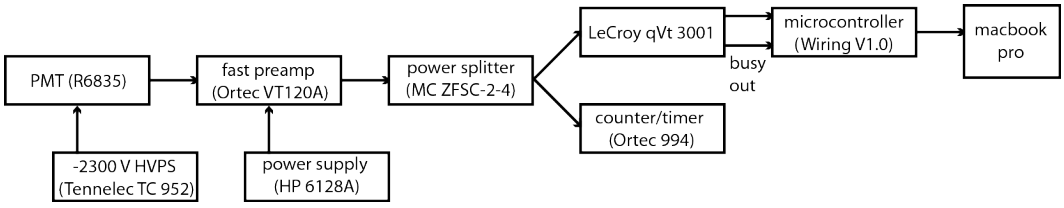

Figure 4.14: Photon-counting electronics.

A time-to-amplitude converter (TAC) measures the time between "start" and "stop" pulses by generating an output pulse with an amplitude proportional to that time difference. In the pulse-timing electronics, one splitter output was sent to the "stop" input of a TAC (Ortec 567), and the other was sent, through a delay line, to the "start" input of the same module. Two PMT pulses sent to this configuration cause the following sequence (1) the undelayed first pulses arrives at "stop" and is ignored, (2) the delayed first pulse arrives at "start", initiating the TAC, (3) the undelayed second pulse arrives at "stop" and TAC generates an output, (4)

the delayed second pulse arrives at "start" and restarts the TAC. The TAC output generated by a pair of PMT pulses is, therefore, proportional to the time difference between the delayed first pulse and the undelayed second pulse. An example of two TAC input pulses, originating from a single PMT pulse, appears in Figure 4.13. A schematic of this pulse timing behavior appears in Figure 4.15. The MCA, operated in the voltage mode (V-mode), was used to obtain pulse-height distributions (PHDs) of TAC output pulses. Based on the time-scale setting of the TAC, these PHDs provided distributions of the times between pulses.

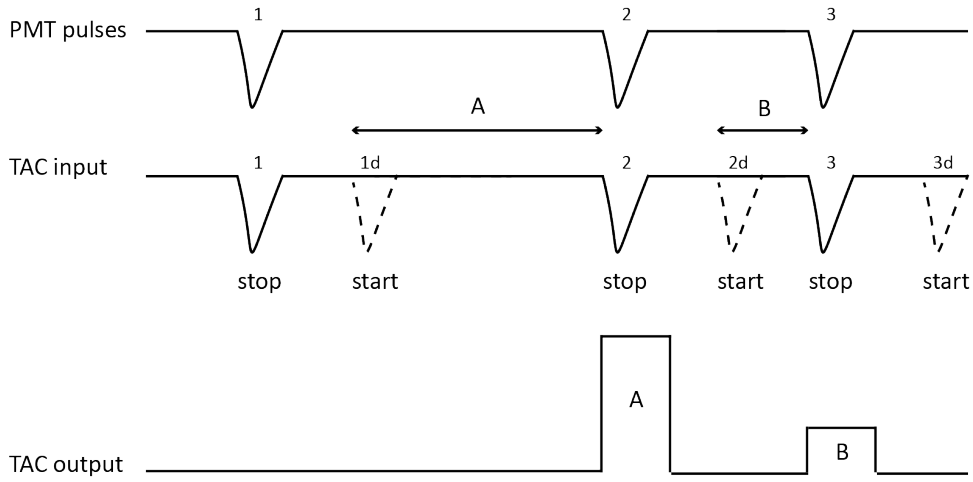

Figure 4.15: Visualization of TAC inputs and outputs. Three PMT pulses create two output pulses from the TAC. The first TAC pulse (A) corresponds to the time difference between the first delayed PMT pulse (1d) and the second PMT pulse (2). The second TAC pulse (B) corresponds to the time difference between the second delayed PMT pulse (2d) and the third PMT pulse (3).

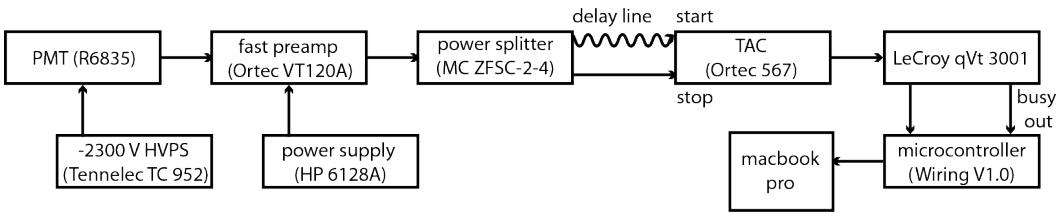

Figure 4.16: Pulse-timing electronics.

A fission-chamber beam monitor was utilized as a reference neutron detector during the scintillation experiments. This detector houses a thin deposit of ^{235}U (458.073 $\mu g/cm^2$) and a small, continuously-circulated volume of P-10 gas (90% argon, 10% methane). Neutrons that are absorbed in this deposit induce fission with an 85% probability, and the resulting fission products ionize the gas. The free charge may then be collected by an anode wire. Pulses from the detector were amplified by a charge-sensitive preamplifier (Tennelec 2273) and a shaping amplifier (Ortec 671), before they were sent to a multichannel analyzer (Tracor Northern 7200). PHDs from this MCA were transferred to a computer using a Perl script. The detector was operated at +125 V.

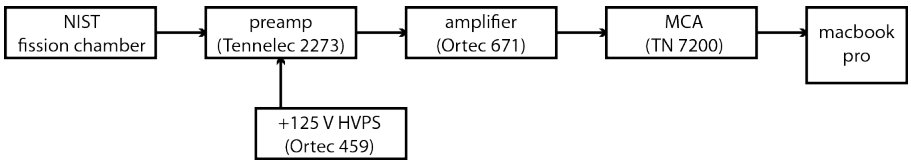

Figure 4.17: Fission-chamber beam-monitor electronics.

4.2.5 Electronics calibration

Excimer scintillation events, as observed by the PMT, often consisted of multiple closely spaced pulses arriving within a window of 0.1-10 μs. Oscilloscope traces of typical scintillation events appear in Figure 4.18. A series of simple calibrations were performed to verify the behavior and listed specifications of the PMT electronics for events of this type. A function generator (Tektronix AFG 3101) was used to introduce pulses of varying amplitudes and frequencies into the preamplifier, the

splitter, the C/T, and the MCA. The shape of a typical PMT pulse was emulated using the fastest settings of the tool: 5 ns rise time, 10 ns plateau, and 5 ns decay. In the amplitude regime, the low-amplitude thresholds of the C/T, and the MCA were observed to be -290 mV and -150 mV, respectively. Neither module exhibited an upper threshold for negative pulses up to -10 V. In the frequency regime, the C/T demonstrated 100% pulse collection at repetition rates up to the generator limit of 50 MHz. Finally, to verify the expected discrepancies between the C/T and the MCA, a pair of pulses were generated at a rate of 1 kHz. The spacing between each pulse in the pair was varied between 1 ms and 1 µs. As expected, the MCA failed to count both pulses at pair spacings shorter than 20 µs, due to its digitization time. Data from the C/T were, therefore, used to determine the absolute number of photon events. PCDs from the MCA were used only to verify the absence of multi-photoelectron pulses from the overall pulse population.

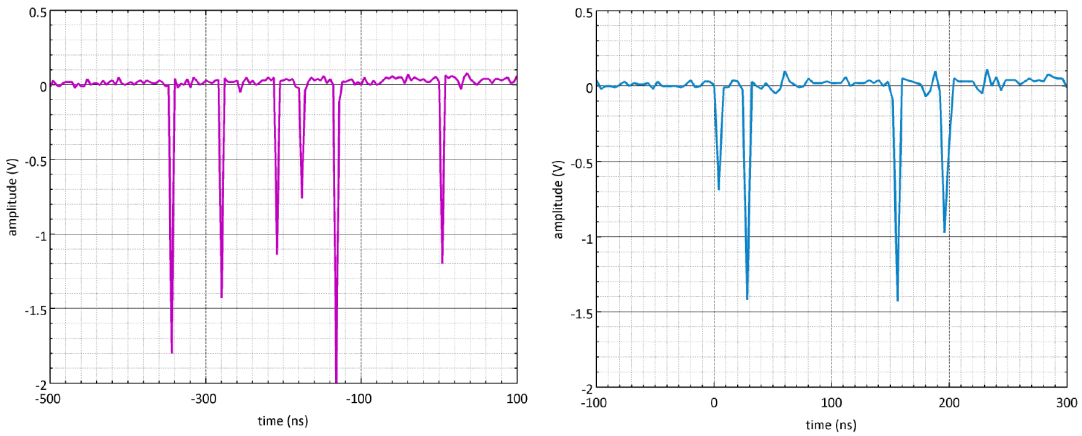

Figure 4.18: Oscilloscope traces from typical scintillation events, showing multiple pulses within 0.5 µs.

4.3 Measurements

After designing, assembling, and testing the various components of the experimental apparatus, a sequence of measurements were made to determine (1) the excimer scintillation yield from thermal-neutron irradiation of boron-10 thin films under Ar, Kr, Xe, and (2) the excimer lifetime under the same conditions.

To measure the excimer scintillation yield, a boron film sample was loaded into the scintillation cell, and the cell was evacuated and baked out overnight. With the reactor operating at 250 kW and the neutron beam propagating through the cell, PMT pulses were collected by the C/T and the MCA, for count periods of 200 seconds. During these measurements, data from the fission-chamber beam monitor were simultaneously collected over 1200-second count periods. Starting with an empty cell, a single noble gas was added to pressures of 50, 100, 150, 200, 300, 400, 600, and 800 torr. Two counts were recorded from the PMT at each pressure: one with lithium glass in front of the cell and one without. By collecting a pair of measurements for each set of experimental conditions, it was possible to isolate the component of the signal attributable to gamma-ray interactions. These measurements were taken consecutively to ensure the consistency of reactor conditions.

Once data from the first gas were gathered, the cell was reevacuated and the same process was repeated for the remaining gases. This entire procedure was repeated for four boron-10 targets of different thicknesses (300, 600, 900, 1200 nm). Background contributions from gamma rays were also measured by placing a "dummy" substrate

within the cell and allowing the mixed beam (neutrons and gammas) to propagate through it. This dummy substrate consisted of 2 nm of natural boron deposited on silicon.

To measure the excimer lifetime, a 1200-nm boron film was loaded into the scintillation cell and the cell was evacuated and baked out overnight. With the reactor, once again, operating at 250 kW, distributions of the times between PMT pulses were collected over 300-second count periods, for the same noble-gas types and the same range of pressures. Depending on the gas type and gas pressure, the TAC output range was adjusted in accordance with the observed distribution. The lithium glass beam block was also used to collect background distributions in this configuration.

The results and analysis of these measurements are discussed in Chapter 9. The calibrations, characterizations, and simulations contributing to this analysis are discussed in Chapters 5 - 8.

Chapter 5

Boron-10 Thin-Film Targets

The excimer scintillation experiment at Maryland utilized thin films of isotopically enriched boron-10 as neutron absorbing targets. These films were fabricated at the NIST Center for Nanoscale Science and Technology (CNST), by physical vapor deposition in an electron-beam evaporator. The films were later characterized using various methods to determine their density, thickness, chemical content, physical structure, and long-term stability. These characterizations took place at both UMD and NIST.

5.1 Fabrication

Boron films have previously been fabricated by many methods including sputtering [104, 105, 106], chemical vapor deposition (CVD) [107, 108, 109], physical vapor deposition (PVD) [110], thermionic vacuum arc [111, 112], electroplating [113], pulsed-laser deposition [114, 115], and even synchrotron-radiation-induced deposition [116]. Past research has examined a variety of boron-containing compounds (BN, B_4C, MgB_2), and a variety of substrates (Si, Fe, Al, NaCl, GaAs, diamond). In this project, boron films were fabricated strictly by physical vapor deposition, us-

ing isotopic ^{10}B of 92% enrichment. The films were deposited on plain silicon (111), as well as silicon treated with an adhesion layer of titanium or chemically-deposited natural boron. Several sets of films were fabricated across a range of thicknesses (0.3 - 2.5 μm) to examine the effects of absorber thickness on scintillation yield from the $^{10}\mathrm{B}(n,\alpha)^{7}\mathrm{Li}$ reaction.

Physical vapor deposition encompasses a number of techniques that rely on physical processes to deposit thin-films under vacuum. Electron-beam evaporation (EBPVD) was used to fabricate the ^{10}B targets for the excimer scintillation experiment. During EBPVD, an electron beam heats a small amount of source material to the point of vaporization. The electron beam, the source, and the source crucible, reside in a vacuum chamber. A portion of the vaporized source material adheres to sample substrates, which are also situated in the vacuum chamber. Both the power of the electron beam, and the distance between the source and the substrates, determine the rate of deposition. A diagram of a typical EBPVD chamber appears in Figure 5.1.

Before fabricating the boron films, it was necessary to prepare substrates upon which the films were deposited. The primary substrates were silicon wafer pieces, 2.54×2.54 cm, with thicknesses of 525 μm. These pieces were scored from 10 cm wafers, using a dicing saw (Microautomation BKSIDE-02) in the UMD FabLab. Each wafer was cleaned with piranha etch (H_2SO_4 and H_2O_2), rinsed in deionized water, and dipped in hydrofluoric acid to remove the native oxide from its surface. The wafers were then broken into squares and heat sealed into aluminized-boPET

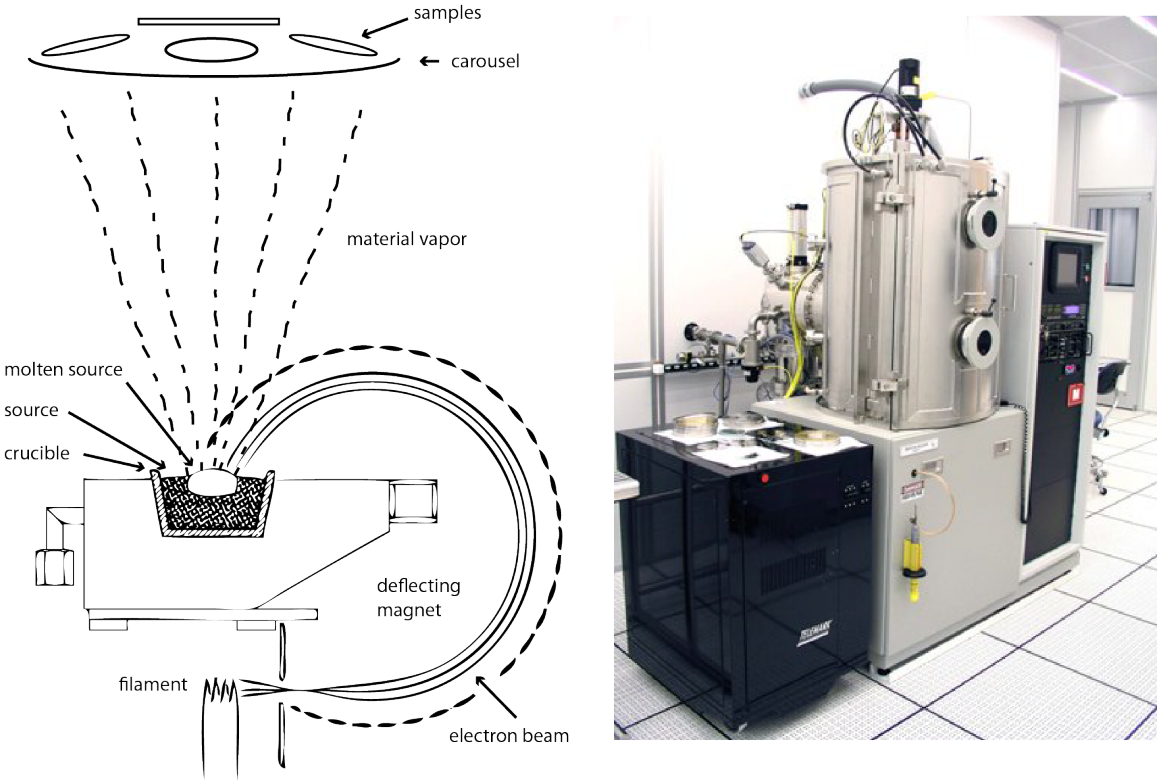

Figure 5.1: Left: Diagram of an electron-beam evaporator. Redrawn from [117]. Right: Denton EBPVD tool used for boron film fabrication [118].

pouches within a nitrogen glove box, to prevent their surfaces from reoxidizing. Additional silicon substrates were provided by Dr. Lis Nanver of the Delft University of Technology. These substrates, fabricated at Delft, were chemically deposited with a 2-nm film of natural boron, providing an epitaxial surface for the enriched ^{10}B to adhere to during the EBPVD process.

The ^{10}B films were fabricated in the NIST CNST NanoFab clean room. The EBPVD tool (Denton Infinity 22) is pictured in Figure 5.1. Prior to loading the substrates, the back of each sample was marked with a diamond scribe as a means of identification. The samples were then mounted to holders and suspended in a carousel rack at the top of the vacuum chamber. Granular ^{10}B source material was also loaded

into 25 cc graphite crucibles at the bottom of the chamber. The ^{10}B source material is pictured in Figure 5.2.

After evacuating the chamber to a pressure $< 5.0 \times 10^{-6}$ torr, the source material was premelted using the electron beam. A low-power premelt prevented boron fragments from dispersing in the chamber during the higher power depositions. An internal shutter blocked the substrates from boron vapor throughout this phase. Following the premelt, the current of the electron beam was increased according to a preset program, and the shutter was opened to begin the deposition. Both the rotation speed of the carousel, and the rastering pattern of the electron beam on the source, were tuned to achieve uniform deposits. A quartz crystal oscillator within the vacuum chamber was used to regulate the deposition rate, and to measure the cumulative deposit thickness. As the mass of deposited material on a quartz oscillator increases, its vibration frequency decreases. In this way, the thickness of each deposit was calculated using a preprogrammed material density, and known characteristics of the crystal. The power of the electron beam was limited to 3.5 kW during the depositions, and the acceleration voltage was held constant at 10 kV. The various program parameters of the EBPVD tool, during these depositions, appear in Table 5.1. The various sets of ^{10}B films will be referred to by their nominal thicknesses, as programmed into the deposition tool.

A thermocouple attached to the carousel was used to determine the temperature of the samples within the chamber. By the end of the longer depositions, this temperature was typically 175°C. For comparison, the melting point of boron is

2075°C at atmospheric pressure [76]. Following the depositions, the samples were allowed to cool below 60°C before they were removed. The films were then packaged in a desiccator, transported to a nitrogen-filled glovebox, and sealed in boPET pouches until further use. An image of one set of boron films, immediately after deposition, appears in Figure 5.2.

Table 5.1: Tool settings during the boron-film depositions and titanium adhesion-layer depositions. Rise, soak, and predeposit parameters describe the rate at which the electron beam current is increased prior to the depositions. Electron-beam powers are listed as percentages of the 10-kW tool maximum.

	Material	
Parameter	Titanium	Boron-10
density (g/cm^3)	4.50	2.54
acoustic impedance (g/cm^2s)	14.06	22.7
rise time to soak (min)	2	4
soak time (min)	1	1
soak power (%)	12	14
rise time to predeposit (min)	1	1
predeposit time (min)	1	0.5
predeposit power (%)	13.5	16
max deposit power (%)	25	35
deposition rate (Å/s)	1	1/2.5/5
tooling factor (%)	136	136

Several sets of films were fabricated across three visits to the CNST NanoFab. The first group, fabricated in July 2011, included film thicknesses of 1.5, 2.0, and 2.5 μm, deposited on pure silicon. These films suffered peeling and delamination from the substrates due to intrinsic stress. An image of the delaminated films appears in Figure 5.3. Both the lack of literature on boron-film fabrication > 1 μm, and the experience of the staff at the CNST, indicate that the practical upper limit of boron-film fabrication by EBPVD lies between 1 - 2 μm. Thinner depositions were next attempted.

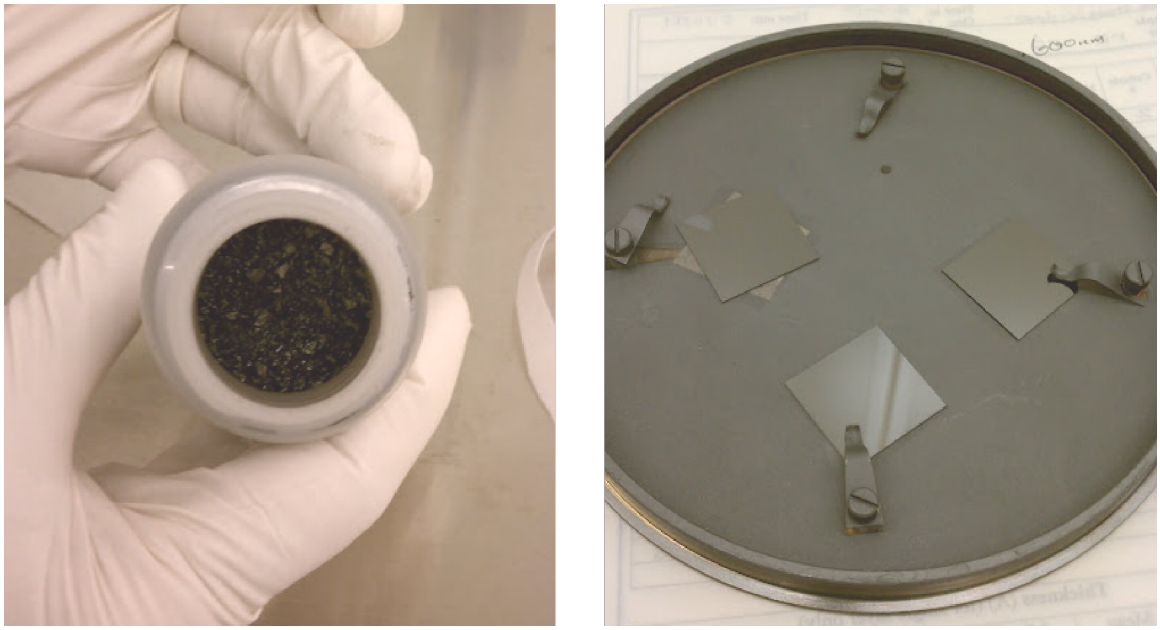

Figure 5.2: Left: Boron-10 source material. Right: 600-nm ^{10}B films mounted to the deposition holder.

The second group of films, fabricated in August 2011, included film thicknesses of 300, 600, and 900 nm. These films were deposited on silicon treated with a 10-nm adhesion layer of titanium. The use of this adhesion layer came by recommendation from the CNST staff, as a means to reduce stress. The titanium was deposited in the same EBPVD tool. The parameters of the titanium depositions appear in Table 5.1. This set of boron films did not show visible signs of physical stress or delamination. Since the stress in the films was naturally lower, as a result of their reduced thicknesses, the stress-reducing contribution of the titanium adhesion layer remains unknown.

A third group of films was fabricated in March 2012, at thicknesses of 1.2 and 1.5 μm. These films were deposited on the epitaxial substrates provided by Dr. Nanver. None of these films delaminated, though the 1.5 μm films developed visible signs of

stress within a day of fabrication, in the form of bubbling and fracturing of the film surface. Ultimately, only the films which demonstrated prolonged physical stability (the 300, 600, 900 nm films from August, and the 1200 nm films from January) were used as targets in the excimer scintillation experiment.

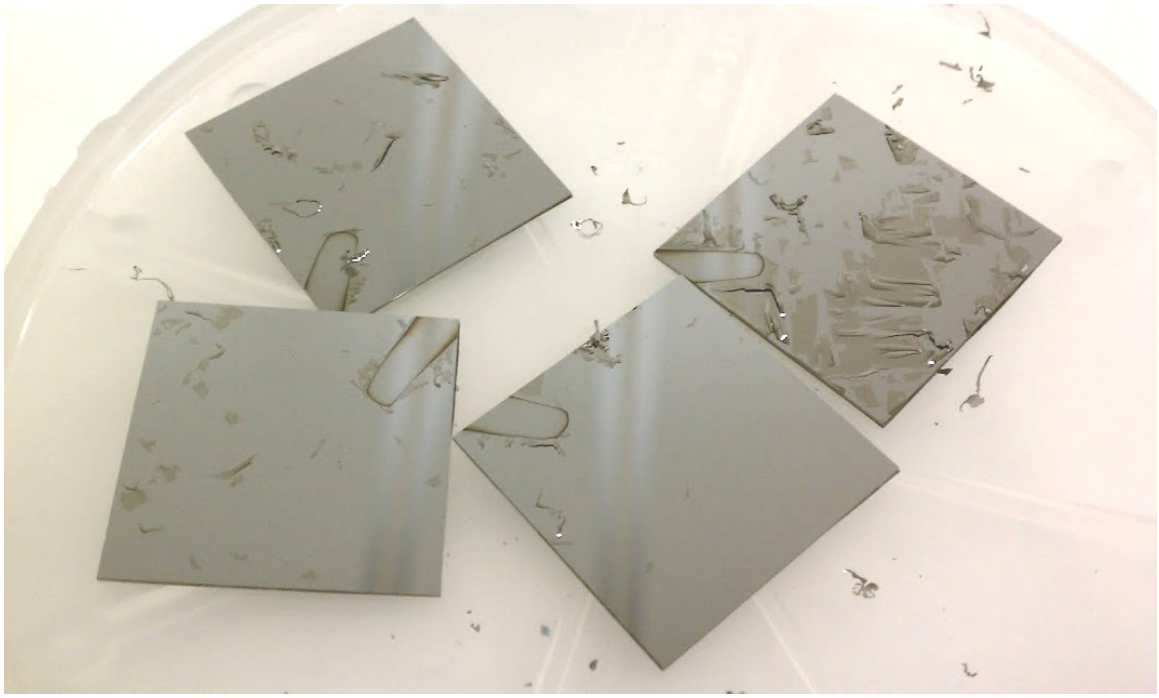

Figure 5.3: Delamination of 2.5 μm films, immediately after deposition.

5.2 Characterization

Several characterizations of the boron thin-film targets were performed to determine their neutron absorbing properties (content, thickness, density), and the stability of those properties over the course of the scintillation measurements. The characterization techniques included neutron imaging, profilometry, x-ray photoelectron spectroscopy (XPS), x-ray diffraction (XRD), scanning electron microscopy (SEM), ellipsometry, and stress measurement.

5.2.1 Neutron imaging

The thermal-neutron absorption properties of the ^{10}B thin films were measured at the neutron imaging facility (NIF/BT2) at the NCNR. This facility uses an intense, collimated beam of thermal neutrons to obtain radiograph images from a spatially sensitive neutron detector. Neutrons from the NBSR pass through a cooled, single-crystal bismuth filter, a series of apertures, and an evacuated flight tube, before impinging on a sample, and a position-sensitive detector. A digram of the neutron imaging facility appears in Figure 5.4. The NIF detector consists of a ^{6}Li conversion layer, a ZnS scintillation layer, and an x-ray imager (Varian PaxScan 2520) made of amorphous silicon. The imager has an active area of 19.3×24.2 cm and a pixel size of 127 μm^2. The fluence of the neutron beam during the boron film imaging was 5.31×10^6 cm^{-2}s^{-1} at the sample position. A diagram of the detector and the sample location appears in Figure 5.5.

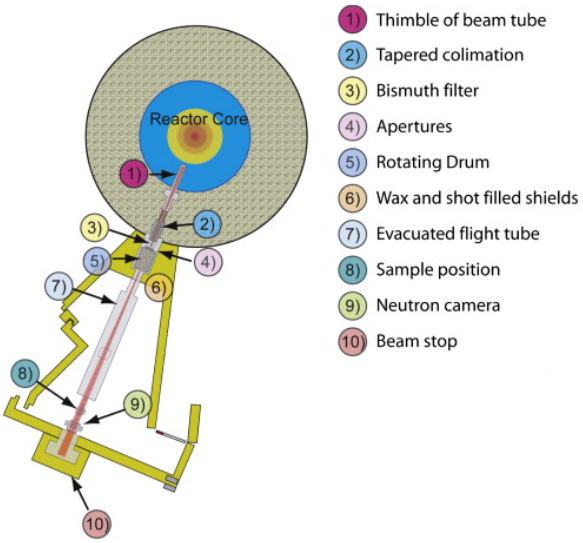

Figure 5.4: Plan view of the NCNR neutron imaging facility [119].

Each boron film used in the scintillation experiments was placed in a holder and mounted at the sample position in the imaging station. A photograph of a boron sample and the sample holder appears in Figure 5.6. Upon opening the beam shutter, the neutron beam illuminated each sample and the detector collected a series of 1800 images, with 1-second exposures. This measurement was repeated, without a sample or a sample holder in the beam, to obtain a flat-field image. All of the images were then corrected for the point spread function (PSF) of the detector system with assistance from Dr. Daniel Hussey. The PSF is a systematic additive background, attributed to diffuse light in the scintillation screen of the detector [120].

Following the PSF corrections, the images of each sample (1800 per sample) were averaged to form a single image. By dividing the averaged flat-field image from the averaged image of each boron film, the fractional absorption of each sample was determined. The resulting images appear in Figures 5.7 - 5.11. From the Beer-

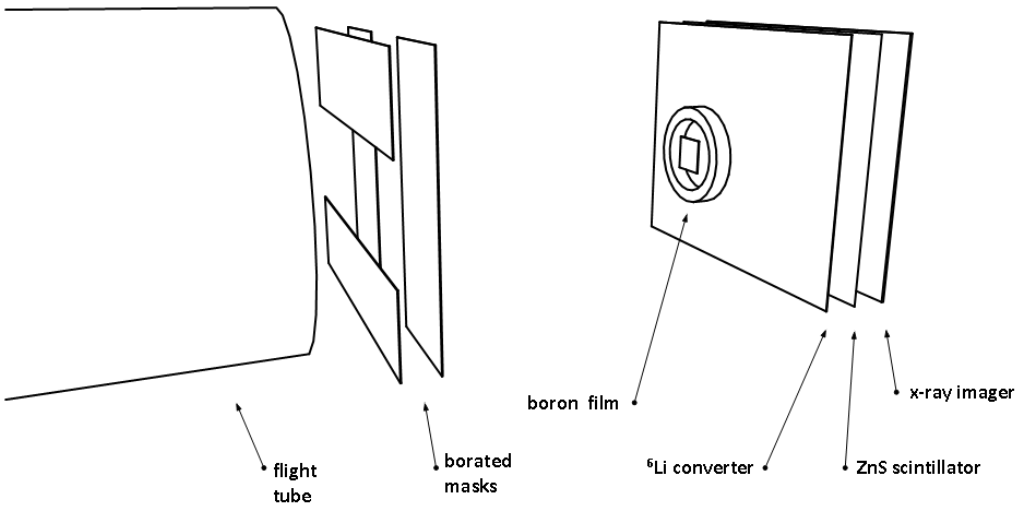

Figure 5.5: Diagram of the NIF detector station. The detector is shown in an exploded view.

Lambert law (see Eq. 2.2), the value of each pixel (P) in these images represents fractional absorption, in the form,

$$P = 1 - \frac{I}{I_0} = 1 - e^{-\Sigma x} \tag{5.1}$$

where I_0 is the intensity of the incident neutron beam, I is the intensity of the neutron beam after passing through the sample, Σ is the macroscopic cross section of the sample, and x is the thickness of the sample. The value of $\frac{I}{I_0}$ is determined by dividing each pixel value in the sample image by the corresponding pixel value in the empty flat-field image. The colormap of each image in Figures 5.7 - 5.11 depicts the neutron absorption fraction between 0 - 10%.

Rearranging Eq. 5.1, each pixel in the neutron image acquires a value,

$$\Sigma x = -\ln(1 - P) \tag{5.2}$$

By averaging the values of (Σx) over the surface of each film, the areal density of the films $((\rho_A)_{10})$ may be determined, with the equation,

$$(\rho_A)_{10} = \frac{\overline{(\Sigma x)}}{\langle\sigma\rangle_{\mathrm{NIF}}} \frac{M_{10}}{N_A} \tag{5.3}$$

where $\overline{(\Sigma x)}$ is the average value of (Σx) determined from the neutron image, $\langle\sigma\rangle_{\mathrm{NIF}}$ is the effective cross section of ^{10}B in the NIF neutron beam, M_{10} is the molar mass of ^{10}B (10.0129 g/mol [76]), and N_A is Avogadro's number (6.022×10^{23} mol^{-1}).

The value of $\langle\sigma\rangle_{\mathrm{NIF}}$ may be determined with a continuous weighted average, in the form,

$$\langle\sigma\rangle_{\mathrm{NIF}} = \frac{\int \sigma_{10}(\lambda)\phi(\lambda)\,\mathrm{d}\lambda}{\int \phi(\lambda)\,\mathrm{d}\lambda} \tag{5.4}$$

where $\sigma_{10}(\lambda)$ is the neutron-wavelength-dependent, microscopic neutron-absorption cross section of ^{10}B, and $\phi(\lambda)$ is the neutron-wavelength distribution of the NIF beam, normalized for each wavelength bin $\left(\frac{\mathrm{d}\phi}{\mathrm{d}\lambda}\right)$. The distribution $\frac{\mathrm{d}\phi}{\mathrm{d}\lambda}$ was previously measured at the NIF with a neutron chopper and time-of-flight spectrometry. The neutron-wavelength distribution of the NIF beam appears in Figure 5.12. In solving Eq. 5.4, the neutron-wavelength parameter space was used, rather than the neutron-energy parameter space, to avoid amplification of noise in the fast and epithermal regions of the $\frac{\mathrm{d}\phi}{\mathrm{d}\lambda}$ data. The value obtained from Eq. 5.4 is $\langle\sigma\rangle_{\mathrm{NIF}} = 3936.1$ b. By comparison, the 2200 m/s cross section of ^{10}B is 3842 ± 8 b [77]. The thermal neutron absorption cross section of silicon is small ($\sigma_0 = 2.16$ b), as demostrated by the nearly invisible substrate in Figure 5.11. Therefore, the absorption of each sample

was attributed completely to absorption by ^{10}B. The values of $(\rho_A)_{10}$, obtained from Eq. 5.3 and 5.4, appear in Table 5.2.

The uncertainties in $(\rho_A)_{10}$ are dominated by the uncertainty in $\langle\sigma\rangle_{\mathrm{NIF}}$. Dr. Daniel Hussey has estimated that the uncertainties in the NIF measurements of $\left(\frac{\mathrm{d}\phi}{\mathrm{d}\lambda}\right)$, lie between 5-10%. A conservative 10% uncertainty has therefore been associated with the values of $(\rho_A)_{10}$ in the final analysis in Chapter 9. However, the relative variations (root mean square (RMS) values) in the measurements of $\overline{(\Sigma x)}$ are ≤ 1 %. Additionally, these RMS values are nearly identical for all of the measured samples (see Table 5.2). Consequently, the RMS values represent a statistical limit imposed by counting time or baseline noise of the NIF detector, and are not correlated to density variations in the ^{10}B samples. They do, however, provide an upper limit for this density variation.

Nominal Thickness (nm)	$\overline{(\Sigma x)}$	RMS	$(\rho_A)_{10}$ (μg/cm^2)
300	0.01740	2.39×10^{-4}	73.50
600	0.03321	2.39×10^{-4}	140.31
900	0.04951	2.39×10^{-4}	209.13
1200	0.06155	2.39×10^{-4}	260.02
substrate	4.80×10^{-4}	2.39×10^{-4}	2.028

Table 5.2: Areal densities of the ^{10}B films obtained though the analysis of neutron imaging data. Nominal film thicknesses indicate the input to the EBPVD deposition tool at the time of film fabrication. Measurements of an epitaxial substrate, deposited with 2-nm of natural boron, are also listed.

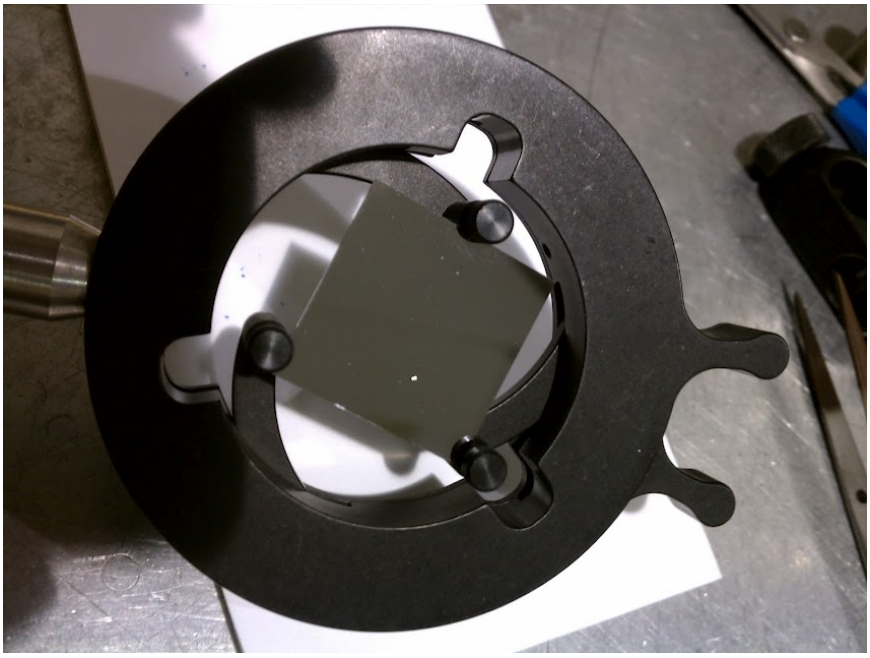

Figure 5.6: Boron-10 film and holder used for neutron imaging

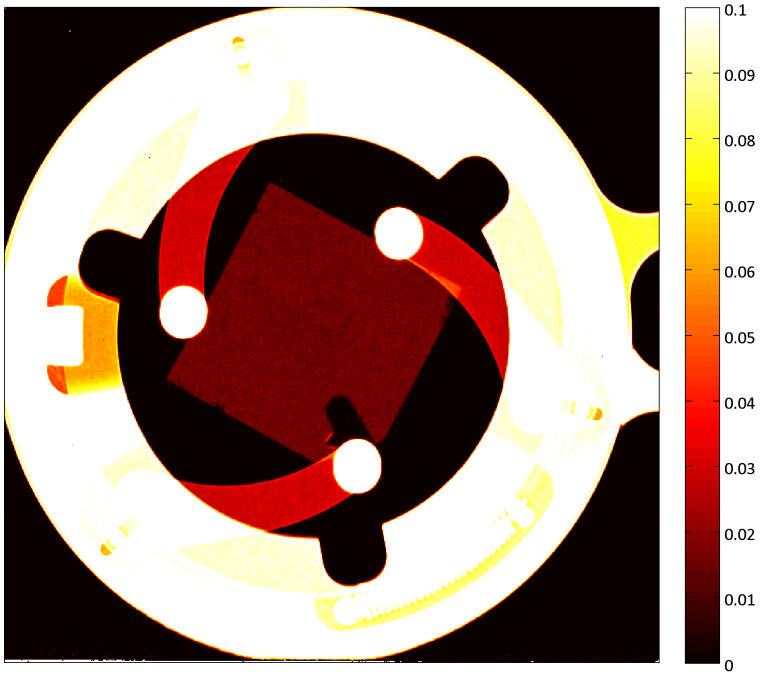

Figure 5.7: Thermal-neutron image of a 300-nm ^{10}B film. The colorscale of the image represents fractional absorption between 0 - 10%.

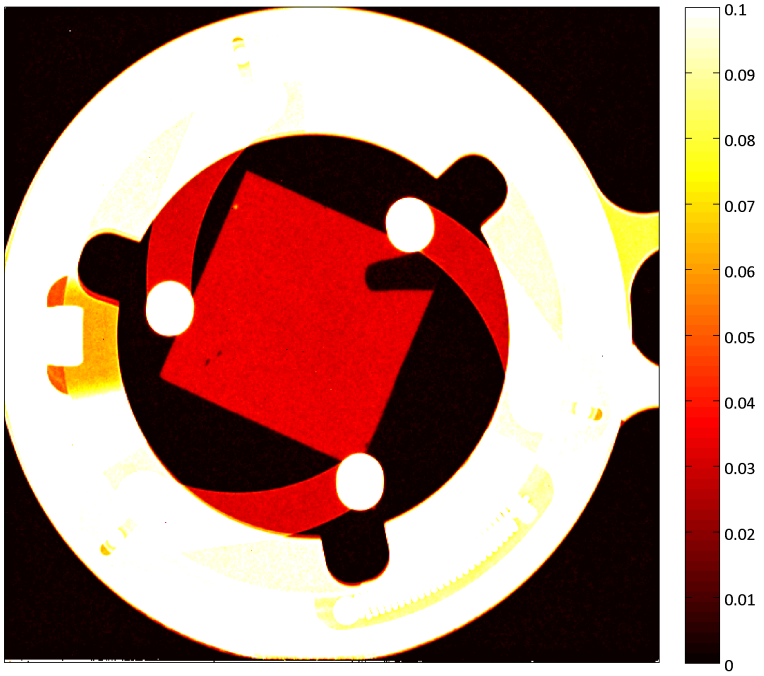

Figure 5.8: Thermal-neutron image of a 600-nm ^{10}B film. The colorscale of the image represents fractional absorption between 0 - 10%.

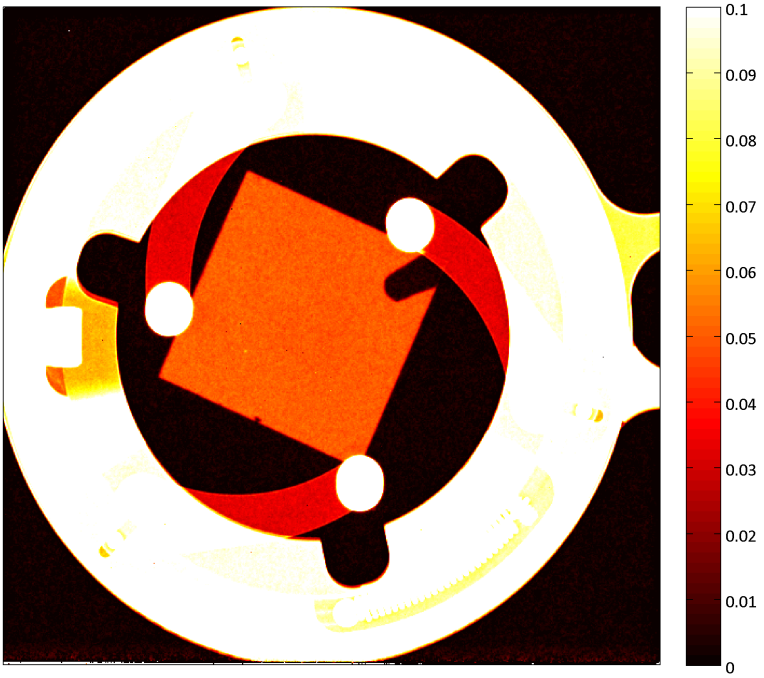

Figure 5.9: Thermal-neutron image of a 900-nm ^{10}B film. The colorscale of the image represents fractional absorption between 0 - 10%.

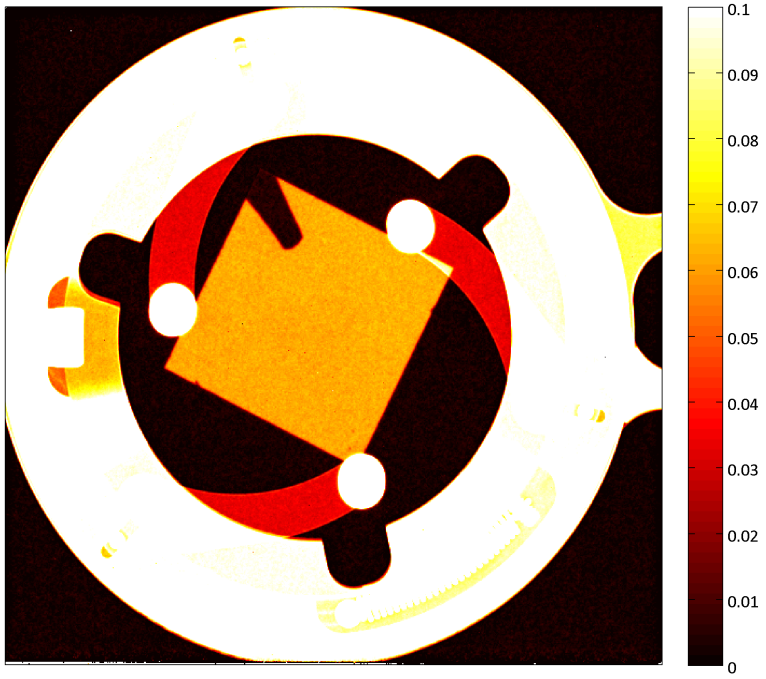

Figure 5.10: Thermal-neutron image of a 1200-nm ^{10}B film. The colorscale of the image represents fractional absorption between 0 - 10%.

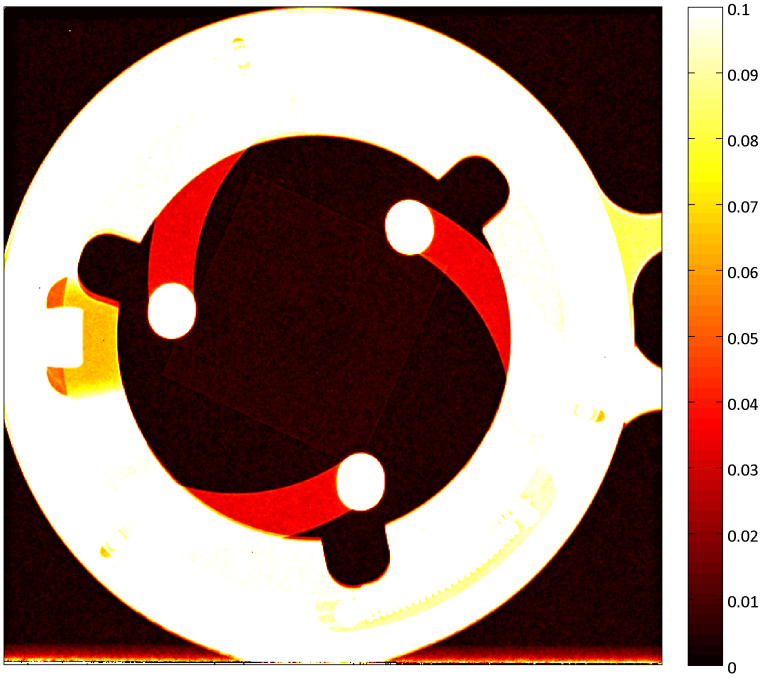

Figure 5.11: Thermal-neutron image of a 2-nm layer of natural boron on a silicon substrate. The colorscale of the image represents fractional absorption between 0 - 10%.

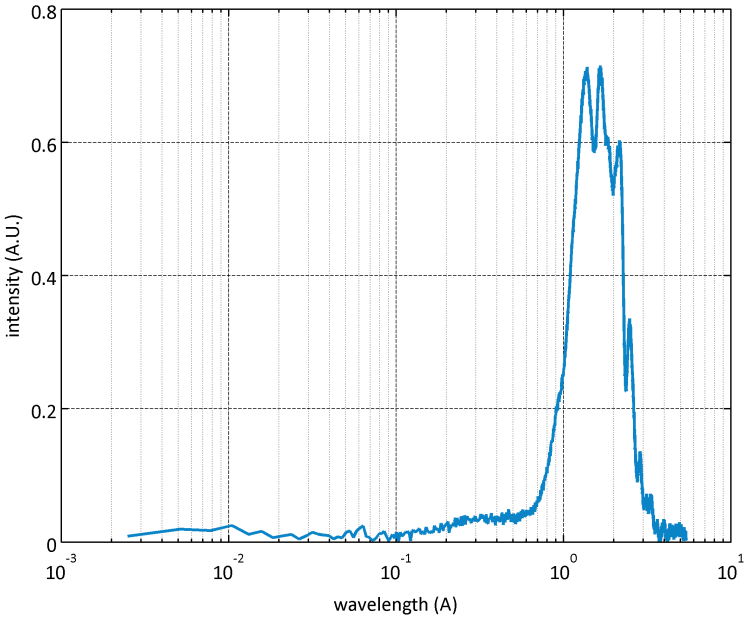

Figure 5.12: Neutron-wavelength distribution of the NIF beam. Secondary peaks are the result of Bragg diffraction due to the Bi-crystal filter.

5.2.2 Profilometry

A contact profilometer (Bruker Dektak XT) located in the CNST NanoFab, was used to measure the thicknesses of the boron films. This tool moves a stylus laterally across a sample to determine the profile of its surface based on the vertical deflection of the stylus. During the evaporation process, the sample clips holding the substrates in the EBPVD tool shielded one corner of each substrate from the boron vapor. This resulted in a bare spot of silicon on each sample, across which each boron film thickness was measured. The clip silhouettes are visible in the neutron images in Figures 5.8 - 5.10.

For each boron sample, several scans of the silicon-boron step were performed at different angles and positions. The parameters of these scans appear in Table 5.3. Typical data from the scans are plotted in Figure 5.13. The step heights and roughnesses of each film were calculated using the Vision 64 software, associated with the profilometer. These outputs were then averaged across several scans of the same sample. The average step heights are within 10% of the nominal film thicknesses, as programmed in the deposition tool. Two different parameters for roughness were determined, R_a and R_z. The value R_a is the average variation of all data points in a scan from the mean of those data points. The value R_z is the average of the differences between the five highest peaks and valleys in a scan. The results appear in Table 5.4.

Table 5.3: Profilometer scan parameters.

Parameter	Value
Scan length	400 µm
Lateral scan resolution	0.044 µm
Stylus force	0.9 mg_f
Stylus radius	0.7 µm
Vertical range	6.5 µm
Vertical resolution	1.0 Å

Table 5.4: Film thicknesses and roughnesses from profilometry. $\overline{h}$ = average step height. δ_h = relative difference between $\overline{h}$ and nominal thickness.

Nominal thickness (nm)	$\overline{h}$ (nm)	δ_h (%)	R_a (nm)	R_z (nm)
300	278.4	7.2	6.44	42.1
600	586.2	2.3	5.01	38.7
900	889.0	1.2	3.64	39.6
1200	1151	4.0	3.86	23.6

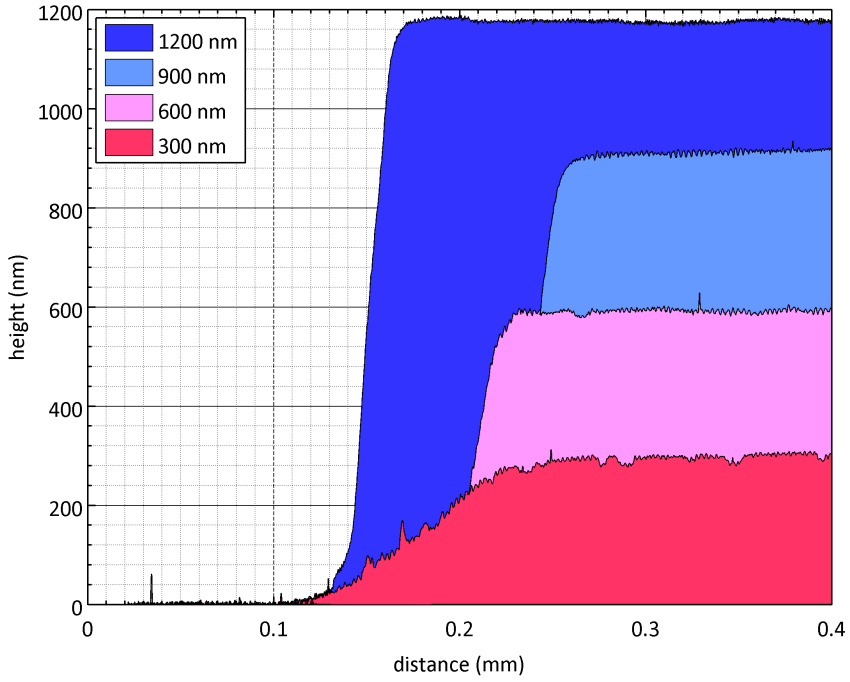

Figure 5.13: Profilometer scans of several ^{10}B thin-film targets.

5.2.3 X-ray photoelectron spectroscopy

X-ray photoelectron spectroscopy (XPS) is a technique used to determine the chemical composition of surfaces. In XPS, a sample is placed under vacuum and irradiated with a collimated beam of soft x-rays. Atoms within 5 - 10 nm of the target surface are ionized by these x-rays, and the resulting electrons are focused towards an electron-energy spectrometer. The spectrometer eliminates all but a narrow passband of electrons, according to their kinetic energies. The mean energy of this passband is tunable to allow scanning across the electron-energy spectrum. After passing through the spectrometer, electrons within the passband impinge on an electron detector. Together, the analyzer, the detector, and the associated electronics measure the distribution of ionized electrons as a function of their kinetic energies.

The kinetic energies of the electrons (E_{KE}) impinging on an XPS detector are given by the equation,

$$E_{KE} = E_{h\nu} - E_{\phi} - E_{BE} \tag{5.5}$$

where $E_{h\nu}$ is the energy of the incident x-rays, E_{ϕ} is the work function of the spectrometer, and E_{BE} is the electron binding energy of the sample. Since $E_{h\nu}$ and E_{ϕ} are known, and the distribution of E_{KE} is measured, the distribution of E_{BE} may be derived from this equation. Electron binding energies are characteristic of specific materials, and they are accurately tabulated for a large number of elements and compounds. A distribution of E_{BE} may be used to identify the chemical composition

of a sample surface. A diagram of a typical XPS setup appears in Figure 5.14.

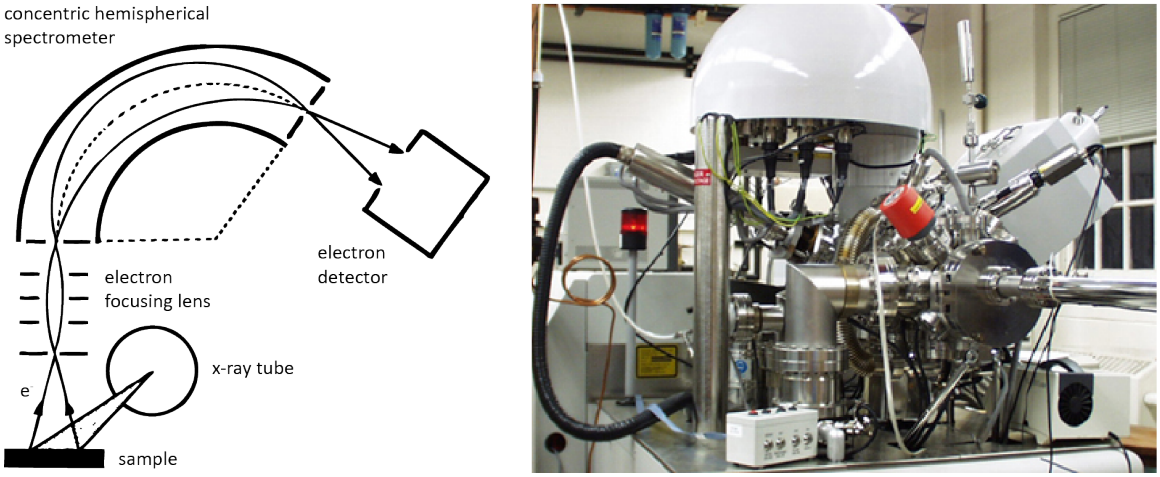

Figure 5.14: Left: Schematic of an XPS tool. Redrawn from [121]. Right: Kratos AXIS 165 used for boron film analysis [122].

Prior to the excimer scintillation experiment, XPS was used to investigate (1) potential oxidation of the boron films, (2) sources of nitrogen and oxygen impurities in the films, and (3) the depth profiles of these impurities. The measurements were performed at the MRSEC, with assistance from Dr. Karen Gaskell. The XPS tool (Kratos AXIS 165) uses a monochromatic (1.486 keV) aluminum x-ray source and a 165-mm concentric hemispherical analyzer. A photograph of this tool appears in Figure 5.14. The base vacuum pressure for these measurements was 3×10^{-9} torr. All measurements were collected at a 90° takeoff angle (electron emission angle with respect to the sample surface).

In the first set of measurements, four boron film samples were analyzed for surface oxidation. Three of these boron samples (300, 600, 900 nm thicknesses) were stored on a workbench, open to atmosphere, for 3.5 months after fabrication. The remaining boron sample (300 nm) was stored in a nitrogen-filled glove box over the same

period. The concentrations and peak centroids derived from the E_{BE} distributions, appear in Table 5.5. For comparison, binding energy peak centroids and widths for various boron compounds appear in Figure 5.15. The E_{BE} distributions for both 300 nm films (stored in N_2, and stored in atmosphere) appear in Figures 5.16 and 5.17. The boron peaks isolated from these distributions appear in Figure 5.18.

As shown in Figure 5.15, the binding energy peak of boron-oxide (B_2O_3) is quite distinct from the elemental boron peak. The E_{BE} distributions, obtained from the XPS measurements, show no signs of a minor B_2O_3 peak from any of the boron samples. The isotopic enrichment of the samples could contribute to the shift of the major boron peak (187.5 eV) from the tabulated value (189.5 eV). While oxygen is apparent in the spectra (531.7 eV), it does not arise from metal oxides (529.5 eV). Rather it most likely comes from hydroxides (531.5 eV). Additionally, a small amount of nitrogen appears in all of the samples (400.3 - 401.5 eV), most closely matching the E_{BE} of ammonium salts (400.5 - 403 eV). The carbon peak arises from adventitious carbon, a contaminant found on nearly every freshly exposed surface [123]. Ultimately, no evidence of oxidation was observed in any of the samples, however, the presence of oxygen and nitrogen in the films was further investigated with XPS.

A second set of measurements was performed to analyze the ^{10}B source material, the melted source material from the EBPVD chamber, and the crucible that contained the melted boron. All three of these samples were shown to contain both oxygen and nitrogen, in amounts comparable to the boron films. The concentrations and peak centroids from these spectra appear in Table 5.6.

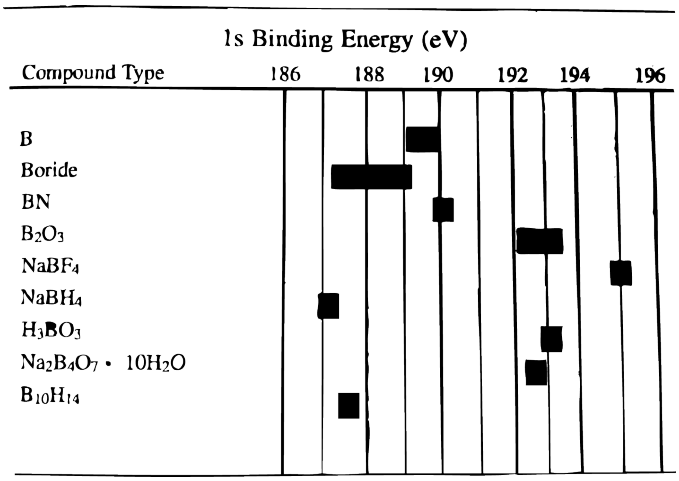

Figure 5.15: Typical E_{BE} and XPS peak widths of boron compounds [124].

To determine the depth profile of nitrogen and oxygen throughout the boron films, one of the samples (600 nm) was sputtered with an argon ion gun (50.84 μA/cm^2) within the XPS chamber. Sputtering removes atoms from the surface of a target by momentum exchange between an energetic ion and an atom in the material. During this process, XPS measurements were collected every 300 s. The sputtering rate of boron was not found in the literature, therefore the ultimate sputter depth is unknown. The measured concentrations are plotted, as a function of sputtering time, in Figure 5.19. Clearly, the nitrogen, oxygen, and carbon, found in the earlier measurements, exist predominantly at the sample surface. After only 300 s of sputtering,

the concentrations of these contaminants were reduced to $< 2\%$. At 6000 s, the sputtering was stopped and the sample was allowed to sit overnight in the vacuum chamber at a base pressure of 3×10^{-9} torr. When measurements were resumed, the same contaminants reappeared. Even in ultrahigh vacuum, trace amounts of the contaminants adhered to the sample surface, demonstrating an affinity of these compounds for boron.

Table 5.5: Concentrations (%) and E_{BE} peak centroids (eV) of surface contaminants in boron films.

Sample	Boron	Nitrogen	Oxygen	Carbon
300 (N_2)	78.94/187.7	0.44/401.5	7.03/531.8	13.58/284.8
300	77.86/187.5	0.72/400.5	8.18/531.7	13.24/284.8
600	78.12/187.5	0.61/401.2	8.53/531.8	12.74/284.8
900	75.31/187.5	0.81/400.3	7.66/531.7	16.22/284.8

Table 5.6: Concentrations (%) and E_{BE} peak centroids (eV) of surface contaminants in boron source materials.

Sample	Boron	Nitrogen	Oxygen	Carbon
Source granule	70.30/187.8	1.06/400.1	11.20/531.8	17.44/284.8
Boron melt	54.84/187.8	3.63/402.0	19.70/532.1	21.83/284.8
Crucible wall	65.76/187.5	0.42/401.6	12.56/531.9	21.26/284.8

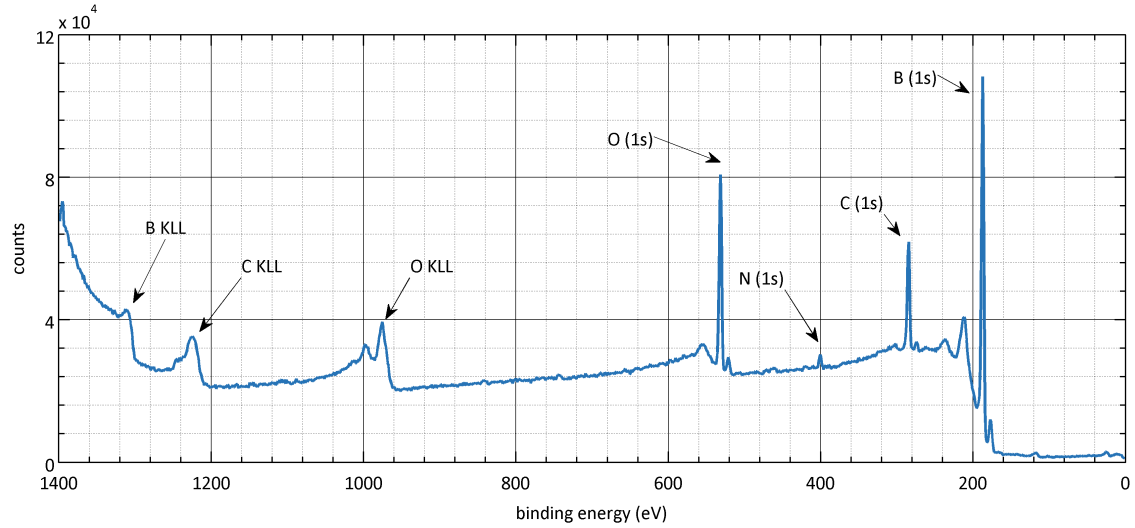

Figure 5.16: E_{BE} distribution for a 300-nm boron film stored in atmosphere. KLL peaks originate from Auger electrons.

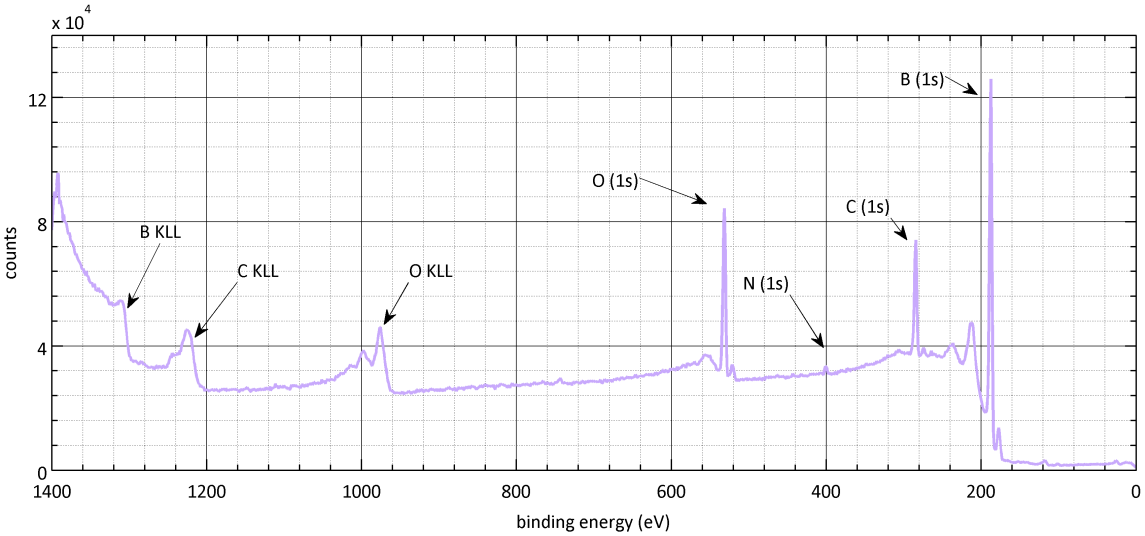

Figure 5.17: E_{BE} distribution for a 300-nm boron film stored in N_2 glovebox. KLL peaks originate from Auger electrons.

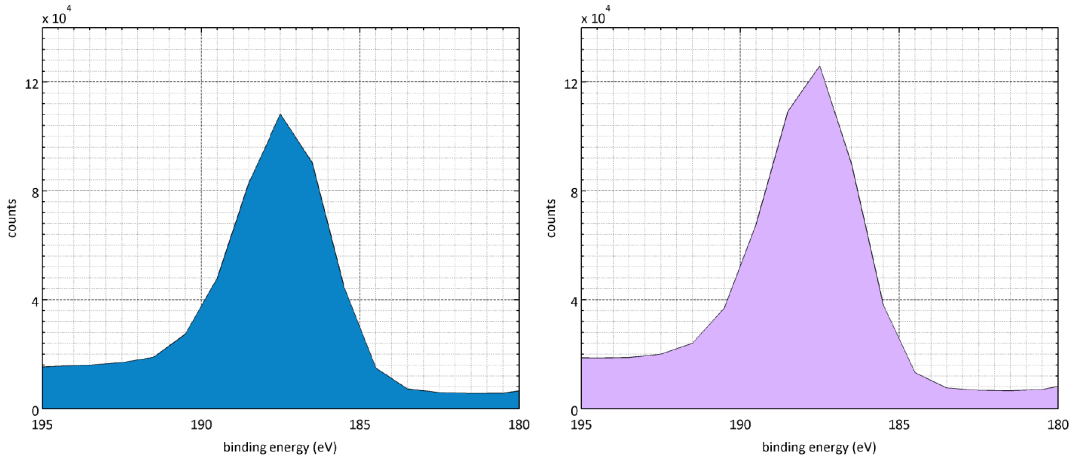

Figure 5.18: Boron (1s) electron peaks from XPS. Left: 300-nm film stored at atmosphere. Right: 300-nm film stored in an N_2 glovebox.

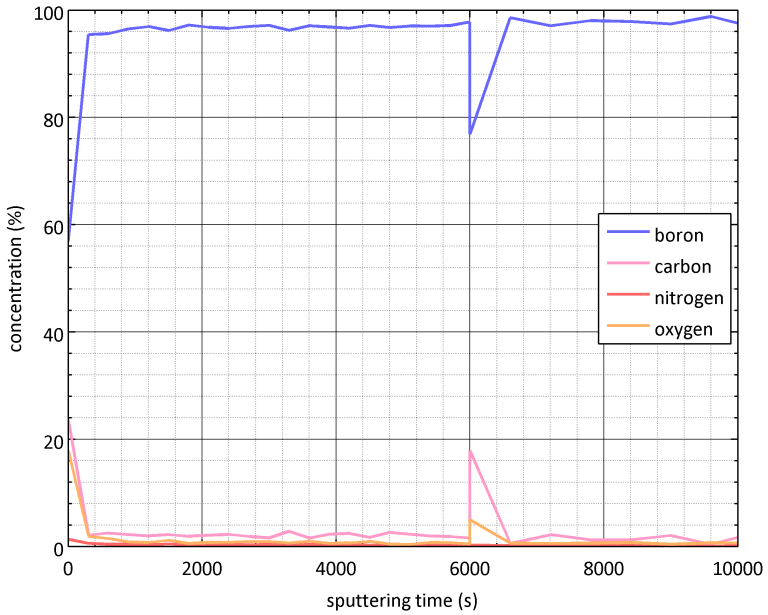

Figure 5.19: Contaminant concentrations in the ^{10}B films during sputtering. Sputtering and XPS measurements were stopped automatically at 6000 s and were resumed 8 hours later.

5.2.4 X-ray diffraction

The crystallinity of the boron films was analyzed with an x-ray powder diffractometer in the X-ray Crystallography Lab at Maryland. X-ray diffraction relies on the specular scattering of x-rays from the atoms in a crystal lattice. Bragg's law is used to describe the conditions for constructive interference between photons reflected from two successive crystal planes, and is given by the equation,

$$2d \sin\theta = n\lambda \tag{5.6}$$

where d is the spacing between the diffracting planes, θ is the angle of incidence of the x-rays, n is an integer, and λ is the x-ray wavelength. A diagram of Bragg scattering appears in Figure 5.20. By irradiating a sample with a collimated beam of x-rays, a scattered interference pattern may be formed on a detector opposite the sample. This pattern is dependent on θ. By scanning over θ, it is possible to determine the crystal structure of a sample based on Bragg peaks in the interference pattern. In powder diffraction, x-rays are scattered from a sample of randomly oriented microcrystals. The resulting interference pattern takes the form of Debye-Scherrer cones, which create rings on a flat plate detector. These rings may be used to determine the lattice spacing of a crystal [125].

The diffractometer used to analyze the boron films was a Bruker Apex2, equipped with a CCD area detector. The only peaks visible in a scan of a 600 nm sample arise from the silicon substrate. The dominant peaks from tetragonal boron ($2\theta = 20.3^\circ$)

and alpha-rhombohedral boron ($2\theta = 21.9°$) do not appear, indicating that the boron films were amorphous. XRD spectra from numerous crystalline forms of boron are discussed in [126]. The XRD spectrum from the 600-nm sample, showing only characteristic silicon peaks, appears in Figure 5.21.

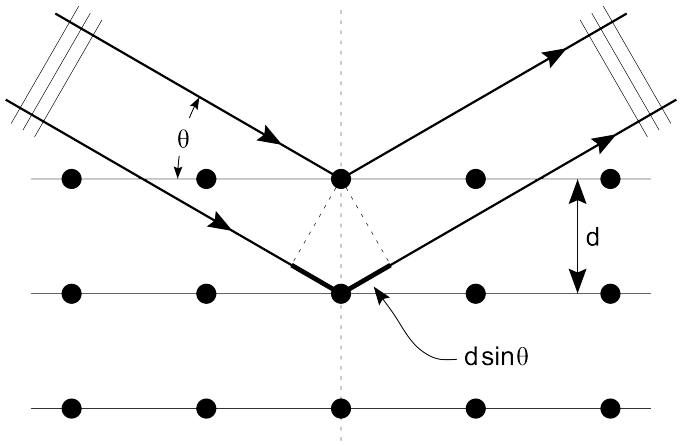

Figure 5.20: Bragg scattering from a crystal lattice.

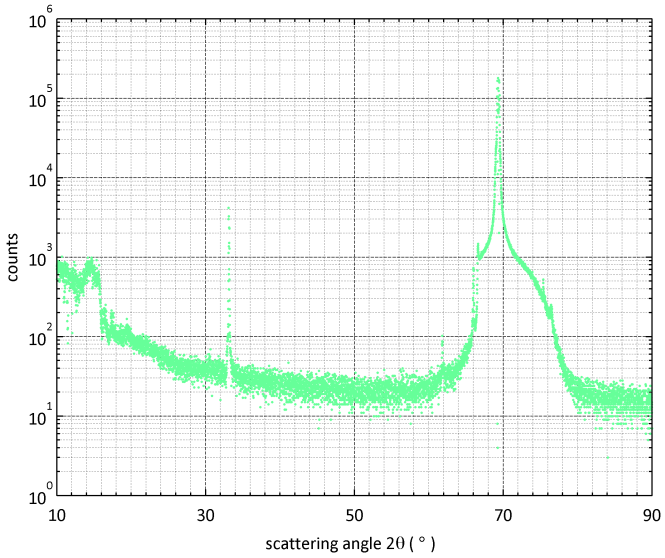

Figure 5.21: X-ray diffraction spectrum from a 600-nm boron film. Prominent Bragg peaks result from x-ray scattering in the silicon substrate.

5.2.5 Scanning electron microscopy

Images of the boron films were taken using a scanning electron microscope (SEM), in the Maryland Nanoscale Imaging Spectroscopy and Properties Laboratory (NISP). These measurements were used to examine the boron film surfaces, and to verify the thicknesses of the films. In an SEM, electrons are thermionically emitted from a cathode filament and focused into a beam by a series of electron lenses. When this beam impinges on a sample, it produces secondary electrons, back-scattered electrons, x-rays, and light. Depending on the tool, one of these signals is collected with a detector. By rastering over the sample surface with the electron beam, a 2D image of the sample is obtained. A diagram of an SEM appears in Figure 5.22.

The tool used to measure the boron films (Hitachi SU-70) utilizes a ZrO/W Schottky emission electron source, and a silicon drift detector. Images from measurements of a 600 and 900 nm sample appear in Figures 5.23 and 5.24, respectively. The images include surface scans at magnifications between 1 mm and 1 μm (50x - 10,000x), and profile scans at a magnification of 5 μm. To obtain clean profile scans, small samples (25 mm^2) were cut from the larger films with a diamond scribe. The cross-sectional images of the films show a narrow layer of boron between adhesive tape and the silicon substrate. The thicknesses derived from these profile images were 594 nm and 892 nm, a 1% difference from the nominal thicknesses of the films (600 nm and 900 nm, respectively).

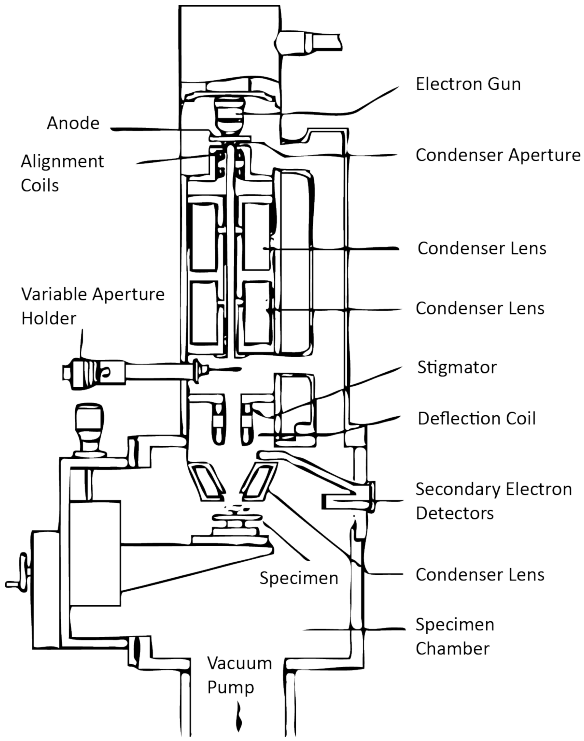

Figure 5.22: Diagram of a scanning electron microscope [127].

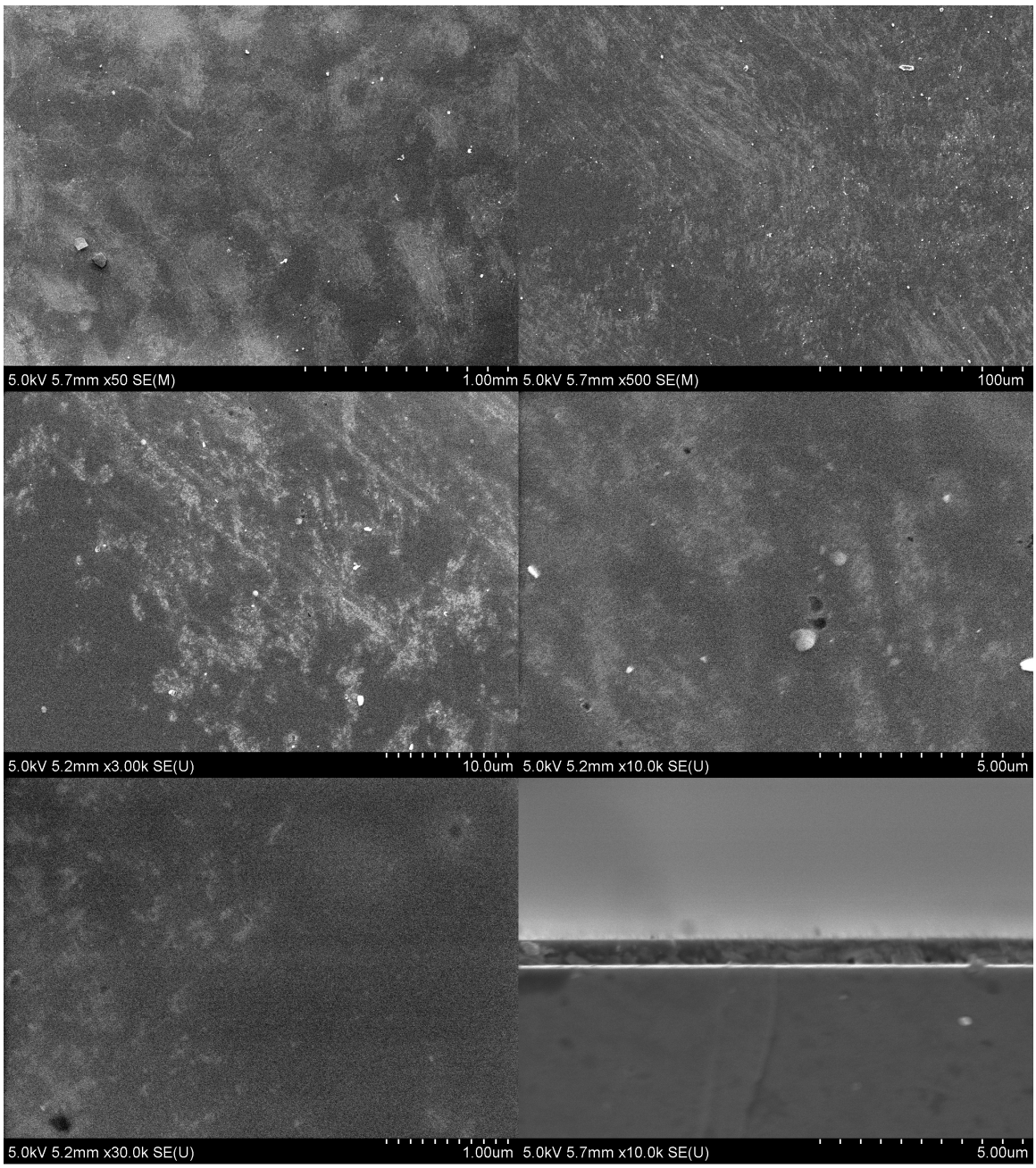

Figure 5.23: SEM images of a 600-nm boron film. Profile images appear on the bottom right.

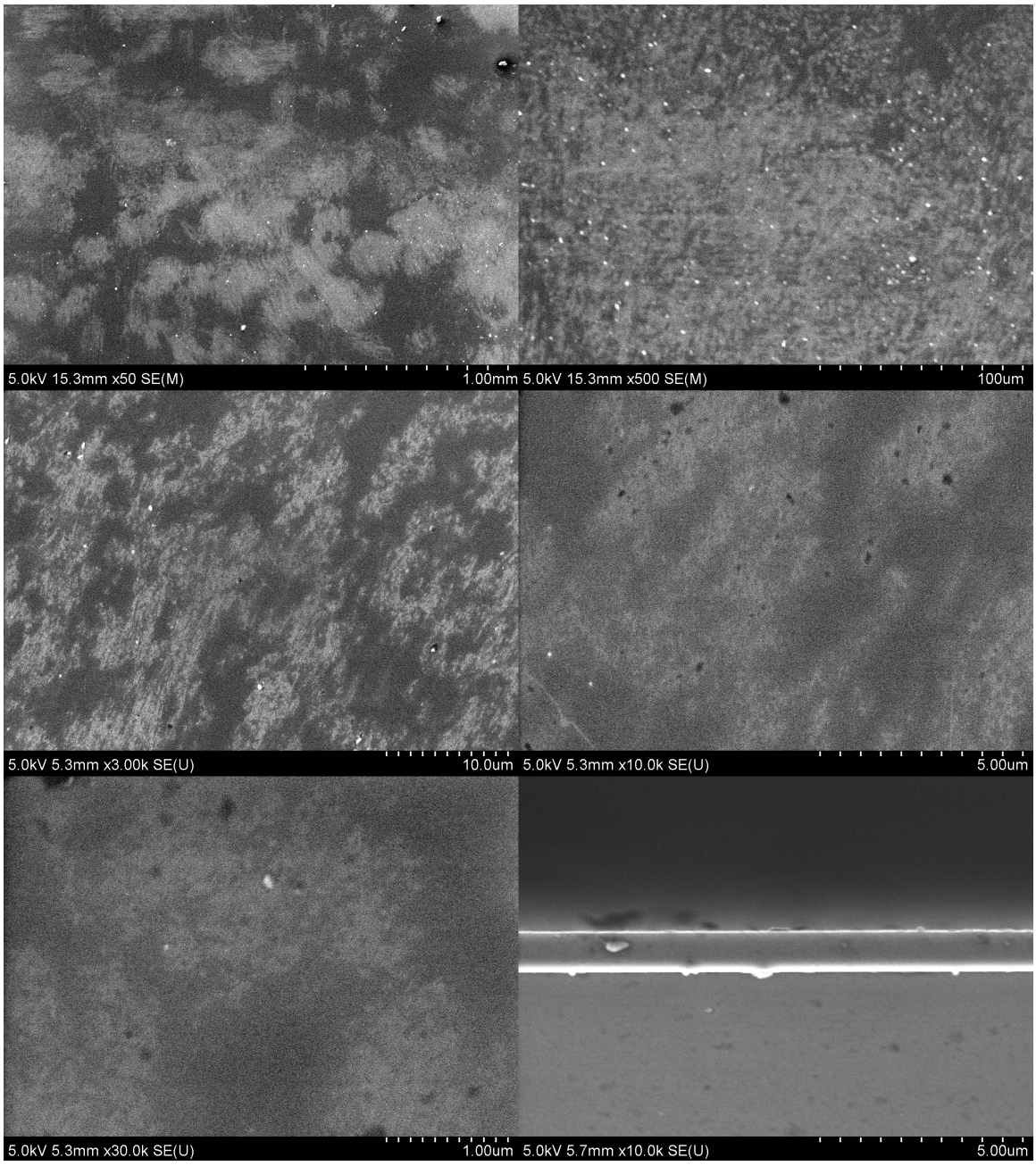

Figure 5.24: SEM images of a 900-nm boron film. Profile images appear on the bottom right.

After a series of characterizations, the boron film targets were determined to be amorphous, stable to oxidation, and representative of the thicknesses programmed into the deposition tool. While surface contaminants (oxygen and nitrogen containing compounds) were found on both the films and the source materials, these contaminants were demonstrated to be predominantly absent from the bulk of the deposits. The areal densities derived from the neutron imaging data will be used in Chapters 7 and 9 to determine the rate of neutron capture during the excimer scintillation measurements.

Chapter 6

Photomultiplier Tube Calibration

The intrinsic efficiency of the photon detector package, used in the excimer scintillation experiment, was measured at the Synchrotron Ultraviolet Radiation Facility (SURF) at NIST. This package consisted of the solar-blind PMT, the PMT housing, the differential volume, and the discrete MgF_2 window. The calibration focused specifically on the FUV region (130 - 210 nm) common to the excimer continua of the heavy noble gases. The intrinsic efficiency of the detector was required to derive absolute yield values from the scintillation measurements in Chapter 9.

6.1 The Synchrotron Ultraviolet Radiation Facility

The Synchrotron Ultraviolet Radiation Facility (SURF III) is a compact electron storage ring located on the NIST campus in Gaithersburg, MD. SURF is a stable source of synchrotron light (see Fig. 6.1), ranging from the infrared to the soft x-ray regions, with a peak output in the extreme ultraviolet [128, 129]. Whereas conventional light sources (gas discharge, arc lamp, plasma) have limited spectral ranges plagued by line structure, synchrotron radiation is continuous, providing an excellent source for photodetector calibrations [130, 131]. Furthermore, the characteristics of

synchrotron light are easily controlled. Variation of synchrotron electron-beam energy changes the resulting photon spectrum. Variation of synchrotron electron-beam current changes the photon-beam intensity. SURF electron energies range between 100 and 400 MeV, and electron beam currents range from 10 pA (1 electron/s) to 1000 A (10^{11} electrons/s). The wavelength-dependent radiant power of SURF at various operating energies appears in Figure 6.2.

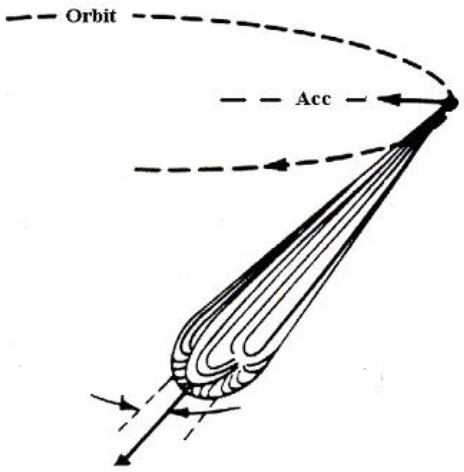

Figure 6.1: As ultrarelativistic electrons accelerate radially in a magnetic field, they emit a collimated beam of photons, known as synchrotron radiation, perpendicular to the direction of acceleration [132].

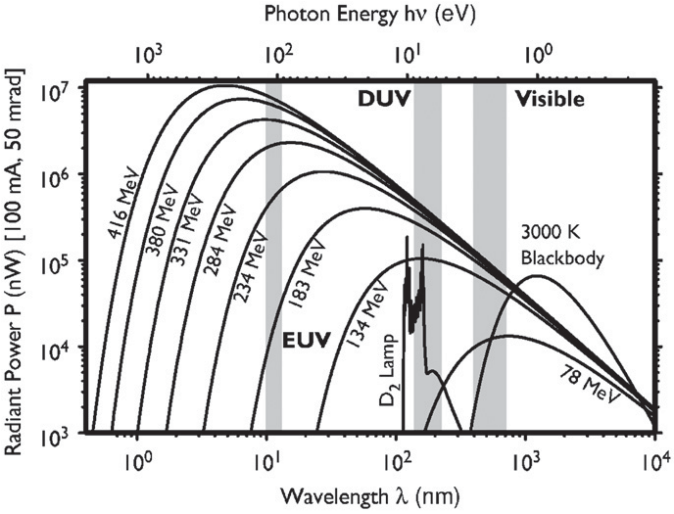

Figure 6.2: SURF III radiant power at various operating energies [131]. Also shown are the output spectra from a 30 W deuterium lamp and a 3000 K blackbody.

Tangential beamlines built around synchrotrons and storage rings direct photon radiation to experiments. SURF hosts a total of thirteen beamlines. Beamline 4 (BL-4), used to calibrate the PMT, was constructed primarily for UV detector calibrations and UV optical material characterization. A schematic of BL-4 appears in Figure 6.4.

After light leaves the SURF storage ring and enters BL-4, two grazing-incidence, fused-silica mirrors image the beam onto the entrance slit of a two-meter, normal-incidence monochromator. This monochromator consists of a normal-incidence mirror and a curved grating with 600 lines/mm. It eliminates all but a small passband of the incident radiation (0.7 nm, at a wavelength of 200 nm), enabling precision wavelength-dependent measurements. Spectral scans are performed by rotating and translating the monochromator along the bisector of the angle between the entrance and exit slits [133]. Beyond the exit slit, monochromatic light is reimaged in the mirror box by two Al-MgF_2 mirrors, before propagating into the detector box containing an x-y linear motion stage and the detector under test. The PMT detector package was mounted to this detector box for calibration against an absolutely-calibrated photodiode.

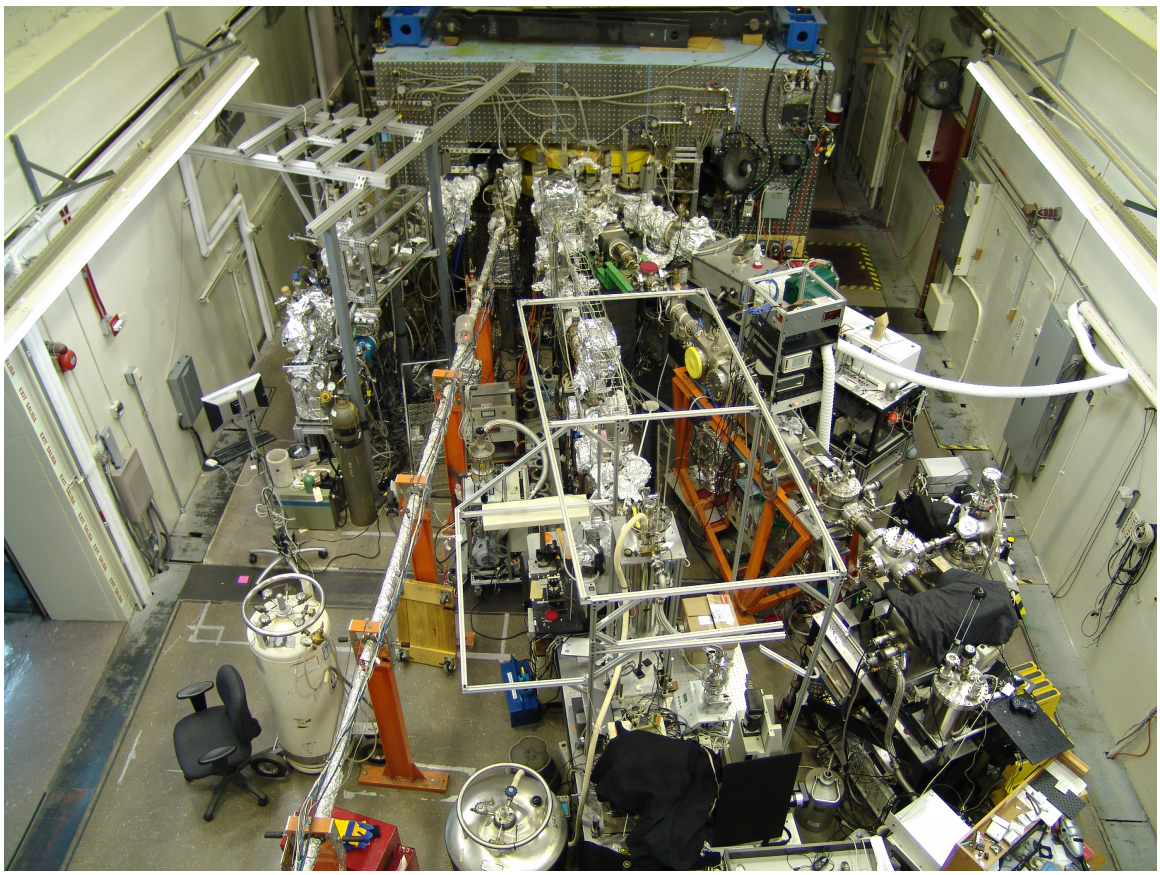

Figure 6.3: The Synchrotron Ultraviolet Radiation Facility at NIST. BL-4 appears second from the right [134].

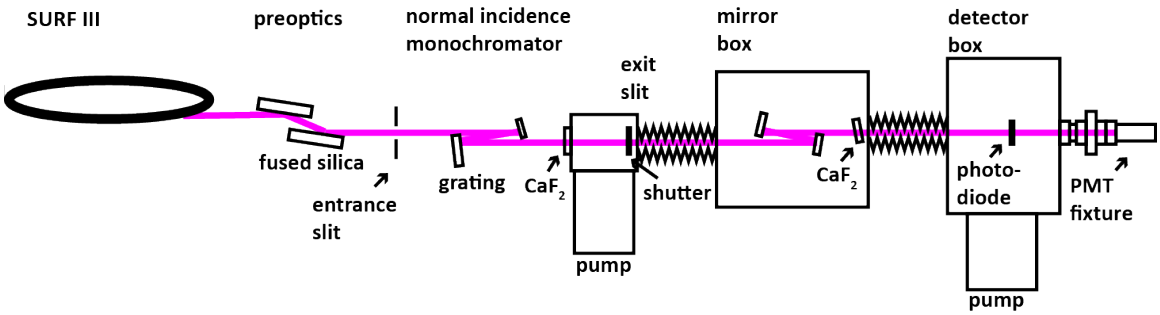

Figure 6.4: Diagram of BL-4 at SURF. The photon beam path is highlighted in magenta. Positions of the photodiode and the photomultiplier tube during the calibration are labeled. Redrawn from [130]. Not to scale.

6.2 Calibration Apparatus

In addition to the beamline components discussed in Section 6.1 and the associated beamline electronics, the calibration setup included the solar-blind PMT (Hamamatsu R6835), a discrete MgF_2 window, a diffusion-type np-junction photodiode (IRD AXUV-100G), a manual x-y translation feedthrough, a number of vacuum adapters, and the electronics necessary for PMT pulse counting (fast preamplifier, power splitter, multichannel analyzer, microcontroller, counter/timer, and high-voltage power supply). These electronics and their settings were identical to those used in the scintillation yield measurements, described in Chapter 4.2.4. The relevant specifications of the photomultiplier tube appear in Table 6.1.

Parameter	Value
Spectral response	115 - 200 nm
Photocathode material	Cs-I
Photocathode diameter	23 mm
Number of dynodes	11
Anode dark current	0.03 nA
Anode pulse rise time	2.8 ns
Electron transit time	22 ns

Table 6.1: Specifications of the Hamamatsu R6835 photomultiplier tube [103].

During the scintillation experiment at the MUTR, the PMT was attached to the scintillation cell behind an evacuated differential volume and an MgF_2 window. These components were configured identically during the PMT calibration. The resulting intrinsic efficiency measurements account for photoabsorption by the discrete MgF_2 window, photoabsorption by the MgF_2 window coupled to the PMT housing, the quantum efficiency of the PMT, and the thresholds of the counting

electronics. These components were mounted on an x-y translation feedthrough to allow scanning of the photon beam over the surface of the detector. This fixture was then mounted behind the BL-4 detector box. The PMT calibration fixture appears in Figure 6.5.

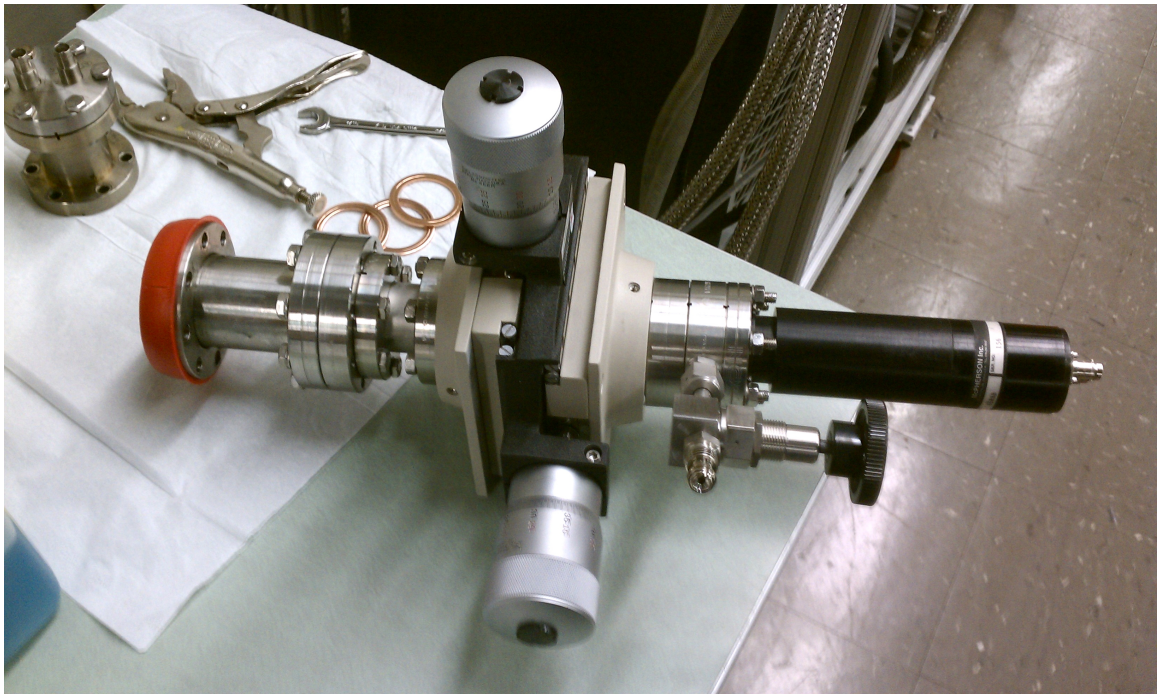

Figure 6.5: The PMT calibration fixture. From right to left: PMT (black housing), differential volume, MgF_2 window, x-y translation stage, vacuum adapters. The photodiode and the BL-4 detector box are not shown.

The photodiode was placed upstream of the PMT within the BL-4 detector box, on a remotely-operated x-y linear-motion stage. This photodiode was previously absolutely calibrated against measurements from a cryogenic radiometer. The active surface of the photodiode (1 cm^2) is composed of n-type silicon. Incident photons with an energy equal to or greater than the silicon bandgap energy (1.1 eV) may excite electrons within this active area into the conduction band. Following excitations near the n-p junction, charge flow is induced by an internal electric field. Photocur-

rent may then be measured with an ammeter in an external circuit to determine the photon flux incident on the detector. A schematic of an np-type photodiode appears in Figure 6.6. With the PMT and the photodiode in place, the detector box, the mirror box, and differential volume were evacuated to high vacuum (10^{-4} mbar) to prevent photoabsorption by O_2.

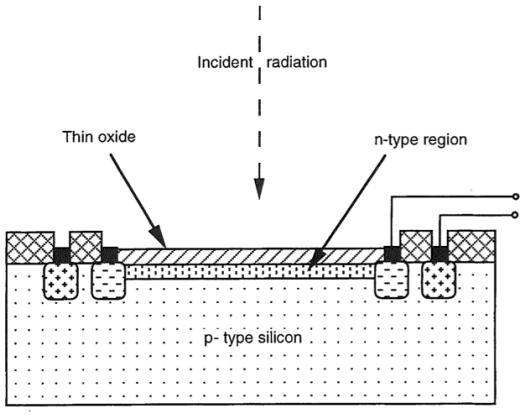

Figure 6.6: Schematic of an np-type VUV photodiode [135].

6.3 Measurements

Due to the steady decay of the SURF electron-beam current after initial beam injection, high beam-current photodiode measurements were made before dumping electrons to collect PMT measurements at lower beam currents. Using the x-y stage within the detector box and one of the BL-4 ammeters, a spatial scan of the photodiode was performed to verify its uniform response, and to center its active area on the photon beam. The incident photon flux was measured over the wavelength range 130 - 210 nm, in 5-nm increments, at electron beam currents of 50, 40, 30, 20, and 10 mA. These measurements were used to determine a linear relationship

between the electron-beam current in the SURF storage ring and the photon flux in the BL-4 detector box at each wavelength. Both the spatial position of the photodiode and the wavelength selection of the monochromator were controlled and automated by LabView.

Following these measurements, the SURF electron-beam current was reduced to 10, 5, and 1 μA, successively. At these lower beam currents, the photon flux in the BL-4 detector box is within the operating range of the PMT. The photodiode was then removed from the photon beam, allowing the beam to strike the PMT detector package. Spectral scans over the same wavelength region were repeated at these reduced currents, and the PMT signal was measured using the associated electronics. During operation at 10 μA, a spatial scan of the detector was performed at a single wavelength (170 nm) using the x-y translation feedthrough. Under the same conditions, counts were recorded at a number of PMT voltages between -1700 and -2500 V. The results of these measurements appear in the following section.

6.4 Results and Analysis

The intrinsic efficiency of the PMT/MgF_2 detector package ($\epsilon_{\rm pmt}(\lambda)$) is defined by the equation,

$$\epsilon_{\rm pmt}(\lambda) = \frac{n_{h\nu}(\lambda)}{N_{h\nu}(\lambda)\, t_{h\nu}} \tag{6.1}$$

where $n_{h\nu}(\lambda)$ is the number of photon pulses observed from the PMT at wavelength λ, $N_{h\nu}$ is the rate at which photons strike the PMT/MgF_2 detector package at wavelength λ, and $t_{h\nu}$ is the time over which PMT pulses were recorded.

The number of photon pulses observed from the PMT is given by the equation,

$$n_{h\nu} = n_{h\nu\,\rm total} - n_{h\nu\,\rm bkgd} \tag{6.2}$$

where $n_{h\nu\,\rm total}$ is the total number of pulses counted over time $t_{h\nu}$, and $n_{h\nu\,\rm bkgd}$ is the number of those pulses which are attributed to backgrounds (dark current). Measurements of $n_{h\nu\,\rm total}$ were recorded by scanning over the FUV wavelength region on SURF BL-4, and counting pulses from the PMT at increments of 5 nm. A single measurement of $n_{h\nu\,\rm bkgd}$ was taken prior to the $n_{h\nu\,\rm total}$ measurements, while the BL-4 shutter was closed. A plot of $n_{h\nu}(\lambda)$ at a SURF electron beam current of 10 μA appears in Figure 6.7.

The uncertainty in $n_{h\nu}$ arises strictly from counting statistics, and may be determined with the equation,

$$\sigma_{n_{h\nu}} = \sqrt{\sigma^2_{n_{h\nu\,\mathrm{total}}} + \sigma^2_{n_{h\nu\,\mathrm{bkgd}}}} \tag{6.3}$$

The standard deviation (σ) of a counting measurement with a value n and a Gaussian parent distribution is given by,

$$\sigma = \sqrt{n} \tag{6.4}$$

Therefore,

$$\sigma_{n_{h\nu}} = \sqrt{n_{h\nu\,\mathrm{total}} + n_{h\nu\,\mathrm{bkgd}}} \tag{6.5}$$

Accordingly, the relative uncertainty in $n_{h\nu}$ is given by,

$$\delta_{n_{h\nu}} = \frac{\sqrt{n_{h\nu\,\mathrm{total}} + n_{h\nu\,\mathrm{bkgd}}}}{(n_{h\nu\,\mathrm{total}} - n_{h\nu\,\mathrm{bkgd}})} \tag{6.6}$$

A plot of the relative statistical uncertainties in $n_{h\nu}(\lambda)$ appears in Figure 6.8.

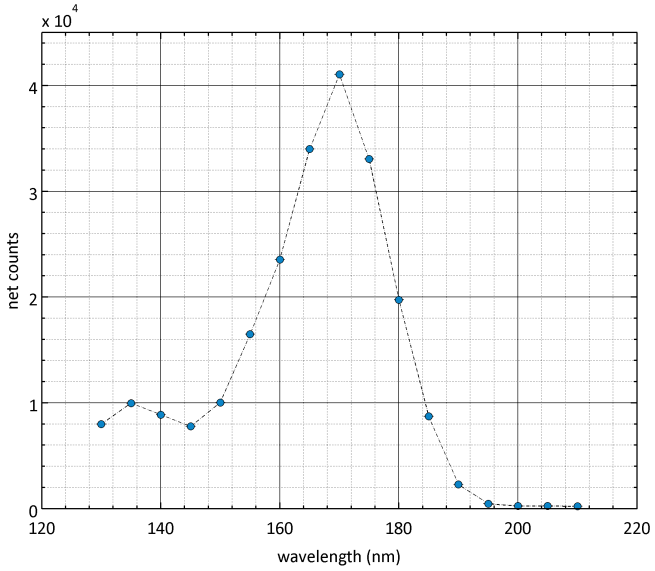

Figure 6.7: Net counts from the PMT during an FUV spectral scan at SURF. Electron beam current $I_{bc} = 10$ μA. Count time $t = 10$ s.

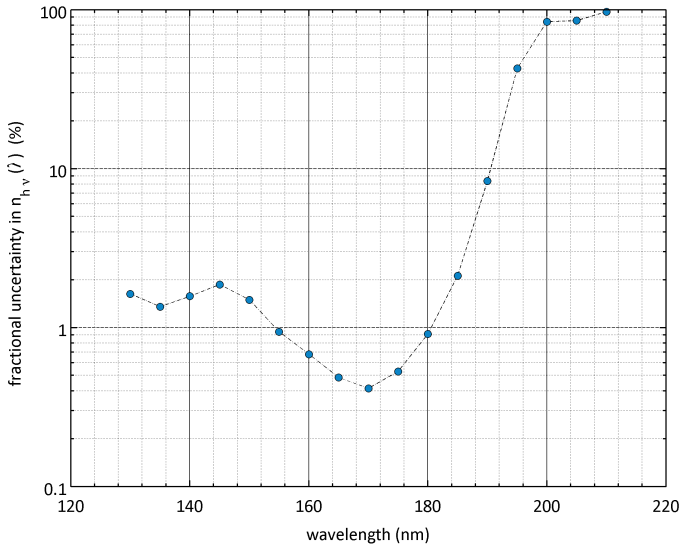

Figure 6.8: Relative statistical uncertainties in $n_{h\nu}(\lambda)$ from a spectral scan of the PMT at SURF. Electron beam current $I_{bc} = 10$ μA. Count time $t = 10$ s.

Values of $N_{h\nu}(\lambda)$ were extrapolated from photodiode measurements of the photon flux in the SURF BL-4 detector box. The photon flux at each wavelength (λ) in the region of interest, was determined at several SURF electron-beam currents (10-50 mA) within the operating range of the photodiode. These values were calculated with the equation,

$$N_{h\nu}(\lambda) = \frac{I_{pd}(\lambda)}{\epsilon_{pd}(\lambda)\, h\nu\, e} \tag{6.7}$$

where $N_{h\nu}$ is given in units of s^{-1}, $I_{pd}(\lambda)$ is the average current from the photodiode at wavelength λ, $\epsilon_{pd}(\lambda)$ is the responsivity of the photodiode at wavelength λ, $h\nu$ is the energy of a photon of wavelength λ (and frequency ν), and e is the electron charge (1.60218×10^{-19} C or J/eV). The BL-4 software automatically records photodiode dark current at the beginning of each data run, and subtracts this value from all measurements of I_{pd}. The responsivity of the photodiode over the FUV region, appears in Figure 6.9.

After calculating values of $N_{h\nu}$ at each wavelength and several SURF electron-beam currents, the values were fit by linear regression to determine the relationship between the SURF electron-beam current and the BL-4 photon flux at each wavelength. This relationship takes the form,

$$N_{h\nu}(\lambda, I_{bc}) = k(\lambda)\, I_{bc} \tag{6.8}$$

where $k(\lambda)$ is the flux coefficient (slope of the fit) at each wavelength λ, and I_{bc} is the SURF electron beam current. Values of $k(\lambda)$, calculated from the photodiode measurements, are plotted in Figure 6.10.

The uncertainties in the flux coefficients were derived from the mean square error of each regression. A linear fit (when forced through zero) is given by,

$$\hat{y}_i = kx_i \tag{6.9}$$

where $\hat{y}_i$ are the fitted values of the dependent variable, x_i are the explanatory values of each measurement, and k is the fit coefficient (slope). The residuals of the fit are given by,

$$y_i - \hat{y}_i \tag{6.10}$$

where y_i is the measured value at x_i. The sum of the squared residuals is then,

$$\mathrm{SSR} = \sum_{i=1}^{N} (y_i - \hat{y}_i)^2 \tag{6.11}$$

Accordingly, the mean square error of the regression is given by,

$$\hat{\sigma}^2 = \frac{\mathrm{SSR}}{N-2} \tag{6.12}$$

where N is the number of measurements. Finally, the standard deviation in the slope parameter of the fit is given by,

$$\sigma_k = \hat{\sigma}^2 \sqrt{\frac{1}{\sum (x_i - \overline{x})^2}} \tag{6.13}$$

where $\overline{x}$ is the mean of the explanatory values. The relative uncertainties in $k(\lambda)$ are plotted in Figure 6.11. The uncertainties are greater at shorter wavelengths due to the reduced throughput of the monochromator in this region.

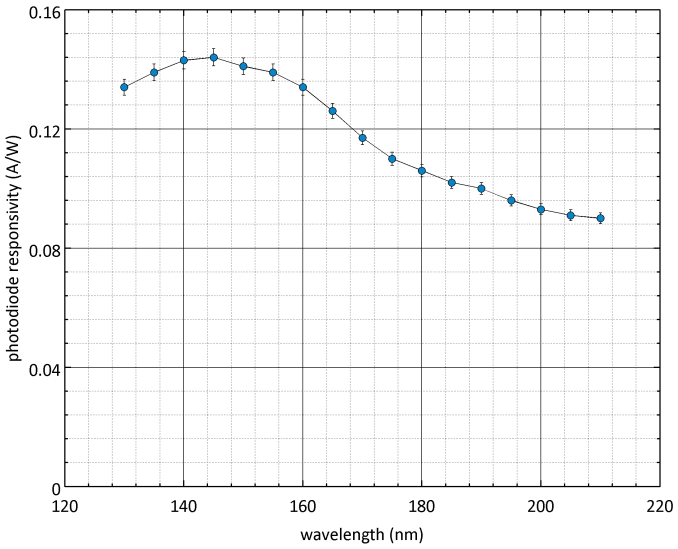

Figure 6.9: Responsivity of an absolutely-calibrated IRD AXUV-100G photodiode ($\epsilon_{pd}(\lambda)$) in the FUV region [136].

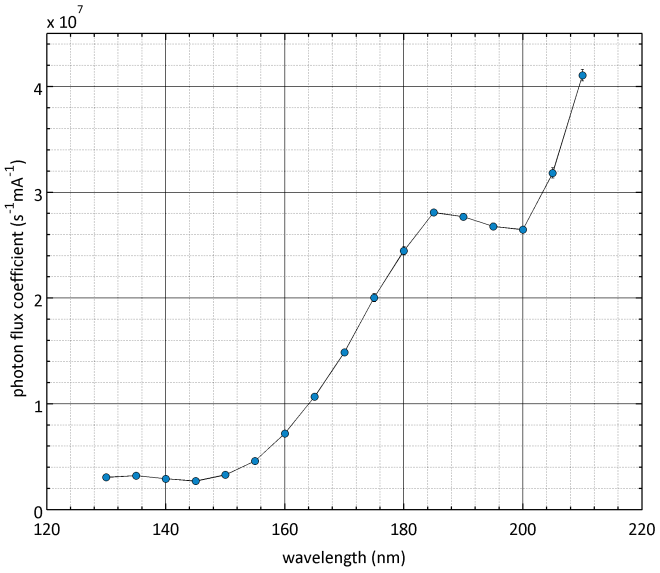

Figure 6.10: Photon flux coefficients ($k(\lambda)$) of SURF BL-4 over the FUV region.

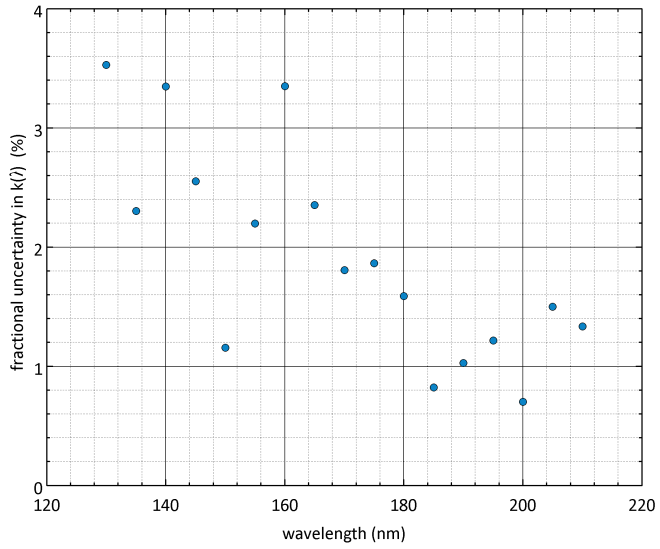

Figure 6.11: Relative uncertainties in $k(\lambda)$.

By extrapolating the regressions from Eq. 6.7 to electron-beam currents in the microampere range, values of $N_{h\nu}(\lambda)$ were determined for each PMT measurement. The intrinsic efficiency of the PMT package was then obtained by substituting $n_{h\nu}(\lambda)$ and $N_{h\nu}(\lambda)$ into Eq. 6.1. A plot of $\epsilon_{\text{pmt}}(\lambda)$ appears in Figure 6.12, at three electron-beam currents. For comparison, the spectral response curve supplied by the manufacturer appears in Figure 6.13. The relative uncertainty in $\epsilon_{\text{pmt}}(\lambda)$ was calculated by propagating the uncertainties in $n_{h\nu}$ and $k(\lambda)$, in the form,

$$\delta_{\epsilon_{\text{pmt}}} = \sqrt{\left(\frac{\sigma_{n_{h\nu}}}{n_{h\nu}}\right)^2 + \left(\frac{\sigma_k}{k}\right)^2} \tag{6.14}$$

The relative uncertainties in $\epsilon_{\text{pmt}}(\lambda)$ are plotted in Figure 6.14.

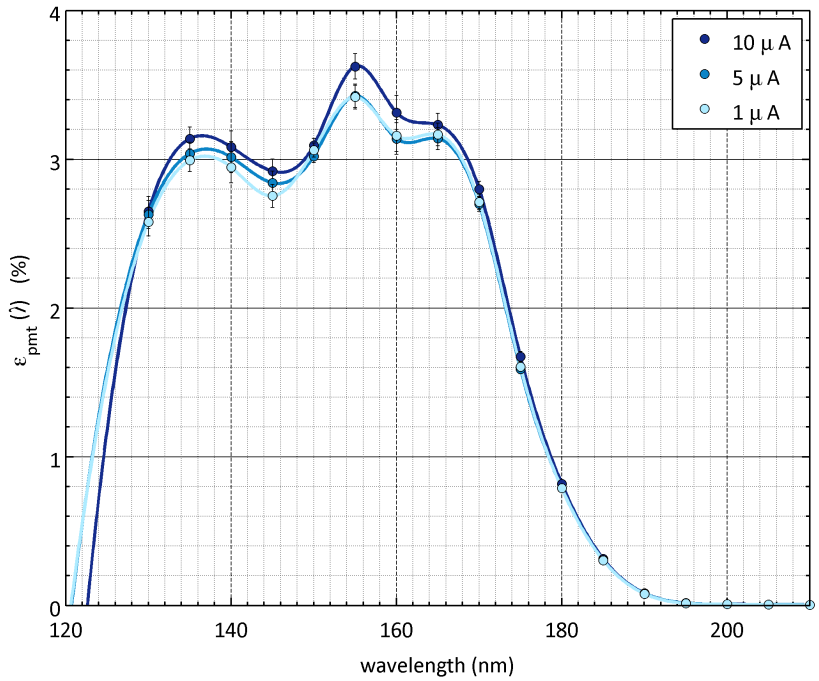

Figure 6.12: Intrinsic efficiency of the PMT/MgF_2 detector package in the FUV region. Fits used in Eq. 6.15 are also shown.

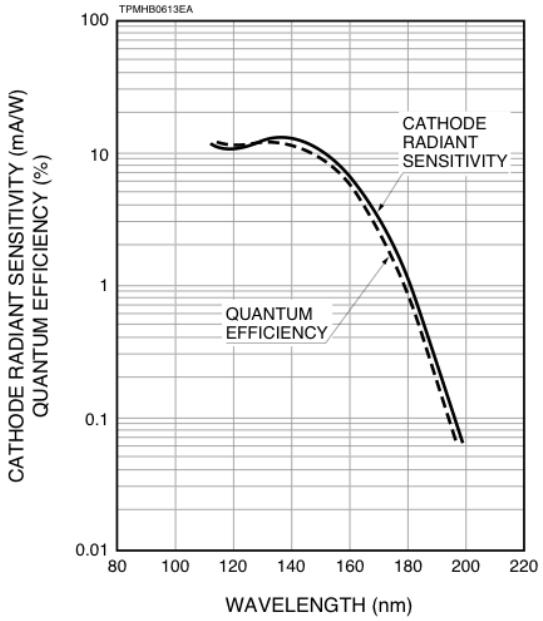

Figure 6.13: Spectral response of the PMT supplied by the manufacturer.

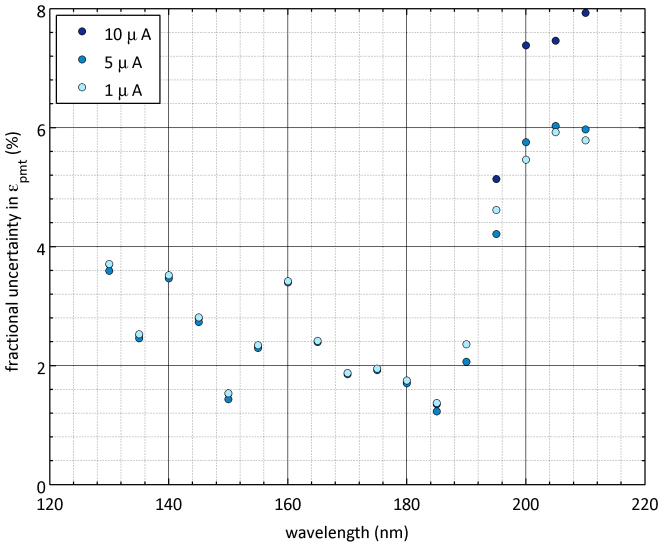

Figure 6.14: Relative uncertainties in $\epsilon_{\mathrm{pmt}}(\lambda)$.

Because excimer emissions occur over broad continua, an effective PMT efficiency was determined for each noble-gas type used in the scintillation experiments. Each effective efficiency was calculated with a continuous weighted average, in the form,

$$\langle \epsilon_{\mathrm{pmt}} \rangle = \frac{\int \epsilon_{\mathrm{fit}}(\lambda)\, s(\lambda)\, \mathrm{d}\lambda}{\int s(\lambda)\, \mathrm{d}\lambda} \tag{6.15}$$

where $\epsilon_{\mathrm{fit}}(\lambda)$ is a cubic spline fit of the discrete values of $\epsilon_{\mathrm{pmt}}(\lambda)$, and $s(\lambda)$ is the wavelength distribution of the noble-gas excimer. The fits ($\epsilon_{\mathrm{fit}}(\lambda)$) appear in Figure 6.12. Values of $s(\lambda)$ were obtained by digitizing excimer emission spectra from [36]. These digitized spectra appear in Figure 1.2. Values of $\langle \epsilon_{\mathrm{pmt}} \rangle$ for Ar, Kr, and Xe appear in Table 6.2. For comparison, values of the 10 μA spline fit ($\epsilon_{\mathrm{fit}}(\lambda)$) at the discrete peak excimer emission wavelengths of each noble gas, also appear in Table 6.2. The uncertainties in $\langle \epsilon_{\mathrm{pmt}} \rangle$ were derived from the average value of the relative uncertainties in $\epsilon_{\mathrm{pmt}}(\lambda)$,

$$\delta_{\langle \epsilon_{\mathrm{pmt}} \rangle} = \overline{\delta}_{\epsilon_{\mathrm{pmt}}(\lambda)} = 3.49\% \tag{6.16}$$

Gas	λ_{peak}	$\epsilon_{\mathrm{pmt}}(\lambda_{\mathrm{peak}})$ (%)	$\langle \epsilon_{\mathrm{pmt}} \rangle$ (%)
Ar	128	2.204 ± 0.108	1.648 ± 0.058
Kr	150	3.094 ± 0.047	3.144 ± 0.110
Xe	175	1.674 ± 0.033	2.607 ± 0.091

Table 6.2: List of (1) intrinsic efficiencies of the PMT/MgF_2 package at peak excimer wavelengths, and (2) effective intrinsic efficiencies as determined by Eq. 6.15.

The results from the spatial scan of the PMT detector package appear in Figures 6.15 and 6.16. These measurements were performed at an electron-beam current of 10 μA. The SURF electron-beam current-lifetime product is nominally 1.5 A

hr. Therefore, in the microampere range SURF provides an incredibly stable light source, with a lifetime of 17.7 years at 10 μA. The calibration fixture and the port it was mounted to were not directly centered on the photon beam. Therefore, only half of the active detector area was measured due to the limits of travel of the x-y translation stage (2.5 × 2.5 cm). The detector response is shown to be relatively uniform over an 18-mm diameter, with a tailing response out to the manufacturer-specified 23-mm diameter. This reduced response towards the edges of the detector package could be the result of irregularities in either MgF_2 window at their periphery, or an indication of a reduced PMT detection efficiency for photons that strike the edges of the photocathode. The spatial response of the detector package will be addressed by the collection efficiency modeling in Chapter 8.

The results from the voltage scan appear in Figure 6.17. This scan was also performed at an electron-beam current of 10 μA. Ideally, the PMT should be operated in a flat region of the voltage curve. Small changes in detector voltage in this plateau region, result in only small changes in the detector response. During both the spectral calibration of the PMT and the excimer scintillation experiment, the PMT was operated at -2300 V, just below the maximum rating of -2500 V.

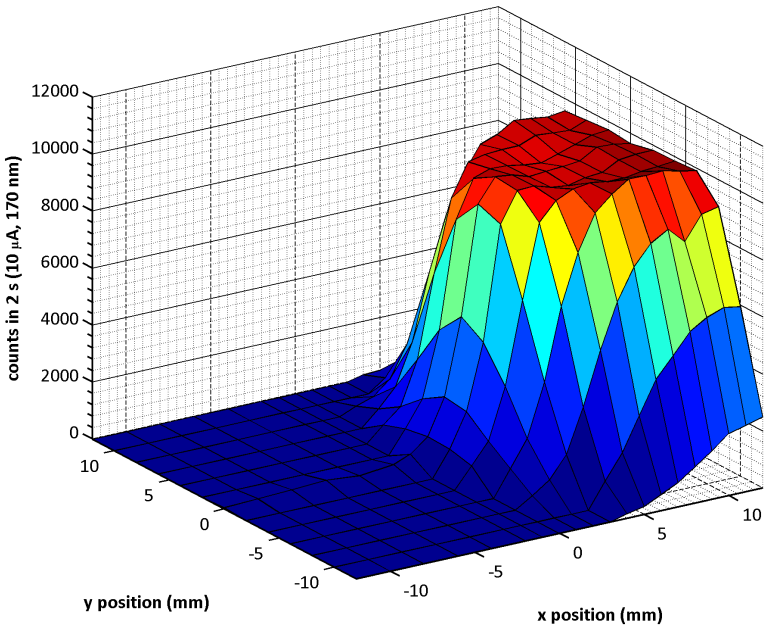

Figure 6.15: Spatial response of PMT/MgF_2 detector package. Beam current $I_{bc} = 10$ μA. $\lambda = 170$ nm. Count time $t = 2$ s.

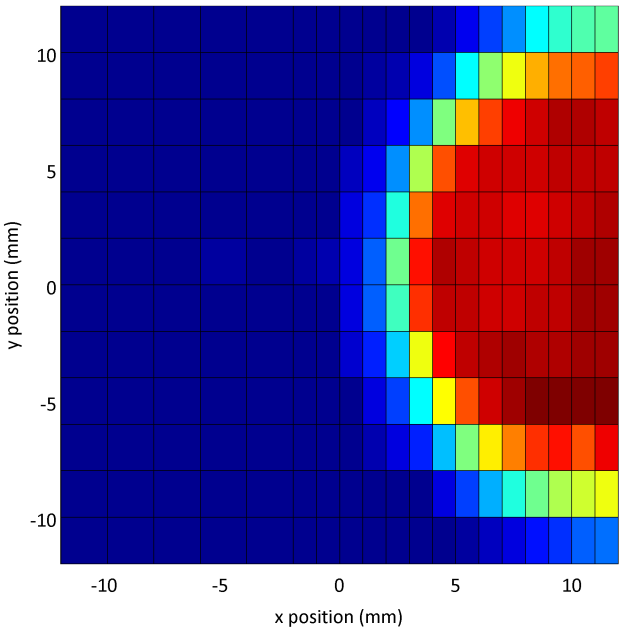

Figure 6.16: Spatial response of PMT/MgF_2 detector package. $I_{bc} = 10$ μA. $\lambda = 170$ nm. Count time $t = 2$ s.

Using SURF as a stable source of FUV synchrotron light, the efficiency of the PMT/MgF_2 detector package was determined for the continua of heavy noble-gas excimer emissions (1.6 - 3.1%). Additionally, a suitable detector voltage was identified (-2300 V) for scintillation photon counting. Lastly, the spatial uniformity of the detector was characterized for interpretation in the collection efficiency modeling of the scintillation cell.

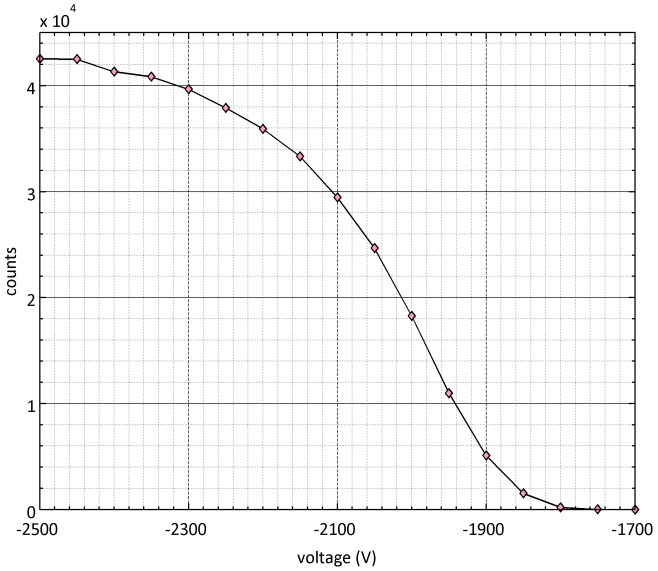

Figure 6.17: PMT response as a function of operating voltage. $I_{bc} = 10$ μA. $\lambda = 170$ nm. Count time $t = 10$ s.

Chapter 7

Neutron Beam Characterization

A thermal-neutron beamline did not exist at the MUTR prior to the excimer scintillation experiment. To obtain a thermal-neutron beam, it was necessary to construct and install a collimator insert in the MUTR thermal column. Subsequently, this beam was characterized in several ways to determine the neutron interaction rate in the excimer scintillation cell.

7.1 Neutron Beam Collimator

The MUTR core hosts five experimental facilities, shown in Figure 4.1. Of these facilities, the thermal column is the best suited for thermal-neutron experiments due to the large volume of graphite (1.50 m) that separates its access cavity from the core. Neutrons diffusing through this graphite are efficiently thermalized by scattering interactions with carbon nuclei. The cavity beyond the graphite volume allows access to these thermal-neutrons for experimental irradiations.

Before the scintillation experiment, a collimator insert was fabricated for the thermal-column access cavity. This insert allows only a narrow beam of neutrons (5.08 cm diameter) to stream past the reactor containment. The use of a collimated beam

during the excimer scintillation measurements enabled operation of the experiment at close proximity, and precise control over the number of neutrons interacting within the apparatus.

The collimator insert was designed using the original MUTR blueprints, and measurements from an existing insert, constructed by Ian Gifford. A carbon-steel frame for the insert was fabricated at the UMD Aerospace Machine Shop. The frame consists of 1/2" steel plate, joined with nickel-free welding rods. A beam tube at the center of the frame provides a void through which neutrons pass. The outer face of the frame was tapped with a matrix of threaded holes for affixing a beam-shutter assembly. The top plates on both sections of the frame were attached with hex bolts so that the frame could be filled with shielding material. The design and dimensions of this frame appear in Figure 7.1. Photographs of the frame appear in Figures 7.2 and 7.3.

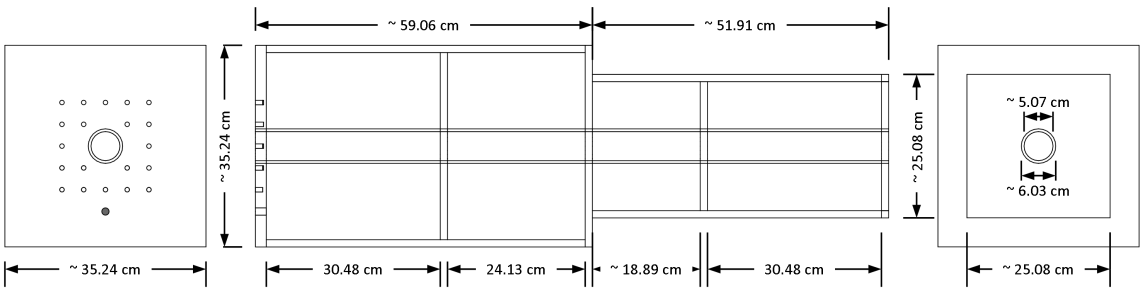

Figure 7.1: Collimator insert design and dimensions. Left: Outer face. Center: Side view. Right: Inner face.

The innermost and outermost sections of the collimator frame were filled with a mixture of paraffin wax, steel shot, and boron carbide (B_4C) powder. This fill mixture attenuates gamma-ray and neutron radiation outside of the beam tube. Prior

to filling, the seams of the frame were sealed with room-temperature vulcanizing (RTV) silicone to prevent leakage of the molten wax. The frame was then wrapped with heating tape and fiberglass insulation. During the filling, a heat gun was used to constantly heat the mixture, allowing the slurry of wax and B_4C to fill the spaces in the steel shot. Approximately 140 kg of steel shot was used to fill the outer segment, and 70 kg was used to fill the inner segment. The volume fraction of the fill material is estimated to be 50% shot, 15% B_4C, and 35% wax. A sample of the fill mixture appears in Figure 7.4. The filled collimator frame appears in Figure 7.5.

A beam shutter, composed of Boral and lead, was affixed to the outer face of the collimator with the matrix of tapped holes. This shutter was used to block radiation leaving the beam tube. The shutter was held in place by an aluminum cradle, mounted on extruded aluminum tracks. The cradle was connected to a toggle lever by pulleys and wire rope, allowing manipulation of the shutter position from the experimental floor. Additionally, a microswitch was installed beneath the shutter seat to illuminate a safety light during beam operation. Photographs of the shutter assembly appear in Figure 7.6.

Following the construction and installation of this collimator, the radiation dose rates in the vicinity of the thermal column were measured to verify the safety of nearby experimenters. The neutron beam was then characterized for use in the scintillation experiments.

Figure 7.2: Thermal-column collimator insert.

Figure 7.3: Collimator insert frame, showing the section partitions and the beam tube.

Figure 7.4: Sample of the collimator fill mixture, composed of wax, steel shot, and boron carbide powder.

Figure 7.5: Collimator insert filled with shielding mixture.

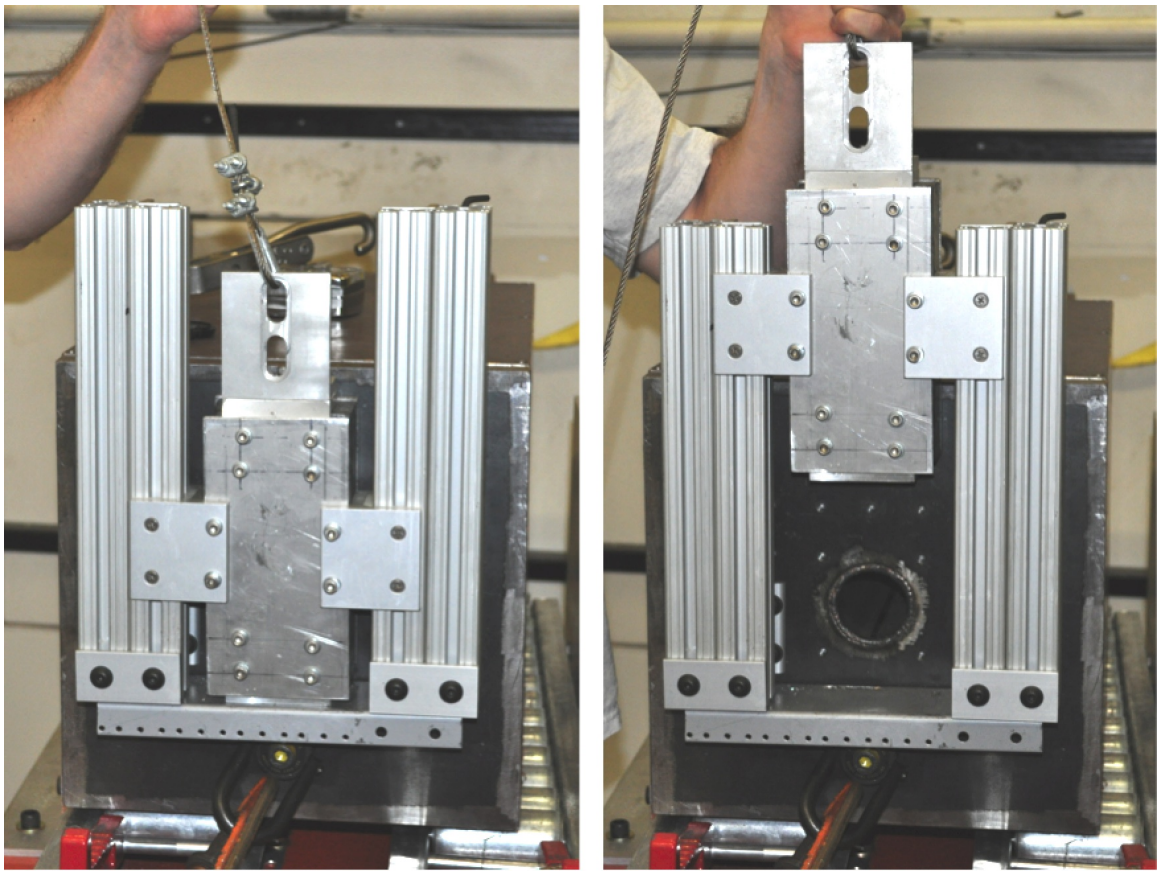

Figure 7.6: Collimator shutter assembly in the closed (left) and open (right) positions.

7.2 Fluence Measurements

During the excimer scintillation experiment, a NIST-calibrated fission chamber was used to continuously monitor the fluence of the thermal-column neutron beam. For all scintillation measurements, the MUTR was operated in automatic mode, at a power level of 250 kW. The fission chamber was placed in front of the scintillation cell and behind a beam aperture (see Fig. 4.9). The aperture was used to reduce the profile of the neutron beam to a size (12.6 mm^2) significantly smaller than both the fission chamber deposit (127 mm^2) and the boron targets (625 mm^2). Pulses from the fission chamber were collected with an MCA, as described in Chapter 4.2.4. A photograph of the detector appears in Figure 7.7.

Figure 7.7: The fission-chamber beam monitor.

The rate at which a thin target absorbs a beam of neutrons may be derived from Beer-Lambert's Law of neutron absorption,

$$F = I_0(1 - e^{-\Sigma_a x}) \tag{7.1}$$

where I_0 is the intensity of the incident neutron beam, Σ_a is the macroscopic cross section of the sample, and x is the thickness of the sample. For $\Sigma_a x \ll 1$, Eq. 7.1 may be approximated by,

$$F = I_0 \left(1 - (1 - \Sigma_a x)\right) = I_0 \, \Sigma_a \, x \tag{7.2}$$

Futhermore,

$$\Sigma_a \, x = N \, \sigma_a \, x = \rho_A \, \frac{N_A}{M} \, \sigma_a \tag{7.3}$$

where N is the atom density of the target, σ_a is the microscopic absorption cross section of the target, ρ_A is the areal mass density of the target, N_A is Avogadro's number (6.0221×10^{23} mol^{-1}), and M is the molar mass of the target material. Thus, Eq. 7.2 becomes,

$$F = \rho_A \, \frac{N_A}{M} \, \sigma_a \, I_0 \tag{7.4}$$

By rearranging Eq. 7.4, the rate at which neutrons propagate through the scintillation cell (N_{beam}) may be determined based on the fission chamber measurements (n_n), with the equation,

$$N_{\text{beam}} = \frac{n_n}{t_n} \, \frac{M_{235}}{\langle \sigma_{235} \rangle \, (\rho_A)_{235} \, N_A} \, \zeta \tag{7.5}$$

where N_{beam} is the beam fluence in units of Hz, t_n is the length of each neutron count period, M_{235} is the molar mass of ^{235}U (235.0439 g/mol), $\langle \sigma_{235} \rangle$ is the effective microscopic absorption cross section of ^{235}U in the MUTR thermal-column beam,

$(\rho_A)_{235}$ is the areal density of the fission chamber deposit (458.073 μg/cm^2), and ζ is a self-absorption correction factor for the fission chamber deposit (1.03756). The factor ζ accounts for fissions in the ^{235}U deposit in which the fission fragments are absorbed before ionizing the P-10 gas. The value of this factor was provided by Dr. Jeffrey Nico. The mass of the fission chamber deposit and its uncertainty were provided by Dr. David Gilliam.

Likewise, Eq. 7.4 may be used to determine the rate at which neutrons in the MUTR thermal column beam are absorbed by a boron thin-film target,

$$N_n = N_{\text{beam}} \frac{\langle \sigma_{10} \rangle \, (\rho_A)_{10} \, N_A}{M_{10}} \, \mu \, \sqrt{2} \tag{7.6}$$

where $\langle \sigma_{10} \rangle$ is the effective microscopic absorption cross section of ^{10}B in the MUTR thermal-column beam, $(\rho_A)_{10}$ is the areal density of the boron thin-film targets, M_{10} is the molar mass of ^{10}B (10.0129 g/mol), and μ is the fraction of the neutrons in the beam which are not absorbed between the fission chamber and the boron target. The areal densities of the boron targets were derived from the neutron imaging data, discussed in Chapter 5.2.1. The path length of the neutron beam through the boron targets was increased by tilting the targets at a 45° angle. The factor $\sqrt{2}$ is included to account for this increased path length.

The absorption rate of the boron targets may be determined directly from the fission chamber measurements, by combining Eq. 7.5 and 7.6,

$$N_n = \frac{n_n}{t_n} \frac{\langle \sigma_{10} \rangle \, (\rho_A)_{10} \, M_{235}}{\langle \sigma_{235} \rangle \, (\rho_A)_{235} \, M_{10}} \, \mu \, \zeta \, \sqrt{2}. \tag{7.7}$$

The net counts from each fission chamber measurement (n_n) is given by the equation,

$$n_n = n_{n\,\mathrm{total}} - n_{n\,\mathrm{bkgd}} \tag{7.8}$$

where $n_{n\,\mathrm{total}}$ is the total number of pulses counted over time t_n, and $n_{n\,\mathrm{bkgd}}$ is the number of those pulses attributed to non-neutron events. Values of n_n were determined by identifying a threshold just above the noise peak in each fission chamber pulse height distribution, and subtracting the counts below that threshold from each measurement of $n_{n\,\mathrm{total}}$. Typical pulse height distributions (PHDs) from the fission chamber appear in Figure 7.8. The noise peaks in these PHDs are highlighted in black. Plots of n_n over each data collection day appear in Figures 7.9 - 7.12.

Due to the need for sufficient counting statistics, the time base of the neutron-count period was set longer than the time base of the photon-count period, $t_n = 1200$ s and $t_{h\nu} = 200$ s. Neutron-count periods often overlapped multiple photon-count periods, and sometimes ended or started in the midst of photon-count periods. Over the course of the reactor day, measurements of n_n typically decreased by 5-10%, as shown in Figures 7.9 - 7.12. This decrease in the count rate (and the neutron beam fluence) was the result of (1) spectrum hardening due to the gradual increase in

the temperature of the pool water and the reactor containment, and (2) flux profile changes in the core due to movements of the reactor control rods. Overcoming fission poisons (negative reactivity insertion) throughout the course of the reactor day requires the addition of positive reactivity, in the form of pool water heating and control rod withdrawal. Because these additions are gradual, the changes in n_n throughout the day were also assumed to be gradual.

To determine a value of n_n corresponding to each photon count, the measurements of n_n were fit by linear regression of the form,

$$\hat{n}_n(t) = k_n t + \hat{n}_0 \tag{7.9}$$

where $\hat{n}_n(t)$ are the fitted values of the neutron count measurements over time t, k_n is the slope of the fit, t is the starting time of of each photon count during the data collection day, and $\hat{n}_0$ is the fitted intercept of the dependent variable, relative to some pivot date-and-time, $t = 0$. The same pivot date was used throughout the analysis of n_n. The linear fits ($\hat{n}_n(t)$) appear in Figures 7.9 - 7.12.

The uncertainties in $\hat{n}_n(t)$ were first determined by propagating the uncertainties in k_n and $\hat{n}_0$. The uncertainties in k_n were determined using the residuals of the fits, as described in Eq. 6.9 - 6.13. The uncertainties in $\hat{n}_0$ were also determined using the residuals of the fits, with the equation:

$$\sigma_{\hat{n}_0} = \hat{\sigma}\sqrt{\frac{1}{N} + \frac{\overline{x}^2}{\sum(x_i - \overline{x})^2}} \tag{7.10}$$

The overall relative uncertainties in the values of $\hat{n}_n(t)$ are given by the equation,

$$\delta_{\hat{n}_n(t)} = \sqrt{\left(\frac{\sigma_{k_n}}{k_n}\right)^2 + \left(\frac{\sigma_{\hat{n}_0}}{\hat{n}_0}\right)^2} \tag{7.11}$$

The uncertainties calculated with Eq. 7.11 are listed in Table 7.1 for each data collection day.

This method of deriving uncertainties in the fits did not produce consistent results. Specifically, the outlying value of $\delta_{\hat{n}_n(t)}$ on March 23 is the product of a very flat linear fit (low absolute values of k_n and $\hat{n}_0$). This flat fit is the result of operating with a cold (low negative reactivity) core, following a period of reactor down time during Spring Recess. With low initial fission poison concentrations, it is possible to continuously run secondary cooling over the course of the reactor day, leading to less heating of the reactor pool and fewer compensating manipulations of the control rods. Under these conditions, the fluence in the thermal-column neutron-beam was observed to be nearly constant in comparison to other data collection days. A simpler method for determining the uncertainties in $\hat{n}_n(t)$ was chosen to avoid this biasing against flat-flux days. The standard deviation in each set of counts was used to determine $\sigma_{\hat{n}_n(t)}$, with the equation,

$$\sigma_{\hat{n}_n(t)} = \sqrt{\frac{1}{N-1}\sum_{i=1}^{N}((n_n)_i - \overline{n}_n)^2} \tag{7.12}$$

where $\overline{n}_n$ is the mean value of the counts from that day, and N is the number of measurements of n_n. Relative uncertainties in $\hat{n}_n(t)$ determined by this method also appear in Table 7.1. These values were used for the final analysis.

Date	k_n	$\hat{n}_0$	$\frac{\sigma_{k_n}}{k_n}$	$\frac{\sigma_{\hat{n}_0}}{\hat{n}_0}$	$\left(\delta_{\hat{n}_n(t)}\right)_1$	$\left(\delta_{\hat{n}_n(t)}\right)_2$	ΔT (°C/hr)
3.09.12	-1739	17787	8.36×10^{-5}	0.0239	0.0239	0.0438	5.53
3.14.12	-1228	19568	1.36×10^{-4}	0.0258	0.0258	0.0317	2.96
3.16.12	-950.1	17774	2.37×10^{-4}	0.0391	0.0391	0.0223	6.51
3.23.12	-11.95	3396.6	0.0279	0.3069	0.3082	0.0161	0.51

Table 7.1: Values and uncertainties from fits of the fission chamber counts. The uncertainty values were determined by (1) linear regression analysis techniques described in Eq. 6.9 - 6.13 and 7.10, and (2) standard deviations of each set of counts. The rate of increase of the reactor pool temperature (ΔT) is also shown for each reactor day.

Following the fitting of the measured values n_n, Eq. 7.7 is reduced to,

$$N_n = \frac{\hat{n}_n(t)}{t_n} \frac{\langle \sigma_{10} \rangle \, (\rho_A)_{10} \, M_{235}}{\langle \sigma_{235} \rangle \, (\rho_A)_{235} \, M_{10}} \, \mu \, \zeta \, \sqrt{2}. \tag{7.13}$$

The remaining unknowns in this equation are the factors $\langle \sigma_{10} \rangle$, $\langle \sigma_{235} \rangle$, and μ. Effective microscopic cross sections ($\langle \sigma \rangle$)must be used in Eq. 7.13, because the MUTR neutron beam is not monoenergetic. An effective cross section may be calculated with a continuous weighted average of the form,

$$\langle \sigma \rangle = \frac{\int \sigma(E) \phi(E) \, \mathrm{d}E}{\int \phi(E) \, \mathrm{d}E} \tag{7.14}$$

where $\sigma(E)$ is the energy-dependent microscopic cross section of the material, and $\phi(E)$ is the energy-dependent flux of the neutron beam. Unfortunately, the energy distribution of the thermal-column neutron beam has not been directly measured (this distribution may be estimated with modeling, as discussed in Section 7.4).

However, the $1/v$ nature of the deposit (^{235}U) and the target (^{10}B) cross sections, and the thermal nature of the neutron beam, enable the elimination of $\phi(E)$ from this calculation.

First, Eq. 7.14 may be rewritten in terms of velocity rather than energy, where $\phi(v) = n(v)v$,

$$\langle\sigma\rangle = \frac{\int \sigma(v)n(v)\, v\, \mathrm{d}v}{\int n(v)\, v\, \mathrm{d}v} \tag{7.15}$$

In the $1/v$ absorption region of $\sigma(v)$, $\sigma \propto v^{-1}$ and, therefore, the product σv is a constant. Equation 7.15 may then be rewritten as,

$$\langle\sigma\rangle = \frac{\sigma v \int n(v)\, \mathrm{d}v}{\int n(v)\, v\, \mathrm{d}v} \tag{7.16}$$

This reduction holds true as long as contributions from neutrons outside the $1/v$ energy region are negligible [41]. The absence of epithermal and fast neutrons from the thermal-column neutron beam was verified by measuring the neutron count rate with a lithium-glass beam block in front of the fission chamber. While the beam block (7.325 mm thick, 6.3% ^{6}Li) eliminates 99.998% of thermal neutrons, it only eliminates 81.84% of neutrons at 1 eV, and 16.37% of neutrons at 100 keV. Measurements with this beam block in place revealed count rates of 0.018 Hz. Comparatively, count rates without the beam block were typically around 2.66 Hz. Additionally, the absence of non-thermal neutrons is demonstrated by the energy-distribution modeling, discussed in Section 7.4.

According to Eq. 7.16, the ratio of the two effective cross sections in Eq. 7.7 may be reduced to,

$$\frac{\langle \sigma_{10} \rangle}{\langle \sigma_{235} \rangle} = \frac{\sigma_{10}\, v \cancel{\int n(v)\, \mathrm{d}v}}{\cancel{\int n(v)\, v\, \mathrm{d}v}} \frac{\cancel{\int n(v)\, v\, \mathrm{d}v}}{\sigma_{235}\, v \cancel{\int n(v)\, \mathrm{d}v}} = \frac{\sigma_{10}}{\sigma_{235}} = \kappa \tag{7.17}$$

where κ is simply the ratio of the two cross sections at energies (or velocities) in the $1/v$ region. While κ is not perfectly constant below 1 eV, it does not vary significantly in the thermal region. Even a 50% uncertainty in the neutron energy at which to select κ, from a centerpoint of $E = 0.025$ eV, results in a variation of κ by only 2.61%. The value of κ at $E = 0.025$ eV (2200 m/s) was selected for this analysis ($\kappa = 6.567$). A relative uncertainty of 2.61% was associated with this value. The cross sections of ^{10}B and ^{235}U are plotted in Figure 7.13. The value of κ over thermal energies is plotted in Figure 7.14.

Following this simplification, Eq. 7.7 is reduced to,

$$N_n = \frac{\hat{n}_n(t)}{t_n}\, \kappa\, \frac{(\rho_A)_{10}\, M_{235}}{(\rho_A)_{235}\, M_{10}}\, \mu\, \zeta\, \sqrt{2}. \tag{7.18}$$

The value μ represents the fraction of neutrons which were not absorbed between the fission chamber reference monitor and the boron thin-film targets. This accounts for absorption by: the fission chamber deposit and housing, the air gap between the fission chamber and the scintillation cell, the silica entrance window of the cell, the foil covering the silica entrance window, the gas in the cell, and the aluminum cylinder coated with Ebonol-C. Thicknesses, macroscopic cross sections (2200 m/s),

and transmission fractions (T) for these components, are listed in Table 7.2. Transmission fractions were determined using Beer-Lambert's Law. The resulting value of μ is 0.995. This value assumes noble gas pressures of 1 atm. The value does not account for neutrons that were scattered out of the beam.

For each scintillation measurement, values of N_n were calculated using measurements from the fission-chamber beam monitor and Eq. 7.18. Values of N_n are later used to determine scintillation yields per neutron absorption, in Chapter 9. The average neutron absorption rate of each ^{10}B target, when irradiated in the thermal-column beam, appears in Table 7.3.

Component	Material	Thickness (mm)	Σ_a (cm^{-1})	T
deposit	^{235}U	2.41×10^{-4}	33.5	0.9992
housing	Al	1	0.0139	0.9986
air	mixture	75	3.83×10^{-5}	0.9997
foil	Al	0.05	0.0139	0.9999
window	SiO_2	0.5	1.41×10^{-3}	0.9999
noble gas	Ar, Kr, Xe	35	$(1.82, 67.4, 66.3) \times 10^{-5}$	0.9999, 0.9976, 0.9977
cylinder	Al	1	0.0139	0.9986
coating	Cu	0.012	0.322	0.9996

Table 7.2: Thicknesses, macroscopic cross sections, and transmission fractions of the materials between the fission-chamber reference detector and the boron thin-film target. Gas values were calculated at atmospheric pressure.

Nominal Thickness (nm)	$(\rho_A)_{10}$ (µg/cm^2)	$\overline{N}_n$ (Hz)
300	73.50	91.7
600	140.31	170.5
900	209.13	256.2
1200	260.02	332.9

Table 7.3: Average neutron absorption rates of each ^{10}B target, as determined by Eq. 7.18 and measurements from the fission-chamber beam monitor. $t_n = 1200$ s.

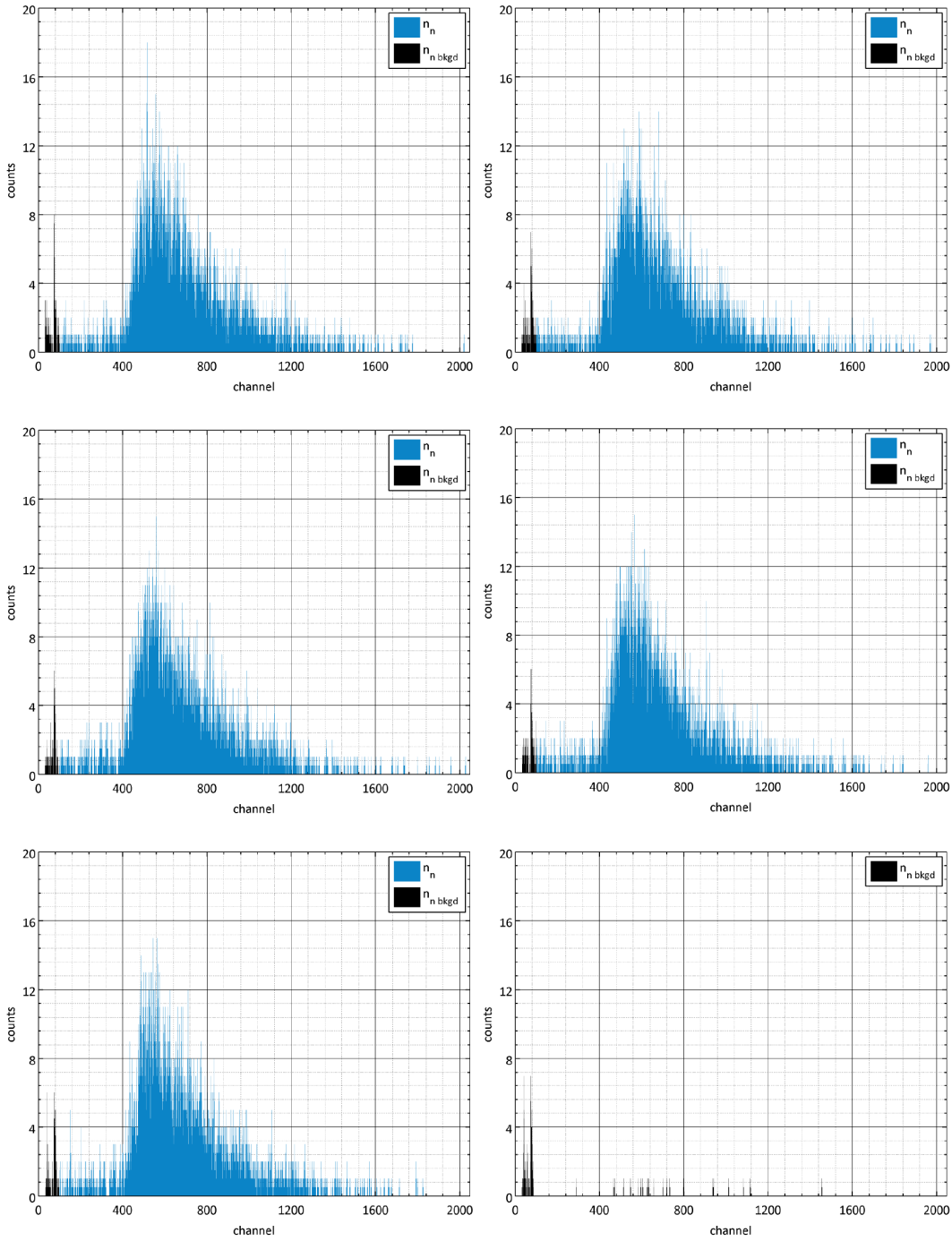

Figure 7.8: Pulse-height distributions from the fission chamber. Noise peaks are represented in black. Bottom-right distribution shows a measurement taken with Li-glass in front of the detector. Count time $t = 1200$ s.

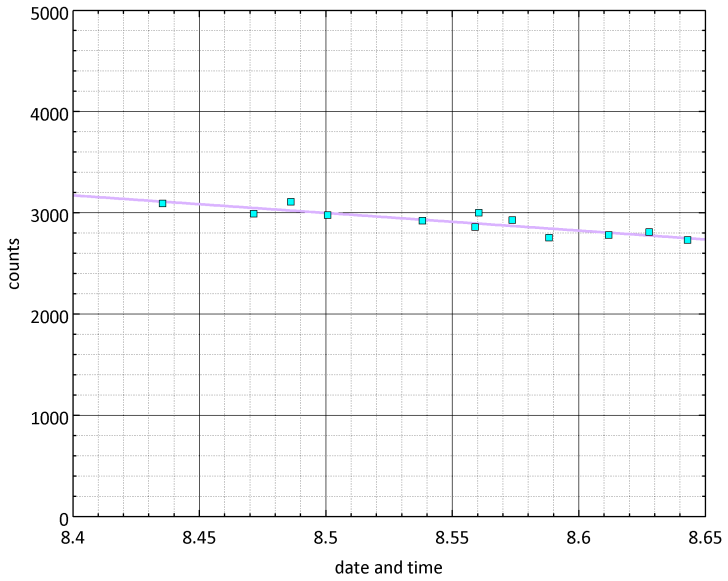

Figure 7.9: Neutron counts on 3.09.12. Count time $t_n = 1200$ s.

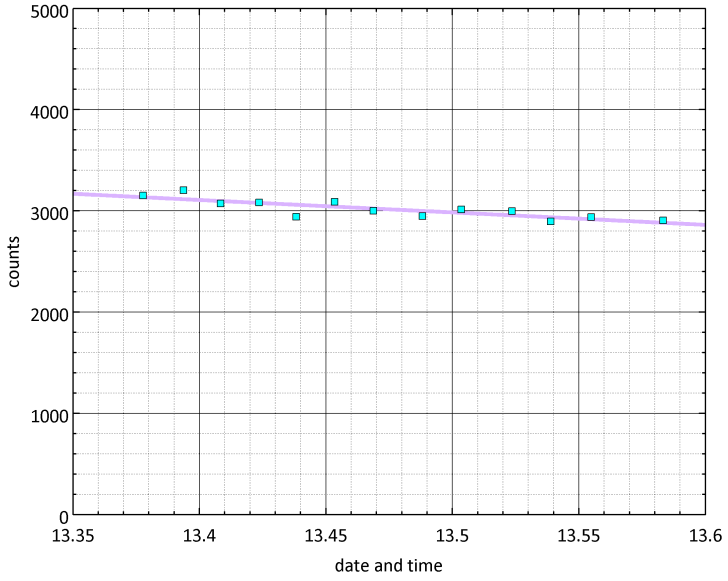

Figure 7.10: Neutron counts on 3.14.12. Count time $t_n = 1200$ s.

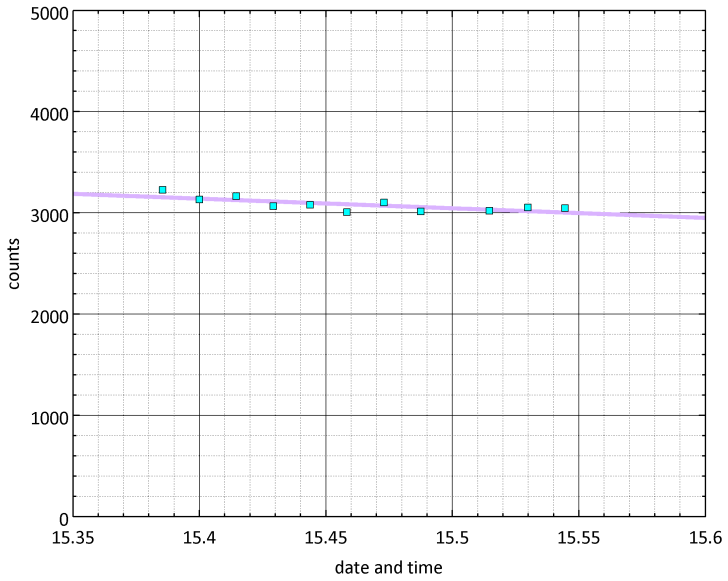

Figure 7.11: Neutron counts on 3.16.12. Count time $t_n = 1200$ s.

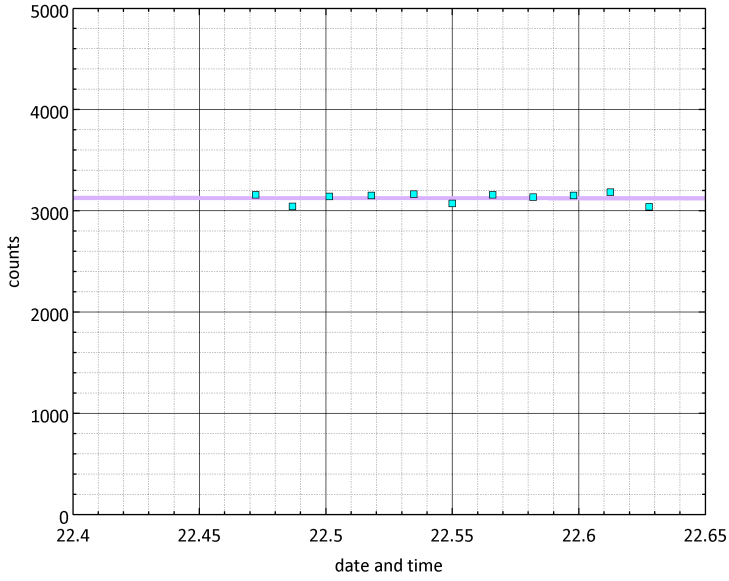

Figure 7.12: Neutron counts on 3.23.12. Count time $t_n = 1200$ s.

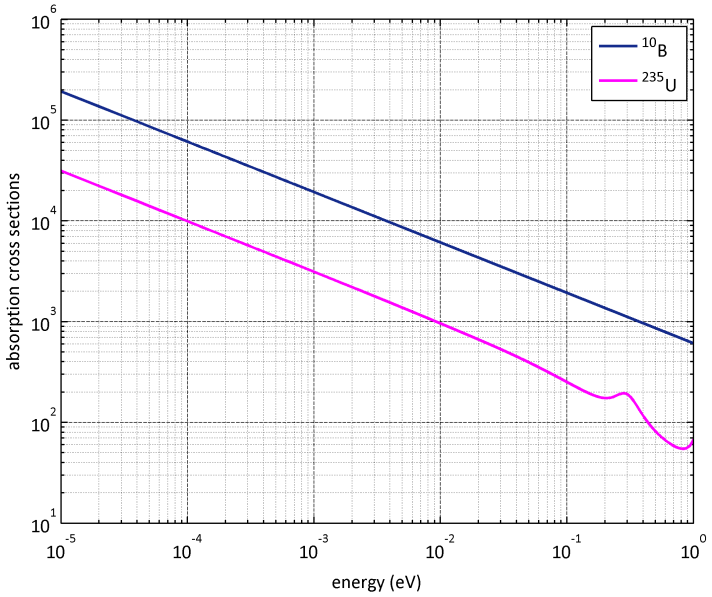

Figure 7.13: Cross sections of ^{10}B and ^{235}U over the thermal energy region.

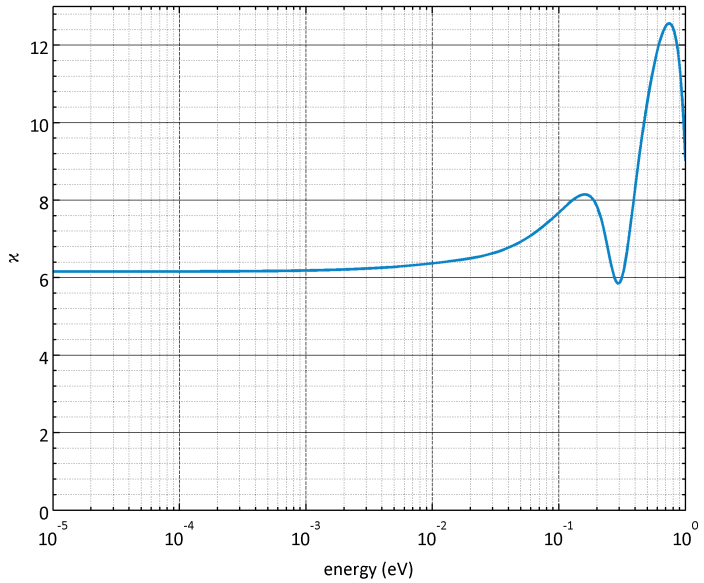

Figure 7.14: Value of κ over the thermal energy region.

7.3 Beam Profile Measurement

A beam profile measurement was performed to verify the limited divergence of the neutron beam between the fission-chamber reference monitor and the ^{10}B targets. Dysprosium foils were irradiated at two locations in the beam (1) directly behind the beam aperture, and (2) 12 cm behind the aperture, in the approximate position of the boron targets. An imaging plate (photostimulable phosphor) was then exposed by the activated foils, and processed to produce images of the neutron beam profile.

Dysprosium-164 has an isotopic abundance of 28.18%, and a large thermal-neutron absorption cross section ($\sigma_0 = 2981$ b) [77, 32]. When irradiated with neutrons, this isotope undergoes the reaction,

$$n + {}^{164}\text{Dy} \rightarrow {}^{165}\text{Dy} \tag{7.19}$$

$$^{165}\text{Dy} \rightarrow {}^{165}\text{Dy} + \beta + 1.25 \text{ MeV} \tag{7.20}$$

from which ^{165}Dy decays with a half-life of 2.334 h. The natural dysprosium foils used in this measurement were 10×10 cm, with areal densities of 0.0213 g/cm^2. The foils were irradiated separately for 45 minutes each, at a reactor power of 200 kW. With the exception of the 4-mm beam aperture, the scintillation cell and the other components of the scintillation experiment were removed from the beamline during the irradiations.

Following both irradiations, the activated foils were transferred to the imaging plate. When β-particles (or other energetic radiation) pass through an imaging plate, they excite electrons in the phosphor. Some of the excited electrons become trapped in the phosphor lattice until stimulated by a light source, at which point their deexcitation releases additional photons (photostimulated luminescence). These β-particles are said to "expose" the imaging plate. Activities of 0.1 $\text{min}^{-1}\text{mm}^{-2}$ can be measured by exposures of less than 1 hour [137]. The Dy foils exposed the imaging plate for 120 minutes. The foils were then removed from the imaging plate and the plate was transported to NIST, where its photostimulated luminescence (PSL) was measured by an image reader (FujiFilm BAS 1800-II). This image reader produced a digital scan of the stored images, with 50 μm resolution.

Two sections of the measured image correspond to the neutron beam profile at each Dy foil location. These sections appear in Figures 7.15 and 7.16. The color value of each pixel in these images is directly proportional to the amount of PSL observed by the image reader at that location. The first image shows the neutron beam profile directly behind the aperture. The Dy foil in this location was irradiated first, and was allowed to decay during the second foil irradiation. Therefore, the resulting image was corrected for this decay time, with the factor

$$\frac{1}{e^{-\lambda t}} = 1.2495 \tag{7.21}$$

where λ is the decay constant of ^{165}Dy (0.00495 min^{-1}), and t is the decay time (45 min). This correction assumes that the PSL from the imaging plate is linearly proportional to the deposited energy.

The second image shows the neutron beam profile 12 cm behind the aperture. This was approximately the distance between the aperture and the boron targets during the scintillation experiment. This image was not corrected since the foil was transferred to the imaging plate directly after irradiation.

The beam spot in Figure 7.15 is slightly larger than the 4-mm aperture. This is due to the "blooming" effect of the imaging plate exposure [137]. The isotropic nature of β-decay causes some electrons to be emitted at glancing angles to the imaging plate, producing a blurring effect at the boundaries of the image. The beam spot in Figure 7.16 has a diameter of approximately 7 mm. Together, these measurement demonstrate that the diameter of the neutron beam spread by approximately 3 mm over the 12 cm distance between the aperture and the boron film. The 7-mm beam spot in Figure 7.16 is still significantly smaller than the boron target size (25×25 mm).

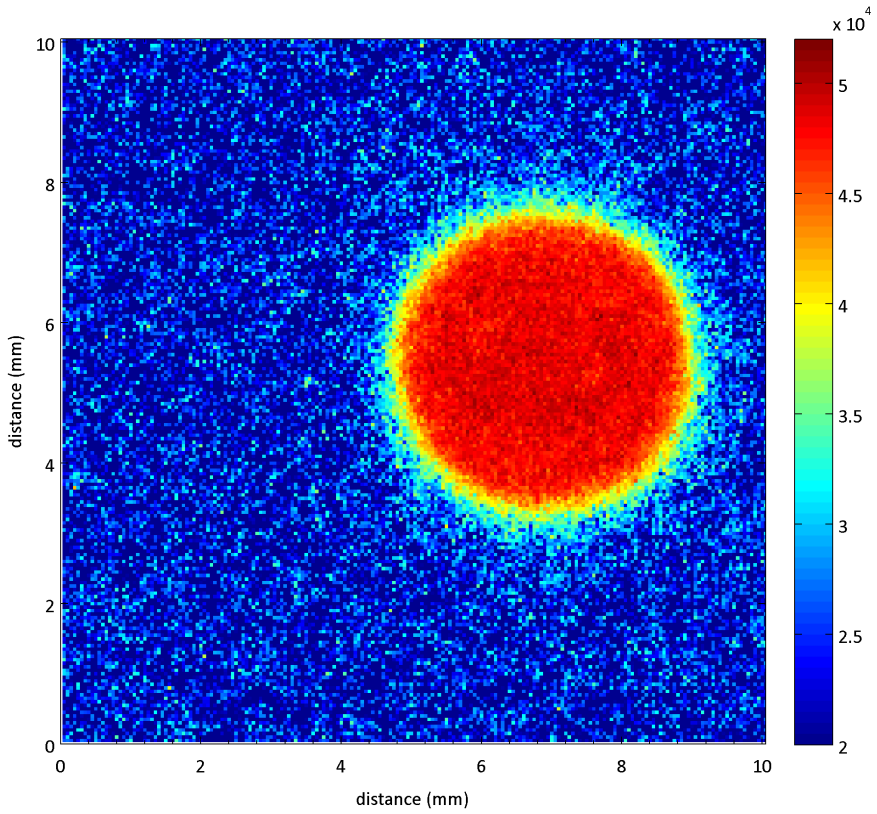

Figure 7.15: Neutron beam profile immediately behind the aperture.

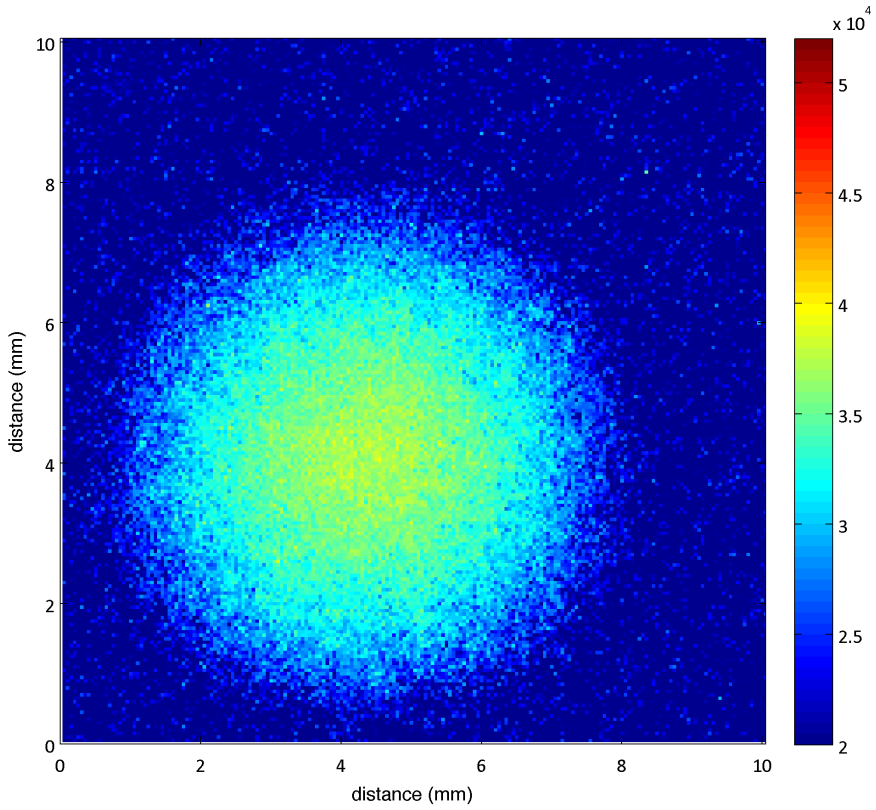

Figure 7.16: Neutron beam profile 12 cm behind the aperture.

7.4 Energy-Distribution Modeling

To derive the fluence of the MUTR thermal-column neutron beam, based on measurements from the fission-chamber beam monitor, it is necessary to estimate the energy distribution of the beam, and the effective cross section of ^{235}U in the beam ($\langle\sigma_{235}\rangle$). These parameters were not required to calculate the number of neutrons absorbed by the boron thin films, as demonstrated in Section 7.2. Nonetheless, they provide useful benchmarks for future experiments that will use the thermal-column beam for neutron irradiations.

Monte Carlo N-Particle (MCNP) transport code is a general-purpose, continuous-energy, coupled neutron/photon/electron transport code developed at Los Alamos National Laboratory [138]. The code implements random number generation to obtain solutions for complex radiation transport calculations. These calculations typically lack deterministic solutions and, therefore, require statistical simulation. Designing an MCNP simulation involves defining geometry, materials, particle sources, and output types. Energy-dependent cross sections for a wide range of materials are provided in the MCNP data libraries. An MCNP model of the MUTR, developed by Ali Mohamed, was modified to simulate the thermalization of neutrons passing through the thermal column. The details of the original model are described in [139].

The geometry of the modified MUTR MCNP model appears in Figure 7.17. This geometry includes the reactor core, the reactor pool, the concrete containment

structure, and the various components of each experimental facility, specifically the thermal-column graphite, and the collimator insert. In modifying the model from [139], the thermal-column graphite was artificially partitioned to demonstrate the thermalization of the neutron spectrum between the core and the access cavity. Each labeled cell in Figure 7.17 represents a flux tally volume within the model. During the simulation, neutrons that enter a particular cell, make a contribution to that cell's tally equal to,

$$C = \frac{WT}{V} \tag{7.22}$$

where T is the particle track length through that cell, V is the volume of the cell, and W is the weight of the particle. Analytically, if $\Phi(\mathbf{r}, E, \mathbf{\Omega})$ is the energy and angular distribution of the neutron fluence as a function of position within the model, flux tallies measure a statistical solution to the equation,

$$\mathrm{FT} = \frac{1}{V} \int_V \mathrm{d}V \int_E \mathrm{d}E \int_{4\pi} \mathrm{d}\Omega \, \Phi(\mathbf{r}, E, \mathbf{\Omega}) \tag{7.23}$$

Particle weights (W) are determined according to the importance value given to the cell through which the particle is traveling. Variance reduction techniques often exploit cell importances to amplify particle populations in a particular segment of the model geometry. In the MUTR simulation, for example, cell importances were assigned according to the proximity of each cell to the thermal-column access cavity. More information on cell importances and geometry splitting techniques is available in [140].

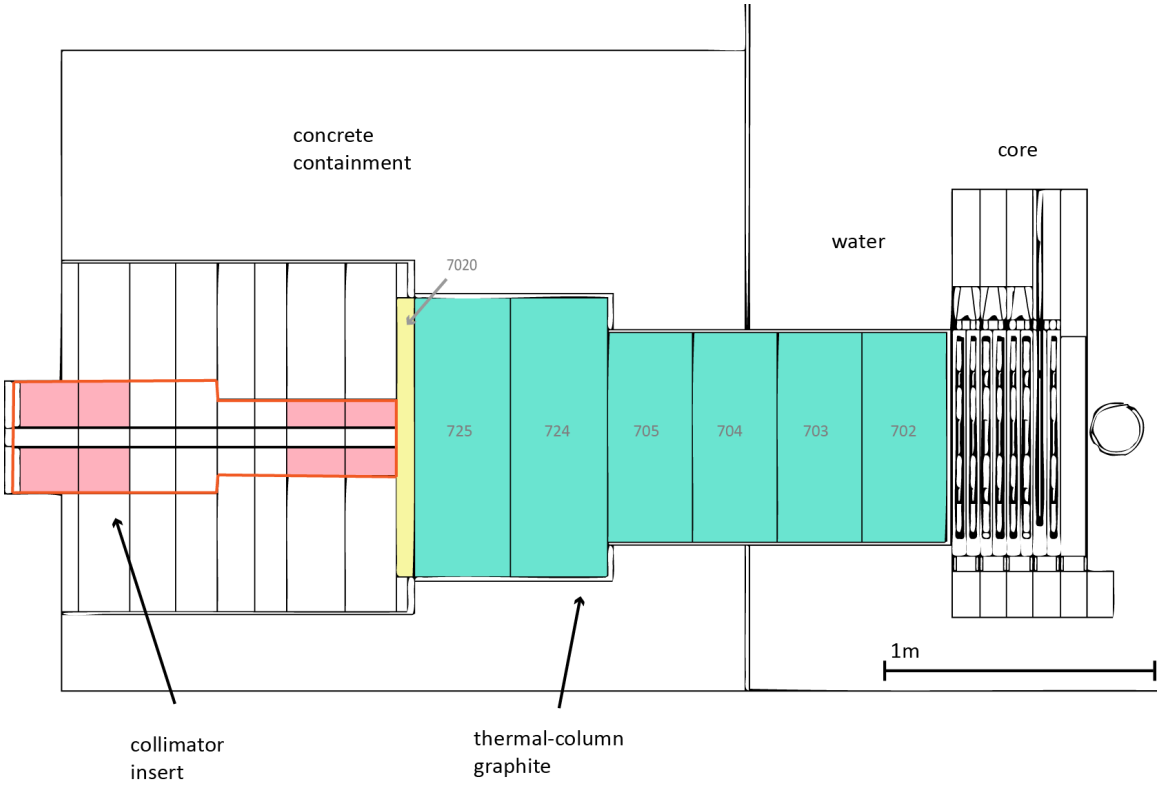

Figure 7.17: Geometry of the MUTR MCNP model, showing a cross sectional view of the thermal-column facility. The geometry has been artificially partitioned to sample the neutron spectrum at various depths in the graphite moderator. The numbered segments correspond to the cells that were used as tally volumes for the simulations.

By creating a histogram of tally contributions according to particle energy, energy distributions may be obtained from each tally volume. Neutron energy distributions ($\phi(E)$) from the various segments of the thermal-column graphite, appear in Figure 7.18. These distributions have been normalized to the peak value of the distribution closest to the core. The thermalization of the neutron population is demonstrated by the thermal-to-fast flux ratio at various distances from the core. This parameter is given by the equation,

$$\mathcal{R} = \frac{\phi_{\text{th}}}{\phi_{\text{fast}}} \tag{7.24}$$

where ϕ_{th} is the number of neutrons below the cadmium cutoff (0.6 eV), and ϕ_{fast} is the number of neutrons above the cadmium cutoff. Values of $\mathcal{R}$ in the thermal-column graphite appear in Figure 7.19 as a function of distance from the core.

Using Eq. 7.14, the microscopic cross section of ^{235}U, and the energy-dependent flux of the thermal column access cavity, the effective cross section of ^{235}U in the thermal-column neutron beam ($\langle\sigma_{235}\rangle$) was calculated to be 483.8 b. For comparison, the 2200 m/s cross section of ^{235}U is 585.1 b. By substituting $\langle\sigma_{235}\rangle$ into Eq. 7.5, the average fluence of the thermal column neutron beam was determined for each data collection day, with the equation,

$$\overline{N}_{\text{TC}} = \frac{\overline{N}_{\text{beam}}}{A} \tag{7.25}$$

where $\overline{N}_{\text{TC}}$ is the average fluence in units of cm^{-2}s^{-1}, $\overline{N}_{\text{beam}}$ is the average fluence behind the beam aperture in units of Hz, and A is the area of the beam aperture opening (0.126 cm^2). Values of $\overline{N}_{\text{TC}}$ appear in Table 7.4. For comparison, the MUTR Safety Analysis Report lists the maximum thermal flux in the fuel as 5.0×10^{12} cm^{-2}s^{-1} [101].

Date	$\overline{n}_n$ (Hz)	$\overline{N}_{\text{TC}}$ (cm^{-2}s^{-1})
3.09.12	2.427	35,297
3.14.12	2.515	36,577
3.16.12	2.569	37,357
3.23.12	2.606	37,894

Table 7.4: Average count rates from the fission chamber ($\overline{n}_n$) and average total neutron fluence in the MUTR thermal-column beam ($\overline{N}_{\text{TC}}$), as determined from $\overline{n}_n$ and the modeled energy distributions.

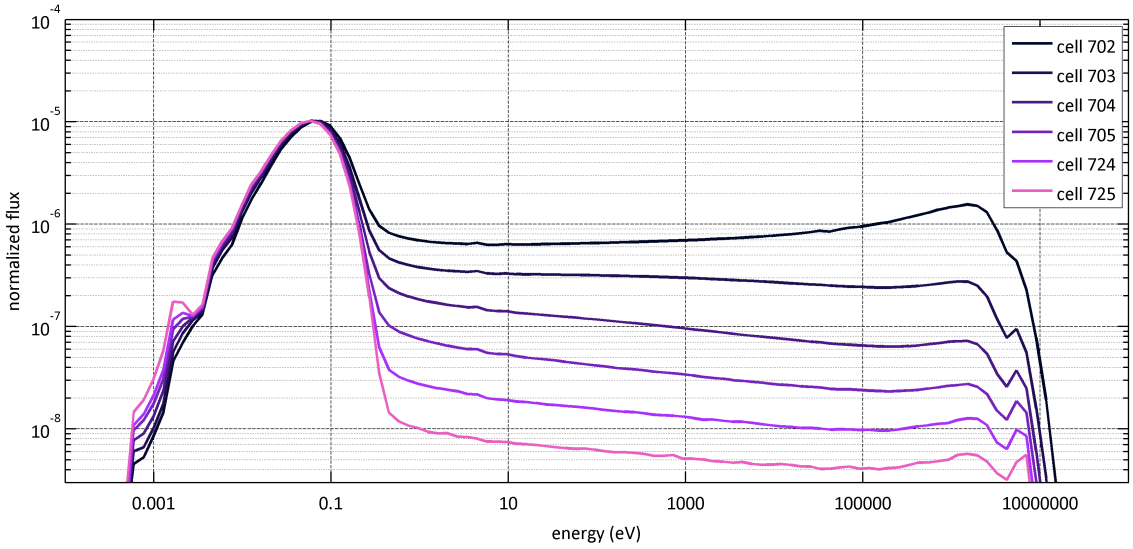

Figure 7.18: Neutron energy distributions at various depths in the MUTR thermal column. Cell numbers correspond to the geometry displayed in Figure 7.17.

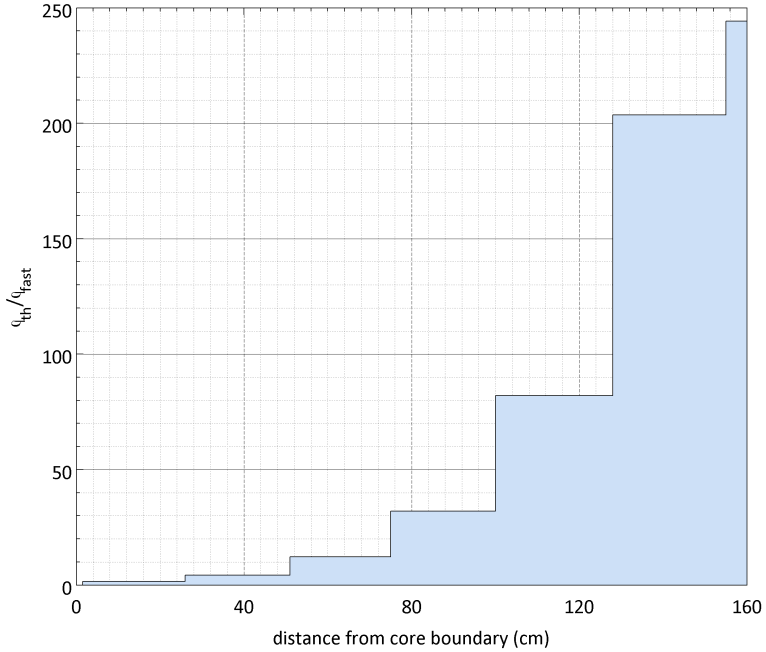

Figure 7.19: Neutron flux ratios across the MUTR thermal column.

With a newly constructed collimator, a neutron beam was obtained from the MUTR thermal-column. Several methods were implemented to characterize this beam. Measurements from the fission-chamber beam monitor were analyzed to determine the rate of absorption in the boron thin film targets (90 - 330 Hz). Foil activation was used to demonstrate the limited divergence of the beam between the aperture and the target position. MCNP simulations were used to demonstrate the thermal nature of the energy distribution, and to derive estimates of the total neutron flux (3.5 - 3.8×10^4 $\mathrm{cm}^{-2}\mathrm{s}^{-1}$).

Chapter 8

Modeling

In conjunction with the excimer scintillation measurements, computer modeling was employed to simulate charged-particle transport from the $^{10}B(n,\alpha)^{7}Li$ reaction, and FUV photon emission within the scintillation cell. The results of these models were used to determine the average energies of charged particles escaping the boron films, the ranges and stopping times of the charged particles in the heavy noble gases, and the photon collection efficiency of the experimental apparatus. The incorporation of these results into the analysis of the scintillation measurements is discussed in Chapter 9.

8.1 Charged-Particle Transport

The TRIM (Transport of Ions in Matter) code is a collection of programs that calculate the stopping and range of ions in matter through statistical simulations of ion-atom collisions [141]. These simulations provide quantum mechanical approximations of Coulomb collisions, long range interactions, and the charge state of each ion as it passes through a target. User inputs to TRIM include ion charge, mass, energy (10 eV - 2 GeV), emission position, and angle, as well as a 3D description of

the target geometry and composition. TRIM outputs include the final distribution of ions within the target, and descriptions of the ions' energy loss and trajectories while slowing down. The code has been actively developed since 1983 and is available at [142].

For this research, TRIM was used to simulate charged-particle emission from boron thin films, and the slowing down of those charged particles in noble gases. Custom TRIM inputs were generated in the TRIM.dat file format, using a MATLAB script to choose random numbers for the various entries. The TRIM.dat inputs specify the emission positions, directions, and starting energies of α and ^{7}Li pairs, according to the characteristics of the $^{10}\mathrm{B}(n,\alpha)^{7}\mathrm{Li}$ reaction. Emission directions were chosen isotropically. Starting energies were chosen according to the branching ratios of the $^{10}\mathrm{B}(n,\alpha)^{7}\mathrm{Li}$ reaction (6% to $E_\alpha = 1777$ keV and $E_{^7\mathrm{Li}} = 1015$ keV, and 94% to $E_\alpha = 1470$ keV and $E_{^7\mathrm{Li}} = 840$ keV). Emission positions were chosen according to the neutron absorption depth profile and the neutron beam width at the locations of the boron films. The absorption depth profile was sampled using an inverse transform of the form,

$$u = 1 - e^{-\Sigma x} \quad u \in [0,1] \tag{8.1}$$

where u is a random number from a uniform distribution, Σ is the macroscopic absorption cross section of ^{10}B, and x is the absorption depth. The input generator allowed variation of the emission-position distribution based on the thicknesses of the boron film targets. The 45° tilt of the film was not considered during these simulations. Target geometries and densities were specified in the TRIM graphical

user interface (GUI). The targets described the thicknesses and density of the boron films, and the types and pressures of the noble gases. All simulations were run in the "quick KP damage" mode for 20,000 particle histories. Typical plots of particle trajectories appear in Figure 8.1.

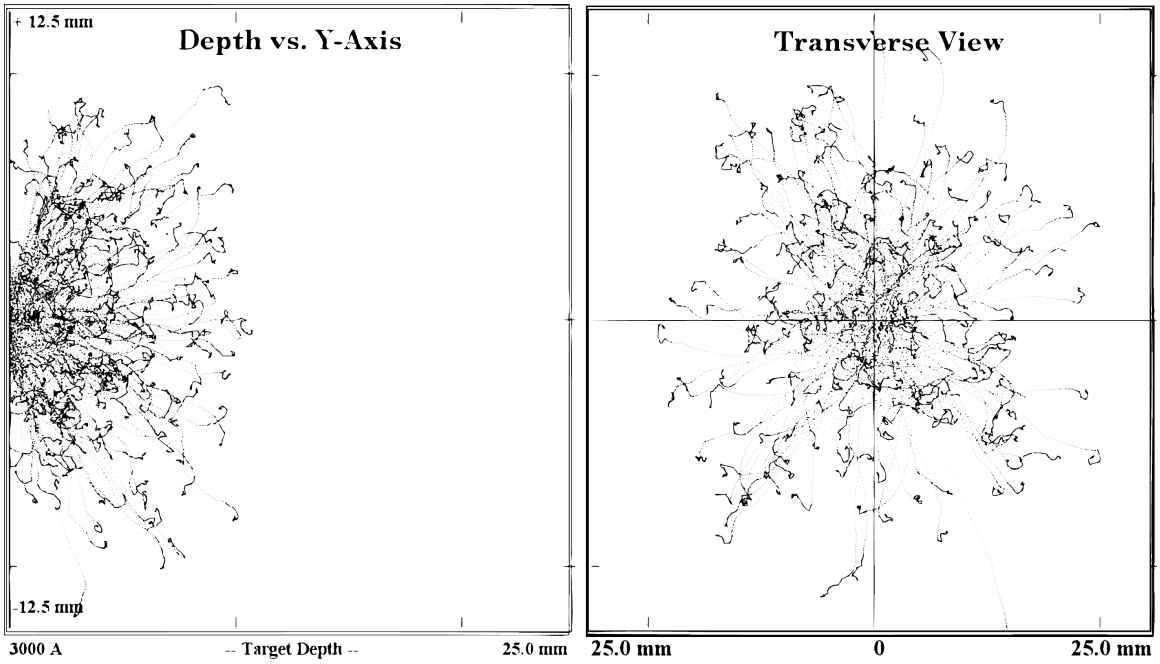

Figure 8.1: Particle trajectory plots from TRIM simulations of the $^{10}\mathrm{B}(n,\alpha)^{7}\mathrm{Li}$ reaction under 400 torr of Xe. Depth plot depicts the boron film at the left-hand border. Transverse plot depicts a head-on view of the boron film.

The first set of TRIM simulations estimated the average kinetic energy of charged-particles escaping the boron films. These simulations were run for a range of film thicknesses (0.1 - 2.0 μm). The results appear in Figure 8.2. These values represent the average energy available to generate noble gas excimers, following each neutron capture. They demonstrate that, on average, 60-85% of the $^{10}\mathrm{B}(n,\alpha)^{7}\mathrm{Li}$ Q-value (2.792 MeV) is deposited in the boron film before the charged particles escape into the gas. From these results, the average escape energies (E_{esc}) were determined

for each boron sample used in the scintillation experiment. The thicknesses of the boron samples were calculated from the NIF data, with the equation,

$$x = \frac{\rho_A}{\rho} \tag{8.2}$$

where ρ_A is the areal density of the boron film, as determined in Chapter 5.2.1, and ρ is the default density of boron in the TRIM library (2.350 g/cm^3). The corresponding values of E_{esc} appear in Table 8.1.

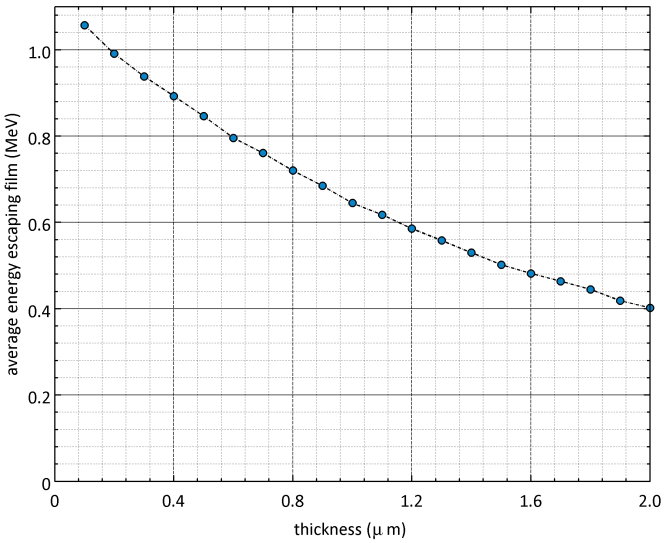

Figure 8.2: Charged-particle escape energy as a function of film thickness. Accounts for both α and ^{7}Li from the $^{10}\text{B}(n,\alpha)^7\text{Li}$ reaction.

Nominal Thickness (nm)	ρ_A (μg/cm^2)	x (nm)	E_{esc} (keV)
300	73.5	312.7	932.2
600	140.3	597.0	797.2
900	209.1	889.8	685.5
1200	260.0	1106.4	615.9

Table 8.1: Boron film thicknesses, as calculated with Eq. 8.2, and average charged-particle escape energies, determined by TRIM simulation.

The second set of TRIM simulations modeled (1) the radial range of the charged particles, (2) the stopping time of the charged particles, and (3) the ionization density in the gas targets, as a function of noble-gas type and pressure. Modeling these parameters is necessary to understand the rate and duration of excimer formation, and the geometry of the photon emission volume. The gas types and gas pressures defined in these simulations were identical to the conditions established in the scintillation measurements. The simulations considered a single target thickness of 300 nm.

The radial range and stopping times determined by TRIM appear in Figure 8.3, as a function of gas pressure. Radial range is given by the equation,

$$R_r = \frac{\sum_{i=1}^{N} \sqrt{y_i^2 + z_i^2}}{N} \tag{8.3}$$

where y and z are the lateral projections of each particle on a plane parallel with the boron film, and N is the number of particle histories. These range values were used to estimate the size of the photon emission volume in Section 8.2. The stopping times were calculated by substituting the range values into the equation,

$$T = \frac{R_r}{K} \sqrt{\frac{m\, M_p}{2\, E_{\text{esc}}}} \tag{8.4}$$

where R_r is the charged particle range, K is an adjustment coefficient (0.6) described in Chapter 2.5, m is the number of nucleons per charged particle (averaged to 5.5), M_p is the mass of the proton (938.272 MeV/c^2), and E is the average escape energy

from a 300-nm film (0.9382 MeV). The stopping times in Figure 8.3 are only order-of-magnitude estimates, since the α and ^{7}Li particles were not modeled independently. Ionization density plots appear in Figures 8.4 - 8.6 for Ar, Kr, and Xe, at a number of gas pressures. The plots show the two-dimensional shape (x-y projection) and the ionization density (z projection) of the volume in which the charged particles deposit their energy. They are contour plots, with a contour drawn at every step of 3×10^{-6} eV/ ion Å. Since the mean free path of Ar, Kr, and Xe atoms at STP are < 100 nm (see Table 2.2), the shape and density of the excimer photon source may be assumed to resemble these ionization volumes, at least for pressures close to 1 atm.

The results of the TRIM simulations provide estimates of the amount of energy available to generate noble gas excimers (600 - 930 keV), the time over which that energy is deposited in the noble gas (1-15 ns), and the size, shape, and ionization density of the volume in which the energy is deposited.

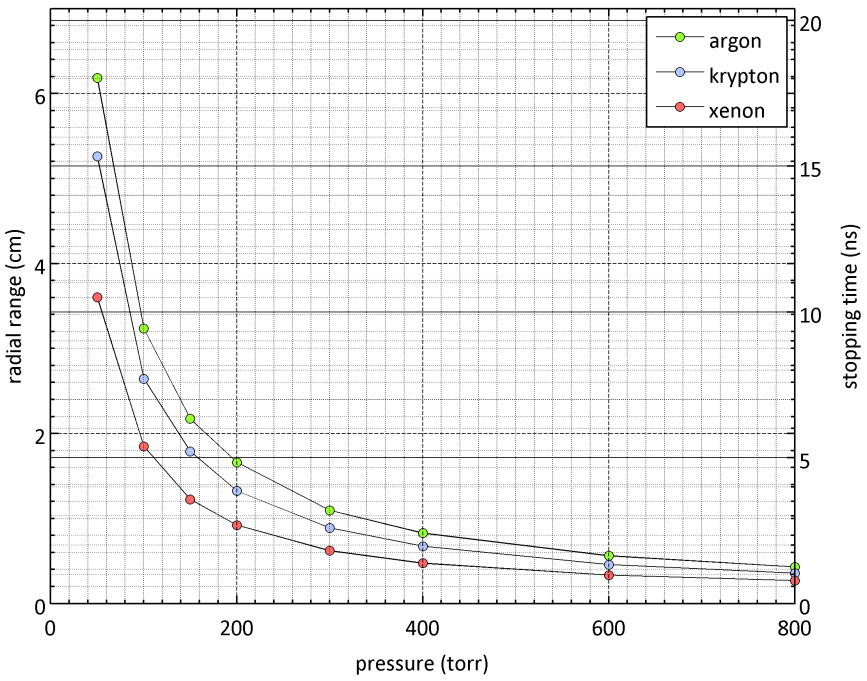

Figure 8.3: Charged-particle range and stopping time in Ar, Kr, and Xe, as a function of gas pressure. Includes contributions from α and ^{7}Li particles.

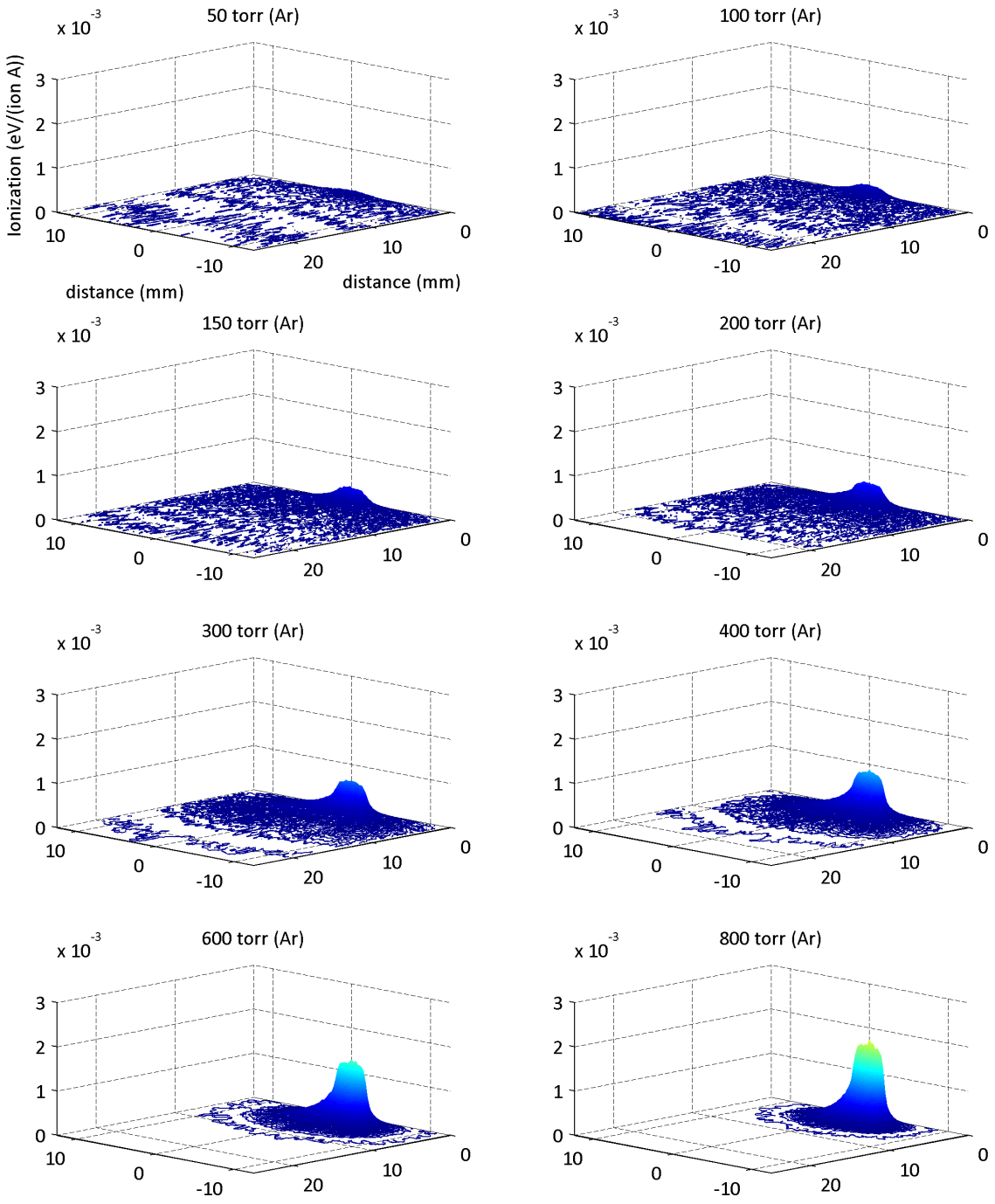

Figure 8.4: Ionization density in argon at various pressures, from neutron irradiation of a 300-nm ^{10}B film. Each right-hand, upright plane represents the surface of the film.

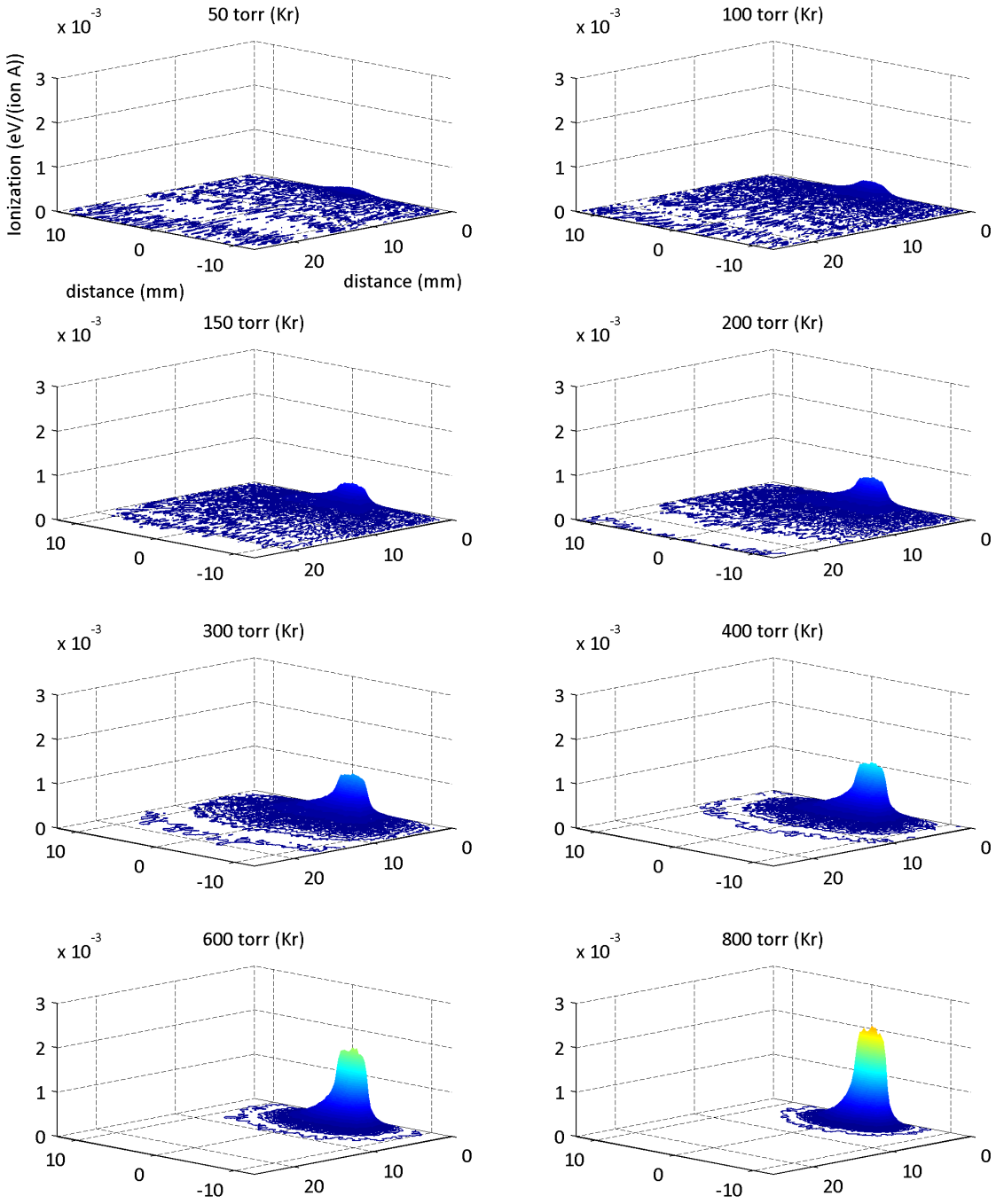

Figure 8.5: Ionization density in krypton at various pressures, from neutron irradiation of a 300-nm ^{10}B film. Each right-hand, upright plane represents the surface of the film.

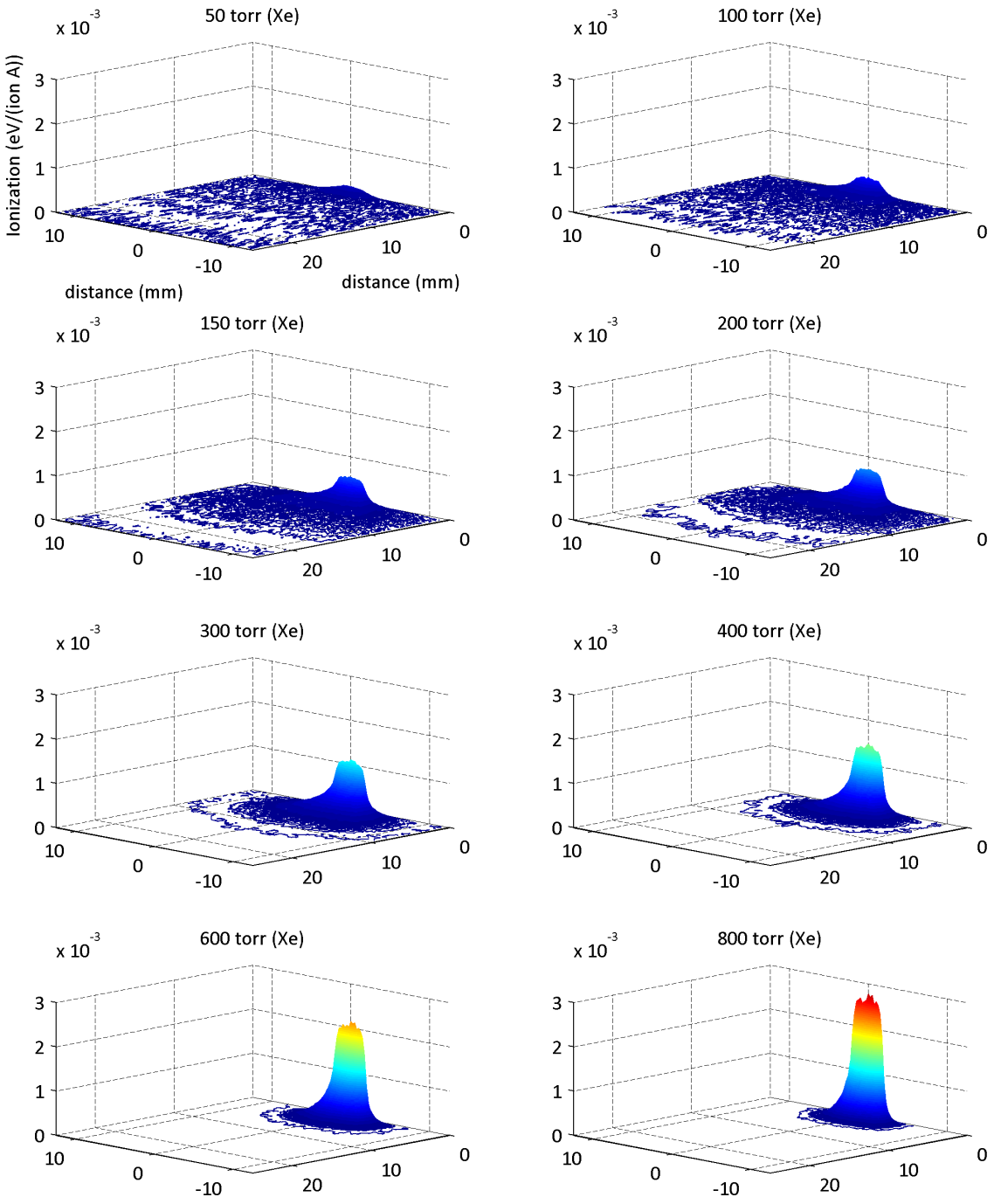

Figure 8.6: Ionization density in xenon at various pressures, from neutron irradiation of a 300-nm ^{10}B film. Each right-hand, upright plane represents the surface of the film.

8.2 Photon Emission and Reflection

Chapter 6 describes measurements of the intrinsic efficiency of the PMT/MgF_2 detector package. This parameter is needed to determine the fraction of photons impinging on the detector which create a countable pulse. Before calculating the absolute scintillation yield, it is also necessary to determine the fraction of all scintillation photons which impinge on the detector. This fraction will be referred to as the collection efficiency of the apparatus, and is given by the equation,

$$\epsilon_{\text{cube}} = \frac{\text{number of radiation quanta incident on detector}}{\text{number of radiation quanta emitted by source}} \tag{8.5}$$

This definition has been slightly modified from Eq. 2.8 to account for all photons incident on the detector, not just those that create a recorded pulse. Additionally, the effective collection efficiency determined by statistical modeling will be referred to as $\langle \epsilon_{\text{cube}} \rangle$.

A point source approximation is the simplest way to determine ϵ_{cube}. This approximation assumes that photons are emitted isotropically from the exact center of the boron target, and is calculated with the equation,

$$\epsilon_{\text{cube}} = \frac{\Omega}{4\pi} = \frac{1}{2}\left(1 - \frac{d}{\sqrt{d^2 + a^2}}\right) \tag{8.6}$$

where Ω is the solid angle subtended by the detector, d is the distance from the source to the detector photocathode (8.58 cm), and a is radius of the detector

photocathode (1.15 mm). The result from this calculation is $\epsilon_{\text{cube}} = 0.4432\%$. This simplification does not take into account the form of the photon emission source, the reflectivities of the surfaces within the apparatus, or the spatial uniformity of the PMT/MgF_2 detector package.

To better approximate the true collection efficiency of the excimer scintillation cell, a Monte Carlo model of the cell was developed using MATLAB. These simulations incorporated both the geometry of the apparatus, and the reflectivity of its various surfaces over the FUV region. A drawing of the model geometry appears in Figure 8.7.

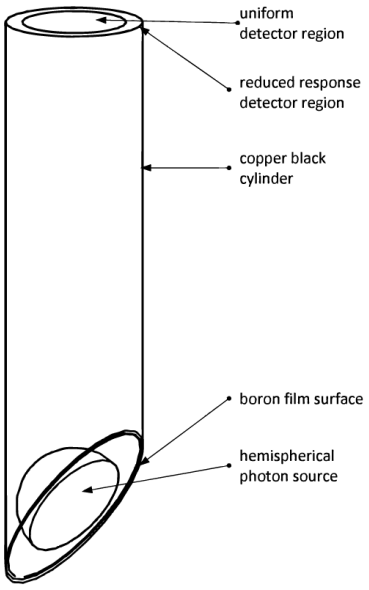

Figure 8.7: Photon-emission model geometry.

The model first generates the emission position of a photon ($\mathbf{x}$), from a uniform and random distribution describing a solid hemisphere. The radius of the hemisphere is an input parameter of the model. A useful resource on sphere point picking is available at [143]. The hemisphere is tilted at a 45° angle with respect to the

detector plane due to the tilt of the boron target. An isotropic vector direction ($\mathbf{u}$) for the photon is then generated from a uniform random distribution. A line drawn from the emission position in the vector direction is represented by the parametric equations,

$$x = x_0 + ut \tag{8.7}$$
$$y = y_0 + vt \tag{8.8}$$
$$z = z_0 + wt \tag{8.9}$$

where (x_0, y_0, z_0) are the components of $\mathbf{x}$, (u, v, w) are the components of $\mathbf{u}$, and t is distance along the line. The intersection of that line with a cylinder is calculated with the equation,

$$t = \frac{-(\mathbf{u}\cdot\mathbf{x} - wz_0) + \sqrt{(\mathbf{u}\cdot\mathbf{x} - wz_0)^2 - (1-w^2)(x_0^2 + y_0^2 - a^2)}}{1-w^2} \tag{8.10}$$

where a is the radius of a cylinder parallel to, and centered on, the z axis. The radius of the cylinder (1.15 cm) describes both the radius of the photocathode, and the radius of the copper-black FUV absorber. According to the location of this intersection, the photon hits one of three surfaces within the model. If the intersection is above the plane of the detector surface, the photon strikes the detector. If the intersection is below the plane of the boron film, the photon strikes the film. If the intersection is between those two planes, the photon strikes the copper-black cylinder.

Based on which surface the photon strikes, it is either collected, reflected, or absorbed. A photon that strikes the detector, adds a score to the detector tally. In this model, the detector is divided into two scoring regions, determined by the spatial scan measurements from Chapter 6.4. These regions appear in Figure 8.8. The inner region (9-mm radius) demonstrated a uniform response with only 3% variation from the mean. The outer region (11.5-mm radius) demonstrated a response that was, on average, 57% of the mean value in the uniform region. In the model, photons striking the uniform region are given a score of 1, and photons striking the outer region are given a score of 0.57.

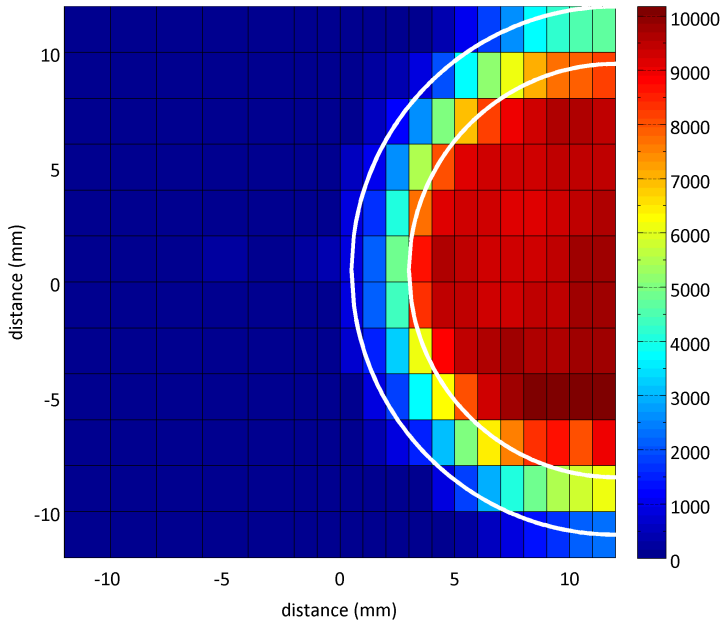

Figure 8.8: Scoring regions overlayed on the spatial response of the PMT, from Chapter 6.4.

A photon that strikes the boron film is specularly reflected with a 35% probability. The reflectivity of boron ($\varrho_{\mathrm{B}} = 0.35$) was obtained from [144]. A plot of boron reflectivity values over the FUV region appears in Figure 8.9. When the photon is

specularly reflected, a new line is drawn from the point of reflection, in the direction,

$$\hat{\mathbf{u}}_s = 2(\hat{\mathbf{u}}_n \cdot \hat{\mathbf{u}}_i)\hat{\mathbf{u}}_n - \hat{\mathbf{u}}_i \tag{8.11}$$

where $\hat{\mathbf{u}}_n$ is the direction normal to the film surface, and $\hat{\mathbf{u}}_i$ is the direction of the incident photon. The intersection of the new line with the cylinder is then determined with Eq. 8.10. If that intersection occurs above the detector plane, the photon strikes the detector. If not, the photon is absorbed. If the photon is not specularly reflected, it is also absorbed.

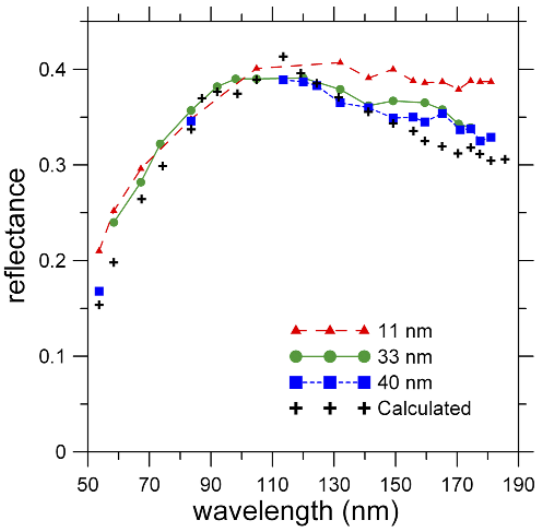

Figure 8.9: Boron reflectivity over the FUV region [144]. Various data series correspond to boron films of different thicknesses.

A photon that strikes the copper-black cylinder, is diffusely reflected with a 1% probability. The diffuse reflectivity of copper black ($\varrho_{\mathrm{Cu}} = 0.01$) is described in [145]. Two plots of bidirectional-reflectance distribution functions (BRDF) for copper black appear in Figure 8.10. When the photon is diffusely reflected, a new isotropic direction is generated from a uniform random distribution, and a line is

drawn from the point of reflection in that direction. The intersection of that line with the cylinder is then determined with Eq. 8.10. If that intersection occurs above the detector plane, the photon strikes the detector. If not, the photon is absorbed. If the photon is not diffusely reflected, it is also absorbed.

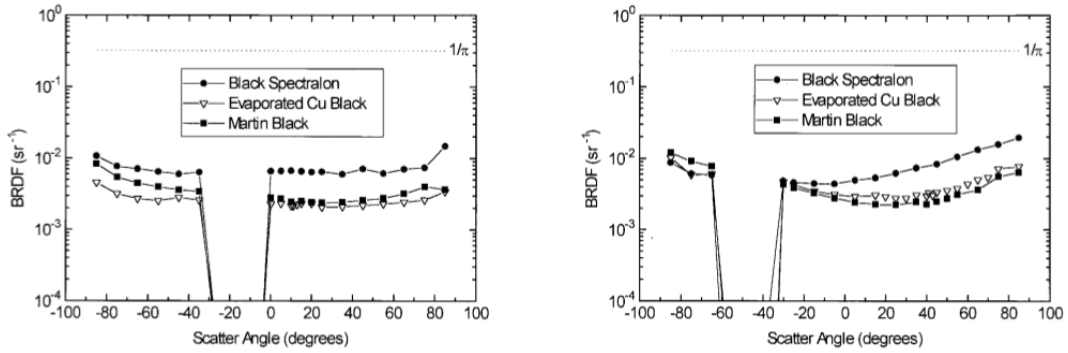

Figure 8.10: Copper-black BRDF data measured at 121.6 nm [145]. Left: 15° angle of incidence. Right: 45° angle of incidence.

By simulating the histories of millions of photons, it is possible to determine the fraction of all scintillation photons impinging on the detector. The collection efficiency may be calculated with the equation,

$$\langle \epsilon_{\text{cube}} \rangle = \frac{n_{\text{inner}} + C_{\text{outer}}\, n_{\text{outer}}}{N} \tag{8.12}$$

where n_{inner} is the number of photons which strike the inner detector region, n_{outer} is the number of photons which strike the outer detector region, C_{outer} is the fractional score given to photons which strike the outer region (0.57), and N is the total number of photons generated by the model. For the geometry and reflectivities specified above, the output of the model for 10 million particle histories is $\langle \epsilon_{\text{cube}} \rangle = (0.5115 \pm 0.0051)\%$. The statistical uncertainty in this value was derived by determining

$\langle \epsilon_{\text{cube}} \rangle$ after every run of 1 million particle histories, and calculating the standard deviation in the outputs from 10 runs.

The photon-emission model was verified by replicating the conditions of the point source approximation, and comparing the statistical solution to the analytical solution of Eq. 8.6. To achieve this, C_{outer} was set to 1, the reflectivities ϱ_{B} and ϱ_{Cu} were set to 0, and the radius of the hemispherical emission source was set to 1 mm. The resulting output of the model was $\langle \epsilon_{\text{cube}} \rangle = (0.4429 \pm 0.0056)\%$, which differs by only 0.07% relative to the analytical solution (0.0003% absolute difference). An early iteration of the model was also compared to a model constructed with the FRED optical analysis code. FRED is a ray tracing code developed by Photon Engineering LLC [146]. The output of the FRED model differed by 7% from the output of the initial MATLAB code. The FRED simulations were performed by Dr. June Tveekrem at NASA's Goddard Space Flight Center.

There are several simplifying assumptions associated with the photon collection model (1) the excimer photon emission volume is assumed to be hemispherical, (2) the distribution of the emissions within this volume are assumed to be uniform, (3) the reflectivities of boron and copper black are assumed to be precisely known, (4) contributions of secondary and tertiary reflections are assumed to be negligible, and (5) refraction by the MgF_2 windows is assumed not to alter the photon path. As a result of these assumptions, it was necessary to ascribe an uncertainty to the value $\langle \epsilon_{\text{cube}} \rangle$. The total uncertainty in $\langle \epsilon_{\text{cube}} \rangle$ was determined by identifying uncertainties in the inputs of the model. The model was then run for an array of

input values, $\varrho_{\mathrm{B}} \in [0.30, 0.40]$, $\varrho_{\mathrm{Cu}} \in [0.005, 0.01]$, $h \in [8.33, 8.83]$ cm. These ranges were chosen according to the range of reflectivity values in [144] and [145], and a physical measurement of the photocathode height. The results of these simulations are plotted in Figures 8.11 and 8.12. The highest and lowest values of $\langle \epsilon_{\mathrm{cube}} \rangle$ were used to determine a relative uncertainty in $\langle \epsilon_{\mathrm{cube}} \rangle$ of 9.69% (relative). Several of the simulation results and their inputs appear in Table 8.2.

Overall, the collection efficiency model incorporates a more realistic approach than the point source approximation, by accounting for reflective surfaces, a non-discrete emission source, and a non-uniform detector surface. While the model does not incorporate every complexity of photon transport within the apparatus, its uncertainty may be estimated by assigning uncertainties to the model inputs. The final value of $\langle \epsilon_{\mathrm{cube}} \rangle$ obtained with the model is 15% larger than the analytical point source solution. The value $\langle \epsilon_{\mathrm{cube}} \rangle = 0.5115\%$ will be used in the analysis on the excimer scintillation measurements in the following chapter.

r (cm)	ϱ_{B} (%)	ϱ_{Cu} (%)	h (cm)	C_{outer}	n	runs	$\langle \epsilon_{\mathrm{cube}} \rangle$ (%)	$\delta_{\langle \epsilon_{\mathrm{cube}} \rangle}$ (%)
1.0	35	1	8.58	0.57	10^6	10	0.5115	1.00
1.0	40	1	8.33	0.57	10^6	10	0.5611	1.30
1.0	30	0.5	8.83	0.57	10^6	10	0.4651	0.69
1.0	0	0	8.58	0.57	10^6	10	0.3852	2.09
0.1	0	0	8.58	0.00	10^6	10	0.2746	1.69
0.1	0	0	8.58	1.00	10^6	10	0.4429	1.26
					Point Source		0.4432	

Table 8.2: Outputs from the collection efficiency model. r = radius of hemispherical emission volume. ϱ_{B} = specular reflectivity of boron. ϱ_{Cu} = diffuse reflectivity of copper black. h = height of photocathode from film centerline. C_{outer} = score value of outer detector hits. n = number of photons per run. $\langle \epsilon \rangle_{\mathrm{cube}}$ = collection efficiency. δ = relative statistical uncertainty in $\langle \epsilon_{\mathrm{cube}} \rangle$ from standard deviation of outputs from all runs. Point source value assumes uniform photocathode radius $a = 11.5$ cm and $h = 8.58$ cm.

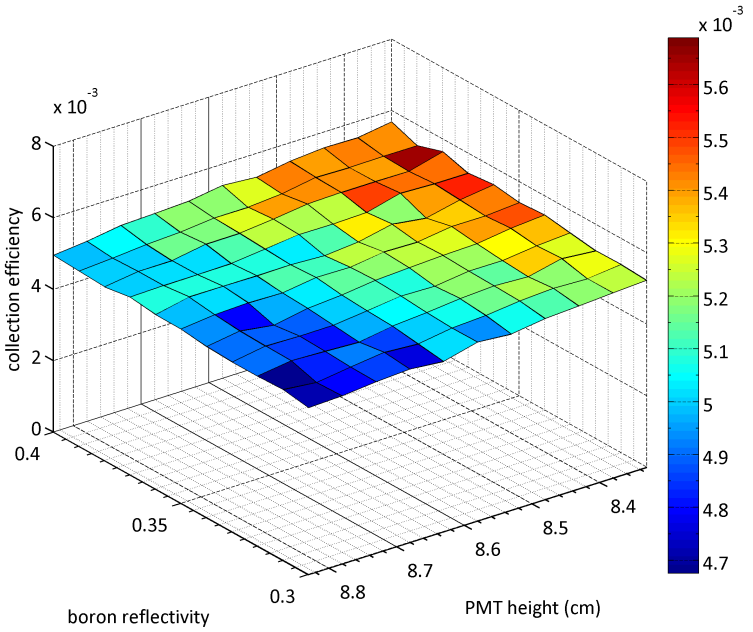

Figure 8.11: Collection efficiency as a function of ϱ_{B} and h.

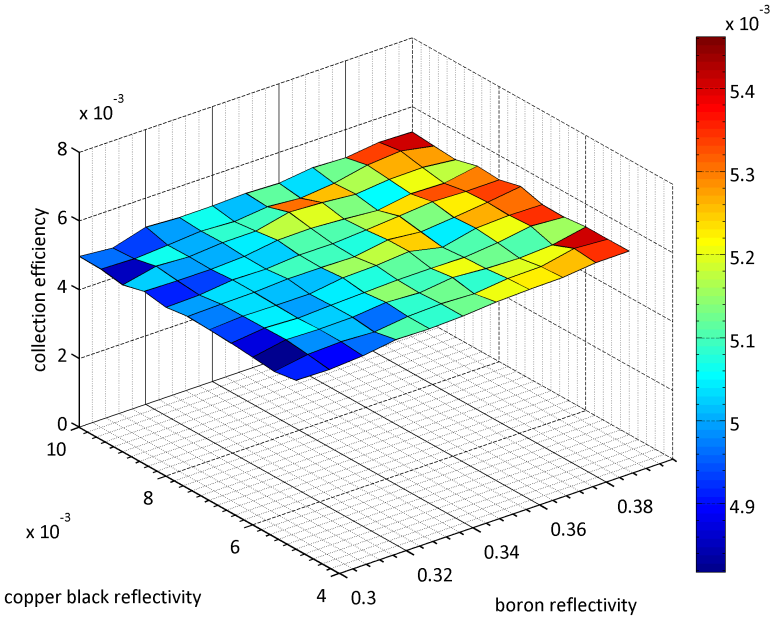

Figure 8.12: Collection efficiency as a function of ϱ_{B} and ϱ_{Cu}.

Chapter 9

Results and Discussion

In this chapter, the results of the excimer scintillation measurements are presented along with the analysis of the data. The characterizations and simulations discussed in Chapters 5 - 8 provide several elements of this analysis, including the areal densities of the boron targets ($(\rho_A)_{10}$), the intrinsic efficiency of the PMT detector package ($\langle\epsilon_{\rm pmt}\rangle$), the neutron absorption rate of the boron targets (N_n), and the collection efficiency of the experimental apparatus ($\langle\epsilon_{\rm cube}\rangle$). Ultimately, the excimer scintillation yield and lifetime are derived from the scintillation data. These quantities are directly relevant to the development of a thermal-neutron detector based on excimer scintillation.

9.1 Excimer Scintillation Yield

Scintillation yield is an essential parameter for optimizing the geometry and collection efficiency of a scintillation detector. It is also necessary to assess the discrimination capabilities of a detection medium. At the MUTR, noble-gas excimer scintillation yield from the $^{10}{\rm B}(n,\alpha)^7{\rm Li}$ reaction was measured as a function of gas type, gas pressure, and ^{10}B target thickness.

The excimer scintillation yield per neutron absorption is given by the equation,

$$Y = \frac{N_{h\nu}}{N_n} \tag{9.1}$$

where $N_{h\nu}$ is the rate at which excimer photons were generated in the scintillation cell, and N_n is the rate at which neutrons were absorbed in the boron targets. Here,

$$N_{h\nu} = \frac{n_{h\nu}}{\langle \epsilon_{\mathrm{pmt}} \rangle \langle \epsilon_{\mathrm{cube}} \rangle \, t_{h\nu}} \tag{9.2}$$

and, from Chapter 7,

$$N_n = \frac{\hat{n}_n(t)}{t_n} \, \kappa \, \frac{(\rho_A)_{10} \, M_{235}}{(\rho_A)_{235} \, M_{10}} \, \mu \, \zeta \, \sqrt{2} \tag{9.3}$$

The rate at which photons were generated in the scintillation cell ($N_{h\nu}$), was determined based on measurements from the photomultiplier tube. The number of excimer photons observed as pulses from the PMT ($n_{h\nu}$), over time $t_{h\nu}$, was calculated with two consecutive, but separate measurements from the PMT and the associated counting electronics. This value is given by the equation,

$$n_{h\nu} = n_{h\nu\,\mathrm{total}} - n_{h\nu\,\mathrm{bkgd}} \tag{9.4}$$

where $n_{h\nu\,\mathrm{total}}$ is the number of pulses counted over time $t_{h\nu}$, and $n_{h\nu\,\mathrm{bkgd}}$ is the number of those pulses which are attributed to gamma-ray backgrounds and dark current. The first value comes from a measurement taken while a mixed neutron and

gamma-ray beam propagated through the scintillation cell. The second value comes from a measurement taken with a lithium-glass beam block in front of the apparatus, which eliminated thermal neutrons from the beam. For comparison, $n_{h\nu\,\mathrm{bkgd}}$ was also measured by placing an epitaxial substrate (2 nm natural boron) in the cell, and irradiating it with a mixed beam. The count time for all scintillation measurements was $t_{h\nu} = 200$ s. Plots of $n_{h\nu}$, and the components $n_{h\nu\,\mathrm{total}}$ and $n_{h\nu\,\mathrm{bkgd}}$, appear in Figures 9.1 - 9.3, for each gas type and film thickness. The results of the substrate irradiations appear in these figures as well. The statistical uncertainties in $n_{h\nu}$ were calculated with Eq. 6.5. The relative statistical uncertainties appear in Figure 9.4.

The three sources which contributed to $n_{h\nu\,\mathrm{bkgd}}$ were (1) dark current, (2) gamma-ray interactions with the PMT and solid components of the scintillation cell, and (3) gamma-ray interactions with the noble gases in the scintillation cell. The first two sources produced a baseline count rate that was independent of gas pressure in the cell. The third source was dependent on noble gas type and pressure. This background signal behavior is apparent in both the data from the substrate irradiations, and the data from irradiations with the lithium beam block in place. The contributions to $n_{h\nu\,\mathrm{total}}$ are described in Figure 9.5.

A multichannel analyzer (MCA) was used to ensure that multi-photoelectron pulses did not significantly contribute to the pulses which were counted by the counter/timer. None of the experimental conditions produced peaks in the pulse-charge distributions (PCDs) outside of the single-photoelectron peak. Typical PMT PCDs appear

in Figure 9.6. The gaussian peak in each of these distributions represents the single-photoelectron peak.

The remaining factors in Eq. 9.2 are the intrinsic efficiency of the PMT detector package ($\langle\epsilon_{\rm pmt}\rangle$), and the collection efficiency of the apparatus ($\langle\epsilon_{\rm cube}\rangle$). Together, they define the fraction of all excimer photons generated within the apparatus which were counted by the PMT electronics. The derivations of these factors are described in Chapters 6 and 8, respectively. The derivation of N_n by Eq. 9.3 is described in Chapter 7.

Based on Eq. 9.2 and 9.3, Y was determined as a function of gas type, gas pressure, and target thickness. Plots of Y appear in Figures 9.7 - 9.9. The results demonstrate yields of 5200 - 6000 photons/neutron from argon, 7500 - 11,000 photons/neutron from krypton, and 9600 - 14,200 photons/neutron from xenon, at pressures of 800 torr. The yields decrease as the target thicknesses increase because they have been normalized per neutron absorption. As shown by the TRIM simulations, charged particles from the $^{10}{\rm B}(n,\alpha)^7{\rm Li}$ reaction lose less energy in thinner films. Thus, while thicker films absorb a larger fraction of the neutron beam, the resulting scintillation yields per neutron capture are lower due to this energy loss. Additionally, the scintillation yields plateau around 600 torr of argon, 400 torr of krypton, and 300 torr of xenon. At these pressures, the charged particles deposit nearly all of their energy within the line of sight of the PMT. This behavior agrees with the TRIM simulations of ionization density (see Fig. 8.4 - 8.6).

The total uncertainty in Y may be calculated by propagating the uncertainties of each of its factors, with the equation,

$$\delta_Y = \sqrt{\sum_{i=1}^{N} (\delta_i)^2} \tag{9.5}$$

where δ_Y is the total relative uncertainty in Y, and δ_i is the relative uncertainty in each factor of Y. A description of each factor of Y and its associated uncertainty appears in Table 9.1. The total relative uncertainty in Y, as determined by Eq. 9.5, falls between 14.7 - 15.5% depending on the experimental conditions. This uncertainty is reflected by the error bars in Figures 9.7 - 9.9.

	Factor	Description	Value(s)	δ (%)	Source
$N_{h\nu}$	$n_{h\nu}$	excimer photon counts	1000 - 80,000 (O)	0.5 - 5 (O)	scintillation measurements
	$\langle\epsilon_{\mathrm{pmt}}\rangle$	PMT intrinsic efficiency	1.6 - 3.1 (%) (O)	3.49	PMT calibration and excimer spectra
	$\langle\epsilon_{\mathrm{cube}}\rangle$	apparatus collection efficiency	0.5115 (%)	9.69	photon emission and reflection simulations
	$t_{h\nu}$	photon count time	200 (s)	–	
N_n	$\hat{n}_n(t)$	fitted neutron counts	2730 - 3150	1.6 - 4.4 (O)	fission-chamber measurements
	κ	^{10}B/^{235}U thermal cross section ratio	6.567	2.61	analysis of cross sections from [77]
	$(\rho_A)_{10}$	areal density of ^{10}B targets	73.5 - 260.0 (μg/cm^2) (O)	10	neutron imaging
	$(\rho_A)_{235}$	areal density of ^{235}U deposit	458.073 (μg/cm^2)	0.5	measurement by David Gilliam
	M_{10}	molar mass of ^{10}B	10.0129 (g/mol)	–	[76]
	M_{235}	molar mass of ^{235}U	235.0439 (g/mol)	–	[76]
	μ	transmission fraction	0.995	–	transmission calculation
	ζ	self-absorption factor	1.03756	–	calculation by Jeffrey Nico
	t_n	neutron count time	1200 (s)	–	

Table 9.1: Values and relative uncertainties of the various inputs to Eq. 9.1. (O) stands for "on the order of", due to multiple values of the same parameter.

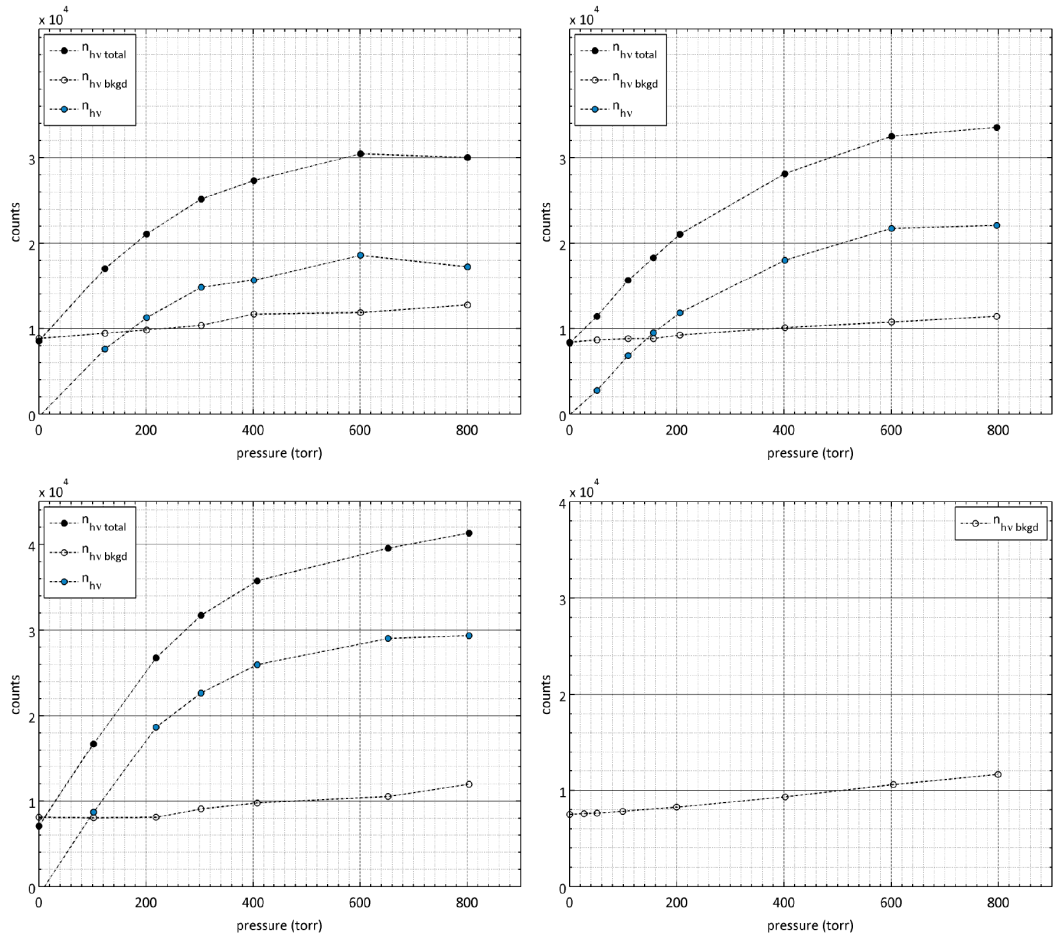

Figure 9.1: Counts from scintillation of argon during irradiation of a 600-nm (top left), 900-nm (top right), and 1200-nm (bottom right) ^{10}B targets, and an epitaxial substrate (bottom left). Count time $t_{h\nu} = 200$ s.

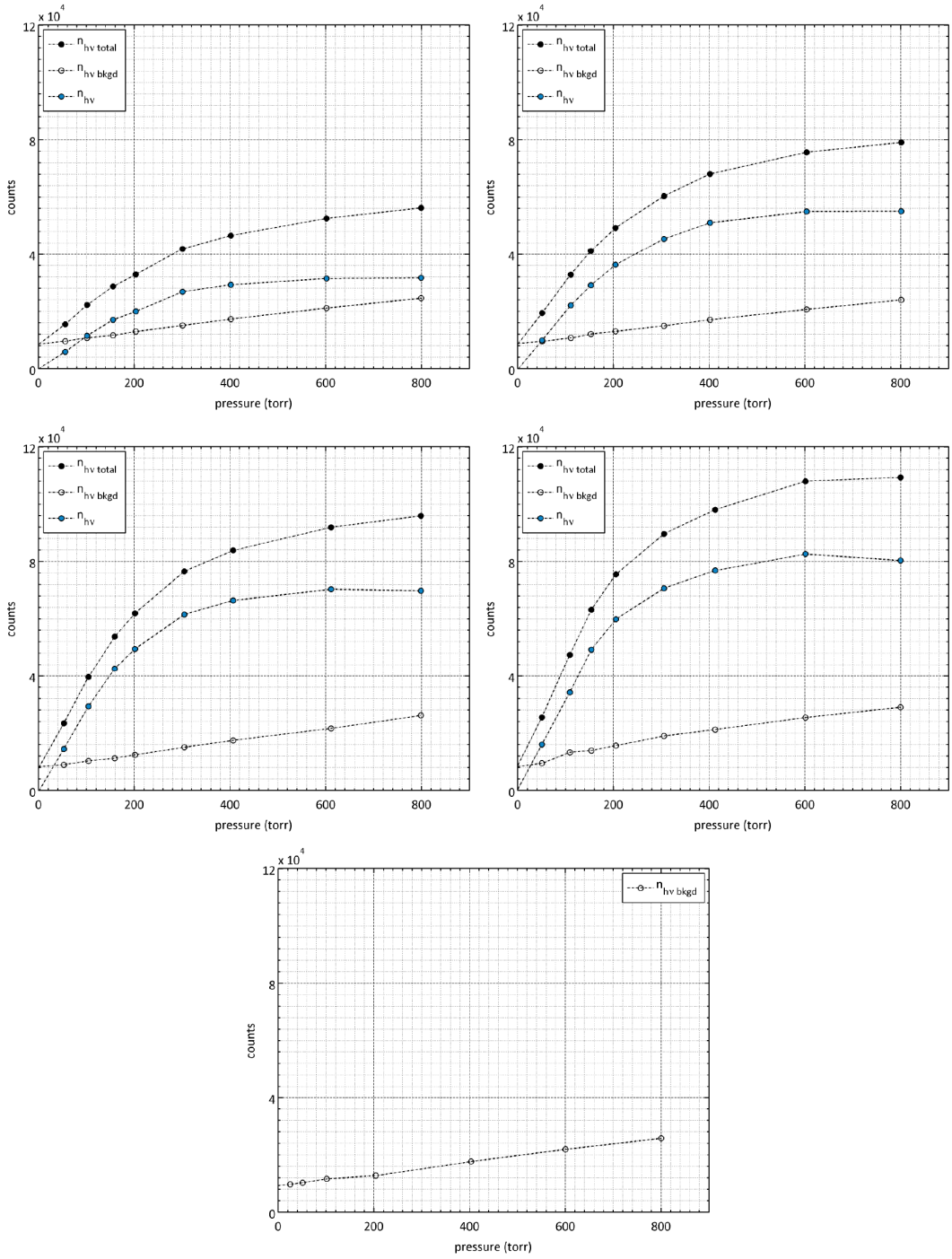

Figure 9.2: Counts from scintillation of krypton during irradiation of a 300-nm (top left), 600-nm (top right), 900-nm (middle left), and 1200-nm (middle right) ^{10}B targets, and an epitaxial substrate (bottom). Count time $t_{h\nu} = 200$ s.

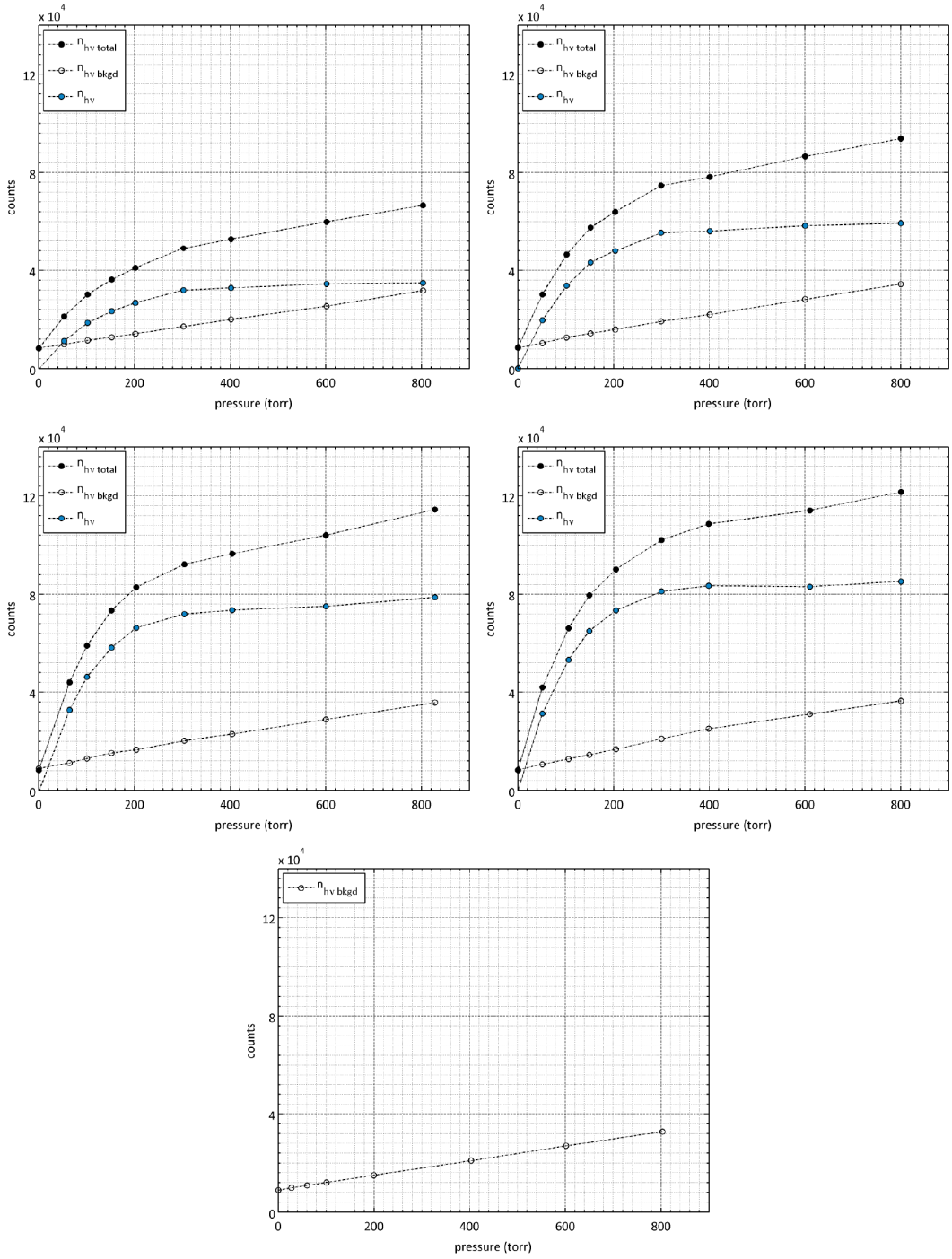

Figure 9.3: Counts from scintillation of xenon during irradiation of a 300-nm (top left), 600-nm (top right), 900-nm (middle left), and 1200-nm (middle right) ^{10}B targets, and an epitaxial substrate (bottom). Count time $t_{h\nu} = 200$ s.

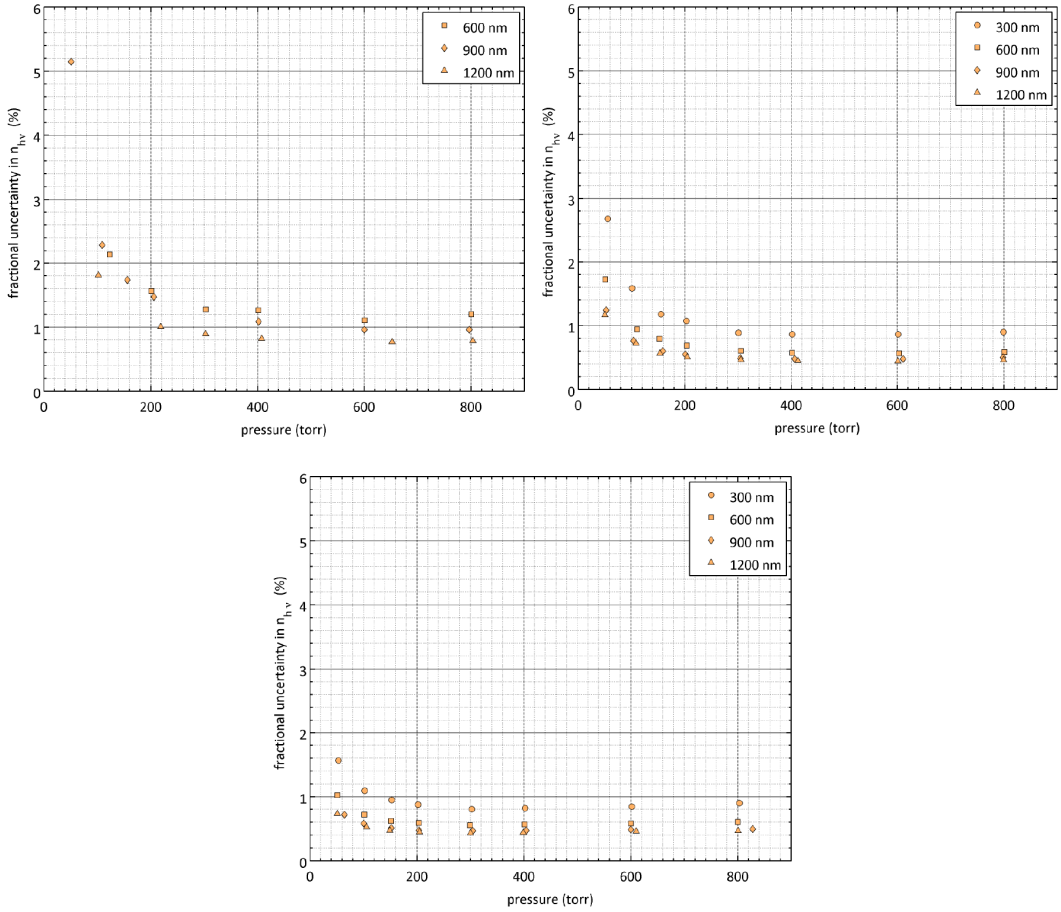

Figure 9.4: Relative uncertainties in $n_{h\nu}$ for argon (top left), krypton (top right), and xenon (bottom) data.

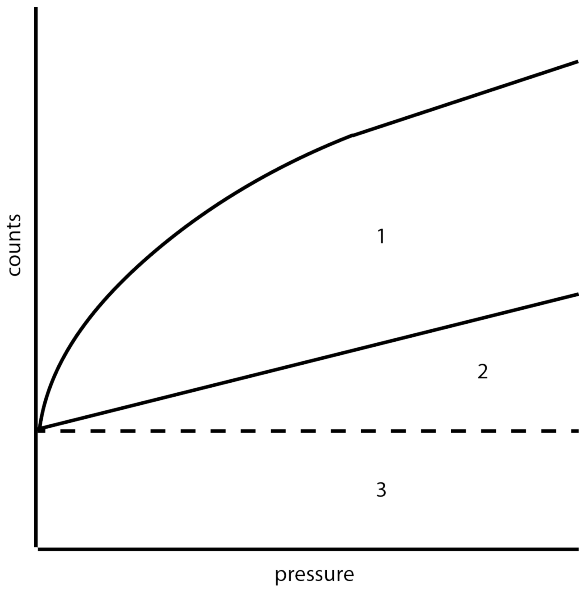

Figure 9.5: Contributions to $n_{h\nu\,\mathrm{total}}$ from (1) excimer scintillation signal, (2) pressure-dependent gamma-ray backgrounds, and (3) dark current and pressure-independent gamma-ray backgrounds.

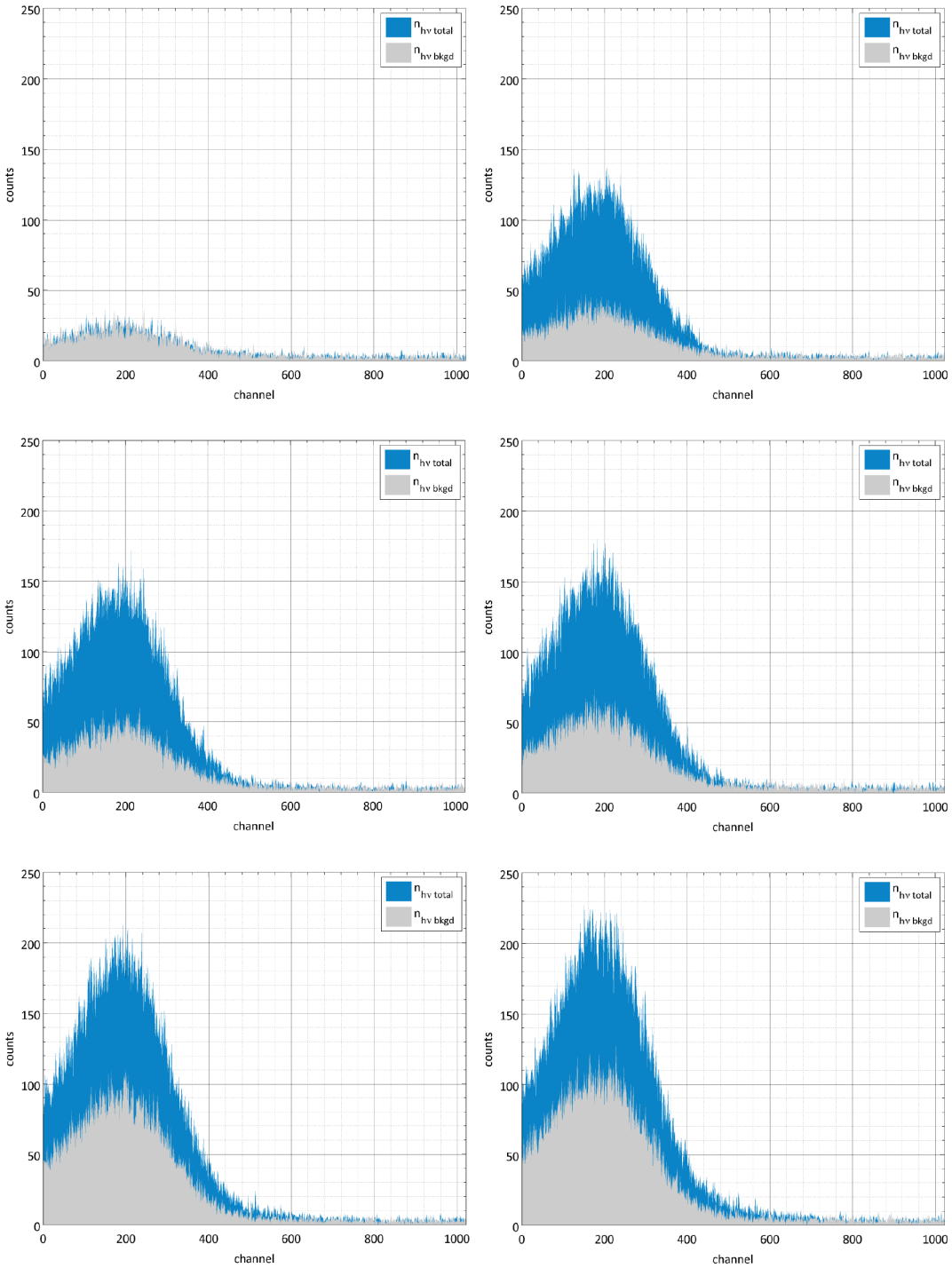

Figure 9.6: Pulse-charge distributions from excimer scintillation of xenon, showing only a single-photoelectron peak. 0 (top left), 100 (top right), 200 (middle left), 300 (middle right), 600 (bottom left), and 800 (bottom right) torr during irradiation of a 1200-nm ^{10}B film. Distributions are shown from measurements with ($n_{h\nu\,\mathrm{total}}$) and without ($n_{h\nu\,\mathrm{bkgd}}$) the lithium glass beam block.

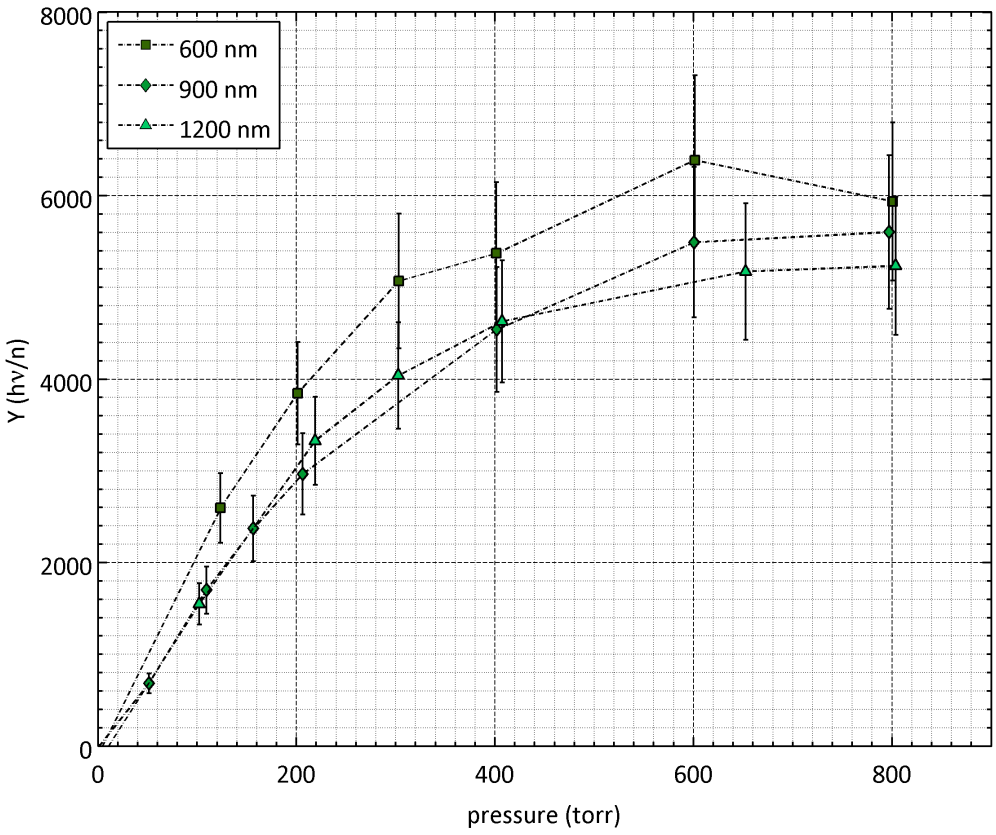

Figure 9.7: Scintillation yield from $^{10}\mathrm{B}(n,\alpha)^{7}\mathrm{Li}$ in argon. Data series correspond to $^{10}\mathrm{B}$ target thicknesses.

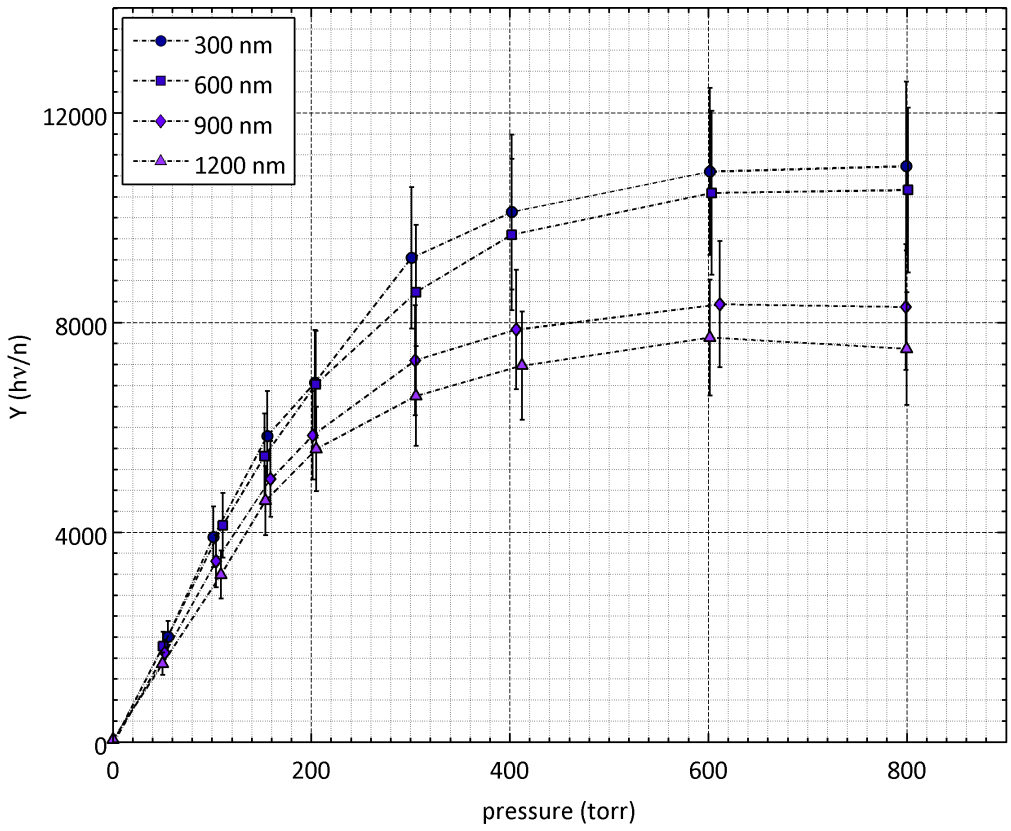

Figure 9.8: Scintillation yield from $^{10}\mathrm{B}(n,\alpha)^{7}\mathrm{Li}$ in krytpon. Data series correspond to $^{10}\mathrm{B}$ target thicknesses.

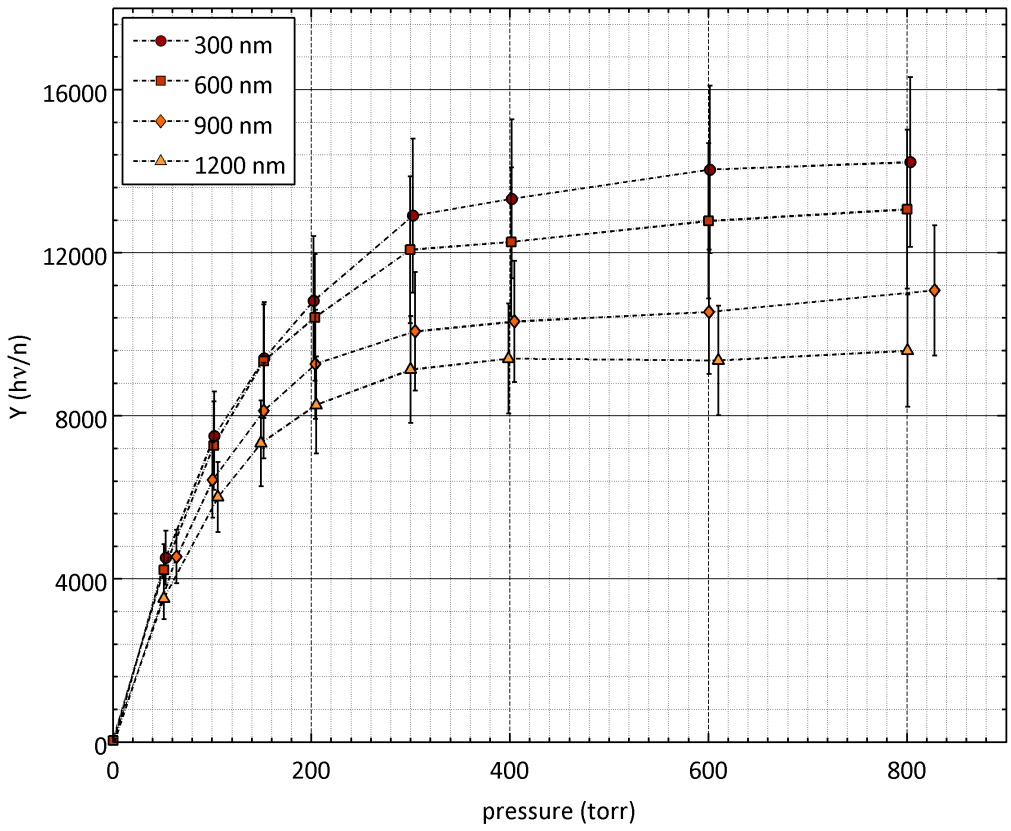

Figure 9.9: Scintillation yield from $^{10}\mathrm{B}(n,\alpha)^{7}\mathrm{Li}$ in xenon. Data series correspond to $^{10}\mathrm{B}$ target thicknesses.

Determining the amount of energy required to produce an excimer photon ($W_{h\nu}$) is necessary to evaluate the energy conversion efficiency of the excimer signal. Additionally, $W_{h\nu}$ may be used to derive the energy resolution of an excimer-based detector. Based on Y, $W_{h\nu}$ values were calculated using the average escape energies from Table 8.1 and the equation,

$$W_{h\nu} = \frac{E_{\text{esc}}}{Y} \tag{9.6}$$

where E_{esc} is the average kinetic energy of the charged particles upon escaping the boron target. The results appear in Figure 9.10. Average values of $W_{h\nu}$ appear in Table 9.2. Equation 9.6 assumes that E_{esc} is fully deposited in the gas. This assumption is valid only at pressures in the plateau region, as described in the previous section. At lower pressures, charged particles may lose energy through collisions with the walls of the copper black cylinder, and, therefore, the scintillation signal is diminished. This "wall effect" is well known in proportional-tube neutron detectors [1].

By dividing the energies of the excimer photons (9.57, 8.42, and 7.42 eV, for Ar, Kr, and Xe) by the $W_{h\nu}$ value, the conversion efficiency of the excimer emission signal may be obtained. For the $W_{h\nu}$ values at 800 torr, these efficiencies are 7.7, 10.4, and 11.8% for Ar, Kr, and Xe, respectively.

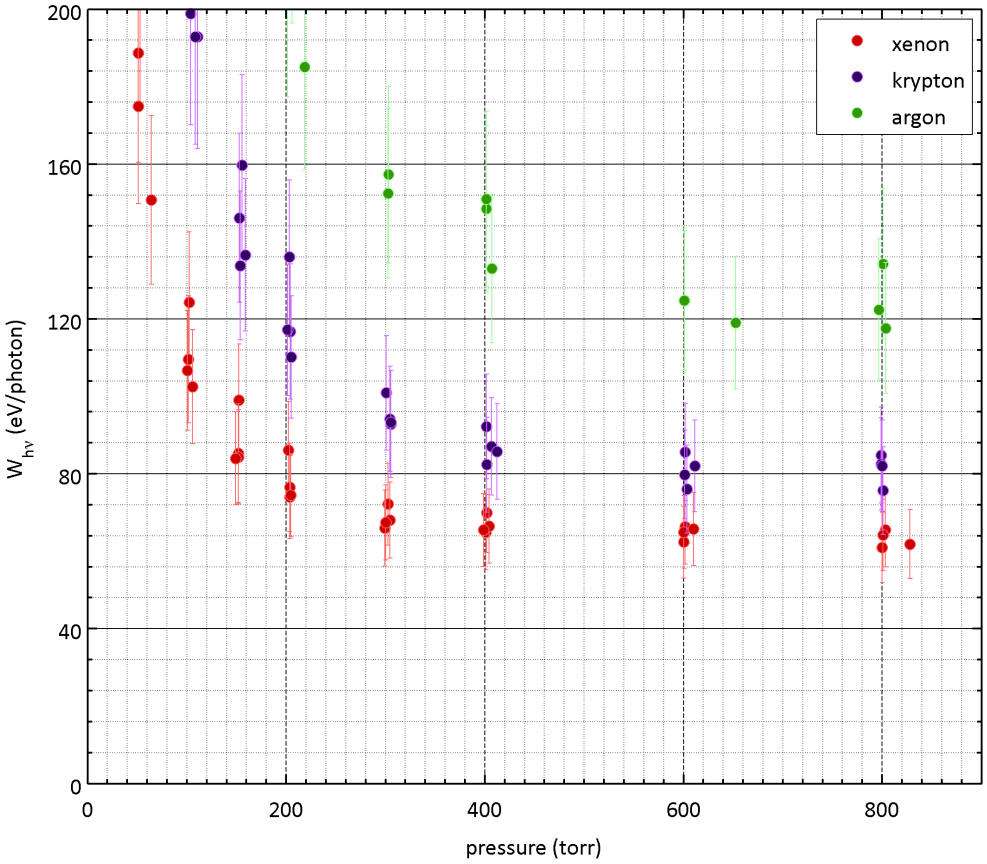

Figure 9.10: $W_{h\nu}$ values as a function of noble-gas type and pressure. Data from all thin-film targets are included.

	$W_{h\nu}$ (eV/photon)		
Pressure (torr)	Argon	Krypon	Xenon
200	227.2	120.0	77.8
400	144.1	86.9	66.7
600	122.9	80.9	64.9
800	124.8	81.3	63.1

Table 9.2: Average values of $W_{h\nu}$ from the $^{10}\mathrm{B}(n,\alpha)^{7}\mathrm{Li}$ reaction. Determined from scintillation measurements and TRIM simulations.

9.2 Excimer Lifetime

Measurements of the excimer scintillation decay time following the $^{10}B(n,\alpha)^{7}Li$ reaction are necessary to determine the pulse-shape discrimination capability and the optimum signal integration width of an excimer-based neutron detector. These measurements were collected with a time-to-amplitude converter (TAC), which provided distributions of the times-between-pulses during excimer scintillation for a range of gas pressures (100 - 800 torr) and gas types (Ar, Kr and Xe). The distributions were analyzed to derive the triplet-state (slow) decay time of each gas.

In this particular configuration, the delay on the "start" line (38 ns) was long with respect to typical fast excimer decay times (4 ns). Therefore, the fast decay was assumed to be unresolved in these distributions. This assumption is justified by the absence of multi-photoelectron pulses in the yield measurement PCDs. Coincidentally, typical fast excimer decay times are very close to the PMT pulse width (3-4 ns). If multiple pulses originating from singlet-state excimer decays of a single scintillation event, were frequently observed, they would inevitably form a multi-photoelectron peak in the PCDs. Since such a peak was not observed, it was assumed that the TAC rarely observed multiple pulses from singlet-decays of the same event. Furthermore, because neutron capture events in the experiment were significantly separated in time (< 340 Hz) with respect to excimer decay times (fast and slow), it was assumed that the times-between-pulses from separate scintillation events far exceeded the TAC range and, therefore, did not create TAC pulses.

Each decay time calculation required two TAC measurements, one with a mixed beam propagating through the cell (total distribution), and one with the lithium beam block in front of the cell (background distribution). The counts in each channel of the background distributions were subtracted from the counts in each channel of the corresponding total distributions. The range settings of the TAC were mapped to the channel numbers of the MCA to translate the abscissa values into times-between-pulses. The delay time of the delay line (38 ns) was then added to these values. Typical distributions from the TAC appear in Figures 9.11 - 9.13. Note that some of the distributions in these figures were collected at different full range settings on the TAC (500 ns - 20 μs), leading to variation in the data point spacing and peak amplitude of each distribution. The changes in the order of the distribution amplitudes in Figures 9.11 - 9.13, with respect to change with respect to gas pressure, may be explained by these range settings.

Following time calibration, the TAC data were fit to an exponential distribution of the form,

$$\hat{y}(t) = Ae^{(-\Lambda t)} \tag{9.7}$$

where $\hat{y}(t)$ is the value of the fit as a function of the time-between-pulses t, A is an arbitrary multiplier based on the amplitude of the distribution, and Λ is the decay constant of the distribution. Examples of these fits appear in Figures 9.11 - 9.13. The time constants obtained from this fitting were then related to the excimer lifetime, with the equation,

$$\tau = \frac{1}{\Lambda} \tag{9.8}$$

Values of the excimer triplet-state lifetime (τ), as a function of gas pressure, appear in Figure 9.14. The uncertainties in these values were determined using the 95% confidence bounds in the fit parameter Λ, as determined by the MATLAB fit function. The relative uncertainties in τ are plotted in Figure 9.15.

The decrease in τ at higher pressures is the result of an increased frequency of collision-induced triplet-singlet transitions [79]. The values of τ calculated from these scintillation data distinctly agree with many of the tabulated values in [84] (see Fig. 2.12), particularly around 400 torr.

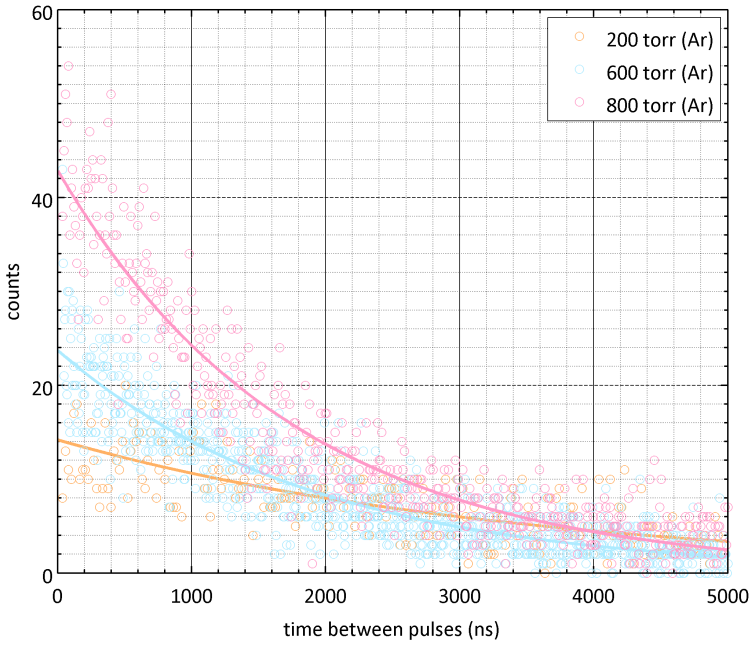

Figure 9.11: Distributions of the times between pulses, and exponential fits of those distributions. Data collected during irradiation of a 1200 nm ^{10}B target in argon. Count time $t = 300$ s.

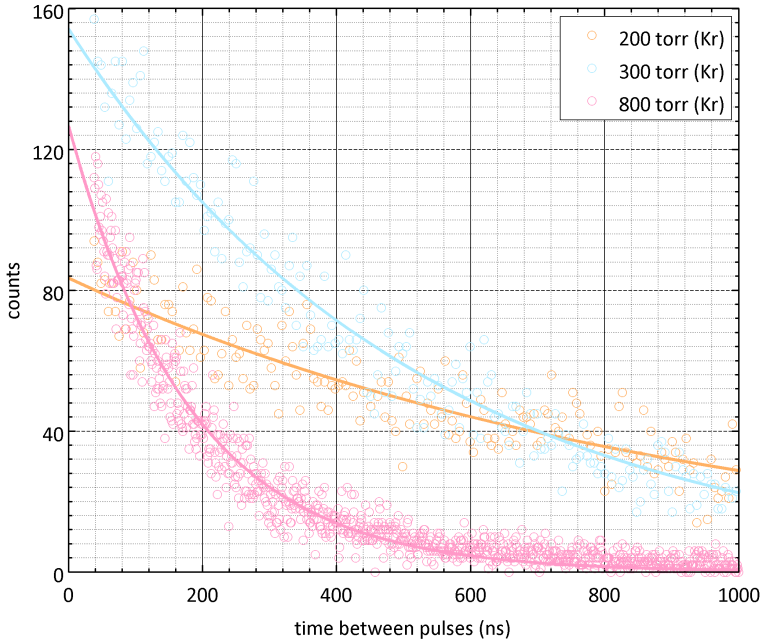

Figure 9.12: Distributions of the times between pulses, and exponential fits of those distributions. Data collected during irradiation of a 1200 nm ^{10}B target in krypton. Count time $t = 300$ s.

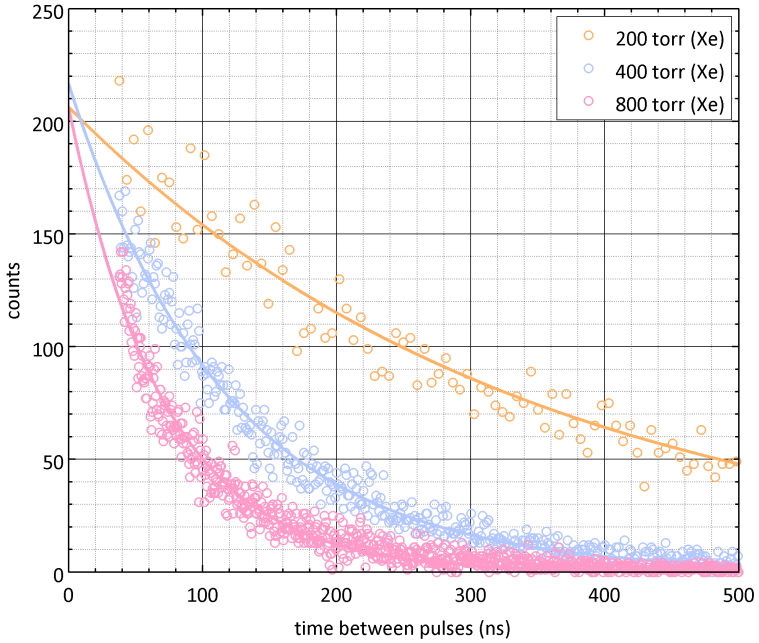

Figure 9.13: Distributions of the times between pulses, and exponential fits of those distributions. Data collected during irradiation of a 1200 nm ^{10}B target in xenon. Count time $t = 300$ s.

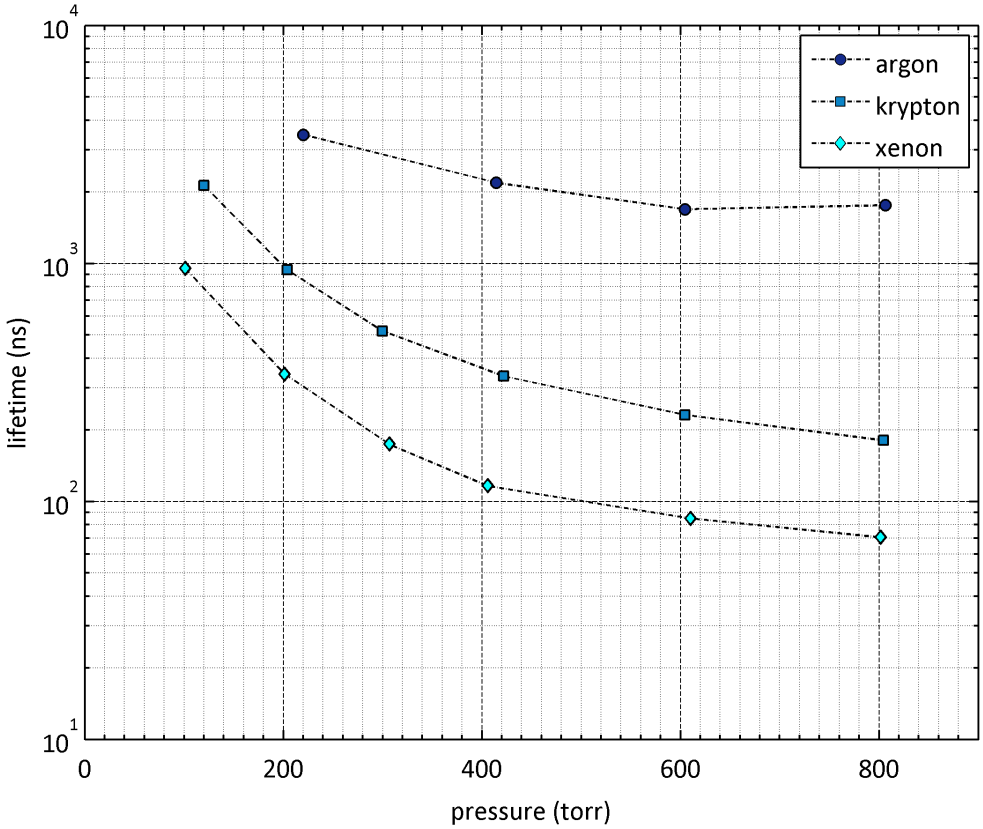

Figure 9.14: Triplet-state lifetimes of Ar, Kr and Xe excimers, as a function of gas pressure, resulting from irradiation of a 1200 nm ^{10}B target.

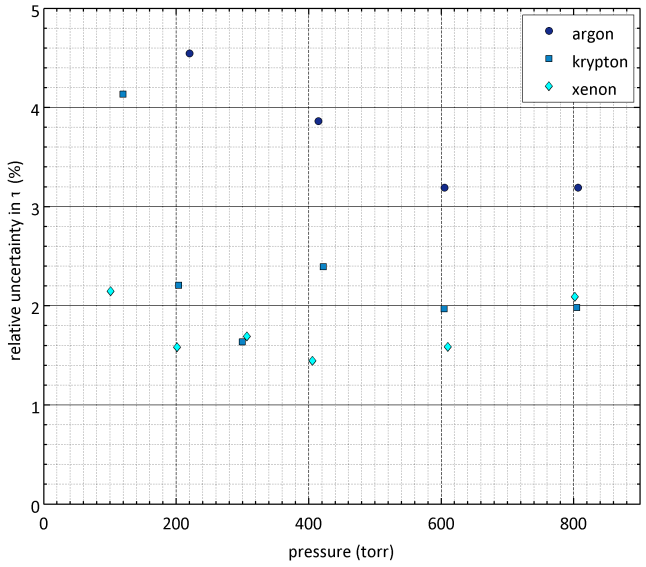

Figure 9.15: Relative uncertainties in τ.

9.3 Conclusions

From the scintillation measurements and their interpretation based on absolute calibrations, it is possible to draw a number of conclusions regarding the behavior of noble-gas excimer scintillation. Most prominently, exothermic neutron capture generates a large excimer scintillation signal due to the large Q-value of the $^{10}\mathrm{B}(n,\alpha)^{7}\mathrm{Li}$ reaction, the ability of charged-particle reaction products to transfer that energy by electronically exciting noble-gas atoms, and the small amount of energy required to form an excimer molecule. The yields of the heavier gases are greater due to the lower excitation energies of these gas species [54]. The yields increase with pressure as a result of (1) an increased frequency of excimer-forming collisions, and (2) a higher density of ionization within the line of sight of the photon detector package.

The excimer yields plateau at pressures at which nearly all of the charged-particle energy escaping the targets is deposited in view of the detector. This is confirmed by the TRIM simulations of ionization density. Additionally, the yields decrease with increasing target thickness due to the larger average energy loss of charged particles escaping thicker films. The starting pressures of the signal plateau regions are dependent on the geometry of this specific experiment – the radius of the photocathode, and the distance of the chamber walls from the location of charged-particle emission. However, the yields in the plateau region are dependent only on the properties of the neutron absorbing targets (though not on the remaining detector geometry).

Despite this specificity, the yields quantitatively describe relationships between parameters of a basic configuration, and these relationships provide a foundation for optimizing a practical detector.

Excimer triplet-state lifetimes decrease with increasing gas pressure as a result of an increased frequency of decay-inducing collisions between excimer molecules and surrounding noble-gas atoms (collisional broadening) [79]. Furthermore, while charged particles from neutron capture produced large populations of triplet-state excimers, gamma-ray radiation did not produce such phosphorescence, and only exhibited fast decays characteristic of singlet-state excimers. This is attributed to the high-LET of charged particles and the low-LET of gamma-rays. This scintillation behavior is well known in other scintillator types [59]. The cross sections of electronic excitation are vastly different for heavy ions and electrons produced by gamma-ray interactions [147]. The distinct scintillation decay behavior from the two radiation types will enable gamma-ray rejection based on pulse-shape discrimination [58].

The observed excimer scintillation signals from the $^{10}\mathrm{B}(n,\alpha)^{7}\mathrm{Li}$ reaction are comparable to the yields of many liquid and solid neutron scintillators [64]. These yields demonstrate that excimer scintillation is a practical means of neutron detection. The observed slow triplet-state decay of $^{10}\mathrm{B}(n,\alpha)^{7}\mathrm{Li}$-induced excimers agrees well with literature values [88]. This behavior can be used in a practical detector to discriminate neutron interactions from gamma-ray interactions. Furthermore, the low densities of noble-gases translate to inherently lower gamma sensitivites than solid scintillators. Other advantages of a practical excimer-based neutron detector

include: immunity to radiation damage, simplified requirements (no need for high voltage, high-pressure gases), flexible geometry (form-fitting scintillation media, interchangeable neutron absorbers), and availability (helium-3 free).

Several characterizations and absolute calibrations have enabled the interpretation of the scintillation measurements in terms of absolute excimer photon yield and excimer scintillation lifetime. The results provide a fundamental understanding of the properties of noble-gas scintillation from the $^{10}\mathrm{B}(n,\alpha)^{7}\mathrm{Li}$ reaction. These results will contribute to the development and optimization of a deployable neutron detector based on noble-gas excimer scintillation. Furthermore, the characterization and simulation methods described by this research provide a framework upon which to develop and characterize a practical detector. Additionally, this research has produced a characterized thermal-neutron-beam facility at the MUTR, which may be used for future detector development.

9.4 Future Work

This research lays the foundation for a number of projects related to the development of an excimer-based neutron detector. These projects involve the optimization of detector efficiency and implementation of background discrimination techniques.

The photon collection efficiency of a practical excimer-based neutron detector can be vastly improved. Wavelength shifters, FUV reflectors, modified geometry, and increased photodetector efficiency are all means of achieving this improvement. The absolute yield measurements from this thesis provide a method to derive the total collection efficiency of a complex apparatus, and to assess changes in that efficiency as a result of changes to the detector design. Additionally, implementing a spatially-sensitive photon detector (ie. CCD) may improve the understanding of the photon source geometry. A large photon collection efficiency will enhance the overall efficiency of the detector, and may enable the differentiation of neutron captures from background events.

The neutron collection efficiency of an excimer-based neutron detector can be improved by investigating new absorber types and geometries. For example, by layering multiple films in an array, thermal-neutron absorption may be increased to nearly 100%. Optimization of this configuration will require a balance between neutron absorption (number of films and film thickness) and light collection (film escape energy and film spacing). The measurements in this thesis describe scintillation yields from various films which have been carefully characterized. These measurements

may be used to implement an array of boron films to increase neutron absorption. Additionally, boron films may be replaced with more exotic targets, such as a honeycomb or a porous foam of neutron absorbing material. These types of absorbers may provide even further leverage for optimizing neutron absorption and light collection. The techniques used for ionization density modeling in Chapter 8 prescribe a means to estimate the size and distribution of the photon emission source from such a neutron absorber.

Discriminating gamma-ray events and dark counts from neutron events is essential for a practical neutron detector. While these signals were measured and subtracted from the scintillation data in this research, they were not identified on an individual basis. As a means of discrimination, a future excimer-based neutron detector may implement an MCA integration time based on the scintillation lifetime measurements in this thesis, and pulse-shape discrimination techniques. Similarly, the lifetime measurements will be useful for developing digital pulse processing algorithms to discriminate backgrounds in a more sophisticated arrangement.

Appendix A

Scintillation from ^{241}Am α-particle Emission

Prior to the excimer scintillation experiment, an α-particle check source was used to demonstrate the scintillation of noble gases due to bombardment by heavy charged-particles. These measurements qualitatively verified the operation of the scintillation cell by generating and detecting FUV photons. They required no use of the thermal-column neutron beam or the MUTR.

The scintillation from ^{241}Am α-particles was measured in a configuration nearly identical to the apparatus described in Chapter 4. An ^{241}Am α-particle source was placed at the bottom of the scintillation cell, with its active surface facing the PMT/MgF_2 detector package. The cell was then sealed, evacuated, and filled with noble gases (Ar, Kr, and Xe) at pressures between 25-800 torr. The FUV cylinder and the boron target were removed from the cell during these measurements.

Americium-241 decays by the reaction,

$$^{241}\mathrm{Am} \rightarrow {}^{237}\mathrm{Np} + \alpha + 5.49 \text{ MeV} \tag{A.1}$$

with a half-life of 432.6 years [32]. This reaction has the potential to generate noble-gas excimers through the same type of energy transfer as the $^{10}\mathrm{B}(n,\alpha)^{7}\mathrm{Li}$ reaction.

The activity of the source used in these measurements was 9.5×10^4 min^{-1} 2π sr^{-1}. The yield electronics were used to count scintillation pulses from these emissions. The resulting PMT signal appears in Figure A.1.

Both the frequency of α-particle emission (1600 Hz) and the energy of each emission (5.49 MeV) were larger during these measurements than during the thermal-neutron irradiations (90 - 330 Hz, and 0.62 - 0.93 MeV). Correspondingly, the signals from all three gases in Figure A.1 are significantly larger than the signals in Figures 9.1 - 9.3. The measurements have not been compared in terms of absolute yield, due to the different collection efficiencies of the two configurations. Without the copper-black FUV-absorbing cylinder, simulating reflections within the cell becomes considerably more complex.

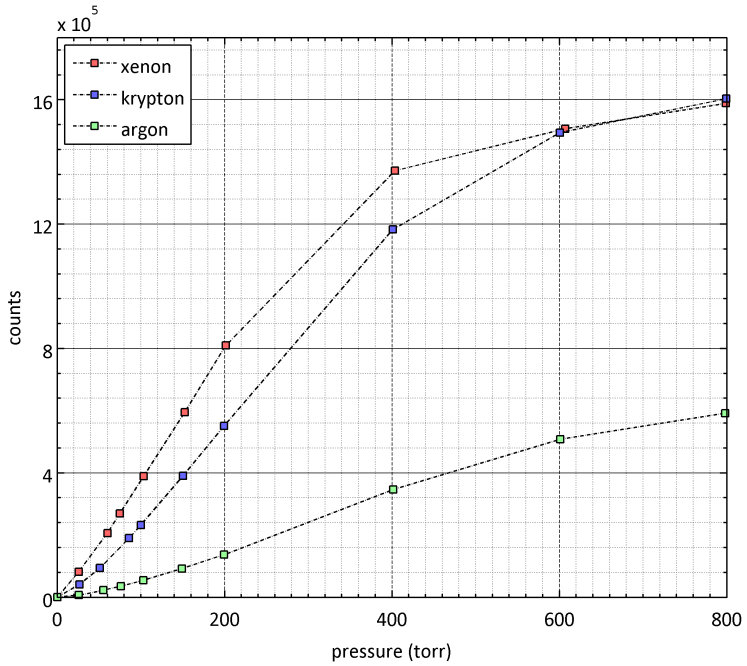

Figure A.1: Noble-gas scintillation signal from ^{241}Am α-particle emitter. Y-axis represents counts from the PMT. Count time $t_{h\nu} = 200$ s.

Appendix B

Construction of an FUV Reflectometer

When modeling the collection efficiency of the scintillation cell (see Chapter 8.2), reflectivity values for the boron and copper black surfaces were taken from [144] and [145], respectively. To verify these reflectivity values, an FUV reflectometer was constructed at SURF. This reflectometer was designed for use at BL-4, described in Chapter 6.1. A diagram of the apparatus appears in Figure B.1. Photographs of the reflectometer appear in Figures B.2 - B.4.

The reflectometer consists of a stainless steel cube (150 mm) with metal-seal flange ports on all sides. Inside the cube, a sample holder and a detector arm rotate independently about a common axis, perpendicular to the incident photon beam. The sample holder is designed to fit a $2.5 \times 2.5 \times 0.05$ cm sample. The sample is held in place on two sides by flexible mounting clips. Two photodiode detectors, of the same type used in the PMT calibration (IRD AXUV-100G), are secured to opposite ends of the detector arm. The detectors are mounted on breadboards perpendicular to the length of the arm, facing in the direction of the incident photon beam. The detector closest to the SURF storage ring measures the intensity of the incident photon beam. The second detector measures the intensity of the reflected photon beam. A collimator is placed around the reflected detector to prevent the interference from

diffuse photon reflections within the chamber. An electrical feedthrough on one side of the chamber connects these detectors to the BL-4 ammeters.

Two rotating feedthroughs on opposite sides of the chamber allow the sample holder and the detector arm to be rotated independently. The feedthroughs enable measurement of the sample reflectivity as a function of incident and reflected angle. Additionally, the BL-4 monochromator allows these reflectivities to be measured at a range of wavelengths in the FUV region. A lubricant-free ceramic bearing was inset at the junction of the sample holder and the detector-arm shaft to facilitate smooth rotation of these components. Additionally, the flanges connecting the feedthroughs to the chamber were sealed with Viton gaskets, to ensure flush alignment of the concentric shafts. The reflectometer is connected to the BL-4 detector box with several vacuum adapters and an x-y translation feedthrough. A 4-mm slit in the sample holder provides a means of aligning the rotation axis with the photon beam, using the reflected photodiode and the x-y translation feedthrough. A vacuum-safe window on the top flange of the chamber will assist in this alignment.

The reflectometer is currently awaiting beam time at SURF. It will be used to measure the FUV reflectivities of the boron-10 thin films, copper black coating (Ebonol-C), and any future components of an excimer-based neutron detector.

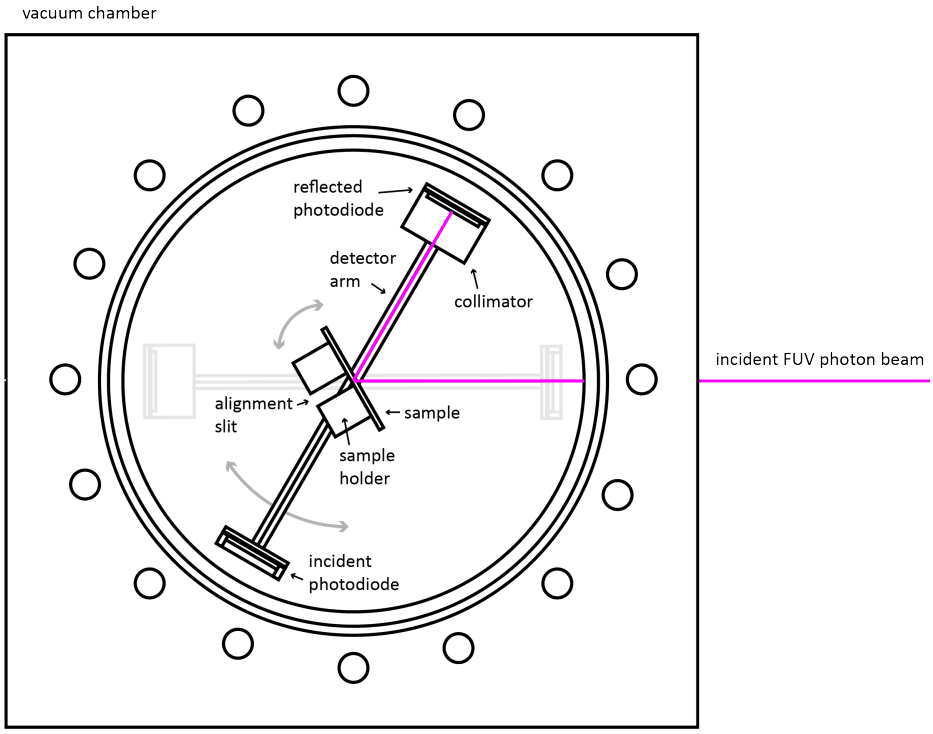

Figure B.1: Diagram of the FUV reflectometer. Faded detector arm represents the incident measurement/alignment position. Not to scale.

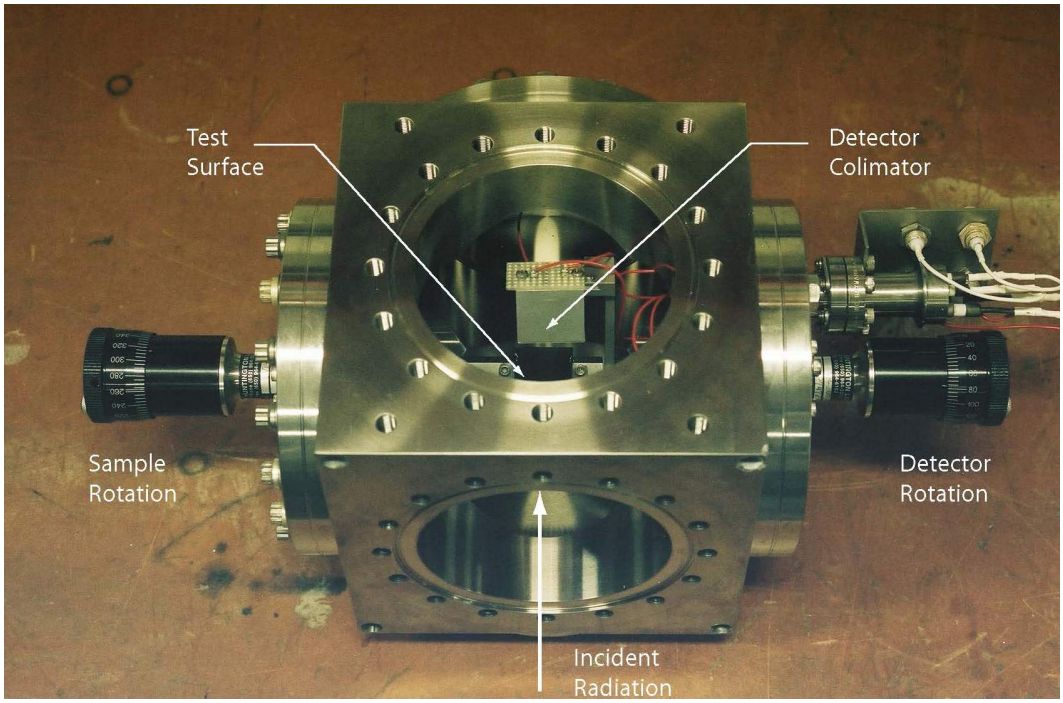

Figure B.2: The FUV reflectometer.

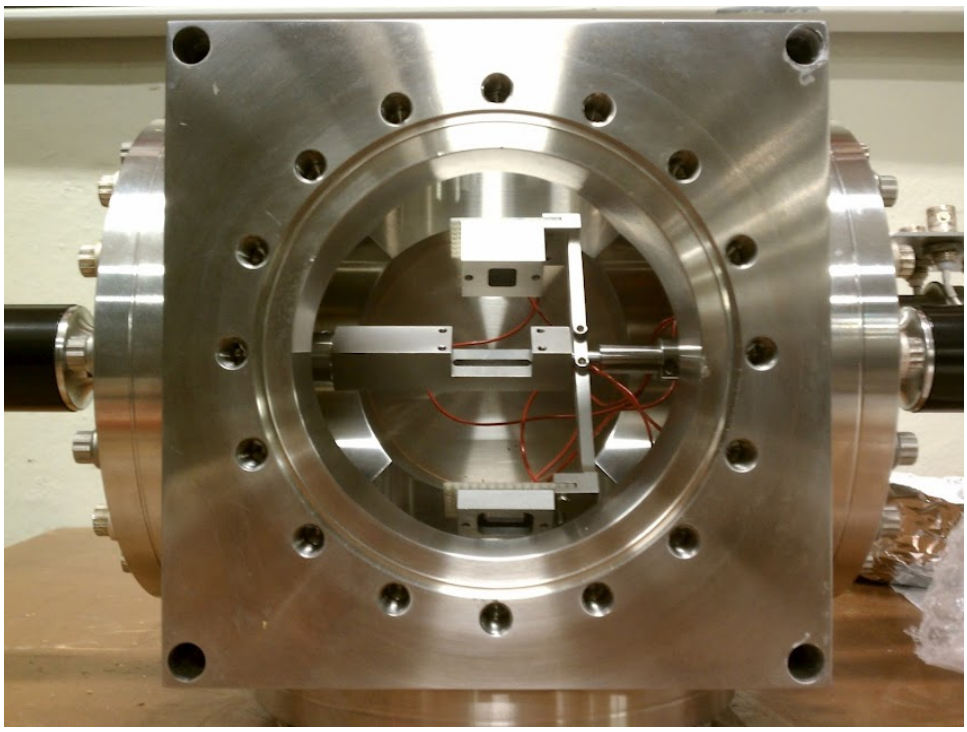

Figure B.3: Head-on view of the FUV reflectometer. The sample holder is empty, exposing the alignment slit.

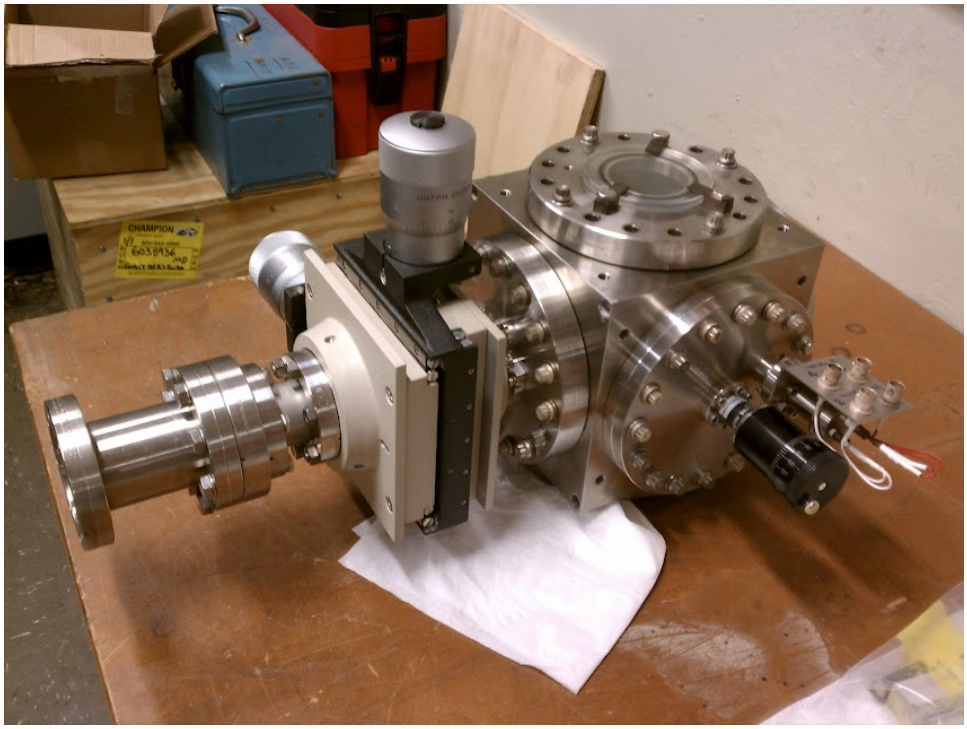

Figure B.4: The reflectometer prepared for installation behind the BL-4 detector box. The x-y translation feedthrough required for alignment is shown.

Bibliography

[1] G. F. Knoll, *Radiation Detection and Measurement*. John Wiley and Sons, 1979.

[2] J. R. Lamarsh and A. J. Baratta, *Introduction to Nuclear Engineering*. Prentice Hall, 3rd ed., 2001.

[3] T. Jaques, H. Ballinger, and F. Wade, "Neutron detectors for reactor instrumentation," *P IEEE*, vol. 100, pp. 110–116, May 1953.

[4] General Electric, "Nuclear reactor instrumentation." http://www.ge-mcs.com/en/nuclear-reactor-instrumentation/neutron-monitoring-instrumentation.html.

[5] R. Hartke, D. Symes, F. Buersgens, L. Ruggles, J. Porter, and T. Ditmire, "Fusion neutron detector calibration using a table-top laser generated plasma neutron source," *Nucl. Instrum. Meth. A*, vol. 540, pp. 464–469, 2005.

[6] S. K. Lee, B.-H. Kang, G.-D. Kim, and Y.-K. Kim, "Fast neutron detector for fusion reactor KSTAR using stilbene scintillator," *arXiv*, December 2011.

[7] T. Elevant, B. Wolle, and A. Weller, "Proposed neutron diagnostics for Wendelstein 7-X stellarator," *Rev. Sci. Instrum.*, vol. 70, no. 1, pp. 1185–1189.

[8] D. Klir, J. Kravarik, P. Kubes, K. Rezac, E. Litseva, K. Tomaszewski, L. Karpinski, M. Paduch, and M. Scholz, "Fusion neutron detector for time-of-flight measurements in z-pinch and plasma focus experiments," *Rev. Sci. Instrum.*, vol. 82, no. 3, pp. 033505–7, 2011.

[9] Y. Jian-Lun, , W. Gen-Xing, Z. Qi-Hua, W. Shu-Huai, L. Zhong-Li, Y. Hong-Qiong, T. Zheng-Yuan, W. Shi-Bin, and W. Fan, "Neutron detector for fusion burn history measurements," *Acta Phys. Sin.-Ov. Ed.*, vol. 8, pp. 768–775, October 1999.

[10] NIST Center for Neutron Research, "How are neutrons useful?." http://www.ncnr.nist.gov/why_neutrons.html, June 2010.

[11] B. Hammouda, *Probing Nanoscale Structures – The SANS Toolbox*. NIST, 2010.

[12] J. Buffet, J. Clergeau, R. Cooper, J. Darpentigny, A. D. Laulany, C. Fermon, S. Fetal, F. Fraga, B. Guerard, R. Kampmann, A. Kastenmueller, G. McIntyre, G. Manzin, F. Meilleur, N. Rhodes, L. Rosta, E. Schooneveld, G. Smith,

H. Takahashi, P. V. Esch, T. V. Vuure, and K. Zeitelhack, "Advances in detectors for single crystal neutron diffraction," *Nucl. Instrum. Meth. A*, vol. 554, pp. 392–405, 2005.

[13] M. Johnson, S. Manolopoulos, N. Rhodes, E. Schooneveld, R. Turchetta, and M. Daymond, "Silicon APS detectors for neutron scattering," *Nucl. Instrum. Meth. A*, vol. 501, pp. 72–79, Mar. 2003.

[14] H. Tanaka, T. Nakamura, H. Yamagishi, K. Soyama, and K. Aizawa, "A two-dimensional gas detector with individual readouts for neutron detection with a high spatial resolution and fast temporal response," *Rev. Sci. Instrum.*, vol. 76, no. 9, p. 093302, 2005.

[15] S. Burgos, J. Forbes, C. Ghag, M. Gold, V. Kudryavtsev, T. Lawson, D. Loomba, P. Majewski, D. Muna, A. S. Murphy, G. Nicklin, S. Paling, A. Petkov, S. Plank, M. Robinson, N. Sanghi, N. Smith, D. Snowden-lfft, N. Spooner, T. Sumner, J. Turk, and E. Tziaferi, "Studies of neutron detection and backgrounds with the DRIFT-IIa dark matter detector," *Astropart. Phys.*, vol. 28, pp. 409–421, December 2007.

[16] D. Chandler, "New detector will aid dark matter search," *MIT TechTalk*, vol. 53, December 2008.

[17] S. Monk, M. Joyce, Z. Jarrah, D. King, and M. Oppenheim, "A portable energy-sensitive cosmic neutron detection instrument," *Rev. Sci. Instrum.*, vol. 79, no. 2, p. 023301, 2008.

[18] P. Mosteiro, "Cosmogenic neutron background in dark matter detectors," presentation, Princeton University, 2012.

[19] M. Oraby, K. Verghese, and R. Gardner, "Investigation of an improved-sensitivity neutron-porosity oil-well logging tool," *Nucl. Instrum. Meth. A*, vol. 299, no. 1-3, pp. 674–681, 1990.

[20] J. Reijonen, "Nuclear tools for oilfield logging-while-drilling applications," *AIP Conf. Proc.*, vol. 1336, no. 1, pp. 433–436, 2011.

[21] W. W. Givens and W. R. Mills, "Directional epithermal neutron detector," patent, United States Patent Office, April 1986.

[22] T. M. Persons and G. Aloise, "Neutron detectors: Alternatives to using helium-3," tech. report GAO-11-753, United States Government Accountability Office, September 2011.

[23] R. Runkle, A. Bernstein, and P. Vanier, "Securing special nuclear material: Recent advances in neutron detection and their role in nonproliferation," *J. Appl. Phys.*, vol. 108, no. 11, p. 111101, 2010.

[24] R. V. Ginhoven, R. Kouzes, and D. Stevens, "Alternative neutron detector technologies for homeland security," tech. report PNNL-18471, Pacific Northwest National Laboratory, 2009.

[25] R. C. Byrd, J. M. Moss, W. C. Priedhorsky, C. Pura, G. Richter, K. Sager, and W. Scarlett, "Nuclear detection to prevent or defeat clandestine nuclear attack," *IEEE Sens. J.*, vol. 5, p. 593, August 2005.

[26] R. T. Kouzes, E. R. Siciliano, J. H. Ely, P. E. Keller, and R. J. McConn, "Passive neutron detection for interdiction of nuclear material at borders," *Nucl. Instrum. Meth. A*, vol. 584, pp. 383–400, January 2008.

[27] J. Hall, S. Asztalos, P. Biltoft, J. Church, M.-A. Descalle, T. Luu, D. Manatt, G. Mauger, E. Norman, D. Petersen, J. Pruet, S. Prussin, and D. Slaughter, "The nuclear car wash: Neutron interrogation of cargo containers to detect hidden SNM," *Nucl. Instrum. Meth. B*, vol. 261, no. 1-2, pp. 337–340, 2007.

[28] J. K. Shultis and R. E. Faw, *Radiation Shielding*. American Nuclear Society, 2000.

[29] Institute of Atomic and Subatomic Physics, "Neutron radiography of a camera." http://www.ati.ac.at/~neutropt/experiments/Radiography/radiography.html, July 2012.

[30] Oak Ridge National Lab, "Preparing for the threats," *Oak Ridge National Laboratory Review*, vol. 39, no. 1, 2006.

[31] R. Kouzes, "The helium-3 supply problem," tech. report PNNL-18388, Pacific Northwest National Laboratory, April 2009.

[32] National Nuclear Data Center, "Chart of nuclides database." http://www.nndc.bnl.gov/chart/, April 2012.

[33] D. Dixon, "Helium-3 shortage could mean nuke detection disaster," *Wired*, April 2010.

[34] G. Aloise and T. M. Persons, "Managing critical isotopes: Weaknesses in DOE's management of helium-3 delayed the federal response to a critical supply shortage," tech. report GAO-11-472, Government Accountability Office, May 2011.

[35] A. Simpson, S. Jones, M. Clapham, and S. McElhaney, "A review of neutron detection technology alternatives to helium-3 for safeguards applications," *INMM Proc.*, July 2011.

[36] R. Huffman, J. Larrabee, and Y. Tanaka, "Rare gas continuum light sources for photoelectric scanning in the vacuum ultraviolet," *Appl. Optics*, vol. 4, pp. 1581–1588, December 1965.

[37] R. Chandrasekharan, M. Messina, and A. Rubbia, "Detection of noble gas scintillation light with large area avalanche photodiodes (LAAPDs)," *Nucl. Instrum. Meth. A*, vol. 546, no. 3, pp. 426–437, 2005.

[38] K. Saito, H. Tawara, T. Sanami, E. Shibamur, and S. Sasaki, "Absolute number of scintillation photons emitted by alpha particles in rare gases," *IEEE T. Nucl. Sci.*, vol. 49, no. 4, pp. 1674–1680, 2002.

[39] P. P. Hughes, M. A. Coplan, A. K. Thompson, R. E. Vest, and C. W. Clark, "Far-ultraviolet signatures of the ^{3}He(n, tp) reaction in noble gas mixtures," *Appl. Phys. Lett.*, vol. 97, no. 23, pp. 234105–3, 2010.

[40] J. Chadwick, "Possible existence of a neutron," *Nature*, vol. 129, no. 3252, p. 312, 1932.

[41] K. S. Krane, *Introductory Nuclear Physics*. USA: John Wiley and Sons, 2 ed., 1988.

[42] R. A. Dunlap, *The Physics of Nuclei and Particles*. Belmont, CA: Thomson, Brooks/Cole, 2004.

[43] CODATA, "The NIST reference on constants, units and uncertainty." http://physics.nist.gov/cuu/Constants/, June 2011.

[44] J. Beringer and *et al.* (Particle Data Group), "The review of particle physics," *Phys. Rev.*, vol. D86, p. 010001, 2012.

[45] R. Golub and P. Huffman, "Search for a neutron electric dipole moment," *J. Res. Natl. Inst. Stan.*, vol. 110, May-June 2005.

[46] S. Mughabghab, *Atlas of Neutron Resonances: Resonance Parameters and Thermal Neutron Cross Sections*. Oxford, UK: Elsevier, 5 ed., 2006.

[47] University of Cambridge: Materials for Nuclear Power Generation, "Plot of neutron cross sections." http://www.doitpoms.ac.uk/tlplib/nuclear_materials/cross_section.php, May 2012.

[48] T. Crane and M. Baker, *Passive Nondestructive Assay of Nuclear Material*, ch. 13. NRC, 1991.

[49] Stony Brook Dept. of Physics and Astronomy, "Gas multiplication curves." http://felix.physics.sunysb.edu/allen/252/PHY251_Geiger.html, August 1998.

[50] R. Kouzes, J. Ely, A. Lintereur, E. Siciliano, and M. Woodring, "BF_3 neutron detector tests," tech. report PNNL-19050, Pacific Northwest National Laboratory, 2009.

[51] A. Lintereur, R. Kouzes, J. Ely, L. Erikson, and E. Siciliano, "Boron-lined neutron detector measurements," Tech. Rep. PNNL-18938, Pacific Northwest National Laboratory, 2009.

[52] R. Kouzes, "Boron-lined straw-tube neutron detector test," tech. report PNNL-19600, Pacific Northwest National Laboratory, August 2010.

[53] C. Morris, T. Bowles, J. Gonzales, R. Hill, G. Hogan, M. Makela, R. Mortenson, J. Ramsey, A. Saunders, S. Seestrom, W. Sondheim, W. Teasdale, H. Back, R. Pattie, A. Holley, A. Young, L. Broussard, K. Hickerson, J. Liu, M. Mendenhall, B. Plaster, R. Mammei, M. Pitt, R. Vogelaar, R. Rios, and J. Martin, "Multi-wire proportional chamber for ultra-cold neutron detection," *Nucl. Instrum. Meth. A*, vol. 599, pp. 248–250, February 2009.

[54] E. Aprile, A. Bolotnikov, A. Bolozdynya, and T. Doke, *Noble Gas Detectors*. Berlin: Wiley VCH, 2006.

[55] R. L. Aamodt, L. J. Brown, and G. M. Smith, "High pressure ^{3}He gas scintillation neutron detector," *Rev. Sci. Instrum.*, vol. 37, pp. 1338–1340, October 1966.

[56] M. S. Derzon, D. R. Slaughter, and S. G. Prussin, "A high-pressure ^{3}He gas scintillation neutron spectrometer," *IEEE T. Nucl. Sci.*, vol. 33, February 1986.

[57] Bruker AXS, Inc., "Diagram of a scintillation neutron detector." http://bruker-axs.de/fileadmin/xrfintro/sec1_6.html, May 2012.

[58] P. Reeder, A. Peurrung, R. Hansen, D. Stromswold, W. Hensley, and C. Hubbard, "Detection of fast neutrons in a plastic scintillator using digital pulse processing to reject gammas," *Nucl. Instrum. Meth. A*, vol. 422, no. 1-3, pp. 84–88, 1999.

[59] S. Yousefi, L. Lucchese, and M. Aspinall, "Digital discrimination of neutrons and gamma-rays in liquid scintillators using wavelets," *Nucl. Instrum. Meth. A*, vol. 598, no. 2, pp. 551–555, 2009.

[60] Wikipedia, "Diagram of fluorescence and phosphorescence." http://en.wikipedia.org/wiki/Phosphorescence, June 2012.

[61] J. Tain, "Neutron detection," presentation, Instituto de Fisica Corpuscular, February 2005.

[62] J. Uher, *3D Neutron Detectors*. PhD thesis, Academy of Sciences of the Czech Republic, 2007.

[63] T. Kojima, M. Katagiri, N. Tsutsui, K. Imai, M. Matsubayashi, and K. Sakasai, "Neutron scintillators with high detection efficiency," *Nucl. Instrum. Meth. A*, vol. 529, pp. 325–328, 2004.

[64] C. van Eijk, A. Bessiere, and P. Dorenbos, "Inorganic thermal-neutron scintillators," *Nucl. Instrum. Meth. A*, vol. 529, pp. 260–267, 2004.

[65] Z. W. Bell, D. Carpenter, S. Cristy, V. Lamberti, A. Burger, B. F. Woodfield, T. Niedermayr, I. D. Hau, S. E. Labov, S. Friedrich, W. G. West, K. R. Pohl, and L. van der Berg, "Neutron detection with cryogenics and semiconductors," *Phys. Status Solidi B*, vol. 2, no. 5, pp. 1592–1605, 2005.

[66] A. Conway, L. Voss, C. Reinhardt, R. Graff, T. Wang, R. Nikolic, N. Deo, and C. Cheung, "Silicon based thermal neutron detectors," presentation, Lawrence Livermore National Laboratory, 2011.

[67] D. McGregor, M. Hammig, Y. Yang, H. Gersch, and R. Klann, "Design considerations for thin film coated semiconductor thermal neutron detectors," *Nucl. Instrum. Meth. A*, vol. 500, pp. 272–308, 2003.

[68] A. Conway, T. Wang, N. Deo, C. Cheung, and R. Nikolic, "Numerical simulations of pillar structured solid state thermal neutron detector efficiency and gamma discrimination," tech. report LLNL-JRNL-405025, Lawrence Livermore National Laboratory, June 2008.

[69] T. Mason, "Neutron detectors for materials research," presentation, Oak Ridge National Laboratory, 2011.

[70] C. Guardiola, J. Rodriguez, C. Fleta, D. Quirion, and M. Lozano, "Portable silicon neutron detector system," *Proc. Span. Conf. Elec. Dev.*, 2011.

[71] S. Almaviva, M. Marinelli, E. Milani, G. Prestopino, A. Tucciarone, C. Verona, G. Verona-Rinati, M. Angelone, D. Lattanzi, M. Pillon, R. Montereali, and M. Vincenti, "Thermal and fast neutron detection in chemical vapor deposition single-crystal diamond detectors," *J. Appl. Phys.*, vol. 103, no. 5, p. 054501, 2008.

[72] G. W. Fraser, J. F. Pearson, and O. S. Al-Horayess, "Thermal neutron imaging using microchannel plates," *Proc. SPIE*, vol. 1737, pp. 298–307, 1993.

[73] S. Dazeley, A. Bernstein, N. Bowden, and R. Svoboda, "Observation of neutrons with a gadolinium doped water Cherenkov detector," *Nucl. Instrum. Meth. A*, vol. 607, pp. 616–619, 2009.

[74] D. Jordan, J. Ely, A. P. L. Bond, J. Collar, M. Flake, M. Knopf, W. Pitts, M. Shaver, A. Sonnenschein, J. Smart, and L. Todd, "Neutron detection via bubble chambers," *Appl. Radiat. Isotopes*, vol. 63, no. 5-6, pp. 645–653, 2005.

[75] T. Niedermayr, I. Hau, T. Miyazaki, S. Terracol, A. Burger, V. Lamberti, Z. Bell, J. Vujic, S. Labov, and S. Friedrich, "Microcalorimeter design for fast-neutron spectroscopy," *Nucl. Instrum. Meth. A*, vol. 520, no. 1-3, pp. 70–72, 2004.

[76] Wolfram Alpha. http://www.wolframalpha.com/, June 2012.

[77] G. Hale and P. Young, "ENDF/B-VII." http://www.nndc.bnl.gov/exfor/endf00.jsp, April 2006.

[78] Z. Wang and C. Morris, "Multi-layer boron thin-film detectors for neutrons," *Nucl. Instrum. Meth. A*, vol. 652, no. 1, pp. 323–325, 2011.

[79] M. Hutchinson, "Excimers and excimer lasers," *Appl. Phys.*, vol. 21, pp. 95–114, 1980.

[80] J. Birks, "Excimers," *Rep. Prog. Phys.*, vol. 38, no. 8, 1975.

[81] C. K. Rhodes, ed., *Excimer Lasers*. Berlin: Springer-Verlag, 2nd ed., 1984.

[82] M. Mutterer, P. Grimm, H. Heckwolf, J. Pannicke, W. Spreng, and J. Theobald, "Response of gas scintillators to heavy charged particles," *Lect. Notes Phys.*, vol. 178, pp. 63–79, 1983.

[83] T. Stewart, G. Hurst, T. Bortner, J. Parks, F. Martin, and H. Weidner, "Proton excitation of continuous emission in the noble gases," *J. Opt. Soc. Am.*, vol. 60, pp. 1290–1297, October 1970.

[84] A. Policarpo, "Light production and gaseous detectors," *Phys. Scripta*, vol. 23, pp. 539–549, 1981.

[85] M. Dantus, R. Bowman, and A. Zewail, "Femtosecond laser observations of molecular vibration and rotation," *Nature*, vol. 343, pp. 737–739, February 1990.

[86] M. Mutterer, J. Theobald, and K.-P. Schelhaas, "A low-pressure noble-gas scintillation counter for heavy-ion detection," *Nucl. Instrum. Meth.*, vol. 144, pp. 159–166, 1977.

[87] H. Koehler, L. Federber, D. Redhead, and P. Ebert, "Vacuum-ultraviolet emission from high-pressure xenon and argon excited by high-current relativistic electron beams," *Phys. Rev. A*, vol. 9, no. 2, 1974.

[88] E. Morikawa, R. Reininger, P. Gurtler, and V. Saile, "Argon, krypton and xenon excimer luminescence: From the dilute gas to the condense phase," *J. Chem. Phys.*, vol. 91, no. 3, 1989.

[89] T. Doke, A. Hitachi, J. Kikuchi, K. Masuda, H. Okada, and E. Shibamura, "Absolute scintillation yields in liquid argon and xenon for various particles," *Jpn. J. Appl. Phys.*, vol. 41, pp. 1538–1545, 2002.

[90] R. Bernabei, P. Belli, A. Incicchitti, and D. Prosperi, "Liquid noble gases for dark matter searches: A synoptic survey," *arXiv*, May 2009.

[91] C. Monteiro, L. Fernandes, J. Lopes, L. Coelho, J. Veloso, J. dos Santos, K. Giboni, and E. Aprile, "Secondary scintillation yield in pure xenon," *J. Instrum.*, vol. 2, May 2007.

[92] M. Miyajima, K. Masude, Y. Hoshi, T. Doke, T. Takahashi, T. Hamada, S. Kubota, A. Nakamoto, and E. Shibamura, "A self-triggered liequid xenon drift chamber by the use of proportional ionization or proportional scintillation," *Nucl. Instrum. Meth.*, vol. 160, pp. 239–246, 1979.

[93] E. Aprile, "Liquid xenon detectors for particle physics and astrophysics," *Rev. Mod. Phys.*, vol. 82, no. 3, pp. 2053–2097, 2010.

[94] T. Dias, F. Santos, P. Rachinhas, F. Borges, J. dos Santos C.A.N. Conde, and A. Stauffer, "Xenon-neon gas proportional scintillation counters: Experimental and simulation results," *J. Appl. Phys.*, vol. 85, no. 9, p. 6303, 1999.

[95] M. Plum, E. Bravin, J. Bosser, and R. Maccaferri, "Nitrogen and xenon gas scintillation cross-section, spectrum and lifetime measurements from 50 MeV to 25 GeV at the CERN PS and Booster," *Nucl. Instrum. Meth. A*, vol. 492, pp. 64–90, 2002.

[96] NIST Center for Neutron Research, "NCNR Instrumentation." http://www.ncnr.nist.gov/instruments/index.html, April 2012.

[97] R. E. Williams, "The NIST research reactor and cold neutron source," presentation, NIST Center for Neutron Research, June 2007.

[98] J. Nico, M. Arif, M. Dewey, T. Gentile, D. Gilliam, P. Huffman, D. Jacobson, and A. Thompson, "The fundamental neutron physics facilities at NIST," *J. Res. Natl. Inst. Stan.*, vol. 110, no. 3, pp. 137–144, 2005.

[99] A. K. Thompson, M. A. Coplan, J. W. Cooper, P. P. Hughes, R. E. Vest, and C. W. Clark, "Observation of the ^{3}He(n, tp) reaction by detection of far-ultraviolet radiation," *J. Res. Natl. Inst. Stan.*, vol. 113, March-April 2008.

[100] J. W. Cooper and P. P. Hughes, "The detection of Lyman-alpha radiation formed by the slowing down of protons and tritons produced by the ^{3}He(n, tp) reaction – a model study," *J. Res. Natl. Inst. Stan.*, vol. 114, no. 3, pp. 185–199, 2009.

[101] Maryland University Training Reactor, *Safety Analysis Report*, February 2000.

[102] T. Koeth, "Photograph of the MUTR core."

[103] Hamamatsu Photonics, Japan, *Photomultiplier Tube R6835*, 2000.

[104] W. Otano-Rivera, L. J. Pilione, J. A. Zapien, and R. Messier, "Cubic boron nitride thin film deposition by unbalanced magnetron sputtering and DC pulsed substrate biasing," *J. Vac. Sci. Technol. A*, vol. 16, no. 3, pp. 1331–1335, 1998.

[105] Y. Tzeng and H. Zhu, "Electron-assisted deposition of cubic boron nitride by RF magnetron sputtering," *Diam. Relat. Mater.*, vol. 8, pp. 1402–1405, 1999.

[106] J. Deng, B. Wang, L. Tan, H. Yan, and G. Chen, "The growth of cubic boron nitride films by RF reactive sputter," *Thin Solid Films*, vol. 368, no. 312-314, 2000.

[107] C. Rohr, J.-H. Boo, and W. Ho, "The growth of hexagonal boron nitride thin films on silicon using single source precursor," *Thin Solid Films*, vol. 322, pp. 9–13, 1998.

[108] T. Ichiki and T. Yoshida, "Preparation of cubic boron nitride films by low-pressure ICP-CVD," *Appl. Phys. Lett.*, vol. 64, no. 851, 1994.

[109] H. Sachdev, F. Muller, and S. Hufner, "Formation of boron-based films and boron nitride layers by CVD of a boron ester," *ChemInform*, vol. 42, no. 28, 2011.

[110] S.-H. Park, H.-S. Kim, and J.-H. Ha, "Fabrication of a GEM-based gas detector for thermal neutron measurement," *J. Korean Phys. Soc.*, vol. 49, no. 5, pp. 1939–1943, 2006.

[111] T. Akan, N. Ekem, S. Pat, U. Issever, M. Balbag, M. Cenik, R. Vladoiu, and G. Musa, "Boron thin film deposition by using thermionic vacuum arc technology," *Mater. Lett.*, vol. 61, pp. 23–26, 2007.

[112] G. Musa, R. Vladoiu, V. Ciupina, C. Lungu, I. Mustata, S. Pat, T. Akan, and N. Ekem, "Characteristics of boron thin films obtained by TVA technology," *J. Optoelectron. Adv. M.*, vol. 8, no. 2, pp. 617–620, 2006.

[113] G. Yukin, "The mechanism of electroplating with boron," *Met. Sci. Heat Treat.*, vol. 13, no. 8, pp. 662–664, 1971.

[114] Z.-F. Song, S.-Z. Yi, Z.-Y. Chen, L. Song, and J. Shen, "Study on boron-film thermal neutron converter prepared by pulsed laser deposition," *Appl. Radiat. Isotopes*, vol. 69, no. 443-447, 2011.

[115] S. ichi Aoqui, H. Miyata, T. Ohshima, T. Ikegami, and K. Ebihara, "Preparation of boron carbide thin film by pulsed KrF excimer laser deposition process," *Thin Solid Films*, vol. 407, pp. 126–131, 2002.

[116] F. Perkins, M. Onellion, S. Lee, D. Li, J. Mazarowski, and P. Dowben, "Synchrotron-radiation-induced deposition of boron and boron carbide films from boranes and carboranes," *Appl. Phys. A*, vol. 54, pp. 442–450, 1992.

[117] Brigham Young University, "Diagram of electron beam evaporation." http://www.cleanroom.byu.edu/metal.phtml.

[118] National Institute of Standards and Technology, "NIST CNST NanoFab Equipment Metal Deposition." http://www.cnst.nist.gov/nanofab/nanofab_equipment/metal_dep.html.

[119] D. Jacobson, D. Hussey, E. Baltic, T. Udovic, J. Rush, and R. Bowman, "Neutron imaging studies of metal-hydride storage beds," in *Asian Hydrogen Energy Conference*, vol. 35, pp. 12837–12845, 2009.

[120] D. Hussey, E. Baltic, K. Coakley, and D. Jacobson, "Improving quantitative neutron radiography through image restoration." unpublished.

[121] Saclay Institue of Matter and Radiation, "Diagram of x-ray photoelectron spectroscopy." http://iramis.cea.fr/en/Phocea/Vie_des_labos/Ast/ast_sstechnique.php, July 2012.

[122] UMD Department of Chemistry and Biochemistry, "Photograph of XPS tool." http://www.chem.umd.edu/researh/sharedinstrumentation/xrayphotoelectronspectroscopy.

[123] H. Piao and N. McIntyre, "Adventitious carbon growth on aluminium and gold-aluminium alloy surfaces," *Surf. Interface Anal.*, vol. 33, pp. 591–594, 2002.

[124] J. F. Moulder, W. F. Stickle, P. E. Sobol, and K. D. Bomben, *Handbook of X-Ray Photoelectron Spectroscopy*. Minnesota, USA: Physical Electronics, 1995.

[125] B. Cullity, *Elements of X-Ray Diffraction*. Reading, Massachusettes: Addison-Wesley Publishing Company, 1956.

[126] J. V. Bhardwaj, *X-ray diffraction study of the structure of boron*. PhD thesis, Rice University, Houston, TX, December 1979.

[127] The University of Iowa, "Diagram of an SEM." http://www.uiowa.edu/~cmrf/methodology/sem/index.html, July 2012.

[128] U. Arp, C. Clark, A. Farrell, E. Fein, M. Furst, and E. Hagley, "Synchrotron ultraviolet radiation facility: SURF III," *Rev. Sci. Instrum.*, vol. 73, no. 3, pp. 1674–1676.

[129] U. Arp, R. Friedman, M. L. Furst, S. Makar, and P. S. Shaw, "SURF III - an improved storage ring for radiometry," *Metrologia*, vol. 37, no. 5, pp. 357–360, 2000.

[130] P.-S. Shaw, K. R. Lykke, R. Gupta, T. R. O'Brian, U. Arp, H. H. White, T. B. Lucatorto, J. L. Dehmer, and A. C. Parr, "Ultraviolet radiometry with synchrotron radiation and ultraviolet radiometry," *Appl. Optics*, vol. 38, no. 1, pp. 18–27, 1999.

[131] U. Arp, C. Clark, L. Deng, N. Faradzhev, A. Farrell, M. Furst, S. Grantham, E. Hagley, S. Hill, T. Lucatorto, P. Shaw, C. Tarrio, and R. Vest, "SURF III : A flexible synchrotron radiation source for radiometry and research," *Nucl. Instrum. Meth. A*, vol. 649, pp. 12–14, 2010.

[132] J. A. Samson and D. L. Ederer, *Vacuum Ultraviolet Spectroscopy*. Academic Press, 2000.

[133] D. Ederer, B. Cole, and J. West, "A high throughput 2 m normal incidence monochromator for SURF-II," *Nucl. Instrum. Meth.*, vol. 172, no. 1-2, pp. 185–190, 1980.

[134] U. Arp, "Photograph of the SURF."

[135] L. Canfield, *Vacuum Ultraviolet Spectroscopy*, ch. Photodiode Detectors. Academic Press, 2000.

[136] R. Vest, "Photodiode Responsivity Data."

[137] Z. Chowdhuri, *Absolute Neutron Measurements in Neutron Decay*. PhD thesis, Indiana University, June 2000.

[138] X-5 Monte Carlo Team, *MCNP – A General Monte Carlo N-Particle Transport Code, Version 5*. Los Alamos National Laboratory, February 2008.

[139] A. B. Mohamed, *Flux Maps Obtained from Core Geometry Approximations: Monte Carlo simulations and benchmark measurements for a 250kW TRIGA reactor*. PhD thesis, University of Maryland, 2009.

[140] J. Shultis and R. Faw, *An MCNP Primer*. Kansas State University, 2006.

[141] J. Ziegler, J. Biersack, and M. Ziegler, *SRIM - The Stopping and Range of Ions in Matter*. James Ziegler, 2008.

[142] J. Ziegler, "SRIM Software." http://www.srim.org.

[143] E. W. Weisstein, "Sphere point picking." http://mathworld.wolfram.com/SpherePointPicking.html, July 2012.

[144] M. Vidal-Dasilva, M. Fernandez-Perea, J. A. Mendez, J. A. Aznarez, and J. I. Larruquert, "Electron-beam deposited boron coatings for the extreme ultraviolet," *Appl. Optics*, vol. 47, pp. 2926–2930, June 2008.

[145] M. P. Newell and R. A. M. Keski-Kuha, "Bidirectional reflectance distribution function of diffuse extreme ultraviolet scatters and extreme ultraviolet baffle materials," *Appl. Optics*, vol. 36, pp. 5471–5475, August 1997.

[146] Photon Engineering, "FRED Software." http://www.photonengr.com/software/, July 2012.

[147] B. Dolgoshein and B. Rodionov, "The noble gas scintillation mechanism," *Elem. Part. and Cosm. Rays*, no. 2, pp. 170–198, 1972.